Strong atom-light interactions along nanostructures: Transition from free-space to nanophotonic interfaces

Thesis by

Akihisa Goban

In Partial Fulfillment of the Requirements

for the Degree of

Doctor of Philosophy

California Institute of Technology

Pasadena, California

2015

(Submitted May 20, 2015)

To my family,

Acknowledgments

First and foremost, I would like to thank my advisor Jeff Kimble for his support and encouragement during the completion of the work presented in this thesis. His keen scientific insight and relentless curiosity have never ceased to be inspiring and have kept me challenged during those years that I had the privilege to be his student. Needless to say, his tireless efforts have played a key role in the progress we have made these past few years. One of the most memorable moments outside the lab was "Quantum Optics Frontier" symposium in celebration of Jeff's 65th birthday. I enjoyed catching a glimpse of the history of quantum optics and quantum information science, and felt excited about the future of these fields. I have also been fortunate to interact with Oskar Painter, whose creativity and perspective opened a new opportunity to investigate atom-photon interaction in the photonics crystal waveguide.

The work described in this thesis is a result of contributions of many people that I would like to acknowledge here. During the completion of this work, I have had the privilege to work with many talented colleagues, in particular, Kyung Soo Choi and Chen-Lung Hung. From day one in Lab 2, Kyung was my mentor. He taught me all the details of complicated experiments patiently, and how critical it is to set the high standards for making things work well in the lab. I admire Kyung for his precise, thorough approach to physics, and his extremely hard work driven by his unquenchable curiosity in physics. Chen-Lung's arrival in Quantum optics group triggered another exciting journey. Taking apart the historic cavity QED experiments in Lab 11 and building up the new lab with him was a great experience. Over the next three years, I learned a tremendous amount from him and enjoyed working with him greatly. Jonathan Hood and Su-Peng Yu's relentless efforts on device fabrication accelerated our progress dramatically. Without their hard work and dedication, this project would not have taken off as of today. I owe them a special debt of gratitude. I have no doubt that its future will be bright in the hands of the Lab 11 crew of Jonathan Hood, Su-Peng Yu,

and Mingwu Lu. I have also been fortunate to interact with Darrick Chang, who has brought a broad range of exciting proposals and grand challenges for our experiments. I have also worked with an amazing set of colleagues on this new project: Juan Andrés Muniz, Andrew McClung, Jae Hoon Lee, Michael Martin, and Lucas Peng in Lab 2, and Richard Norte, Justin Cohen, and Seán Meenehan in Painter group. Particularly, Juan has been a good friend and co-worker, and a separate paragraph of gratitude could be written about him. It was great to have so many other graduate students and postdocs to talk to and learn from over the past years, including Dalziel Wilson, Daniel Alton, Ding Ding, Scott Papp, Cindy Regal, Kang-Kuen Ni, Clément Lacroûte, Martin Pototshcnig, and Pol Forn-Diaz.

I would also like to acknowledge the Nakajima Foundation for their financial support throughout my PhD research.

Finally, I deeply appreciate the support I have received from my family. Their unquestioning support has been essential to the completion of this work.

Abstract

An exciting frontier in quantum information science is the integration of otherwise "simple" quantum elements into complex quantum networks. The laboratory realization of even small quantum networks enables the exploration of physical systems that have not heretofore existed in the natural world. Within this context, there is active research to achieve nanoscale quantum optical circuits, for which atoms are trapped near nano-scopic dielectric structures and "wired" together by photons propagating through the circuit elements. Single atoms and atomic ensembles endow quantum functionality for otherwise linear optical circuits and thereby enable the capability of building quantum networks component by component. Toward these goals, we have experimentally investigated three different systems, from conventional to rather exotic systems : free-space atomic ensembles, optical nano fibers, and photonics crystal waveguides. First, we demonstrate measurement-induced quadripartite entanglement among four quantum memories. Next, following the landmark realization of a nanofiber trap, we demonstrate the implementation of a state-insensitive, compensated nanofiber trap. Finally, we reach more exotic systems based on photonics crystal devices. Beyond conventional topologies of resonators and waveguides, new opportunities emerge from the powerful capabilities of dispersion and modal engineering in photonic crystal waveguides. We have implemented an integrated optical circuit with a photonics crystal waveguide capable of both trapping and interfacing atoms with guided photons, and have observed the collective effect, superradiance, mediated by the guided photons. These advances provide an important capability for engineered light-matter interactions, enabling explorations of novel quantum transport and quantum many-body phenomena.

Contents

List of Figures

Chapter 1

Introduction

1.1 Quantum networks

In quantum information science, quantum networks provide a broad frontier of scientific opportunities [1], including quantum computation [2, 3], communication [4], and metrology [5]. Quantum networks are composed of quantum nodes where quantum information is generated, processed and stored locally, and these nodes are linked by quantum channels to transfer the quantum information. From a different point of view, a quantum network can be viewed as a quantum 'simulator', enabling one to investigate the evolution of quantum many-body systems arising from interactions among the nodes mediated by the channels [6, 7]. The physical realization of quantum networks requires dynamical systems capable of generating and storing entangled states among multiple quantum memories, and efficiently transferring stored entanglement into quantum channels with high fidelity for distribution across the networks.

While photons are ideal carriers for transporting quantum information faithfully over long distances as flying qubits, atoms can be used to process and store quantum information as stationary qubits. The major challenge of distributing quantum states across a quantum network is to reversibly map quantum states between photons and atoms. The coherent control of the atom-photon interaction at the single-photon level provides a basis for quantum networks, which leads to successful operation of many quantum information protocols, including entanglement generation and swapping between two distant atoms, and implementation of elementary quantum gates. In order to create such efficient quantum interfaces, the realization of strong atom-photon interaction is a long-standing goal of both fundamental and technological significance.

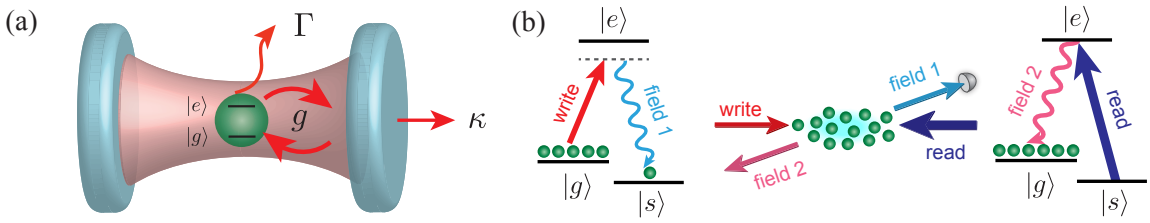

Figure 1.1: **Schematics of cavity QED with a single atom and of the DLCZ protocol with an atomic ensemble.** (a) A two-level atom with ground state $|g\rangle$ and excited state $|e\rangle$ couples to the high finesse cavity with a coupling rate g. The condition for the observation of coherent dynamics reads $g > (\kappa, \Gamma)$, where the decay rate out of the cavity κ and the atomic decay rate Γ. (b) A schematic of DLCZ building block. Initially, all the atoms are prepared in the ground state $|g\rangle$. A weak 'write' pulse induces spontaneous Raman transitions to the metastable state $|s\rangle$, resulting in the emission of a photon 'field 1' together with the storage of a collective excitation. After a programmable delay, a strong 'read' pulse retrieves the single excitation to another photonic mode 'field 2' with high efficiency due to the collective interaction.

1.2 Conventional strong atom-photon interaction

Strong atom-photon interaction is essential for successful operation of quantum information protocols [8]. However, a single atom does not interact with photons easily in free space due to the diffraction of a tightly focused beam. There are two well-known approaches to enhance the atom-photon coupling rate: (i) cavity-enhanced interaction and (ii) collectively enhanced interaction of an atomic ensemble.

1.2.1 Cavity QED with a single atom

One approach for enhancing the atom-photon coupling is to use a high finesse cavity where the photon is spatially confined and trapped [9–11]. The atom-photon coupling is enhanced by the number of bounces the photon makes between the two mirrors before being lost from the cavity. The "strong-coupling" regime of cavity QED is achieved when the coupling rate g of absorption or emission of a single photon by the atom is larger than both the decay rate κ out of the cavity and the atomic decay rate Γ, typically characterized by a single-atom cooperativity parameter $C \equiv \frac{(2g)^2}{2\kappa\Gamma} > 1$. The optical nonlinearity arises from the saturation of atomic absorption since the single atom can absorb or emit only one photon at a given time. A large cooperativity $C > 1$ ensures that even a single photon can modify the response of a single atom inside the cavity. Such single-atom cavity QED systems have been used to demonstrate a variety of nonlinear effects (i.e., nonlinear phase shifts with single photons [12, 13] and generation of non-classical state of light [14]) and their application to elementary quantum networking between two quantum nodes [15]. In the

microwave regime, significant progress has been made by using Rydberg atoms in high-Q cavities [16], and superconducting circuits as artificial atoms [17].

1.2.2 Collective atom-photon coupling with atomic ensembles

An alternative approach is to prepare a collective state of N atoms (i.e., Dicke state or superradiant state [18]) that exhibits enhanced coupling to a single electromagnetic mode. As illustrated in Fig. 1.1(b), for three-level atoms with two stable ground states $|g\rangle, |s\rangle$, the collective state $|\bar{s}_\epsilon\rangle \frac{1}{\sqrt{N}} \sum_{i=1}^{N} |g \cdots s_i \cdots g\rangle_\epsilon$ can be viewed as a spin wave, where a single excitation is shared among N atoms. This single excitation can be efficiently converted into a propagating photon by applying a strong phase-matched beam. A remarkable protocol for scalable quantum networks, the so-called "DLCZ" protocol, provides a new avenue for entanglement distribution by way of quantum-repeater architecture [4]. The DLCZ protocol is a probabilistic but heralded scheme based on entanglement generation among atomic ensembles via detection events of single photons in which the sources are intrinsically indistinguishable. Furthermore, the protocol is designed to be robust against experimental imperfections, including losses in propagation and detection, and detector dark counts. Indeed, the scheme functions with "built-in entanglement purification" and enables entanglement to be extended beyond the separation of two ensembles in an efficient and scalable fashion.

Based on the DLCZ protocol, remarkable experimental progresses has been achieved in demonstration of single-photon sources [19, 20], storage and retrieval of single photon [21–23], entanglement generation between two atomic ensembles [24, 25], and deterministic mapping of photonic entanglement into and out of atomic ensembles [26]. Later, the storage time of the quantum memory for single excitations is significantly improved to $\gtrsim 1$ s by suppressing the dephasing induced by the atomic motion [27–30]. These progresses are important steps towards the realization of long-distance quantum networks.

Despite its inherently multipartite nature, entanglement has been studied primarily for bipartite systems [2]. Beyond diverse bipartite systems, multipartite W states with a single photon shared among four optical modes has been unambiguously verified [31, 32]. Based on this entanglement verification technique, we have demonstrated measurement-induced entanglement of spin waves among four quantum memories, which is a promising advance towards multipartite quantum networks (Chapter 2) [33].

1.3 Integration of atoms and nanophotonics

An exciting frontier in quantum information science is the integration of otherwise "simple" quantum elements into complex quantum networks. Despite the remarkable advances in both cavity-QED-based networks and networks implemented using the DLCZ protocol, free-space approaches are unfavorable for large-scale quantum networks due to the technical complexities. Therefore, the laboratory realization of even small quantum networks enables the exploration of physical systems that have not heretofore existed in the natural world. Within this context, there is active research to achieve lithographic quantum optical circuits, for which atoms are trapped near micro- and nano-scopic dielectric structures and "wired" together by photons propagating through the circuit elements.

1.3.1 Cavity QED with micro- and nanoscopic cavities

Nano- and microscale optical systems have shown great progress towards realizing efficient and scalable quantum interfaces through enhanced atom-field coupling in cavity QED systems, including microtroidal and microsphere resonators [34–36], bottle micro-resonators [37], fiber cavities [38, 39], and photonic crystal cavities [40]. Most recently, the Lukin group demonstrated a photonics phase gate by using a single trapped atom evanescently coupled to the photonics crystal cavity with precise control of the position of the atom [41, 42]. Instead of using atoms, which have a drawback of finite trap lifetime in the cavity, it is also possible to use "artificial atoms" in a solid-state system, such as quantum dots [43–45] and nitrogen vacancy centers in diamond [46–48]. Such artificial atoms consist of effective two-level systems that have been used to demonstrate a variety of nonlinear effects similar to the "real" atom cavity QED systems [43–45, 49, 50].

1.3.2 Waveguide QED

Recently, there has been great effort to achieve the "strong coupling" regime in 1D waveguide systems, meaning that the Purcell factor $P \equiv \frac{\Gamma_{1D}}{\Gamma'}$ is larger than unity, where the decay rate into the guided mode Γ_{1D} and into all the other channels Γ', as illustrated in Fig. 1.2. Waveguide-QED systems benefit from the sub-wavelength confinement of light field inside the 1D waveguide, which couples to nearby atoms or embedded artificial atoms. Compared to cavity-QED systems, the key difference in the waveguide QED system is that

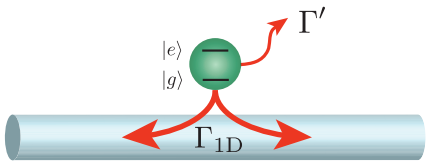

Figure 1.2: **A schematic of a single atom coupled to a 1D waveguide.** (a) A single atom couples to a waveguide mode with a coupling rate Γ_{1D}, while it also emits photons into all the other channels with a decay rate Γ'. The "strong coupling" regime in waveguide QED is categorized by the Purcell factor $P \equiv \frac{\Gamma_{1D}}{\Gamma'} > 1$.

the atoms couple to a continuum of guided modes. This relaxes the restriction of working with a narrow cavity bandwidth and avoids the complex tuning to match the cavity and the atomic resonances. 1D waveguide-QED systems are emerging as promising candidates for quantum information processing, motivated by tremendous experimental progress in a wide variety of systems, including plasmonic nanowires [51], hollow core fibers [52, 53], tapered nanofibres [54], quantum dot or diamond nanowires [55–57], and 1D open superconduting transmission lines [58–60].

In 2010, Rauschenbeutel group has demonstrated trapping and interfacing $\sim$ 2000 atoms by using a tapered nanofiber [61, 62], which has opened a new field of waveguide-QED with cold atomic ensembles. Following this landmark realization of the nanofiber trap, we switched our gear from free-space ensembles to fiber-coupled atomic ensembles. We have proposed and implemented a state-insensitive and compensated trap, with an optical depth per atom $d_1 \simeq 0.08$, improved by a factor of > 10 (Chapter 4 and 5)[63–65] compared to the pioneering work [61, 62]. However, due to the surface potential, it is practically difficult to trap atoms closer to the nanofiber, resulting in a small single-atom coupling rate $\Gamma_{1D}/\Gamma' \sim 0.04 \ll 1$. Despite the small coupling rate, there have been many advances, including directional spontaneous emission into the guided mode [66] and detection of a sub-Poissonian atom number distribution [67], with the help of a large number of trapped atoms coupled to the guided mode.

1.4 New avenue with photonic crystal waveguides

Around 2012, we began to collaborate with Painter's group to achieve both single-atom "strong coupling" $P > 1$ and interfacing ensembles of atoms by using lithographically patterned photonic crystal waveguides

(PCWs). Beyond conventional topologies of resonators and waveguides, powerful capabilities for dispersion and modal engineering in photonic crystal waveguides provide new opportunities to study nonlinear interactions between the atoms and the 1D guided mode. For example, the edge of a photonic band gap aligned near an atomic transition strongly enhances single atom emission into the one-dimensional PCW due to a van-Hove singularity at the band edge, i.e., a slow-light effect, which has been intensively studied in quantum-dot systems [68–70]. Because the Bloch function for a guided mode near the band edge approaches a standing-wave, symmetric optical excitations can be induced in an array of trapped atoms, resulting in superradiant emission. Finally, we made a rudimentary but crucial advance toward scalable quantum networks and quantum phases of light and matter by trapping and interfacing multiple atoms and observing cooperative emission mediated by the guided mode (Chapter 7).

1.4.1 Many-body physics with strongly interacting photons

Over the past few years, a single atom strongly coupled to a 1D waveguide has been studied extensively in theory [71–77]. Based on the strong nonlinear interactions between the atom and the guided mode, there have been many interesting proposals, including photon-photon bound states [72, 73], single-photon switches [74–76], and generation of long-distance entanglement [77]. Most proposals envision to generate single photons and control interactions between individual photons by controlling individual atoms, enabling one to generate highly correlated states of light.

On the other hand, correlated states can emerge from the simultaneous interaction among multiple atoms mediated by guided photons [8]. Early proposals considered an array of interacting cavities containing the atoms [78–80]. The competition between the tunneling interaction of photons between cavities and the on-site interaction of photons occupying the same cavity is predicted to induce quantum phase transitions, i.e., superfluid-to-Mott-insulator transition. Recent works study transport properties of photons along 1D cold atomic gas, where the photon-photon interactions are induced using single-atom nonlinearities [81] or strong interactions between atoms in Rydberg states [82, 83].

In the PCWs, remarkable phenomena arise when atomic frequencies can be tuned into photonic band gaps, including the ability to control the range, strength, and functional form of optical interactions between

atoms [84–86]. For example, atoms trapped near perfect photonic crystal structures can act as dielectric defects that seed atom-induced cavities [87] and thereby allow atomic excitations to be exchanged with proximal atoms [85]. The atom-induced cavities can be dynamically controlled with external lasers, enabling the realization of nearly arbitrary long-range spin Hamiltonians and spatial interactions (such as an effective Coulomb potential mediated by PCW photons) [87], which is a promising tool to perform quantum simulations. Furthermore, control over PCW dispersion is also expected to facilitate novel atomic traps based upon quantum vacuum forces [88].

1.5 Thesis outline

The work in this thesis begins with free-space quantum interfaces where we have demonstrated measurement-induced entanglement among four atomic ensembles, and then transitions into the development and implementation of interfacing atoms with optical nanofibers. The recent work with a 1D photonic crystal waveguide has focused on enhancing single-atom coupling rate to study photon-mediated interaction between multiple atoms. Below, we briefly summarize topics covered in each chapter:

- In Chapter 2, we describe a systematic study of the generation and storage of quadripartite entangled states of spin-waves among four atomic ensembles, as well as of the coherent transfer of the entangled components of the atomic state into individual photonic channels. We observe transitions from fully quadripartite entangled to unentangled via controlled spin-wave statistics of the atomic memories.

- In Chapter 3, we discuss the underlying physics of of atom-photon interactions along a 1D waveguide. First, we describe photon transport properties in the presence of a single atom, including reflection and transmission spectra, saturation behavior, and photon correlation. Then, we consider the cooperative effects that emerge with multiple atoms coupled to the guided mode.

- In Chapter 4, we propose a robust method of trapping single Cesium atoms with a two-color state-insensitive evanescent wave around a dielectric nanofiber. Specifically, we show that vector light shifts induced by the inherent ellipticity of the forward-propagating evanescent wave can be effectively suppressed by a backward-propagating evanescent wave. Furthermore, by operating the trapping lasers at

the magic wavelengths, we remove the differential scalar light shift between ground and excited states, thereby allowing for resonant driving of the optical D_2 transition.

- In Chapter 5, we describe the experimental realization of an optical trap that localizes single Cs atoms $\simeq 215$ nm from surface of a dielectric nanofiber. By operating at magic wavelengths for pairs of counter-propagating red- and blue-detuned trapping beams, differential scalar light shifts are eliminated, and vector shifts are suppressed by ≈ 250. We thereby measure an absorption linewidth $\Gamma/2\pi = 5.7 \pm 0.1$ MHz for the Cs $6S_{1/2}, F = 4 \rightarrow 6P_{3/2}, F' = 5$ transition, where $\Gamma_0/2\pi = 5.2$ MHz in free space. Optical depth $d \simeq 66$ is observed, corresponding to an optical depth per atom $d_1 \simeq 0.08$.

- In Chapter 6, we present the development of an integrated optical circuit with a photonic crystal capable of both localizing and interfacing atoms with guided photons. From reflection spectra measured with average atom number $\bar{N} = 1.1 \pm 0.4$, we infer that atoms are localized within the PCW by optical dipole forces. The fraction of single-atom radiative decay into the PCW is $\Gamma_{1\mathrm{D}}/\Gamma' \simeq (0.32 \pm 0.08)$, where $\Gamma_{1\mathrm{D}}$ is the rate of emission into the guided mode and Γ' is the decay rate into all other channels.

- In Chapter 7, we discuss our observations of superradiance for atoms trapped in the near field of a PCW. By fabricating the PCW with a band edge near the D_1 transition of cesium, we observe a superradiant emission rate scaling as $\bar{\Gamma}_{\mathrm{SR}} \propto \bar{N} \cdot \Gamma_{1\mathrm{D}}$ for average atom number $0.19 \lesssim \bar{N} \lesssim 2.6$ atoms, where the peak single-atom decay rate $\Gamma_{1\mathrm{D}}/\Gamma_0 = 1.1 \pm 0.1$.

- In Chapter 8, we discuss the outlook of our experiment to integrate ultracold atoms and nanophotonic waveguide and cavities.

Chapter 2

Entanglement of spin waves among four quantum memories

2.1 Introduction

Diverse applications in quantum information science require coherent control of the generation, storage, and transfer of entanglement among spatially separated physical systems [1–4, 6, 7]. Despite its inherently multipartite nature, entanglement has been studied primarily for bipartite systems [2], where remarkable progress has been made in harnessing physical processes to generate 'push-button' [89, 90] and 'heralded' entanglement [24, 25, 91, 92], as well as to map entangled states to and from atoms, photons, and phonons [26, 93].

For multipartite systems, the 'size' of a physical state, described by the system's density matrix $\hat{\rho}_N$, grows exponentially with the number of subsystems N and makes the entangled states exceedingly difficult to represent with classical information. Importantly, this complexity for $\hat{\rho}_N$ increases the potential utility of multipartite entanglement in quantum information science, including for quantum algorithms [2, 3] and simulation [6]. Redundant encoding of quantum information into multipartite entangled states enables quantum error correction and fault-tolerant computation [2, 3]. Intricate long-range correlation of many-body systems is intimately intertwined with the behavior of multipartite entanglement [94, 95]. In addition, mobilizing multipartite entanglement across quantum networks could lead to novel quantum phase transitions for the network [7].

This chapter is largely based on Ref. [33].

Counterposed to these opportunities, the complex structure of multipartite entanglement presents serious challenges both for its formal characterization and physical realization [2, 95–97]. Indeed, there are relatively few examples of laboratory systems that have successfully generated multipartite entanglement [32, 98–102]. Most works have considered the entanglement for spin systems, notably trapped ions [98, 99], which are applicable to the matter nodes of quantum networks. But the methodologies for verifying multipartite entanglement are problematic for infinite-dimensional bosonic systems of the quantum channels (e.g., multipartite quadrature [100, 101] and number-state [32] entanglement for optical modes). *A posteriori* multipartite entanglement has been inferred from a small subset of preferred detection events of photons from parametric downconversion [102].

In addition to the characterization of multipartite entanglement, an important capability for quantum networks is provided by quantum interfaces capable of generating, storing, and dynamically allocating the entanglement of matter nodes into photonic channels (see ref. [103] and references therein). As illustrated in Fig. 2.1a, we introduce here such a quantum interface for quadripartite entangled states based upon coherent, collective emission from matter to light. We present a systematic study of the generation and storage of quadripartite entangled states of spin-waves in a set of four nodes of atomic memories, as well as of the coherent transfer of the entangled components of the material state into individual photonic channels. We observe transitions of M to $(M-1)$-partite entangled states via controlled spin-wave statistics of the atomic memories, as well as the dynamic evolution of multipartite entanglement in a dissipative environment, from fully quadripartite entangled to unentangled.

2.2 Generation and characterization of W-state

2.2.1 Experimental procedure

Our experiment proceeds in four steps. First, in step (1) an entangled state $\hat{\rho}_W^{(A)}$ of four atomic ensembles is generated by quantum interference in a quantum measurement show in Fig. 2.1b [4, 24]. Given a photoelectric detection event at D_h, the conditional atomic state is ideally a quadripartite entangled state

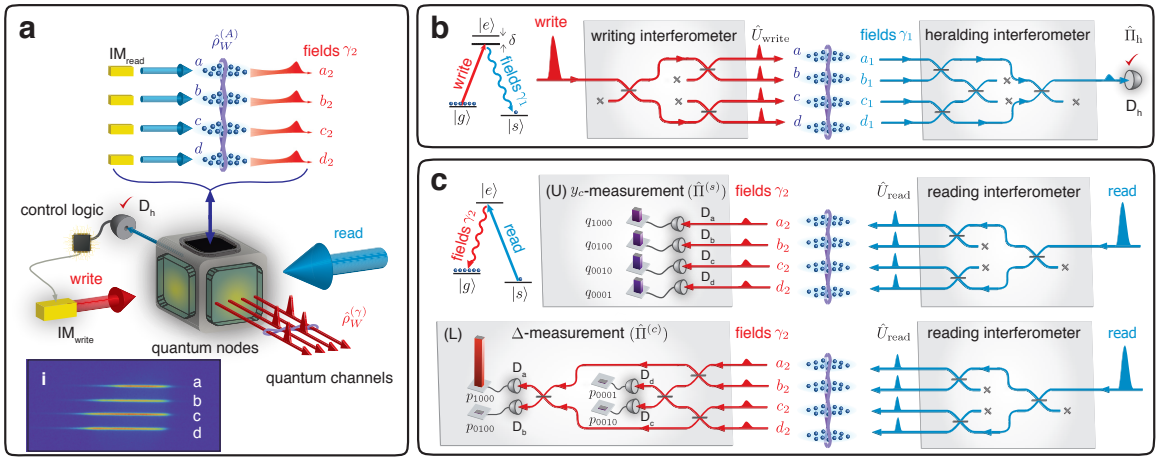

Figure 2.1: **Overview of the experiment. a,** Quantum interfaces for multipartite quantum networks. Inset **i**, a fluorescence image of the laser-cooled atomic ensembles $\{a, b, c, d\}$ that become entangled (see details in Section 2.5.2). **b,** Entanglement generation. A weak write laser is split into four components to excite the atomic ensembles via parametric interactions $\hat{U}_{\text{write}}$, leading to Raman scattered fields $\gamma_1 = \{a_1, b_1, c_1, d_1\}$ emitted by the ensembles. Entangled state $\hat{\rho}_W^{(A)}$ for four atomic ensembles $\epsilon = \{a, b, c, d\}$ in Eq. (2.1) is heralded by a projective measurement $\hat{\Pi}_h$ at detector D_h, derived from quantum interference of four fields γ_1 in the heralding interferometer. **c,** Quantum-state exchange and entanglement verification. Read lasers are applied to the ensembles to coherently transform the atomic entangled state $\hat{\rho}_W^{(A)}$ into quadripartite entangled beams of light $\hat{\rho}_W^{(\gamma)}$ in Eq. (2.2) via quantum-state transfers, $\hat{U}_{\text{read}}$, with each beam propagating through quantum channels $\gamma_2 = \{a_2, b_2, c_2, d_2\}$. (U) Upper panel for y_c-measurement − The quantum statistics $\{q_{ijkl}\}$ for the individual modes of $\hat{\rho}_W^{(\gamma)}$ with $i, j, k, l \in \{0, 1\}$ photons are measured with projectors $\{\hat{\Pi}_i^{(s)}\}$ at detectors $D_{a,b,c,d}$. (L) Lower panel for Δ-measurement − Mutual coherences for $\hat{\rho}_W^{(A)}$ are accessed with projectors $\{\hat{\Pi}_i^{(c)}\}$ from detection statistics $\{p_{ijkl}\}$ at $D_{a,b,c,d}$. Further details are given in Section 2.5.4.

$\hat{\rho}_W^{(A)} = |W\rangle_A\langle W|$ with

$$|W\rangle_A = \tfrac{1}{2}[(|\overline{s}_a, \overline{g}_b, \overline{g}_c, \overline{g}_d\rangle + e^{i\phi_1}|\overline{g}_a, \overline{s}_b, \overline{g}_c, \overline{g}_d\rangle) + e^{i\phi_2}(|\overline{g}_a, \overline{g}_b, \overline{s}_c, \overline{g}_d\rangle + e^{i\phi_3}|\overline{g}_a, \overline{g}_b, \overline{g}_c, \overline{s}_d\rangle)], \tag{2.1}$$

whose single quantum spin-wave $|\overline{s}_\epsilon\rangle$ is coherently shared among four ensembles $\epsilon = \{a, b, c, d\}$. These entangled states are known as W-states, comprised of atomic ground states $|\overline{g}_\epsilon\rangle = |g \cdots g\rangle_\epsilon$ and single collective excitations $|\overline{s}_\epsilon\rangle = \frac{1}{\sqrt{N_{A,\epsilon}}}\sum_{i=1}^{N_{A,\epsilon}} |g \cdots s_i \cdots g\rangle_\epsilon$, where $N_{A,\epsilon}$ is the number of atoms in ensemble ϵ.

After the heralding event, step (2) consists of storage of $\hat{\rho}_W^{(A)}$ in the ensembles for a user-controlled time τ. At the end of this interval, step (3) is initiated with read beams to coherently transfer the entangled atomic components of $\hat{\rho}_W^{(A)}$ into a quadripartite entangled state of light $\hat{\rho}_W^{(\gamma)} = |W\rangle_\gamma\langle W|$ via cooperative emissions

[4] (Fig. 2.1c), where

$$|W\rangle_\gamma = \frac{1}{2}[(|1000\rangle + e^{i\phi_1'}|0100\rangle) + e^{i\phi_2'}(|0010\rangle + e^{i\phi_3'}|0001\rangle)]. \tag{2.2}$$

This photonic state is a mode-entangled W-state [32, 104], which shares a single delocalized photon among four spatially separated optical modes $\gamma_2 = \{a_2, b_2, c_2, d_2\}$.

Finally, in step (4) we characterize the heralded entanglement for $\hat{\rho}_W^{(\gamma)}$ from complementary measurements of photon statistics and coherence shown in Fig. 2.1c [32, 104]. In particular, we consider a reduced density matrix $\hat{\rho}_r = p_0\hat{\rho}_0 + p_1\hat{\rho}_1 + p_{\geq 2}\hat{\rho}_{\geq 2}$ containing up to one photon per mode, which leads to a lower bound for the entanglement of the actual physical states $\{\hat{\rho}_W^{(A)}, \hat{\rho}_W^{(\gamma)}\}$. Here, $\{p_0, p_1, p_{\geq 2}\}$ are the probabilities for 0 and 1-photon $\hat{\rho}_{0,1}$, and higher-order subspaces $\hat{\rho}_{\geq 2}$, which can be populated for any realistic system. As illustrated in the upper panel of Fig. 2.1c, we characterize the statistical contamination for $\hat{\rho}_W^{(\gamma)}$ due to $\{\hat{\rho}_0, \hat{\rho}_{\geq 2}\}$ with a normalized measure [104], namely $y_c \equiv \frac{8}{3}\frac{p_{\geq 2}p_0}{p_1^2}$, ranging from $y_c = 0$ for a single excitation to $y_c = 1$ for balanced coherent states, by detecting the photon statistics q_{ijkl} of γ_2 at the output faces of the ensembles.

We also quantify the mutual coherences for $\hat{\rho}_W^{(\gamma)}$ by measuring photon probabilities $\{p_{1000}, p_{0100}, p_{0010}, p_{0001}\}$ at the outputs of the verification (v) interferometer. We determine the sum uncertainty $\Delta \equiv \sum_{i=1}^{N=4} \langle(\hat{\Pi}_i^{(c)})^2 - \langle\hat{\Pi}_i^{(c)}\rangle^2\rangle$ for the variables $\{\hat{\Pi}_i^{(c)}\} = \{|W_i\rangle_v\langle W_i|\}$, which project $\hat{\rho}_r$ onto a set of four orthonormal W-states $\{|W_i\rangle_v\}$ with phases $\{\beta_1, \beta_2, \beta_3\}_v$ selected by the actively stabilized paths in the verification interferometer (see details in Section 2.5.1). Hence, for the ideal W-state in Eq. (2.2) with $\beta_i = \phi_i'$, we have $\Delta = 0$ associated with $p_{1000} = 1$ and $p_{0100} = p_{0010} = p_{0001} = 0$, as observed in the bar plots of the lower panel of Fig. 2.1c for $y_c = 0.04 \pm 0.01$. In contrast, mixed states with no phase coherences would result in balanced probabilities ($p_{1000} = p_{0100} = p_{0010} = p_{0001} = 1/4$) and $\Delta = 0.75$.

The pair $\{\Delta, y_c\}$ thereby defines the parameter space for the multipartite entanglement employed in our experiment, with the entanglement parameters $\{\Delta, y_c\}$ serving as a nonlocal, nonlinear entanglement witness [104]. Our criterion for 'genuine' M-partite entanglement takes the most stringent form of non-separability [96] and excludes all weaker forms of entanglement. Specifically, for a given value of y_c, we determine the boundary $\Delta_b^{(M-1)}$ for the minimal uncertainty possible for all states containing at most $(M-1)$-mode

entanglement and their mixtures (see details in Section 2.5.4). For our quadripartite states with $N = 4$, we derive $\{\Delta_b^{(3)}, \Delta_b^{(2)}, \Delta_b^{(1)}\}$ for tripartite, bipartite entangled, and fully separable states, as functions of y_c. Thus, a measurement of quantum statistics y_c and the associated coherence Δ with $\Delta < \Delta_b^{(1,2,3)}$ manifestly confirms the presence of genuine $M = 4$ partite entanglement [32, 104]. Furthermore, we can unambiguously distinguish genuine M and $(M-1)$-partite entangled states for any $M \leq N$ by observing Δ below $\Delta_b^{(M-1)}$.

2.2.2 W-state among four atomic ensembles

Figure 2.2 presents our results for quadripartite entanglement for storage time $\tau_0 = 0.2$ μs. We first investigate off-diagonal coherence for the purportedly entangled atomic and photonic states, $\{\hat{\rho}_W^{(A)}, \hat{\rho}_W^{(\gamma)}\}$, in Fig. 2.2a. As the bipartite phase β_2 is varied, we observe interferences in $\{p_{1000}, p_{0100}, p_{0010}, p_{0001}\}$, and hence a variation in Δ that results from the coherence between the bipartite entangled components of $\hat{\rho}_W^{(\gamma)}$ for the modes $\{a_2, b_2\}$ and $\{c_2, d_2\}$. Furthermore, for optimal settings of β_2, the observed values of Δ fall below the bounds $\{\Delta_b^{(3)}, \Delta_b^{(2)}, \Delta_b^{(1)}\}$ (red, green, purple bands) for $y_c = 0.06 \pm 0.02$, and signal the generation of a fully quadripartite entangled state. The observed quadripartite entanglement arises from the intrinsic indistinguishability of probability amplitudes for one collective excitation $|\overline{s}_\epsilon\rangle$ among the four ensembles. We also present results from a control experiment with a 'crossed' state $\hat{\rho}_\times^{(A)}$ (orange points) that consists of an incoherent mixture of entangled pairs $\{a, b\}$ and $\{c, d\}$ (see details in Section 2.5.5).

Next, we characterize $\hat{\rho}_W^{(\gamma)}$ (and $\hat{\rho}_W^{(A)}$) over the full parameter space $\{\Delta, y_c\}$. In a regime of weak excitation ($\xi \ll 1$) for the ensemble-field pairs $\{\epsilon, \gamma_1\}$, the heralded state $\hat{\rho}_W^{(A)}$ is approximately

$$\hat{\rho}_W^{(A)}(\tau = 0) \simeq (1 - 3\xi)|W\rangle_A\langle W| + 3\xi\hat{\rho}_{\geq 2}^{(A)} + \mathcal{O}(\xi^2), \tag{2.3}$$

where $\hat{\rho}_{\geq 2}^{(A)}$ includes uncorrelated spin-waves with two or more quanta in the set of four ensembles due to atomic noise. For $\xi \to 0$, a heralding event at D_h leads to a state with high fidelity to $|W\rangle_A$ stored in the four ensembles. However, for increasing ξ, $\hat{\rho}_{\geq 2}^{(A)}$ becomes important, leading to modifications of the spin-wave statistics for $\hat{\rho}_W^{(A)}$ and thereby to the entanglement parameters $\{\Delta^{\text{th}}, y_c^{\text{th}}\}$. Hence, by varying ξ via the overall intensity for the write beam, we adjust the quantum statistics y_c and coherence Δ of the entangled states

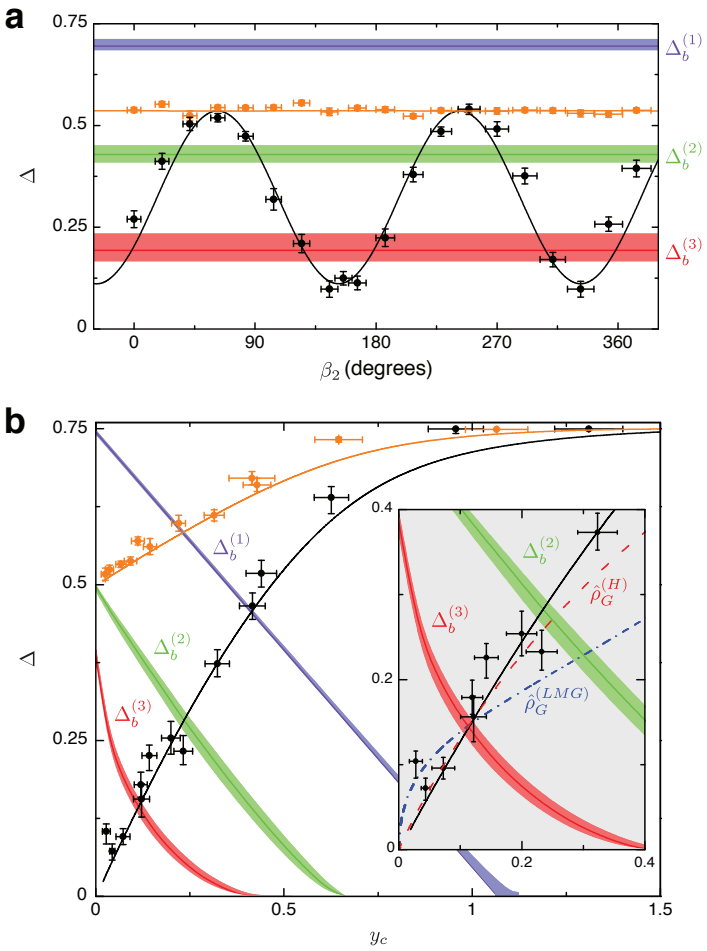

Figure 2.2: **Quadripartite entanglement among four atomic ensembles. a,** Quantum interference between the bipartite entangled pairs of the full quadripartite state (black points) as a function of bipartite phase β_2. **b,** Exploring the entanglement space $\{\Delta, y_c\}$ for quadripartite states. By controlling the spin-wave statistics, we observe transitions from quadripartite, to tripartite, to bipartite entangled states, and to fully separable states (black points). We also display our results for the 'crossed' quantum state $\hat{\rho}_{\times}^{(A)}$ (orange points), as further described in Section 2.5.5. Inset, expanded view of entanglement parameters $\{\Delta, y_c\}$. Results for entanglement thermalization $\{\Delta^{(T)}, y_c^{(T)}\}$ of the spin systems $\hat{\rho}_G^{(\mathrm{H})}$ ($\hat{\rho}_G^{(\mathrm{LMG})}$) are shown by the red dashed (blue dash-dotted) line. The red, green, and purple bands represent the minimum uncertainties for 3-mode ($\Delta_b^{(3)}$) and 2-mode entanglement ($\Delta_b^{(2)}$), and for fully separable states ($\Delta_b^{(1)}$), with thicknesses of the bands from the central lines corresponding to $\pm$1-s.d. of the bounds $\{\Delta_b^{(3)}, \Delta_b^{(2)}, \Delta_b^{(1)}\}$. In all cases, error bars for the data reflect the statistical and systematic uncertainties.

$\{\hat{\rho}_W^{(A)}, \hat{\rho}_W^{(\gamma)}\}$.

This procedure is employed in Fig. 2.2b to parametrically increase $\{\Delta, y_c\}$ in tandem. As y_c is raised from $y_c \simeq 0$ in the quantum domain to the classical regime with $y_c \simeq 1$, we observe transitions of the directly measured photonic states $\hat{\rho}_W^{(\gamma)}$ (black points) from fully quadripartite entangled ($\Delta < \Delta_b^{(3)}$) to tripartite entangled ($\Delta_b^{(3)} < \Delta < \Delta_b^{(2)}$), to bipartite entangled ($\Delta_b^{(2)} < \Delta < \Delta_b^{(1)}$), and finally to fully separable states ($\Delta_b^{(1)} < \Delta$). As shown by the curves, our observations correspond well to a theoretical model for

entanglement generation, transfer, and verification. In comparison to the former work on coherent splitting of a photon [32], the heralded atomic and photonic W-states $\{\hat{\rho}_W^{(A)}, \hat{\rho}_W^{(\gamma)}\}$ offer qualitatively richer statistical passages through the entanglement spaces delineated by $\{\Delta, y_c\}$. Here, the quantum coherence Δ is intrinsically linked to the statistical character y_c due to quantum correlations between the heralding fields γ_1 and the excitation statistics of the ensembles.

For $\xi \ll 1$, the coherent contribution $\hat{\rho}_c^{(A)}$ of the delocalized single quantum strongly dominates over any other processes for the full quadripartite state $\hat{\rho}_W^{(A)}$ in Eq. (2.3). With a heralding probability $p_h \simeq 3 \times 10^{-4}$ ($\xi \simeq 5 \times 10^{-3}$), we achieve the smallest entanglement parameters $\Delta^{\text{min}} = 0.07^{+0.01}_{-0.02}$ and $y_c^{\text{min}} = 0.038 \pm 0.006$ for the generated quadripartite entangled states. These parameters are suppressed below the closest 3-mode boundary $\Delta_b^{(3)}$ by ten standard deviations. Furthermore, because the local mapping of quantum states from matter to light cannot increase entanglement [24], our measurements of $\hat{\rho}_W^{(\gamma)}$ unambiguously provide a lower bound of the quadripartite entanglement stored in $\hat{\rho}_W^{(A)}$. Therefore, the observed strong violation of the uncertainty relations for $\{\Delta^{\text{min}}, y_c^{\text{min}}\}$ categorically certifies for the creation of measurement-induced entanglement of spin-waves among four quantum memories, as well as for the coherent transfer of the stored quadripartite entangled states to an entangled state of four propagating electromagnetic fields.

In terms of state fidelity, our approach for heralded multipartite entanglement generation compares favorably to matter systems utilizing local interactions (e.g., trapped ions [98, 99]). Despite the intrinsically low preparation probability, the resulting quadripartite entangled state $\hat{\rho}_W^{(A)}$ stored in the four ensembles has high fidelity with the ideal W-state, namely $F^{(A)} = {}_A\langle W|\hat{\rho}_W^{(A)}|W\rangle_A$. As discussed in Section 2.5.7, we estimate a lower bound for the unconditional entanglement fidelity $F^{(A)} \geq 0.9 \pm 0.1$, as compared to the theoretical fidelity $F_{\text{th}}^{(A)} = 0.98$ derived for the parameters in our experiment.

Apart from the creation of novel multipartite entangled spin-waves, an important benchmark of a quantum interface is the transfer efficiency λ of multipartite entanglement from matter to light [26]. Since no known measure applies to our case, we tentatively define the entanglement transfer $\lambda = F^{(\gamma)}/F^{(A)}$, with physical fidelity $F^{(\gamma)} = {}_\gamma\langle W|\hat{\rho}_W^{(\gamma)}|W\rangle_\gamma$ for the photonic state $\hat{\rho}_W^{(\gamma)}$. In particular for $\xi \ll 1$, we obtain $F_{\text{th}}^{(\gamma)} \simeq \eta_{\text{read}} F_{\text{th}}^{(A)}$, which thereby gives $\lambda_{\text{th}} \simeq \eta_{\text{read}} = 38 \pm 4\%$ dictated by the retrieval efficiency η_{read}. While fidelity is an often used measure, we emphasize that $F^{(\gamma)}$ cannot be used to set a threshold for entanglement, since

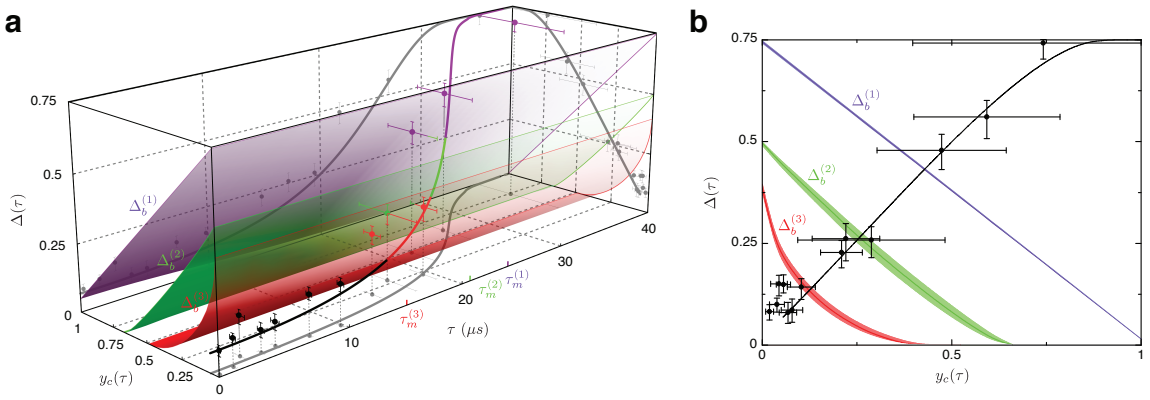

Figure 2.3: **Dissipative dynamics of atomic entanglement.** **a,** Dynamic evolution of entanglement parameters $\{\Delta(\tau), y_c(\tau)\}$ for the multipartite quantum state. We observe crossing of the boundaries defined by 3-mode (red surface, $\Delta_b^{(3)}$), 2-mode (green surface, $\Delta_b^{(2)}$) entangled states, and separable states (purple surface, $\Delta_b^{(1)}$). We indicate various entanglement orders for quadripartite (black), tripartite (red), bipartite entangled (green) states, and fully separable states (purple) for the data points and the curve. The projections of the data points into the planes (y_c, τ) and (Δ, τ) display the individual passages of $\{\Delta(\tau), y_c(\tau)\}$. **b,** Projection of entanglement dynamics onto the (Δ, y_c) plane. The curves in **a** and **b** are from a theoretical model including motional dephasing. Error bars for the data represent the statistical and systematic uncertainties.

$\hat{\rho}_W^{(\gamma)}$ can exhibit multipartite entanglement for any $F^{(\gamma)} > 0$.

2.3 Dissipative dynamics of atomic entanglement

To investigate the dynamical behavior of the observed quadripartite entangled states, we study the temporal evolution of multipartite entanglement stored in the atomic ensembles as a function of a storage time τ. Decoherence for the atomic W-state is governed by motional dephasing of spin-waves [105], in which the imprinted atomic phases in $|\overline{s}_\epsilon\rangle$ evolve independently due to thermal motion, thereby transforming the initial collective state into a subradiant state uncorrelated with the heralding fields γ_1. The net effect is an increase of both entanglement parameters $\{\Delta, y_c\}$ with a time-scale $\tau_m \simeq 17\ \mu s$ (see details in Section 2.5.3). Eventually, the growth in $\{\Delta(\tau), y_c(\tau)\}$ leads to time-dependent losses of entanglement, marked by successive crossings of the boundaries set by $\{\Delta_b^{(3)}, \Delta_b^{(2)}, \Delta_b^{(1)}\}$.

We examine the dissipative dynamics of multipartite entanglement for the quantum memories of four ensembles via the evolution of both $\{\Delta, y_c\}$ in Fig. 2.3a. We observe the passage of the initial quadripartite entangled state $\hat{\rho}_W^{(A)}(\tau_0)$ at $\tau_0 = 0.2\ \mu s$ through various domains, progressively evolving from M-partite entanglement to $(M-1)$-partite entanglement at memory times $\tau = \tau_m^{(M-1)}$, with the final state $\hat{\rho}_W^{(A)}(\tau_f)$

measured at $\tau_f = 36.2$ μs. The crossings of the bounds $\{\Delta_b^{(3)}, \Delta_b^{(2)}, \Delta_b^{(1)}\}$ occur at $\tau_m^{(3)} = 15$ μs, $\tau_m^{(2)} = 21$ μs, and $\tau_m^{(1)} = 24$ μs, respectively. In addition, the measured entanglement parameters evolve in qualitative agreement to the simulated dynamics derived for $\hat{\rho}_W^{(A)}(\tau)$ from our theoretical model (solid line), with deviations (especially for Δ_{th}). Fig. 2.3b displays the parametric losses of entanglement via $\{\Delta(\tau), y_c(\tau)\}$.

Finally, an interesting extension is to relate the characterization of multipartite entanglement via $\{\Delta, y_c\}$ to the relaxations of entanglement in quantum many-body systems [94, 95]. We consider two ferromagnetic spin models (Heisenberg-like and Lipkin-Meshkov-Glick Hamiltonians $\hat{H}_{\text{H}}$, $\hat{H}_{\text{LMG}}$) as well as their thermal entanglement $\{\Delta^{(T)}, y_c^{(T)}\}$. Results of our analysis are shown in the inset of Fig. 2.2b by the red dashed (blue dash-dotted) lines for the Gibbs thermal equilibrium states $\hat{\rho}_G^{(\text{H})}$ ($\hat{\rho}_G^{(\text{LMG})}$) of $\hat{H}_{\text{H}}$ ($\hat{H}_{\text{LMG}}$). The statistical character of $\hat{\rho}_W^{(A)}$ for our system of four ensembles follows the thermalization of $\hat{\rho}_G^{(\text{H})}$ ($\hat{\rho}_G^{(\text{LMG})}$) for $y_c \lesssim 0.2$, whereby $\hat{\rho}_{\geq 2}^{(A)}$ is thermally populated. This comparison suggests that our method for entanglement characterization could be applied to access the link between off-diagonal long-range order and multipartite entangled spin-waves in thermalized quantum magnets [94, 95].

2.4 Conclusion and outlook

In conclusion, our measurements explicitly demonstrate a coherent matter-light quantum interface for multipartite entanglement by way of the operational metric of quantum uncertainty relations [32, 104, 106]. High-fidelity entangled spin-waves are generated in four spatially separated atomic ensembles and coherently transferred to quadripartite entangled beams of light. The quantum memories are individually addressable and can be readily read-out at different times for conditional control of entanglement [4]. With recent advances by other groups, the short memory times obtained in Fig. 2.3 could be improved beyond 1 s (see details in Section 2.5.8).

Further possibilities include the creation of yet larger multipartite entangled states with efficient scaling [4] for the realization of multipartite quantum networks. For example, quadripartite entangled states of ensemble sets $\{a, b, c, d\}$ and $\{a', b', c', d'\}$ could be extended by swapping between $\{a, a'\}$ to prepare a hexapartite entangled state for $\{b, b', c, c', d, d'\}$. Generalization of such processes will prepare a single

macroscopic entangled state for observing entanglement percolation [7] and extreme non-locality of W-states [107], as well as for studying phase transitions in strongly-correlated systems [94, 95]. Finally, the entangled spin-waves can be applied for quantum metrology to detect a phase shift of π on an unknown component of $\hat{\rho}_W^{(A)}$ with efficiency beyond any separable state (see details in Section 2.5.9).

2.5 Experimental details

2.5.1 Preparation of cold atomic ensembles

The experiment consists of a 22 ms preparation stage and a 3 ms period for operating the quantum interface in Fig. 2.1 with a repetition rate 40 Hz and a duty cycle $D_c = 3/25$. For the preparation, we load and laser-cool Cesium atoms (peak optical depth $\approx$ 30) in a magneto-optical trap for 18 ms, after which the atoms are released from the trap with dynamically compensated eddy-currents. The atoms are further cooled in an optical molasses ($T_t \simeq 150\ \mu K$) for 3.8 ms, and optically pumped to $|g\rangle$ for 0.2 ms. During this time, a phase-reference laser ($F = 3 \leftrightarrow F' = 4'$ transition) also propagates through the atomic ensembles for the active stabilization of the verification interferometer in Fig. 2.1c via *ex-situ* phase-modulation spectroscopy [32], which does not affect the operation of the quantum interface. Concurrently, dense Cesium atoms in paraffin coated vapor cells located at the heralding and verification ports are prepared to the respective ground states $|g\rangle$ ($|s\rangle$) for filtering the coherent-state lasers scattered into the quantum fields γ_1 (γ_2).

2.5.2 Quantum interface

For the quantum interface to function during the 3 ms window, in step (1) 20-ns writing (red-detuned $\delta = 10$ MHz from $|g\rangle - |e\rangle$ transition) and 100-ns repumping (resonant with $|s\rangle - |e\rangle$) pulses are applied sequentially to the ensembles ϵ, synchronized to a clock running at $R_c \simeq 2$ MHz. This process creates pairwise correlated excitations [4] between the collective atomic modes $|\overline{s}_\epsilon\rangle$ of the ensembles ϵ and the optical fields γ_1 ($\delta = 10$ MHz below $|s\rangle - |e\rangle$). Photodetection of a single photon for the combined fields γ_1 at the output of the heralding interferometer effectively erases the which-path information for γ_1, and imprints the entangled spin-wave $\hat{\rho}_W^{(A)}$ in Eq. (2.3) onto the ensembles $\{a, b, c, d\}$ via $\mathrm{Tr}_h(\hat{\Pi}_h \hat{U}_{\text{write}}^\dagger \hat{\rho}_g^{(A)} \hat{U}_{\text{write}})$. The heralding

event at D_h triggers control logic in Fig. 2.1a which deactivates intensity modulators of the writing (IM_{write}), repumping and reading lasers (IM_{read}) for the quantum storage of $\hat{\rho}_W^{(A)}$ in step (2). After a user-controlled delay τ, step (3) is initiated with 20-ns strong read pulses (Rabi frequency 24 MHz, resonant with $|s\rangle - |e\rangle$) that address the ensembles in Fig. 2.1c and coherently transfer the entangled atomic components $\{a, b, c, d\}$ of $\hat{\rho}_W^{(A)}(\tau)$ one-by-one to propagating beams $\gamma_2 = \{a_2, b_2, c_2, d_2\}$, comprising the entangled photonic state $\hat{\rho}_W^{(\gamma)}(\tau)$, via the operation $\hat{\rho}_W^{(\gamma)} = \text{Tr}_A(\hat{U}_{\text{read}}^{\dagger}\hat{\rho}_W^{(A)}\hat{U}_{\text{read}})$. Here, Tr_A traces over the atomic systems which are later shelved into the ground states $|\overline{g}_\epsilon\rangle$. The retrieval efficiency η_{read} is collectively enhanced for large N_A (ref. [4]), leading to $\eta_{\text{read}} = 0.38 \pm 0.06$ in our experiment. The average production rate for the atomic quadripartite entanglement with $\{\Delta^{\min}, y_c^{\min}\}$ is $r_p = R_c D_c p_h \simeq 60$ Hz, while the actual rate during the 3 ms operating window is $r_q = R_c p_h \simeq 500$ Hz. The atomic level diagrams for entanglement generation and quantum-state exchanges are shown as insets to Figs. 1b and 1c. States $|g\rangle$, $|s\rangle$ are hyperfine ground states $F = 4$, $F = 3$ of $6S_{1/2}$ in atomic Cesium; state $|e\rangle$ is the hyperfine level $F' = 4$ of the electronic excited state $6P_{3/2}$.

2.5.3 Spin-wave quantum memories

The quantum information of the entangled state for Eq. (2.1) is encoded in the quantum numbers of spin-waves (collective excitations) for the pseudo-spin of the hyperfine ground electronic levels $6S_{1/2}$ ($F = 3, F = 4$) in atomic Cesium. The fluorescence images shown in the inset of Fig. 2.1a depict the collective atomic modes of ensembles $\epsilon = \{a, b, c, d\}$ for exciting the entangled spin-waves $\hat{\rho}_W^{(A)}$ with 1 mm separations and 60 μm waists. The geometry of the collective excitations for the four ensembles $\{a, b, c, d\}$ is defined by the spread functions of the imaging systems for the fields $\{\gamma_1, \gamma_2\}$, consisting a cold cloud of $N_{A,\epsilon} \approx 10^6$ Cesium atoms. We use an off-axial configuration [108] for individually addressing each ensemble ϵ with an angle $\theta = 2.5^\circ$ between the classical and nonclassical beams, which creates spin-waves $|\overline{s}_\epsilon\rangle$ associated with wave-numbers $\delta\vec{k} = \vec{k}_{\text{write}} - \vec{k}_{\gamma_1}$ for each ϵ. These spin-waves are analogous to other types of collective excitations in many-body systems, such as magnons and plasmons, and the spin-waves can be converted to dark-state polaritons for the coherent transfer $\hat{U}_{\text{read}}$ of entanglement. For the phase-matching configuration and temperature of our ensembles, the memory times $\{\tau_m^{(3)}, \tau_m^{(2)}, \tau_m^{(1)}\}$ in Fig. 2.3 are dominantly determined

by the motional dephasing of the spin-waves $|\overline{s}_\epsilon\rangle$ (ref. [105]). With thermal velocity of $v_t \simeq 14$ cm/s, we estimate a memory time $\tau_m \simeq \frac{0.85\,\mu m}{4\pi \sin(\theta/2) v_t} = 17\ \mu s$. On the other hand, the ground-state dephasing due to inhomogeneous broadening is expected to be $> 50\ \mu s$ in our experiment, inferred from two-photon Raman spectroscopy.

2.5.4 Quantum uncertainty relations and genuine multipartite entanglement

In order to verify the entanglement by way of $\{\Delta, y_c\}$, we first evaluate the photon statistics $\{p_0, p_1, p_{\geq 2}\}$ for the y_c-measurement. Operationally, this is accomplished by measuring the individual probabilities q_{ijkl} for $i, j, k, l \in \{0, 1\}$ photons to occupy the respective optical modes $\gamma_2 = \{a_2, b_2, c_2, d_2\}$ at the output faces of the ensembles via photoelectric detections $\{\hat{\Pi}_i^{(s)}\}$. For the Δ-measurement, we quantify the off-diagonal coherence $\overline{d}$ of $\hat{\rho}_W^{(\gamma)}$ by pairwise interferences of all possible sets of modes $\alpha, \beta \in \{a_2, b_2, c_2, d_2\}$ with the verification interferometer. The photon probabilities $\{p_{1000}, p_{0100}, p_{0010}, p_{0001}\}$ at the output modes of the verification interferometer thereby result from the coherent interferences of the four purportedly entangled fields γ_2 that depend on the phase orientations $\{\beta_1, \beta_2, \beta_3\}_v$ of $\{\hat{\Pi}_i^{(c)}\}$.

Our conclusion of genuine multipartite entanglement for the atomic and photonic states $\{\hat{\rho}_W^{(A)}, \hat{\rho}_W^{(\gamma)}\}$ does not rely on weaker conditions based on the non-separability along any fixed bipartition of $\{\hat{\rho}_W^{(A)}, \hat{\rho}_W^{(\gamma)}\}$. The genuine M-partite entangled states created from our experiment can only be represented as mixtures of pure states that *all* possess M-partite entanglement, as for the case of genuine 'k-producibility' in multipartite spin models [94, 95]. We take caution that our entanglement verification protocol cannot be applied for verifying the *absence* of entanglement for the physical state $\hat{\rho}_W^{(\gamma)}$ in an infinite dimension [109]. Finally, we emphasize that our analysis makes use of the full physical state $\{\hat{\rho}_W^{(A)}, \hat{\rho}_W^{(\gamma)}\}$ including the vacuum component $\hat{\rho}_0$ and higher order terms $\hat{\rho}_{\geq 2}$, and does not rely upon a spurious post-diction based upon a preferred set of detection events.

2.5.5 Generation and characterization of a 'crossed' quantum state

As a control experiment, we reconfigure the heralding interferometer such that path-information could in principle be revealed up to the bipartite split of the ensemble pairs $\{a, b\}$ and $\{c, d\}$ by analyzing the polar-

ization state of the heralding photon γ_1. In this case, the heralding measurement $\hat{\Pi}_\times$ prepares a 'crossed' atomic state $\hat{\rho}_\times^{(A)}$ with no coherence shared between $\{a,b\}$ and $\{c,d\}$. Thus, we observe an absence of interference in Fig. 2.2a (orange points). However, this modified $\hat{\Pi}_\times$ preserves the bipartite entanglement within $\{a,b\}$ and $\{c,d\}$, which explains our observation of the uncertainty Δ reduced below the 1-mode bound $\Delta_b^{(1)}$ for $y_c = 0.07 \pm 0.01$. Similarly, we also detect the statistical transition of the bipartite entanglement to fully separable states for the 'crossed' state in Fig. 2.2b, despite the disentanglement for the bipartition (|) of $\{a,b\}|\{c,d\}$.

2.5.6 Relationship between quantum uncertainty and off-diagonal coherences.

We derive here the general expression for the upper bound of the sum uncertainty Δ as a function of the coherence $\overline{d}$. First, we note that Δ is only sensitive to the 1-excitation subspace $\hat{\rho}_1$ of $\hat{\rho}_r$ with

$$\hat{\rho}_1 = \begin{pmatrix} s_{1000} & d_{ab} & d_{ac} & d_{ad} \\ d_{ba}^* & s_{0100} & d_{bc} & d_{bd} \\ d_{ca}^* & d_{cb}^* & s_{0010} & d_{cd} \\ d_{da}^* & d_{db}^* & d_{dc}^* & s_{0001} \end{pmatrix},$$

normalized such that $\mathrm{Tr}(\hat{\rho}_1) = s_{1000} + s_{0100} + s_{0010} + s_{0001} = 1$. Here, the diagonal elements $\vec{s}_1 = \{s_{1000}, s_{0100}, s_{0010}, s_{0001}\}$ of $\hat{\rho}_1$ are related to the 1-photon probabilities $\vec{q}_1 = \{q_{1000}, q_{0100}, q_{0010}, q_{0001}\}$ at the faces of the ensembles via $p_1\vec{s}_1 = \vec{q}_1$. By transforming $\hat{\rho}_1$ into the basis spanned by $\{|W_i\rangle_v\}$, we find the expressions for the normalized output photon probabilities $\{p_{1000}, p_{0100}, p_{0010}, p_{0001}\}$ of the verification interferometer as functions of $\vec{s}_1$ and $d_{\alpha\beta}$. The sum uncertainty Δ is then expressed as $\Delta = \frac{3}{4} - \{(|d_{ab}| + |d_{cd}|)^2 + (|d_{ac}| + |d_{bd}|)^2 + (|d_{ad}| + |d_{bc}|)^2\}$. Thus, we obtain $\Delta \lesssim \frac{3}{4}(1 - 16\overline{d}^2)$. The average value of the six unique off-diagonal elements is $\overline{d} = \frac{1}{6}\sum_{\alpha,\beta} |d_{\alpha\beta}|$ with $0 \leq \overline{d} \leq 1/4$, and the effective interference visibility is given by $V_{\text{eff}} = 4\overline{d}$.

2.5.7 Derivation of entanglement fidelity

We obtain here the expression for the lower bound unconditional entanglement fidelity $F^{(A)} = \tilde{p}_1 F_1$, where $\tilde{p}_1$ is the probability for a single spin-wave $\hat{\rho}_1^{(A)}$ in the heralded state $\hat{\rho}_W^{(A)}$, and $F_1 = \langle W_1|\hat{\rho}_1^{(A)}|W_1\rangle$ is the conditional fidelity for $\hat{\rho}_1^{(A)}$. We start by noting that the projective measurement $\hat{\Pi}_i^{(c)}$ for Δ gives the conditional fidelity F_1 of $\hat{\rho}_r$ onto one of four orthonormal W-states, $|W_i\rangle_v = |W_1\rangle_v$, for example, $|1000\rangle + e^{i\beta_1}|0100\rangle + e^{i\beta_2}(|0010\rangle + e^{i\beta_3}|0001\rangle)$. Hence, we can define $\Delta = 1 - F_1^2 - \sum_{i=2}^4 F_i^2$ in terms of the respective overlaps F_i. Because of the orthonormality $\sum_{i=1}^4 F_i = 1$, the sum uncertainty is bounded by $\Delta \geq 1 - F_1^2 - (1-F_1)^2$, whereby we obtain $F_1 \geq \sqrt{\frac{1}{2}(\frac{1}{2} - \Delta)} + \frac{1}{2}$. Finally, by combining the probability $\tilde{p}_1$ for exciting one spin-wave distributed among the four ensembles, we access the lower bound fidelity $F^{(A)} \geq \tilde{p}_1(\sqrt{\frac{1}{2}(\frac{1}{2} - \Delta)} + \frac{1}{2})$ obtained unconditionally for the heralded atomic state $\hat{\rho}_W^{(A)}$. In principle, the imbalances in the interferometer can rotate the projectors into non-orthonormal sets [104]. However, the measured losses and the beam-splitter ratios are sufficiently balanced such that any changes in $F^{(A)}$ due to modified projectors are well within the uncertainties of the data, as evidenced by the close-to-unity projection fidelity $F^{(\pi)} = 99.9^{+0.1}_{-0.2}\%$. In the experiment, $\tilde{p}_1$ and F_1 are determined from the inferences of the spin-wave statistics (via y_c), and of the coherences (via Δ), respectively.

2.5.8 Prospects for improving memory time and matter-light transfer efficiency

By operating the clock speed at $R_c \to 10$ MHz and $\tau_m^{(3)} \approx 20\mu s$, we could prepare hexapartite ($M = 6$) entanglement with probability $3z\eta_{\text{read}}p_h^2/8 \approx 10^{-5}$ by connecting two quadripartite states $\hat{\rho}_W^{(A)}$ for $\{\Delta^{\min}, y_c^{\min}\}$, with enhancement factor $z = 400$ (ref. [110]), thereby giving a local production rate of $r_q \approx 50 - 100$ Hz, or an average rate $r_p \approx 5 - 10$ Hz with our current duty cycle D_c. The most challenging aspect of verifying the hexpartite entangled states is the quantification of the higher-order contamination $\hat{\rho}_{\geq 2}$, which we estimate ~ 1 event per 10 hr. This integration rate is feasible with our current system. More generally, M_1 and M_2-partite entangled states can be fused together by entanglement connection to create a $M = (M_1 + M_2 - 2)$-partite entangled state. However, the memory times $\{\tau_m^{(3)}, \tau_m^{(2)}, \tau_m^{(1)}\}$ in Fig. 2.3 and the entanglement transfer λ from matter to light limit our capability to scale the multipartite entanglement beyond $M > 6$ by way of conditional control and connection of entanglement [110, 111] with our current experimental parameters.

The prerequisite storage techniques for suppressing both the internal and motional spin-wave dephasings can be extended for τ_m with advances in ensemble-based quantum memories [27, 28, 112]. Recent experiments with single ensembles have achieved coherence times up to $\tau_m \simeq 1.5$ seconds in quantum degenerate gases [29, 30] albeit with efficiencies $\lesssim 1\%$. The transfer efficiency can also be increased to $\lambda_{\text{th}} \simeq 0.9$ by enclosing the ensembles with high finesse cavities [105]. System integrations by way of atom-chip technology and waveguide coupling [61, 113] hold great potential for scalability given the strong cooperativity and the long coherence [114]. At this level, two or more heralded processes of multipartite entanglement generations can be made 'on-demand' on time scales of $\tau_{\text{det}} \sim \frac{1}{R_c p_h} = 1$ ms, with $\tau_m \gg \tau_{\text{det}}$ (refs. [110, 111]).

Realistically, the expansion of multipartite entangled states $\hat{\rho}_W^{(A)}$ will be limited by the intrinsic degradations of the entanglement parameters $\{\Delta, y_c\}$ that inevitably increase with each step of entanglement connection [111], and by the specific quantum repeater architecture implemented on $\hat{\rho}_W^{(A)}$. The latter is an extremely rich area of research in view of the large classes of methods for connecting multipartite entangled states, making it premature to specify a particular architecture for multipartite entanglement expansion. However, our experiment will hopefully stimulate theoretical studies of complex repeater architectures for multipartite systems, beyond traditional one-to-one networks [115].

2.5.9 Quantum-enhanced parameter estimation with entangled spin-waves

We describe a quantum-enhanced parameter estimation protocol whereby a phase shift on a single ensemble ϵ_i of the quadripartite state $\epsilon_i \in \{a, b, c, d\}$ can be detected with efficiency beyond that for any separable state. Specifically, we consider a π-phase shift $\hat{U}_{\pi,\epsilon_i} = \exp(i\pi\hat{n}_{\epsilon_i})$ applied on an unknown spin-wave component $\epsilon_i \in \{a, b, c, d\}$ ($\hat{n}_{\epsilon_i} = \hat{S}_{\epsilon_i}^\dagger \hat{S}_{\epsilon_i}$) of the atomic state $\hat{\rho}_W^{(A)}$, or on a spatial field mode $\gamma_{2i} \in \{a_2, b_2, c_2, d_2\}$ of the photonic state $\hat{\rho}_W^{(\gamma)}$ ($\hat{n}_{\gamma_{2i}} = \hat{a}_{\gamma_{2i}}^\dagger \hat{a}_{\gamma_{2i}}$). Our goal is to find the π-phase shifted ensemble ϵ_i (optical mode γ_{2i}), in a *single-measurement* under the condition that an average of one spin-wave is populated in total; i.e., $\sum_i \text{Tr}(\hat{n}_{\epsilon_i}\hat{\rho}_W^{(A)}) = 1$ (or $\sum_i \text{Tr}(\hat{n}_{\gamma_{2i}}\hat{\rho}_W^{(\gamma)}) = 1$ for optical modes). As a quantum benchmark, we consider an average success probability $P_s = \frac{1}{4}\sum_{\epsilon_i} \text{Tr}(\hat{\Pi}_{\epsilon_i}^{(u)}\hat{U}_{\pi,\epsilon_i}^\dagger \hat{\rho}_W^{(A)}\hat{U}_{\pi,\epsilon_i})$ (failure probability $P_f = 1 - P_s$) for distinguishing the phase shifted ensemble ϵ_i (mode γ_{2i}) among the four possibilities $\{a, b, c, d\}$ ($\{a_2, b_2, c_2, d_2\}$) by way of *unambiguous quantum-state discrimination* $\{\hat{\Pi}_{\epsilon_i}^{(u)}\}$ (refs. [116–119]).

First, we consider an ideal W-state $|W\rangle_o = |W\rangle_A$ (or $|W\rangle_{\gamma_2}$) with atomic phases $\phi_i \in \{\phi_1, \phi_2, \phi_3\}$ (photonic phases $\phi_i' \in \{\phi_1', \phi_2', \phi_3'\}$). In this case, the π-phase shifted entangled W-states $|W_{\epsilon_i}\rangle_f \in \{|W_a^{(\pi)}\rangle_f$, $|W_b^{(\pi)}\rangle_f, |W_c^{(\pi)}\rangle_f, |W_d^{(\pi)}\rangle_f\}$ can be detected deterministically, because $|W_{\epsilon_i}^{(\pi)}\rangle_f = \hat{U}_{\pi,\epsilon_i}|W\rangle_o$ forms an orthonormal complete set that spans the state-space $\hat{\rho}_1$, resulting from the underlying symmetry of $|W\rangle_o$ with respect to any rotation $\hat{U}_{\pi,\epsilon_i}$ on a generalized Bloch sphere. Operationally, we set the verification phases $\beta_{1,2} - \phi_{1,2}' = 0$ and $\beta_3 - \phi_3' = \pi$. Then, the π-phase shifted ensemble ϵ_i can be unambiguously discriminated because the otherwise balanced output photon probabilities $\vec{p}_v = \{p_{1000}, p_{0100}, p_{0010}, p_{0001}\} = \{0.25, 0.25, 0.25, 0.25\}$ of the verification interferometer will be transformed to $\vec{p}_v = \{1, 0, 0, 0\}$ for a π-phase induced on ensemble a, to $\vec{p}_v = \{0, 1, 0, 0\}$ on ensemble b, to $\vec{p}_v = \{0, 0, 1, 0\}$ on ensemble c, and to $\vec{p}_v = \{0, 0, 0, 1\}$ on ensemble d, each with success probability $P_s^{(ent)} = 1$.

For fully separable states $|\Psi\rangle_o = |\psi_a\rangle_a|\psi_b\rangle_b|\psi_c\rangle_c|\psi_d\rangle_d$ with $|\psi_{\epsilon_i}\rangle_{\epsilon_i} = \sum_{n=0}^{\infty} c_{\epsilon_i}^{(n)}|n\rangle_{\epsilon_i}$, we displace the resulting π-phase shifted state $|\Psi_{\epsilon_i}^{(\pi)}\rangle_f = \hat{U}_{\pi,\epsilon_i}|\Psi\rangle_o$ with a local unitary transformation $\hat{V}_{\epsilon_i}|\psi_{\epsilon_i}\rangle_{\epsilon_i} = |0\rangle_{\epsilon_i}$. The overall process $\hat{V}_a\hat{V}_b\hat{V}_c\hat{V}_d\hat{U}_{\pi,\epsilon_i}$ maps the initial product state $|\Psi\rangle_o$ into $\hat{V}_a\hat{U}_{\pi,a}|\psi_a\rangle_a|0\rangle_b|0\rangle_c|0\rangle_d$ (phase shift on ensemble a), $|0\rangle_a\hat{V}_b\hat{U}_{\pi,b}|\psi_b\rangle_b|0\rangle_c|0\rangle_d$ (ensemble b), $|0\rangle_a|0\rangle_b\hat{V}_c\hat{U}_{\pi,c}|\psi_c\rangle_c|0\rangle_d$ (ensemble c), and $|0\rangle_a|0\rangle_b|0\rangle_c\hat{V}_d\hat{U}_{\pi,d}|\psi_d\rangle_d$ (ensemble d), with only one ϵ_i containing $\langle\hat{n}_{\epsilon_i}\rangle > 0$ excitations. Thus, we can *unambiguously* identify the phase shifted ensemble ϵ_i given a photodetection, albeit with a failure probability $P_f = \frac{1}{4}\sum_{\epsilon_i}|_{\epsilon_i}\langle 0|\hat{V}_{\epsilon_i}\hat{U}_{\pi,\epsilon_i}|\psi_{\epsilon_i}\rangle_{\epsilon_i}|^2 = \frac{1}{4}\sum_{\epsilon_i}|_{\epsilon_i}\langle\psi_{\epsilon_i}|\hat{U}_{\pi,\epsilon_i}|\psi_{\epsilon_i}\rangle_{\epsilon_i}|^2$ arising from *inconclusive* null events (i.e., $|0000\rangle\langle 0000|$). We derive the maximum success probability $P_s^{(max)} = 1 - P_f^{(min)}$ and the optimal state $|\Psi\rangle_o = |\Psi\rangle_{opt}$ by minimizing $P_f^{(min)}$ over all possible realizations of $c_{\epsilon_i}^{(n)}$ satisfying $\sum_{\epsilon_i}\langle\psi_{\epsilon_i}|\hat{n}_{\epsilon_i}|\psi_{\epsilon_i}\rangle_{\epsilon_i} = 1$. Specifically, we find that an optimal (pure) separable state $|\Psi\rangle_{opt} = \prod_{\epsilon_i}(\sqrt{3/4}|0\rangle_{\epsilon_i} + \sqrt{1/4}|1\rangle_{\epsilon_i})$ can be used for the parameter estimation protocol to infer ϵ_i with $P_s^{(max)} = 0.75$. Similarly, maximum success probability $P_s^{(coh)}$ can be derived for multimode coherent states $\prod_{\epsilon_i}|\alpha_{\epsilon_i}\rangle_{\epsilon_i}$, giving a classical bound of $P_s^{(coh)} = 1 - 1/e$.

Finally, we consider the upper bound $P_s^{(max)}$ for mixed separable states $\hat{\rho}_o^{(sep)}$ with pure state decompositions $\hat{\rho}_o^{(sep)} = \sum_m p_m|\Psi_m\rangle_o\langle\Psi_m|$. Generally, the transformations $\hat{V}_{\epsilon_i}$, as discussed above, do not exist for $\hat{\rho}_o^{(sep)}$, excluding the possibility of an unambiguous state discrimination. Thus, the success probability $P_s(\hat{\rho}_o^{(sep)})$ is upper bounded by the convex combinations of $\{|\Psi_m\rangle\}$, thereby $P_s(\hat{\rho}_o^{(sep)}) \leq$

$\sum_m p_m P_s(|\Psi_m\rangle_o\langle\Psi_m|) \leq P_s^{(max)} = 0.75$. Importantly, the maximum success probability $P_s^{(max)} = 0.75$, attainable for any $\hat{\rho}_o^{(sep)}$, is less than $P_s^{(ent)} = 1$ for entangled states $|W\rangle_o$. Thus, the entangled spin-waves in the experiment can be applied for sensing an atomic phase shift beyond the limit for any unentangled state. Comprehensive analysis of our protocol including experimental imperfections (e.g., detection efficiency) as well as other measurement strategies will be discussed elsewhere.

Chapter 3

Atom-light interactions: waveguide QED

3.1 Introduction

In this chapter, we describe the underlying physics of atom-photon interactions along a 1D waveguide. First, we describe photon transport properties in the presence of a single photon, including reflection transmission spectra, saturation behavior, and photon correlation. Then we discuss the collective effects that emerge with two atoms coupled to the waveguide mode. Depending on the distance between atoms, the collective effects change from superradiance to dipole-dipole interaction. We further consider N atom coupled to the 1D PCW, which can separate these two collective effects across the band edge of the PCW and introduce finite-range dipole-dipole interaction inside the band gap of the PCW.

3.2 Single atom coupled to a 1D waveguide

3.2.1 System Hamiltonian

We consider a simple system where a two-level atom, consisting of ground state $|g\rangle$ and excited states $|e\rangle$ separated by transition frequency ω_0, couples to a 1D continuum waveguide mode. The corresponding Hamiltonian is described by a term denoting the energy levels of the atom H_{atom}, freely propagating photons in a

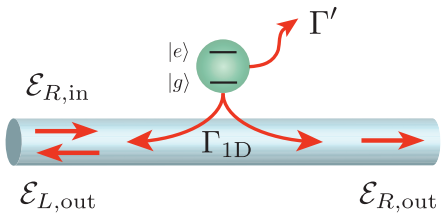

Figure 3.1: **Schematic of a single atom coupled to a 1D waveguide.** A two-level atom, consisting of ground state $|g\rangle$ and excited state $|e\rangle$, couples to the 1D waveguide with a decay rate Γ_{1D} and to all the other channels with a decay rate Γ'.

waveguide H_{ph}, and dipole-interaction term H_{int} with the rotating-wave approximation as [71, 74],

$$H_{\mathrm{tot}}/\hbar = H_{\mathrm{atom}} + H_{\mathrm{ph}} + H_{\mathrm{int}} \tag{3.1}$$

$$= \omega_0 \sigma_{ee} + \int dk \omega_k a_k^\dagger a_k + \int dk g \left(\sigma_{eg} a_k e^{ikx} + \mathrm{h.c.}\right), \tag{3.2}$$

where $\sigma_{ij} = |i\rangle\langle j|$, a_k is the annihilation operator for the mode with wavevector k, and the frequency ω_k of the propagating mode. While the atom couples to the waveguide mode with the dipole-coupling amplitude g, the atom also emits photons into all the other mode (i.e. free space) with the decay rate Γ'. The evolution of the atom is described by a master equation for an atomic density operator ρ,

$$\dot{\rho} = \frac{1}{i\hbar}\left[H_{\mathrm{tot}}, \rho\right] + L[\rho], \tag{3.3}$$

where the Lindblad term is given by,

$$L[\rho] = -\frac{\Gamma'}{2}\sum_j \left(\sigma_{eg}^j \sigma_{ge}^j \rho + \rho \sigma_{eg}^j \sigma_{ge}^j - 2\sigma_{ge}^j \rho \sigma_{eg}^j\right). \tag{3.4}$$

From Eq. (3.2), we obtain Heisenberg-Langevin equations for the atomic operators, which are useful for studying photon transport properties under large coherent excitation (see details in Appendix A).

3.2.2 Basic rates of a single atom

Figure 3.1 illustrates the basic rates of a single atom coupled to the waveguide: the decay rate into the guided mode Γ_{1D} and the decay rate into all the other modes Γ'. The decay rate into the guided mode is written by

(see Appendix A),

$$\Gamma_{1\mathrm{D}} = \frac{4\pi g^2}{v_g} = \frac{1}{2}\frac{c}{v_g}\frac{\sigma_0}{A_{\mathrm{m}}}\Gamma_0, \tag{3.5}$$

where Γ_0 is a Einstein A coefficient in free space, σ_0 is a cross section of the atom, and A_{m} is an effective mode area. Here, the group velocity is defined as $v_g \equiv \left|\frac{\partial\omega}{\partial k}\right| = \frac{c}{n_g}$ where a group index is $n_g \simeq 1.5$ of a SiO_2 nanofiber and $n_g \simeq 2.0$ of a SiN waveguide. The Purcell factor is defined as a ratio of the decay rate into the guided mode $\Gamma_{1\mathrm{D}}$ to that into all the other channels Γ',

$$P \equiv \frac{\Gamma_{1\mathrm{D}}}{\Gamma'}, \tag{3.6}$$

which quantifies how the atomic excitation decays: in the limit $P \to \infty$, all the excitation will decay into the guided mode. For a typical 1D waveguide considered here (i.e., nanofiber and double nano beam), the decay rate into all the other channels is $\Gamma' \sim \Gamma_0$ without significant suppression [120]. A large Purcell factor can be achieved by enhanced $\Gamma_{1\mathrm{D}}$ via small effective mode area, $A_{\mathrm{m}} \leq \sigma_0$, and a small group velocity $v_g \ll c$. On resonance, the atom has a maximal scattering cross section that is proportional to the square of the wavelength, $\sigma_0 \approx \lambda^2$, requiring the sub-wavelength confinement $A_{\mathrm{m}} \leq \lambda^2$. We will discuss an enhanced group index $n_g \gg 1$ via slow light effect of the PCW near the band edge in Section 3.4.

3.2.3 Coherent field transport

We consider a single atom, excited by right-going coherent state with a field amplitude, $\mathcal{E}_{R,\mathrm{in}} = \mathcal{E}_0$, and calculate the reflectivity of a single atom. The equations of motion for the operator mean values of slowly-varying variables, $s_{ge} = \langle\tilde{\sigma}_{ge}\rangle$, $s_z = \langle\tilde{\sigma}_z\rangle$, are written by

$$\dot{s}_{ge} = \left(i\Delta - \frac{\Gamma_{\mathrm{tot}}}{2}\right) s_{ge} + i2\sqrt{2\pi}g\mathcal{E}_0 s_z, \tag{3.7a}$$

$$\dot{s}_z = -\Gamma_{\mathrm{tot}}\left(s_z + \frac{1}{2}\right) - i\sqrt{2\pi}g\left(\mathcal{E}_0 s_{eg} - \mathcal{E}_0^* s_{ge}\right), \tag{3.7b}$$

where the total decay rate $\Gamma_{\rm tot} = \Gamma_{\rm 1D} + \Gamma'$ and the detuning $\Delta = \omega_{\rm L} - \omega_0$ with a probe frequency $\omega_{\rm L}$. The equations above can be cast into a compact and convenient form as,

$$\dot{\mathbf{s}} = \mathbf{D} \cdot \mathbf{s} + \mathbf{f}, \tag{3.8}$$

with a time-independent matrix $\mathbf{D}$ and a vector $\mathbf{f}$,

$$\mathbf{s} = \begin{pmatrix} s_{ge} \\ s_{eg} \\ s_z \end{pmatrix}, \quad \mathbf{D} = \begin{pmatrix} i\Delta - \frac{\Gamma_{\rm tot}}{2} & 0 & 2i\Omega_c \\ 0 & -i\Delta - \frac{\Gamma_{\rm tot}}{2} & -2i\Omega_c^* \\ i\Omega_c^* & -i\Omega_c & -\Gamma_{\rm tot} \end{pmatrix}, \quad \mathbf{f} = \begin{pmatrix} 0 \\ 0 \\ -\frac{\Gamma_{\rm tot}}{2} \end{pmatrix}, \tag{3.9}$$

where the Rabi frequency of the input field $\Omega_c = \sqrt{2\pi} g \mathcal{E}_0$. This $\mathbf{D}$ matrix enables us to calculate higher-order correlation functions using the quantum regression theorem (see Section 3.2.4). Then, the steady-state values $\bar{\mathbf{s}} = \mathbf{s}(t \to \infty)$ are obtained by,

$$\bar{s}_z = -\frac{\Gamma_{\rm tot}^2 + 4\Delta^2}{2(\Gamma_{\rm tot}^2 + 4\Delta^2 + 8|\Omega_c|^2)}, \quad \bar{s}_{ge} = \frac{2\Delta - i\Gamma_{\rm tot}}{\Gamma_{\rm tot}^2 + 4\Delta^2 + 8|\Omega_c|^2} 2\Omega_c. \tag{3.10}$$

Given the steady-state atomic coherence $\bar{s}_{ge}$, one can compute the transmission and reflection by using the input-output relation (Appendix A). The reflected (left-going) field amplitude is written by

$$\mathcal{E}_{L,\rm out} = -i\sqrt{\frac{\Gamma_{\rm 1D}}{2v_g}} \bar{s}_{ge}. \tag{3.11}$$

Then, the steady-state reflectivity of a single atom is expressed as [58, 74],

$$r_1(\Delta, \Omega_c) = \frac{\mathcal{E}_{L,\rm out}}{\mathcal{E}_{R,\rm in}} = -\frac{\Gamma_{\rm 1D}}{\Gamma_{\rm tot}} \frac{1 + i\frac{2\Delta}{\Gamma_{\rm tot}}}{1 + \frac{4\Delta^2}{\Gamma_{\rm tot}^2} + \frac{8|\Omega_c|^2}{\Gamma_{\rm tot}^2}}. \tag{3.12}$$

For a resonant incident field ($\Delta = 0$), a single atom is saturated at a Rabi frequency $\Omega_c \sim \Gamma_{\rm tot}$, suggesting that the saturation intensity $I_{\rm sat} \propto \Omega_c^2$ is proportional to $\Gamma_{\rm tot}^2$. Figure 3.2 shows saturation dependence of transmission $T = |1 + r_1(\Delta, \Omega_c)|^2$ and reflection spectra $R = |r_1(\Delta, \Omega_c)|^2$ with various values of Ω_c.

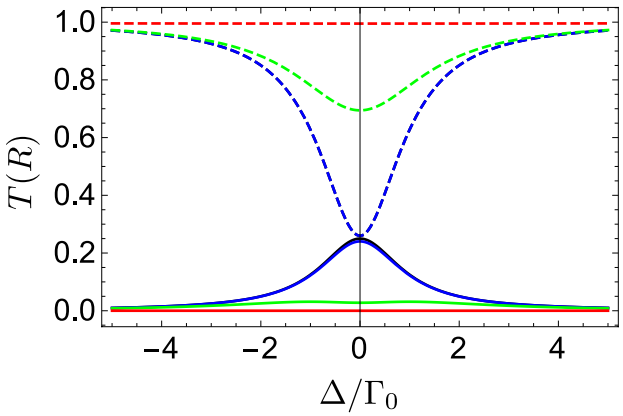

Figure 3.2: **Saturation dependence of transmission and reflection spectra.** The transmission (dashed) and reflection spectra (solid curves), with $\Omega_c/\Gamma_0 = 0.01$ (black), 0.1 (blue), 1 (green), and 10 (red), where $\Gamma_{1D} = \Gamma' = \Gamma_0$.

In the weak excitation limit $\Omega_c \to 0$, the reflectivity of a single atom is simplified to

$$r_1(\Delta) = -\frac{\Gamma_{1D}}{\Gamma_{1D} + \Gamma' - 2i\Delta}. \tag{3.13}$$

One can easily show that the reflectivity of the single atom with incident single photon is identical to that with the weak coherent state [71, 74].

3.2.4 Photon correlation for coherent incident field

The nonclassical properties of photons scattered by a single atom are evident in photon correlation. They are often characterized by the normalized second-order correlation function in the steady state ($t \to \infty$),

$$g_\ell^{(2)}(\tau) = \frac{\langle a_{\ell,\mathrm{out}}^\dagger(t) a_{\ell,\mathrm{out}}^\dagger(t+\tau) a_{\ell,\mathrm{out}}(t+\tau) a_{\ell,\mathrm{out}}(t)\rangle_{\mathrm{ss}}}{\langle a_{\ell,\mathrm{out}}^\dagger(t) a_{\ell,\mathrm{out}}(t)\rangle_{\mathrm{ss}}^2}, \tag{3.14}$$

where $\ell = R$ for transmission (right-going) field and $\ell = L$ for reflection (left-going) field. In the weak excitation limit, by solving Eq. (3.8) for higher-order correlation functions, the normalized second-order

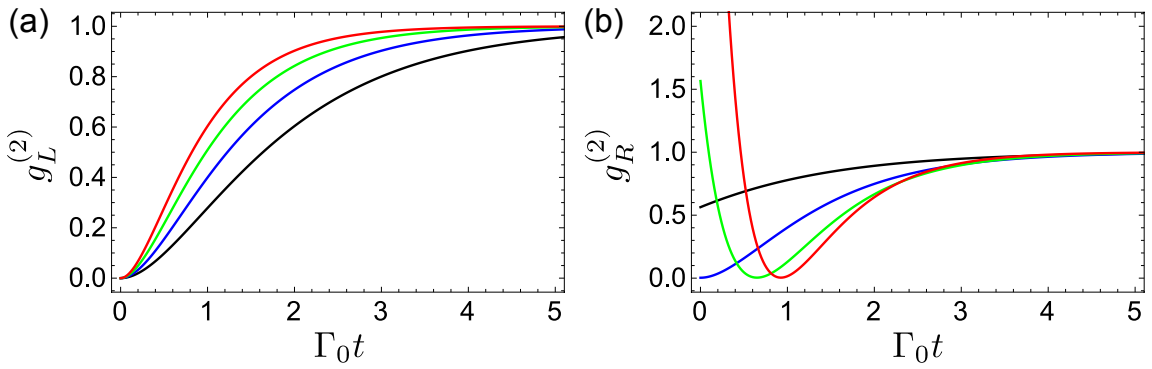

Figure 3.3: **Normalized second-order correlation function $g_\ell^{(2)}$ in the weak excitation regime** $(\Omega/\Gamma_0 = 0.01)$**.** (a) $g_L^{(2)}$ for the reflected (left-going) field as a function of normalized time $\Gamma_0 t$, (b) $g_R^{(2)}$ for the transmitted (right-going) field, with $\Gamma_{1D}/\Gamma_0 = 0.5$ (black), 1 (blue), 1.5 (green), and 2 (red), where $\Gamma' = \Gamma_0$.

correlation functions for the reflected and transmitted fields are approximately given by,

$$g_L^{(2)}(\tau) \approx e^{-\Gamma_{\rm tot}\tau}\left(1 - e^{-\Gamma_{\rm tot}\tau/2}\right)^2, \tag{3.15a}$$

$$g_R^{(2)}(\tau) \approx e^{-\Gamma_{\rm tot}\tau}\left(\xi_0^2 - e^{-\Gamma_{\rm tot}\tau/2}\right)^2, \tag{3.15b}$$

where $\xi_0 = \frac{\Gamma_{1D}}{\Gamma'}$. As shown in Fig. 3.3 (a), $g_L^{(2)}(\tau)$ shows the anti-bunching at $\tau = 0$, regardless of the magnitude of the coupling rate $\xi_0 = \frac{\Gamma_{1D}}{\Gamma'}$, since the reflected field purely comes from the scattered field of the atom [74, 77]. Figure 3.3 (b) exhibits the unique photon correlation of transmitted fields, which arises from the quantum interference between the scattered and incident fields, as shown in Eq. (3.15b). As increasing ξ_0 at $\xi_0 < 1$, $g_R^{(2)}(0)$ decreases further and the initial antibunching gets strongest at $\xi_0 = 1$. For $\xi_0 \gg 1$, pronounced bunching is predicted at $\tau = 0$, where two and higher-order photon components of the coherent state are transmitted with increased probability while the single-photon component is reflected. Then the pronounced bunching is followed by anti-bunching at a subsequent time $\tau_0 = \frac{4\log\xi_0}{\Gamma_{1D}}$ [74, 77]. In the case of two-photon transport, a two-photon bound state is predicted to pass through the single atom as a composite photon. Thus, effective attractive or repulsive interaction between photons could be induced by the presence of the single atom [72, 121].

Beyond the weak excitation limit, the saturation behavior is included by using the exact expression of Eq. (3.14). Figure 3.4 displays the saturation dependence of photon correlation $g_{R/L}^{(2)}$, which indeed approaches

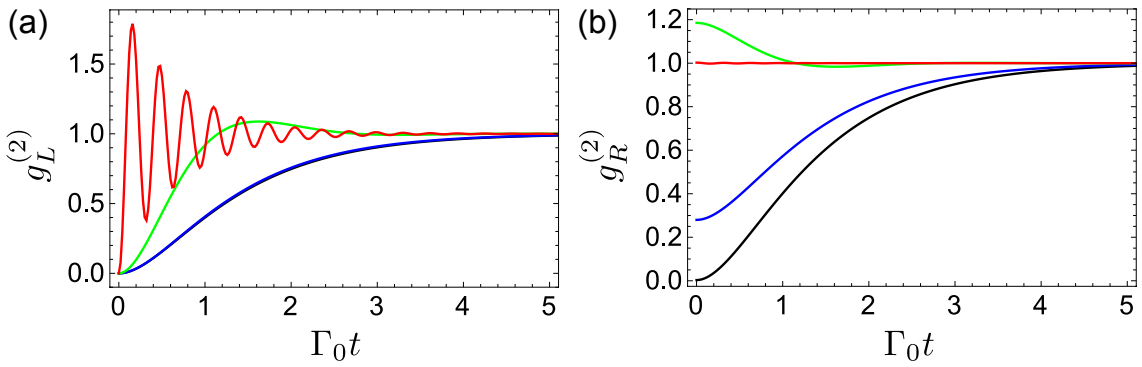

Figure 3.4: **Staturation behavior of $g_\ell^{(2)}$.** (a) $g_L^{(2)}$ for the reflected field as a function of normalized time $\Gamma_0 t$, (b) $g_R^{(2)}$ for the transmitted field, with $\Omega_c/\Gamma_0 = 0.01$ (black), 0.1 (blue) 1 (green), and 10 (red), where $\Gamma_{1D} = \Gamma' = \Gamma_0$.

unity for the strong incident fields ($\Omega_c \gg \Gamma_0$).

3.2.5 Transfer matrix in the weak excitation limit

For a linear system, we can define a transfer matrix which relates the field amplitudes on the left-side of an optical element to the field amplitudes on the right-side, instead of relating the outgoing modes to the incoming ones, as illustrated in Fig. 3.5. The advantage of the transfer matrix method is that it is easy to scale up a system: the transfer matrix of a composite system is just the product of the matrices of its components [122].

In the weak excitation limit, where atomic saturation is ignored, the response of a single atom is linear, enabling us to determine the transfer matrix of a single atoms. As described in Appendix A, the input-output

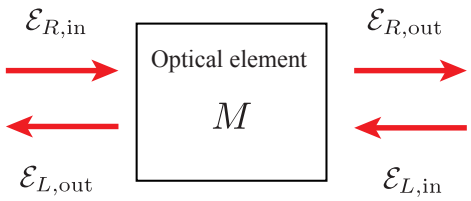

Figure 3.5: **Diagram of a transfer matrix.** A transfer matrix M relates the field amplitudes on the left-side ($\mathcal{E}_{R,\mathrm{in}}$, $\mathcal{E}_{L,\mathrm{out}}$) of an optical element to the field amplitudes on the right-side ($\mathcal{E}_{R,\mathrm{out}}$, $\mathcal{E}_{L,\mathrm{in}}$).

relations for incident coherent fields from both sides read

$$\mathcal{E}_{R,\mathrm{out}} = \mathcal{E}_{R,\mathrm{in}} - i\sqrt{\frac{\Gamma_{1\mathrm{D}}}{2v_g}}\bar{s}_{ge}, \tag{3.16a}$$

$$\mathcal{E}_{L,\mathrm{out}} = \mathcal{E}_{L,\mathrm{in}} - i\sqrt{\frac{\Gamma_{1\mathrm{D}}}{2v_g}}\bar{s}_{ge}, \tag{3.16b}$$

and the steady-state coherence is given by,

$$\bar{s}_{ge} = i\frac{\sqrt{2\Gamma_{1\mathrm{D}}v_g}}{\Gamma_{1\mathrm{D}} + \Gamma' - 2i\Delta}\left(\mathcal{E}_{R,\mathrm{in}} + \mathcal{E}_{L,\mathrm{in}}\right). \tag{3.17}$$

Thus, the input-output relation can be transformed to transfer matrix representation as,

$$\begin{pmatrix} \mathcal{E}_{R,\mathrm{out}} \\ \mathcal{E}_{L,\mathrm{in}} \end{pmatrix} = M_{\mathrm{atom}} \begin{pmatrix} \mathcal{E}_{R,\mathrm{in}} \\ \mathcal{E}_{L,\mathrm{out}} \end{pmatrix}, \tag{3.18}$$

with a transfer matrix of the single atom for incident coherent fields

$$M_{\mathrm{atom}} = \begin{pmatrix} 1+i\xi & i\xi \\ -i\xi & 1-i\xi \end{pmatrix}, \tag{3.19}$$

where

$$\xi = -\frac{\xi_0}{i+\delta}, \quad \xi_0 = \frac{\Gamma_{1\mathrm{D}}}{\Gamma'}, \quad \text{and} \quad \delta = \frac{2\Delta}{\Gamma'}. \tag{3.20}$$

The transfer matrix in Eq. (3.19) is consistent with the one derived from the 1D Helmholtz equation in Ref. [123].

3.3 Multiple atoms coupled to the 1D waveguide

Next, we study the collective effects induced by photon-mediated interactions between atoms. Depending on the distance between the atoms, the exchange of real or virtual photons between atoms gives rise to

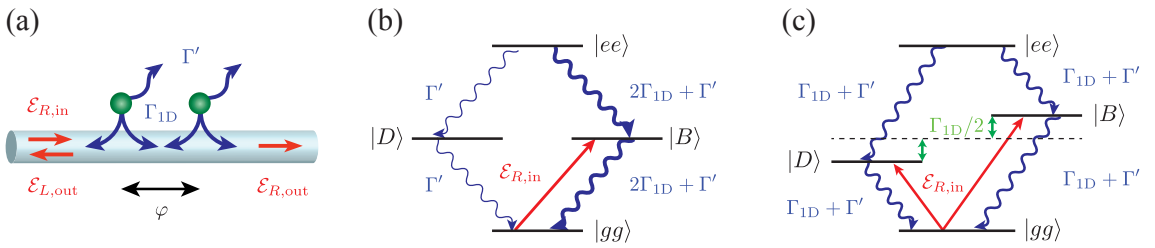

Figure 3.6: **Schematic energy level diagram for two atoms interacting with a 1D waveguide.** (a) Two atoms interact with a 1D waveguide at a separation $\varphi = k|x_1 - x_2|$. (b) Superradiance at $\varphi = \pi$ between two atoms. $\mathcal{E}_{R,\mathrm{in}}$ (red arrow) represents a weakly-exciting guided mode, which only drives the superradiant emission via the bright state $|B\rangle$. The dark state $|D\rangle$ cannot be driven directly from the ground state $|gg\rangle$. (c) Dipole-dipole interaction with $\varphi = \pi/2$. The energy levels of $|B\rangle$ and $|D\rangle$ states are shifted by $\pm\Gamma_{1D}/2$ by exchanging virtual photons. Both $|B\rangle$ and $|D\rangle$ states are driven by the guide mode $\mathcal{E}_{R\mathrm{in}}$.

superradiance or dipole-dipole interaction.

3.3.1 Interacting spin Hamiltonian

The dynamics of N atoms is equivalently described by an non-hermitian Hamiltonian in the quantum jump description of an open system (Appendix A) [124, 125] as

$$H_{\mathrm{eff}}/\hbar = -\sum_j \left(\Delta + i\frac{\Gamma_{1D}+\Gamma'}{2}\right)\tilde{\sigma}^j_{ee} - \sum_j \Omega_c\left(\tilde{\sigma}^j_{eg}e^{ikx_j} + \mathrm{h.c.}\right) - i\frac{\Gamma_{1D}}{2}\sum_{j'\neq j}\tilde{\sigma}^j_{eg}\tilde{\sigma}^{j'}_{ge}e^{ik|x_j-x_{j'}|}, \quad (3.21)$$

where x_j is the position of the j-th atom. To illustrate the basic properties of "waveguide QED", we consider two examples: (i) superradiance of two atoms separated by $\varphi = k|x_1 - x_2| = \pi$ and (ii) dipole-dipole interaction between two atoms separated by $\varphi = \pi/2$ [126–128]. For simplicity, we set $x_1 = 0$ and $kx_2 = \varphi$. We obtain more transparent form of the effective Hamiltonian by introducing the dressed-state operators,

$$\tilde{\sigma}^B_{ge} = \frac{-\tilde{\sigma}^{(1)}_{ge} + \tilde{\sigma}^{(2)}_{ge}}{\sqrt{2}}, \qquad \tilde{\sigma}^D_{ge} = \frac{\tilde{\sigma}^{(1)}_{ge} + \tilde{\sigma}^{(2)}_{ge}}{\sqrt{2}}, \quad (3.22)$$

which decouples the dynamics of atoms into bright and dark states, as we will see in the following sections.

3.3.1.1 Two atoms: superradiance at the separation $\varphi = \pi$

The effective Hamiltonian at the separation $\varphi = \pi$ is given by $H_{\rm eff} = H^B_{\rm eff} + H^D_{\rm eff}$ with

$$H^B_{\rm eff}/\hbar = -\left(\Delta + i\frac{2\Gamma_{\rm 1D} + \Gamma'}{2}\right)\tilde{\sigma}^B_{eg}\tilde{\sigma}^B_{ge} + \sqrt{2}\Omega_c\left(\tilde{\sigma}^B_{eg} + \tilde{\sigma}^B_{ge}\right), \tag{3.23a}$$

$$H^D_{\rm eff}/\hbar = -\left(\Delta + i\frac{\Gamma'}{2}\right)\tilde{\sigma}^D_{eg}\tilde{\sigma}^D_{ge}, \tag{3.23b}$$

where the jump operators of H_B and H_D describe the superradiance with $2\Gamma_{\rm 1D} + \Gamma'$ and subradiance with Γ', respectively. Eq. (3.23b) indicates that the dark state $|D\rangle$ cannot be driven directly from the ground state $|gg\rangle$ by guided-mode fields. Thus, in the weak-excitation regime, atoms are driven to the bright state $|B\rangle$, resulting in the superradiance, as illustrated in Fig. 3.6 (b). On the other hand, when the atoms are driven identically (i.e., external illumination with the same phase), the driving term of the Hamiltonian is given by $H_{\rm ex} \propto \left(\tilde{\sigma}^D_{eg} + \tilde{\sigma}^D_{ge}\right)$, leading to the excitation of the subradiant state $|D\rangle$.

3.3.1.2 Two atoms: dipole-dipole interaction at the separation $\varphi = \pi/2$

In the case of $\varphi = \pi/2$, each effective Hamiltonian is written by

$$H^B_{\rm eff}/\hbar = -\left(\Delta + \frac{\Gamma_{\rm 1D}}{2} + i\frac{\Gamma_{\rm 1D} + \Gamma'}{2}\right)\tilde{\sigma}^B_{eg}\tilde{\sigma}^B_{ge} + \Omega_c e^{i\frac{3\pi}{4}}\left(\tilde{\sigma}^B_{eg} + \tilde{\sigma}^B_{ge}\right), \tag{3.24a}$$

$$H^D_{\rm eff}/\hbar = -\left(\Delta - \frac{\Gamma_{\rm 1D}}{2} + i\frac{\Gamma_{\rm 1D} + \Gamma'}{2}\right)\tilde{\sigma}^D_{eg}\tilde{\sigma}^D_{ge} + \Omega_c e^{i\frac{\pi}{4}}\left(\tilde{\sigma}^D_{eg} + \tilde{\sigma}^D_{ge}\right). \tag{3.24b}$$

The energy levels of $|B\rangle$ and $|D\rangle$ states are shifted by $\pm\Gamma_{\rm 1D}/2$ due to the exchange of photons, as illustrated in Fig. 3.6 (c). Both states are driven by the guide mode with the equal amplitude of Rabi frequency Ω_c. While the frequency difference between $|B\rangle$ and $|D\rangle$ is $\Gamma_{\rm 1D}$, the linewidth of both states are larger, $\Gamma_{\rm 1D} + \Gamma'$, meaning that we cannot distinguish two resonances even with large $\Gamma_{\rm 1D}$ by using a guided mode.

3.3.2 Field response in the weak-excitation limit

Once we obtain the atomic response from the Heisenberg-Langevin equations, we can reconstruct the field response via the input-output relation. In the weak excitation regime, the equation of motion for the operator

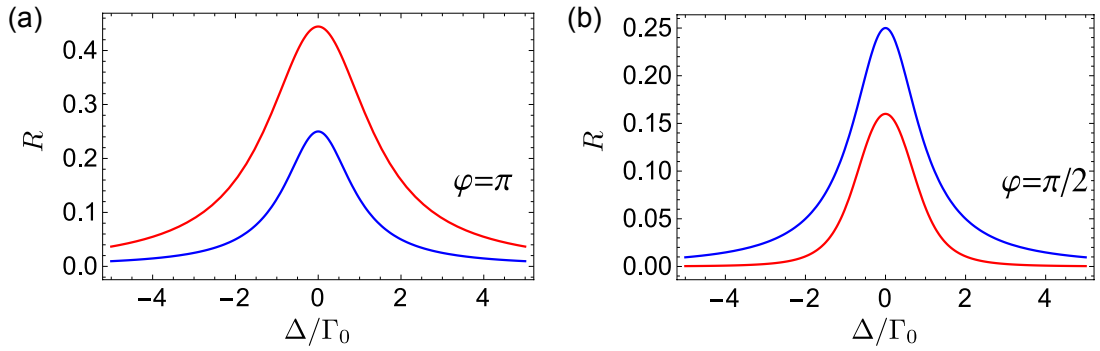

Figure 3.7: **Reflection spectra with $N = 2$ atoms in the weak excitation limit.** (a) the reflection spectrum $R = |r_2(\pi)|^2$ (red) of two atoms separated by $\varphi = \pi$ and single atom spectrum $|r_1|^2$ (blue). Here, $\Gamma_{1D} = \Gamma' = \Gamma_0$. (b) the reflection spectrum $R = |r_2(\pi/2)|^2$ (red) of two atoms separated by $\varphi = \pi/2$ and single atom spectrum (blue). Due to the destructive interference, the reflectivity of two atoms is smaller than that of the single atom.

mean value, $s^j_{ge} = \langle \tilde{\sigma}^j_{ge} \rangle$, is written as

$$\dot{s}^j_{ge} = \left(i\Delta - \frac{\Gamma_{1D} + \Gamma'}{2} \right) s^j_{ge} - i\Omega_c e^{ikx_j} - \frac{\Gamma_{1D}}{2} \sum_{j' \neq j} s^{j'}_{ge} e^{ik|x_j - x_{j'}|}. \tag{3.25}$$

To study the field response (i.e., reflection spectrum), we again consider the same examples: (i) two-atom superradiance at the separation $\varphi = \pi$ and (ii) dipole-dipole interaction at the separation $\varphi = \pi/2$.

3.3.2.1 Superradiance at the separation $\varphi = \pi$

By using the input-output relation (Appendix A), the reflected field amplitude is given by

$$\mathcal{E}_{L,\text{out}} = -i\sqrt{\frac{\Gamma_{1D}}{2v_g}} \left(\bar{s}^{(1)}_{ge} + e^{i\pi} \bar{s}^{(2)}_{ge} \right), \tag{3.26}$$

where the steady-state coherence $\bar{s}^j_{ge} = s^j_{ge}(t \to \infty)$. From Eq. (3.25), we obtain the steady-state coherence $\bar{s}^j_{ge}$ as

$$\bar{s}^{(1)}_{ge} = e^{i\pi} \bar{s}^{(2)}_{ge} = -\frac{i2\Omega_c}{2\Gamma_{1D} + \Gamma' - 2i\Delta}. \tag{3.27}$$

Thus, the reflectivity of two atoms at $\varphi = \pi$ is expressed as

$$r_2(\pi) = \frac{\mathcal{E}_{L,\mathrm{out}}}{\mathcal{E}_{R,\mathrm{in}}} = -\frac{2\Gamma_{1\mathrm{D}}}{2\Gamma_{1\mathrm{D}} + \Gamma' - 2i\Delta}, \tag{3.28}$$

where the linewidth is enhanced by the superradiance, $2\Gamma_{1\mathrm{D}} + \Gamma'$ shown in Fig. 3.7 (a). In the case of N atoms, we can see the cooperative decay rate, $(N-1)\Gamma_{1\mathrm{D}}$, from the last term of Eq. (3.25), leading to the total decay rate $\Gamma_{\mathrm{tot}} = N\Gamma_{1\mathrm{D}} + \Gamma'$. The reflectivity in Eq. (3.28) is consistent with the intuitive picture given by the interacting spin Hamiltonian in Section 3.3.1.1.

3.3.2.2 Dipole-dipole interaction at the separation $\varphi = \pi/2$

Similarly, the reflectivity of two atoms at $\varphi = \pi/2$ is obtained by

$$r_2(\pi/2) = -i\left[\frac{\Gamma_{1\mathrm{D}}}{\Gamma_{1\mathrm{D}} + \Gamma' - 2i(\Delta - \Gamma_{1\mathrm{D}}/2)} - \frac{\Gamma_{1\mathrm{D}}}{\Gamma_{1\mathrm{D}} + \Gamma' - 2i(\Delta + \Gamma_{1\mathrm{D}}/2)}\right]. \tag{3.29}$$

The reflectivity consists of two Lorentzians with a linewidth $\Gamma_{1\mathrm{D}} + \Gamma'$ and frequency shift $\pm\frac{\Gamma_{1\mathrm{D}}}{2}$. Due to the destructive interference of these two modes, the peak reflectivity is smaller than the single atom reflectivity shown by blue curve in Fig. 3.7. Note that one can get the same results for both $\varphi = \pi$ and $\pi/2$ by using the transfer matrix method. For $N \geq 3$ at $\varphi = \pi/2$, the atomic response is a mixture of superradiance and dipole-dipole interaction, resulting in a complicated reflection spectrum. We will discuss an alternative approach to study dipole-dipole interaction of $N \geq 3$ atoms with the help of photonics crystal waveguides in Section 3.4.

3.4 Photonic crystal waveguide near the band edge

In practice, the atoms must be trapped at ~ 200 nm away from the surface of the SiO_2 nanofiber, to protect atoms from the surface potential in the trapping scheme of Refs. [61, 64]. Due to the atom-photon coupling via evanescent fields, the projected coupling rate is only $\Gamma_{1\mathrm{D}}/\Gamma' = 0.04$ for Cs D_2 line transition [120]. As shown in Eq. (3.1), the enhanced coupling rate $\Gamma_{1\mathrm{D}}$ can be achieved via slow light effect, $v_g \ll c$, due to

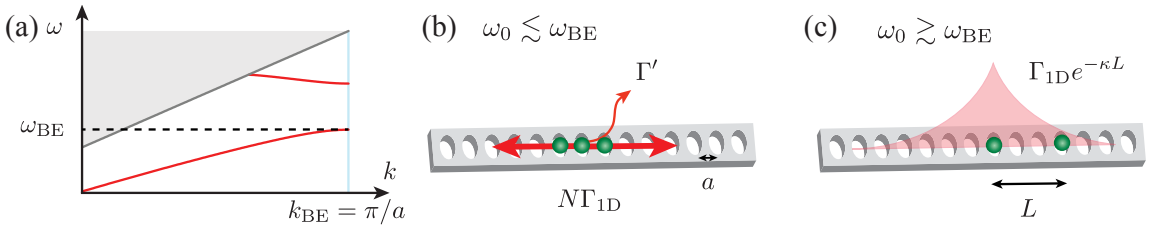

Figure 3.8: **Schematic of a 1D photonic crystal waveguide and dispersion relation.** (a) A typical dispersion relation of the 1D photonic crystal waveguide (PCW), illustrating the guided mode frequency ω versus the Bloch wavevector k in the reduced first Brillouin zone near the band edge ($k_{\rm BE} = \pi/a$ at $\omega_{\rm BE}$). (b) A schematic image of superradiance for N atoms near the band edge of the PCW ($\omega_{\rm atom} \lesssim \omega_{\rm BE}$). (c) A schematic image of finite-range atom-atom interaction mediated by virtual photons inside the band gap ($\omega_{\rm atom} \gtrsim \omega_{\rm BE}$).

the flat dispersion relation of the Bloch modes near the band edge of a photonic crystal waveguide (PCW), illustrated in Fig. 3.8 (a) [68].

Near the band edge, the PCW separates two collective effects, superradiance and dipole-dipole interaction, either inside or outside of the band gap as illustrated in Fig. 3.8 (b,c). Outside the band gap, $\omega_0 \lesssim \omega_{\rm BE}$, because the Bloch function for a guided mode near the band edge approaches a standing-wave, symmetric optical excitations can be induced in an array of trapped atoms, resulting in superradiant emission [18, 129]. On the other hand, inside the band gap, $\omega_0 \gtrsim \omega_{\rm BE}$, the emitted field forms the localized mode with an exponentially decaying envelope, leading to the finite-range dipole-dipole interaction between atoms by exchanging virtual photons without dissipation into the waveguide [87].

3.4.1 Outside the band gap: Superradiance

Near the band edge $\omega_{\rm atom} \lesssim \omega_{\rm BE}$, the Bloch function for a guided mode approaches a standing-wave, resulting in the effective spin Hamiltonian given by

$$H_{\rm eff}/\hbar = -\sum_j \left(\Delta + i\frac{\Gamma_{\rm 1D}+\Gamma'}{2}\right)\tilde{\sigma}^j_{ee} - i\frac{\Gamma_{\rm 1D}}{2}\sum_{j\neq j'}(-1)^{j-j'}\tilde{\sigma}^j_{eg}\tilde{\sigma}^{j'}_{ge}, \tag{3.30}$$

where we assume that atoms are localized at the center of each unit cell. The last term of Eq. (3.30) describes the correlated decay between N atoms. Here, we introduce a dressed-state operator for N atoms as $\tilde{\sigma}^{B_N}_{ge} = \frac{1}{\sqrt{N}}\sum_j(-1)^j\tilde{\sigma}^j_{ge}$. Then, in the weak excitation limit, the equation of motion for the operator mean value,

$s_{ge}^{B_N} = \langle \tilde{\sigma}_{ge}^{B_N} \rangle$, is simply written as

$$\dot{s}_{ge}^{B_N} = \left(i\Delta - \frac{N \cdot \Gamma_{1\mathrm{D}} + \Gamma'}{2} \right) s_{ge}^{B_N} - i\sqrt{N}\Omega_c, \tag{3.31}$$

where all the other modes are not driven by the guided mode due to the symmetric excitation near the band edge. Therefore, the reflectivity of N atoms reads,

$$r_N(\Delta) = -\frac{N \cdot \Gamma_{1\mathrm{D}}}{N \cdot \Gamma_{1\mathrm{D}} + \Gamma' - 2i\Delta}, \tag{3.32}$$

which illustrates a superradinance of N atoms with enhanced total decay rate $N \cdot \Gamma_{1\mathrm{D}} + \Gamma'$.

3.4.2 Inside the bandgap: Finite-range dipole-dipole interaction

Inside the band gap $\omega_{\mathrm{atom}} \gtrsim \omega_{\mathrm{BE}}$, assuming that atoms are localized at the center of each unit cell, the effective spin Hamiltonian is written by

$$H_{\mathrm{eff}}/\hbar = -\sum_j \left(\Delta - \frac{\Gamma_{1\mathrm{D}}}{2} + i\frac{\Gamma'}{2} \right) \tilde{\sigma}_{ee}^j + \frac{\Gamma_{1\mathrm{D}}}{2} \sum_{j \neq j'} (-1)^{j-j'} \tilde{\sigma}_{eg}^j \tilde{\sigma}_{ge}^{j'} e^{-\kappa |x_j - x_{j'}|}, \tag{3.33}$$

where the single-atom coupling rate turns into the frequency shift $\frac{\Gamma_{1\mathrm{D}}}{2}$ inside the band gap. The last term describes the finite-range dipole-dipole interaction parametrized by the decay constant κ. For simplicity, we define a dimensionless interaction length $L_{\mathrm{eff}} \equiv \frac{1}{\kappa |x_j - x_{j+1}|} = \frac{1}{\kappa a}$. Here, we consider a limiting case with infinite-range interaction, $L_{\mathrm{eff}} \to \infty$. In the weak excitation limit, the equation of motion for the dressed operator, $s_{ge}^{B_N}$, is given by,

$$\dot{s}_{ge}^{B_N} = \left[i \left(\Delta - \frac{N \cdot \Gamma_{1\mathrm{D}}}{2} \right) - \frac{\Gamma'}{2} \right] s_{ge}^{B_N}, \tag{3.34}$$

which shows an additional frequency shift of $(N-1) \cdot \Gamma_{1\mathrm{D}}/2$, relative to a localized case at $L_{\mathrm{eff}} \to 0$.

Chapter 4

Design of a state-insensitive, compensated nanofiber trap

4.1 Introduction

The development of a matter-light quantum interface using cold atoms and optical fibers has been an active field of research over the past years [1]. Recent advances towards this goal include the observation of electromagnetically induced transparency and the loading of ultracold atoms in hollow-core optical fibers [52, 130–132], as well as the trapping and probing of atomic ensembles via the evanescent fields surrounding tapered nanofibers [61, 133–135]. While prominent examples of off-resonant interaction between evanescent waves and matter have used a plane dielectric geometry for atom optics and interferometry [136, 137] as well as for surface traps of quantum degenerate gases [138–140], recent progress of atom-light interactions with optical waveguides [52, 132–135] sets the stage for the fiber integration of free-space quantum systems in a quantum network via quantum-state transfer between matter and light [26, 112, 115, 141] and for strong coupling of single atoms and photons trapped near microcavities [34, 113, 142–145]. Furthermore, these effective 1-dimensional (1D) systems may be applied for investigating quantum many-body phenomena in low dimensions with long-range interactions mediated by the waveguide [74, 146–148].

One major drawback of many optical traps is that spatially inhomogeneous energy shifts $U(\mathbf{r})$ generally depend on the atomic electronic state, limiting long-lived trap and coherence times necessary for repeated

This chapter is largely based on Ref. [63], now corrected in Ref. [65].

coherent operations [149]. This is traditionally alleviated by constructing a *state-insensitive* optical trap designed to decouple atomic transition frequencies from the spatially varying potential of each electronic state [150]. Specifically, at the "magic" wavelength conditions, the differential response of the dynamic scalar polarizabilities $\alpha^{(0)}(\omega)$ for the ground and excited states $\alpha^{(0)}_{|g\rangle}, \alpha^{(0)}_{|e\rangle}$ at the optical frequency ω can be tailored such that both levels are perturbed identically with $\alpha^{(0)}_{|g\rangle} = \alpha^{(0)}_{|e\rangle}$. This leads to a vanishing differential atomic level shift $\delta U_{\mathrm{scalar}} = 0$ [150–152]. Differential shifts for the hyperfine ground states can be minimized by using far off-resonant beams, whereas Zeeman coherence can be conveniently protected by using linearly polarized light in which the vector light shifts are zero.

Although such magic wavelengths can be used for nanofiber traps [153], the strongly guiding nature of the waveguide inevitably leads to non-negligible longitudinal electric fields $\mathbf{E}_z$ in the evanescent region, which are out of phase with the transverse field $\mathbf{E}_\perp = (\mathbf{E}_x, \mathbf{E}_y)$. Here, z refers to the direction parallel to the fiber axis, while x and y are the coordinates perpendicular to the fiber axis. The resulting local polarization at location $\mathbf{r}$ is in general elliptical even for linearly polarized input beams, and induces vector shifts U_{vector}. The differential vector shift $\delta U_{\mathrm{vector}}$ in turn manifests itself as a "fictitious magnetic field", leading to inhomogeneous Zeeman broadening [154]. Furthermore, the spatially varying elliptical polarization of the evanescent field on a scale $\delta r < \lambda$ renders it difficult to cancel $\delta U_{\mathrm{vector}}$ using bias fields, resulting in increased heating rate [149] and limited coherence time [155].

Building upon the recent realization of a nanofiber trap as proposed in Ref. [156] and demonstrated in Refs. [61, 62], we propose a promising strategy for a state-insensitive evanescent field trap. Differential scalar shifts $\delta U_{\mathrm{scalar}}$ between $|g\rangle$ and $|e\rangle$ are canceled using "magic" wavelength conditions. The inhomogeneous Zeeman broadening $\delta U_{\mathrm{vector}}$ caused by a forward propagating blue-detuned field $\mathbf{E}^{(\mathrm{fwd})}$ is canceled by a backward propagating field $\mathbf{E}^{(\mathrm{bwd})}$ with a small relative frequency detuning δ_{fb}. Thus, our scheme can compensate for the light shifts of the strongly guided evanescent waves to the first order in the space external to the dielectric fiber, leading to favorable parameters for the realization of a long-lived fiber-integrated quantum memory and resonant coupling to ultra-high quality micro-cavities based on optically trapped atoms.

This chapter is organized as follows: Section 4.2 presents our scheme for generating a state-insensitive nanofiber trap. We start by introducing the general Hamiltonian for the atom-light dipole interaction (Sec-

tion 4.2.1); we next describe in details the spatially-varying electric field polarization of the evanescent wave (Section 4.2.2) and then discuss the principle of evanescent optical traps around a nanofiber (Section 4.2.3). We finally show how to cancel the subsequent vector (Section 4.2.4) and scalar (Section 4.2.5) light shifts induced on the D_2 transition of cesium. In Section 4.3 the benefits of using our proposed scheme are shown. We first describe the total Hamiltonian used for calculating the trapping potentials (Section 4.3.1). We then plot the adiabatic potentials obtained with our scheme and an estimate of residual differential shifts is provided (Section 4.3.2). We proceed to our concluding remarks in Section 4.4.

4.2 A state-insensitive nanofiber trap

In this section, we discuss a calculation of the optical nanofiber trap for atomic cesium. We show that the light shifts caused by the elliptically polarized components of the fiber's evanescent field are not negligible. We then propose a scheme to cancel these shifts and generate a two-color, state-insensitive, three-dimensional trap for Cs atoms along the nanofiber.

4.2.1 AC Stark shift Hamiltonian

We start by considering the Hamiltonian for an atom interacting with an electric field $\mathbf{E}$ in the dipole approximation:

$$H_{\rm ls} = -\mathbf{d}\cdot\mathbf{E}, \tag{4.1}$$

where $\mathbf{d}$ is the electric dipole operator and $\mathbf{E}$ is the electric field operator. Taking into account the atomic hyperfine structure, this Hamiltonian can be decomposed into its Cartesian components parameterized by the dynamic polarizability $\alpha(\omega)$ (see the explicit expressions in Appendix B) [65, 157, 158]:

$$\begin{aligned} H_{\rm ls} &= H_0 + H_1 + H_2 \\ &= -\alpha^{(0)}\mathbf{E}^{(-)}\cdot\mathbf{E}^{(+)} - i\alpha^{(1)}\tfrac{\left(\mathbf{E}^{(-)}\times\mathbf{E}^{(+)}\right)\cdot\mathbf{F}}{2F} \\ &- \sum_{\mu,\nu}\alpha^{(2)}E_\mu^{(-)}E_\nu^{(+)}\tfrac{3}{F(2F-1)}\left[\tfrac{1}{2}(F_\mu F_\nu + F_\nu F_\mu) - \tfrac{1}{3}F^2\delta_{\mu\nu}\right], \end{aligned} \tag{4.2}$$

where $\alpha^{(0)}$, $\alpha^{(1)}$, and $\alpha^{(2)}$ are the scalar, vector, and tensor atomic dynamic polarizabilities, $\mathbf{E}^{(+)}$ and $\mathbf{E}^{(-)}$ are the positive and negative frequency components of the electric field, $\mathbf{F} = \mathbf{I} + \mathbf{J}$ is the atomic total angular momentum operator, with $\mathbf{I}$ and $\mathbf{J}$ the nuclear and electronic angular momentum operators, $\mu, \nu \in \{x, y, z\}$ are components in the Cartesian basis, and H_0, H_1, and H_2 are the terms associated with the scalar, vector, and tensor light shifts, respectively.

For two-level atoms with ground and excited states $|g\rangle, |e\rangle$, the scalar shift U_{scalar} can be approximated by $U_{\text{scalar}} \propto |\mathbf{E}|^2/\delta$ for detunings $\delta = \omega - \omega_a$ large compared to the excited state decay rate Γ, where ω is the electric field angular frequency and ω_a is the $|g\rangle \rightarrow |e\rangle$ transition frequency. The ground state will experience a repulsive potential for blue-detuned ($\delta > 0$) electric fields, and an attractive potential for red-detuned ($\delta < 0$) electric fields. The scalar dynamic polarizability $\alpha^{(0)}$ is in general different for the states $|g\rangle$ and $|e\rangle$, resulting in a differential scalar shift and a mismatch of the ground and excited state potentials. For the typically anti-trapped excited state, near-resonant driving of the transition by an additional beam with frequency $\omega_2 \simeq \omega_a$ can cause significant heating of a trapped atom [149]. This situation can be remedied by the use of "magic" wavelengths for which $\alpha^{(0)}_{|g\rangle} = \alpha^{(0)}_{|e\rangle}$ [150, 152].

The vector term H_1 of Eq. (4.2) induces a Zeeman-like splitting proportional to a projection of the total atomic angular momentum $\mathbf{F}$ and arises from a so-called "fictitious magnetic field" proportional to the ellipticity of the electric field [154]. In the case of a free-space plane wave propagating along the z axis, H_1 can be expressed in terms of the Stokes operators $\mathbf{S} = (S_0, S_x, S_y, S_z)$ as [159]:

$$H_1 \propto \alpha^{(1)}(\omega)\epsilon\frac{F_z}{F}, \tag{4.3}$$

where $\epsilon = \langle S_z\rangle/\langle S_0\rangle = \frac{|E_{+1}|^2 - |E_{-1}|^2}{|E_{+1}|^2 + |E_{-1}|^2}$ is the ellipticity of the electric field. For an elliptically polarized beam, the vector shift can be as large as the scalar shift, and can, for example, be used to cancel the differential light shifts of Rubidium atoms confined in a 3D optical lattice [160].

The last term H_2 in Eq. (4.2) represents the tensor shift. It vanishes for atoms with total angular momentum $F = 1/2$ [159]. In the case of the D_2 transition of Cs that we consider here, it will depend only on the electronic angular momentum $\mathbf{J}$ for detunings large compared to the $6P_{3/2}$ excited state hyperfine structure,

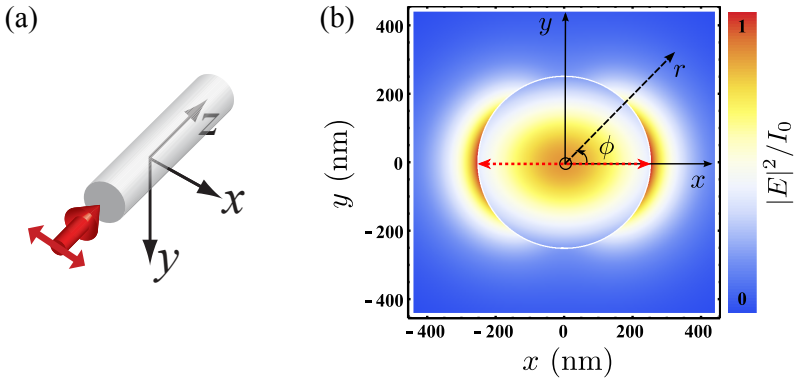

Figure 4.1: **Electric field intensity of HE$_{11}$ mode.** (a) An input beam is shown by red thick arrow with its polarization indicated by the thin arrow along the x axis. The gray shaded structure represents a nanofiber. (b) Field intensity $|E|^2$ in the plane transverse to the fiber for a single, x-polarized beam at $\lambda = 935$ nm. $|E|^2$ is normalized to the intensity just outside the fiber $I_0 = |E(r = a_+, \phi = 0)|^2$, with a radius $a = 250$ nm and $a_+ = a + |r - a|$, $r \to a$. The red dashed arrow indicates the input polarization.

and vanish for $J = \frac{1}{2}$ [157, 158]. It will therefore only act on the excited state of the Cs D_2 transition, inducing shifts on the Zeeman $m_{F'}$ sublevels proportional to $m_{F'}^2$.

4.2.2 HE$_{11}$ mode - Electric field distribution and polarization

When the radius a of an optical fiber is reduced well below the propagating field wavelength λ, the resulting cladding-to-air waveguide supports only the "hybrid" fundamental mode HE$_{11}$ [133, 161]. Here, we consider an infinite SiO_2 cylindrical waveguide of radius $a = 250$ nm. In this strongly guiding regime, a significant fraction of energy of the HE$_{11}$ mode is carried in the form of an evanescent wave outside of the nanofiber. The fundamental mode HE$_{11}$ is often referred to as "quasi-linear" when excited with a linearly polarized input beam. However, for a dielectric waveguide in the strong-guiding regime with indices of refraction $n_1 \approx 1.5$ inside the waveguide and $n_2 \approx 1.0$ outside, the HE$_{11}$ mode actually exhibits a significant ellipticity for $a \lesssim \lambda/2$, leading to vector shifts of the Zeeman sublevels. Formally, for a linearly polarized input, the evanescent field $\mathbf{E} = (E_x, E_y, E_z)$ of the fundamental mode propagating in the fiber can be expressed as

follows for $r \geq a$ [133, 161, 162]:

$$E_x(r,\phi,z,t) = A_{\text{lin}}\frac{\beta_{11}J_1(h_{11}a)}{2q_{11}K_1(q_{11}a)} \times[(1-s_{11})K_0(q_{11}r)\cos(\varphi_0)+(1+s_{11})K_2(q_{11}r)\cos(2\phi-\varphi_0)]e^{i(\omega t-\beta_{11}z)}, \tag{4.4a}$$

$$E_y(r,\phi,z,t) = A_{\text{lin}}\frac{\beta_{11}J_1(h_{11}a)}{2q_{11}K_1(q_{11}a)} \times[(1-s_{11})K_0(q_{11}r)\sin(\varphi_0)+(1+s_{11})K_2(q_{11}r)\sin(2\phi-\varphi_0)]e^{i(\omega t-\beta_{11}z)}, \tag{4.4b}$$

$$E_z(r,\phi,z,t) = iA_{\text{lin}}\frac{J_1(h_{11}a)}{K_1(q_{11}a)}K_1(q_{11}r)\cos(\phi-\varphi_0)e^{i(\omega t-\beta_{11}z)}, \tag{4.4c}$$

with

$$s_{11} = \left[\frac{1}{(h_{11}a)^2}+\frac{1}{(q_{11}a)^2}\right]\left[\frac{J_1'(h_{11}a)}{h_{11}aJ_1(h_{11}a)}+\frac{K_1'(q_{11}a)}{q_{11}aK_1(q_{11}a)}\right], \tag{4.5a}$$

$$h_{11} = \sqrt{k_0^2n_1^2-\beta_{11}^2}, \tag{4.5b}$$

$$q_{11} = \sqrt{\beta_{11}^2-k_0^2n_2^2}. \tag{4.5c}$$

Here, (r,ϕ) denote the cylindrical coordinates in the transverse plane (x,y) (Fig. 4.1(b)), φ_0 indicates the polarization axis for the input polarization relative to the x axis, n_1 and n_2 are the indices of refraction inside and outside the waveguide, β_{11} is the mode propagation constant, $1/h_{11}$ is the characteristic decay length for the guided mode inside the fiber, $1/q_{11}$ is the characteristic decay length for the guided mode outside the fiber, A_{lin} is the real-valued amplitude for the linearly polarized input, J_l is the l-th Bessel function of the first kind, and K_l is the l-th modified Bessel function of the second kind.

It is clear from Eq. (4.4) that the electric field intensity $|E|^2 = |E_x|^2 + |E_y|^2 + |E_z|^2$ is not azimuthally symmetric. For a incident beam linearly polarized along the x axis, i.e., $\varphi_0 = 0$, the intensity at the fiber's outer surface is maximum for $\phi = 0,\ \pi$ and minimum for $\phi = \pm\pi/2$, as shown in Fig. 4.1(b). This azimuthal asymmetry can be used to confine atoms along azimuthal direction.

Notably, the evanescent modes of the nanofiber have a significant longitudinal component E_z along the fiber propagation direction, which is $\pi/2$ out-of-phase with the transverse components (E_x, E_y) (Eq. (4.4c)). At the outer fiber surface, E_z is maximum for $\phi = \varphi_0, \varphi_0+\pi$ (i.e., along the input polarization axis), and

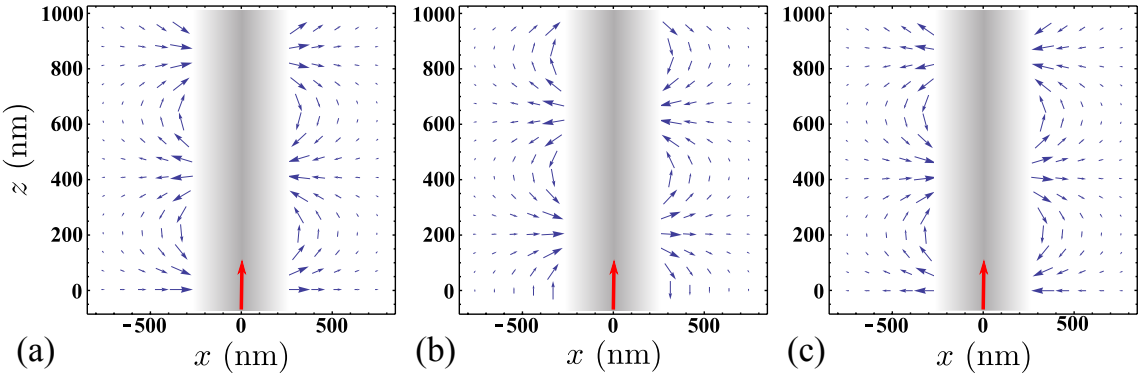

Figure 4.2: **Time-dependent electric field of a single incident beam.** Electric field $\mathbf{E}(x, y, z, t)$ of a single propagating beam in the plane $y = 0$. The input beam is x-polarized. The electric field $\mathrm{Re}[\mathbf{E}(x, y, z, t)]$, with $\mathbf{E}(x, y, z, t)$ defined as in Eq. 4.4, is shown by the blue arrows. The red arrow indicates the beam propagation direction. The field is shown for (a) $\omega t = 0$, (b) $\omega t = \pi/2$, and (c) $\omega t = \pi$.

vanishes for $\phi = \varphi_0 \pm \pi/2$. For an x-polarized input at 935 nm and a nanofiber of radius $a = 250$ nm, $\frac{|E_z|^2}{|E|^2}\,(r = a_+, \phi = 0) \simeq 20\%$. As a consequence, the polarization of a single propagating beam will be elliptical everywhere except for $\phi = \varphi_0 \pm \pi/2$. The ellipticity of the beam will be maximum for $\phi = \varphi_0,\ \varphi_0 + \pi$ as illustrated in Fig. 4.2, giving rise to significant vector shifts. We can rewrite Eqs. (4.4) as follows:

$$E_x(r, \phi, z, t) = Ae^{i(\omega t - \beta_{11} z)}, \tag{4.6a}$$

$$E_y(r, \phi, z, t) = Be^{i(\omega t - \beta_{11} z)}, \tag{4.6b}$$

$$E_z(r, \phi, z, t) = iCe^{i(\omega t - \beta_{11} z)}, \tag{4.6c}$$

where A, B, and C are real functions of r and ϕ. In particular, if one combines a forward-propagating beam $\mathbf{E}^{(\mathrm{fwd})}$ expressed as Eq. (4.6c) with a backward-propagating beam of same amplitude and input polarization $\mathbf{E}^{(\mathrm{bwd})} = Ae^{i(\omega t + \beta_{11} z)}\mathbf{e}_x + Be^{i(\omega t + \beta_{11} z)}\mathbf{e}_y - iCe^{i(\omega t + \beta_{11} z)}\mathbf{e}_z$ with the unit vectors $(\mathbf{e}_x, \mathbf{e}_y, \mathbf{e}_z)$ in the Cartesian basis, the total field can be expressed as,

$$\mathbf{E}^{(\mathrm{tot})} = \mathbf{E}^{(\mathrm{fwd})} + \mathbf{E}^{(\mathrm{bwd})} = 2\left[A\cos(\beta_{11} z)\mathbf{e}_x + B\cos(\beta_{11} z)\mathbf{e}_y + C\sin(\beta_{11} z)\mathbf{e}_z\right] \cdot e^{i\omega t}. \tag{4.7}$$

The resulting electric field $\mathbf{E}^{(\mathrm{tot})} = \mathbf{E}^{(\mathrm{fwd})} + \mathbf{E}^{(\mathrm{bwd})}$ forms an optical lattice with spatially rotating linear

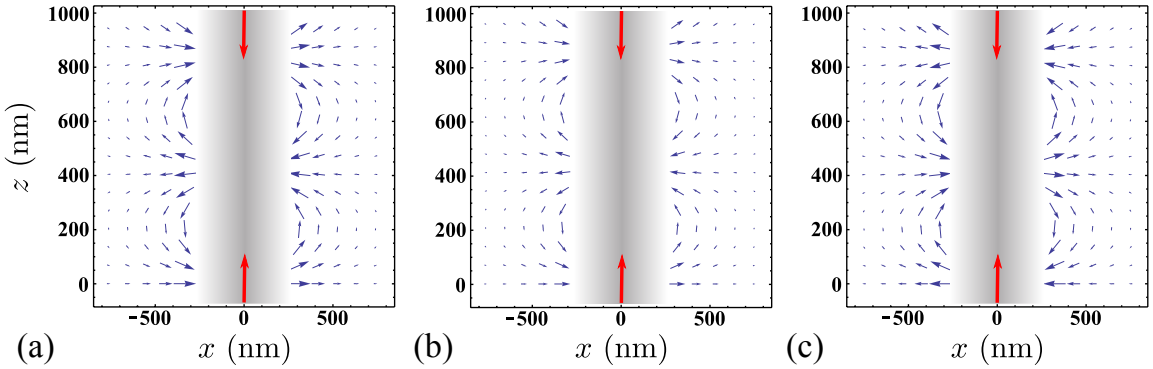

Figure 4.3: **Time-dependent electric field of a standing wave** Total electric field $\mathbf{E}(x, y, z, t)$ for two counter-propagating beams in the plane $y = 0$. The input beams are x-polarized. The electric field $\mathrm{Re}[\mathbf{E}(x, y, z, t)]$ is shown by the blue arrows. The red arrows indicate the beams propagation directions. The electric field is shown for (a) $\omega t = 0$, (b) $\omega t = \pi/4$, and (c) $\omega t = \pi$. As opposed to Fig. 4.2, the polarization of the electric field is linear at any point $|\mathbf{r}| > a$ (i.e., the polarization vector has no ellipticity and $\mathbf{E}$ does not rotate in time at a given position $\mathbf{r}$).

polarization, as illustrated in Fig. 4.3.

4.2.3 3D nanofiber trap

By appropriately combining blue- and red-detuned fields $\mathbf{E}_{\mathrm{red}}$ and $\mathbf{E}_{\mathrm{blue}}$ in an optical nanofiber, an atomic trapping potential can be engineered from the evanescent electric fields, in the presence of van der Waals potential [156]. The red-detuned field $\mathbf{E}_{\mathrm{red}}$, as well as the van der Waals force, attract the atoms towards the nanofiber, while the blue-detuned field $\mathbf{E}_{\mathrm{blue}}$ repels the atoms from the nanofiber, preventing atoms from crashing onto the nanofiber surface. Because of the different radial decay lengths of the red- and blue-detuned evanescent fields, one can find a radial potential minimum at ~ 200 nm away from the nanofiber surface by appropriately choosing the respective powers. The longitudinal confinement along the nanofiber axis is achieved by launching an additional counterpropagating red-detuned field, which generates a 1D optical lattice. Both blue- and red-detuned fields are linearly polarized along the x axis at the waveguide input to ensure azimuthal confinement for trapped atoms.

4.2.4 Cancellation of the vector shifts

The scheme that we propose makes use of four beams with parallel linear input polarizations along the x axis shown in Fig. 4.4. As discussed in Section 4.2.2, the vector shifts of both the ground and excited states can

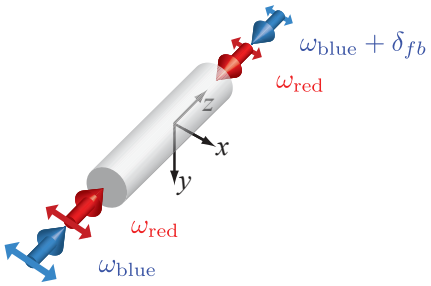

Figure 4.4: **Trap scheme for cancellation of the vector shifts.** Red (blue)-detuned beams are shown by red (blue) thick arrows. Input polarizations are shown by the thin arrows along the x axis.

be canceled for both the red and blue-detuned fields by using pairs of counter-propagating beams. In the x-z plane, the vector shift for each pair becomes $H_1 \propto (\alpha^{(1)}(\omega^{(\mathrm{fwd})}) - \alpha^{(1)}(\omega^{(\mathrm{bwd})}))\frac{F_y}{F}$ with $\omega^{(\mathrm{fwd})} \simeq \omega^{(\mathrm{bwd})}$, where $\omega^{(\mathrm{fwd,bwd})}$ are the angular frequencies for the forward and backward propagating beams, and $\delta \pm \delta_{fb}/2$ are their detunings from the atomic transition frequency ω_a, with two-photon detuning $\delta_{fb} = \omega^{(\mathrm{fwd})} - \omega^{(\mathrm{bwd})}$. For an atom in the x-z plane, the total electric field is also contained in the x-z plane, such that the scalar product $\left(\mathbf{E}^{(-)} \times \mathbf{E}^{(+)}\right) \cdot \mathbf{F}$ in Eq. (4.2) is proportional to F_y.

In the case of the red-detuned lattice, $\omega_{\mathrm{red}}^{(\mathrm{fwd})} = \omega_{\mathrm{red}}^{(\mathrm{bwd})}$ and $H_1^{(\mathrm{red})} = 0$, precisely as in Ref. [61]. Adding a blue-detuned lattice with $\delta_{fb} = 0$ would result in two superimposed lattices with unmatched spatial periods $2\pi/\beta_{11}^{\mathrm{red}}$, $2\pi/\beta_{11}^{\mathrm{blue}}$. To avoid this effect, the interference between the counter-propagating blue-detuned fields $\mathbf{E}_{\mathrm{blue}}^{(\mathrm{fwd})}$ and $\mathbf{E}_{\mathrm{blue}}^{(\mathrm{bwd})}$ can be averaged over times that are short compared to the time scale of the motional and internal dynamics of a trapped atom by offsetting the frequencies of the two fields by $\delta_{fb} \gg (\omega_{\mathrm{trap}}, \delta_{\mathrm{hfs}})$, where ω_{trap} and δ_{hfs} are the trap angular frequency and the hyperfine splitting for the ground state, respectively. This will also suppress spurious two-photon processes (e.g., two-photon Stark shift [163]) as well as parametric heating due to intensity modulation [164].

For $\omega_{\mathrm{blue}}^{(\mathrm{fwd,bwd})} = \omega_a + (\delta \pm \delta_{fb}/2)$, we achieve a vector shift cancellation for the blue-detuned field to the first order in $1/\delta$, namely

$$H_1^{(\mathrm{blue})} \propto \frac{\delta_{fb}}{\delta^2}\frac{F_y}{F} + \mathcal{O}(1/\delta^3). \tag{4.8}$$

For typical values of $\delta = 85$ THz and $\delta_{fb} = 30$ GHz, $\delta_{fb}/\delta = 3.5 \times 10^{-4}$.

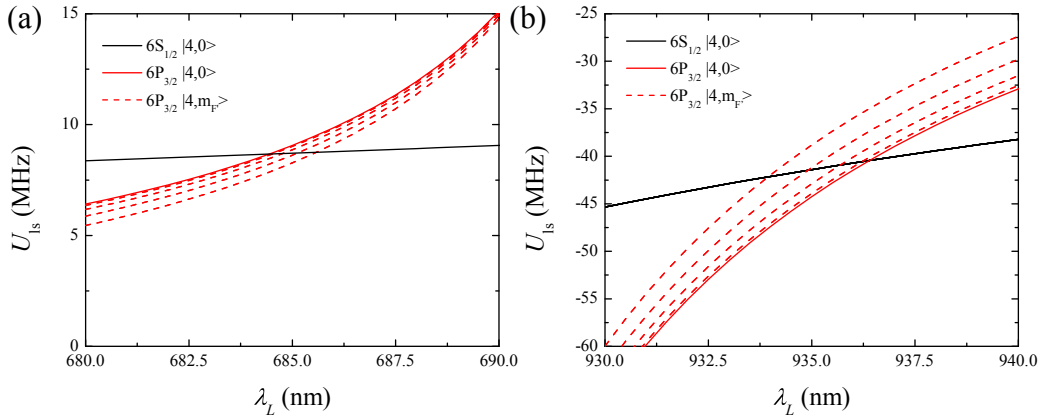

Figure 4.5: **Magic wavelengths of the Cs D_2 line.** We display the light shift $U_{\rm ls}$ for a linearly polarized beam with constant intensity $2.9 \times 10^9 \mathrm{W/m^2}$ around (a) the blue-detuned magic wavelength at $\lambda_{\rm blue} \simeq 685$ nm, and (b) red-detuned magic wavelength at $\lambda_{\rm red} \simeq 935$ nm (as corrected in Ref. [65]).

4.2.5 Magic wavelengths for an evanescent field trap

To make the nanofiber trap state-insensitive, it is necessary to cancel the differential scalar shift $\delta U_{\rm scalar}$ of the $6S_{1/2}$ and $6P_{3/2}$ states by operating the trap at the magic wavelengths, as proposed in Ref. [153], in which only the effects of the scalar and tensor shifts were considered. Here we deal with the full complexity of the vector field $\mathbf{E}(\mathbf{r})$ and the resulting vector light shifts. We numerically determine the red-detuned and blue-detuned magic wavelengths for the $6S_{1/2} \rightarrow 6P_{3/2}$ transition [150, 152, 157, 158, 165, 166]. The calculation includes the contributions of all the hyperfine levels F and Zeeman sublevels m_F of the electronic states $\{6S_{1/2}, \cdots, 15S_{1/2}\}$, $\{6P_{1/2}, \cdots, 11P_{1/2}\}$, $\{6P_{3/2}, \cdots, 11P_{3/2}\}$, $\{6D_{3/2}, \cdots, 11D_{3/2}\}$, and $\{6D_{5/2}, \cdots, 11D_{5/2}\}$, given in Table I and II in Ref. [65]. Further complete table of higher electronics states can be found in Ref. [158] and these contributions are discussed in Appendix B.2. The effect of the tensor shifts on the $6P_{3/2}$ excited state is manifest in the quadratic splitting of the $m_{F'}$ sublevels (Fig. 4.5). We find a red-detuned magic-wavelength located around 935nm, in accordance with the previously published values [152, 166]. In the next sections, we will use the value $\lambda_{\rm red} = 935$ nm, which is determined by the average over magic wavelengths for different $m_{F'}$ where $\delta U_{\rm ls}$ for the $6P_{3/2}$ excited state $|F' = 4, m_{F'}\rangle$ is canceled [65]. We choose $F' = 4$ due to its relevance to coherent two-photons processes [26, 112, 141]. There are several blue-detuned magic wavelengths [153, 166]. For our trap, we use the magic wavelength $\lambda_{\rm blue}$ at approximately 685 nm, determined in the same fashion as red-detuned magic wavelength [65, 153].

Since this is the second closest blue-detuned magic wavelength to 852 nm, it has the second highest ground-state polarizability and therefore requires the second lowest optical intensity to generate the required trapping potential (we do not consider the magic wavelength at $792\ \mathrm{nm}$, as it is too close to the $8S_{1/2}$ to $6P_{3/2}$ transition at $794\ \mathrm{nm}$).

We have neglected higher order processes in our analysis, including two-photon and electric quadrupole transitions, near 685 nm [167].

4.3 Numerical results: Trapping potentials

Using the atomic interaction Hamiltonian in the dipole approximation with the actual polarization profile of the evanescent field, we proceed to analyze the adiabatic potentials for the nanofiber trap for a Cs atom in its $6S_{1/2}$ ground and $6P_{3/2}$ excited states.

4.3.1 Total potential

For a specific atomic state of Cs, the total atomic trap potential U_{trap} consists of the total light-shift potential U_{ls} calculated from the full Stark shift Hamiltonian (Eq. (4.2)), as well as the surface interaction potential of an atom with the dielectric waveguide U_{surface}, namely

$$U_{\mathrm{trap}} = U_{\mathrm{ls}} + U_{\mathrm{surface}}. \tag{4.9}$$

The Casimir-Polder interaction between the atom and dielectric surface has a significant effect on the atomic motion at distance scales near 100 nm [144, 168–171]. The surface potential of a ground state Cs atom near a planar dielectric surface can be reasonably approximated by the van der Waals potential, which decays as d^{-3}, where $d = r - a$:

$$U_{\mathrm{surface}} = -\frac{C_3}{d^3}, \tag{4.10}$$

where we use $C_3(6S_{1/2})/h = 1.16\ \mathrm{kHz}\ \mu\mathrm{m}^3$ [145]. Because the retarded Casimir-Polder forces (d^{-4} scaling) decrease faster away from the surface than the van der Waals forces, using U_{surface} overestimates the

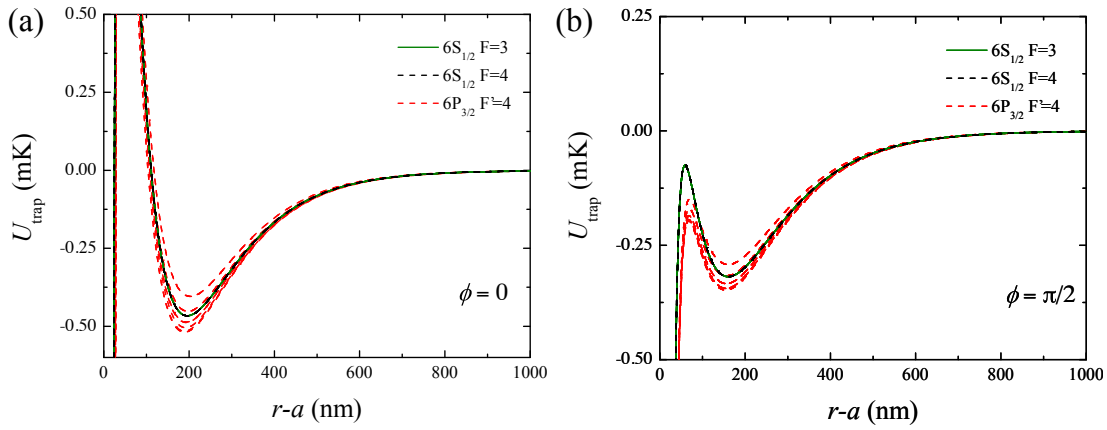

Figure 4.6: **Trap potential along the radial direction.** Radial dependence of the trapping potentials of the ground and excited states using the magic wavelengths and the configuration shown in Fig. 4.4. All beams are polarized along $\phi = 0$ (i.e., φ_0=0). The 935 nm beams each have a power of 0.95 mW. The 685 nm beams each have a power of 16 mW. (a) Radial potentials along $\phi = 0$ (i.e., $\varphi_0 = 0$). The trap minimum for $6S_{1/2}$ is located about 200 nm from the fiber surface. Both electronic ground and excited states are trapped, with residual splittings of the excited states due to the tensor shifts. (b) Radial potential along $\phi = \pi/2$ (as corrected in Ref. [65]).

surface interaction at the trap location $d \approx 200$ nm. Additionally, the curvature of the nanofiber cylindrical geometry reduces the potential strength even further [145, 172]. The d^{-3} scaling of the van der Waals expression for a planar surface is therefore an overestimate of the actual surface potential. We use it for simplicity in the calculations presented here, with more complete expressions for Cs presented in Ref. [145]. Furthermore, we neglect any dependence on the $m_{F'}$ sublevels of the excited state $6P_{3/2}$ for the Casimir-Polder shift, and simply approximate $C_3(6P_{3/2}) \approx 2\, C_3(6S_{1/2})$ [173].

We calculate the adiabatic potential of Eq. (4.9) by diagonalizing the total interaction Hamiltonian $H = H_{\rm ls} + H_{\rm surface}$ at each point in space, where $H_{\rm surface}$ is the scalar surface Hamiltonian. At each point $\mathbf{r}(r, \phi, z)$, we obtain a set of eigenstates and the corresponding eigenenergies. These eigenstates are superpositions of the $|F, m_F\rangle$ bare Zeeman sublevels. Due to the complex polarization of the trapping fields, the energy eigenstates are not necessarily eigenstates of any projection of the angular momentum operator.

4.3.2 State-insensitive trapping potential

Now, we analyze our proposed "magic compensation" scheme (as illustrated in Fig. 4.4), demonstrating how using magic wavelength beams and compensating the trap ellipticity can reduce inhomogeneous broadening

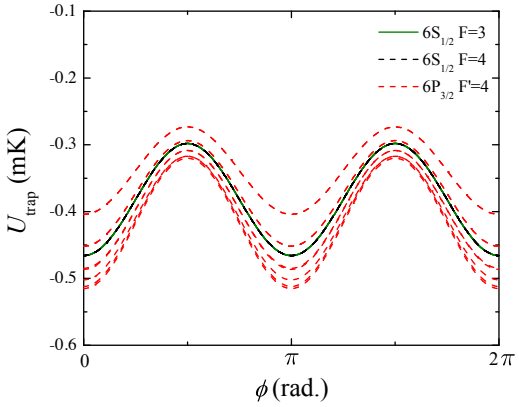

Figure 4.7: **Trap potential along the azimuthal direction.** Azimuthal dependence of the trapping potential of the ground and excited state for the "magic compensated" trap with the parameters used in Fig. 4.6, for $r - a = 200$ nm. The effect of the compensation beam in Fig. 4.4 is to suppress the vector shifts and to reduce the ground-state splittings $\delta\nu_\phi$ in the transverse plane for $\phi \neq 0,\ \pi$ (as corrected in Ref. [65]).

of the Zeeman sublevels in a nanofiber trap. For this trap, we use a pair of counter-propagating x-polarized ($\varphi_0 = 0$) red-detuned beams $\mathbf{E}_{\rm red} = \mathbf{E}_{\rm red}^{\rm (fwd)} + \mathbf{E}_{\rm red}^{\rm (bwd)}$ ($P_{\rm red} = 2 \times 0.95$ mW) at the "magic" wavelength $\lambda_{\rm red} = 935$ nm, forming a 1D optical lattice. Counter-propagating, x-polarized blue-detuned beams at the second magic wavelength $\lambda_{\rm blue} = 685$ nm are used with a power $P_{\rm blue} = 2 \times 16$ mW. The resulting interference is averaged out by detuning the beams by $\delta_{fb} = 30$ GHz, as explained in section 4.2.4, leading to a first-order cancellation of vector light shifts as expressed by Eq. (4.8). The beam intensities are chosen to generate a trap of similar depth as the one demonstrated in Ref. [61]. The resulting adiabatic potential $U_{\rm trap}$ allows for state-insensitive 3D confinement of cold Cs atoms around a SiO_2 nanofiber of radius $a = 250$ nm.

In Fig. 4.6, we show the radial trapping potential $U_{\rm trap}(r, \phi, z)$ of the ground and excited states for $z = 0$, $\phi = 0$ (x-axis) in Fig. 4.6 (a) and for $z = 0$, $\phi = \pi/2$ (y-axis) in Fig. 4.6(b). Because the trapping fields are now effectively linearly polarized, the ground states are degenerate at both $\phi = 0$ and $\phi = \pi/2$. In contrast to a non-magic wavelength trap, the excited states are trapped with gradients that closely map that of the ground states. The sublevels of $6P_{3/2}$ are still non-degenerate due to the tensor shifts. For $P_{\rm red}$, $P_{\rm blue}$ specified above, we find that the trap depth is $U_{\rm depth} = -0.4$ mK, located at $r - a \simeq r_{\rm trap} - a = 200$ nm and $\phi = 0, \pi$.

The azimuthal confinement of the atoms is shown by Fig. 4.7. The inhomogeneous Zeeman broadening from the ellipticity of $\mathbf{E}_{\rm blue}$ is greatly reduced thanks to the compensation scheme of Fig. 4.4. It is non-zero,

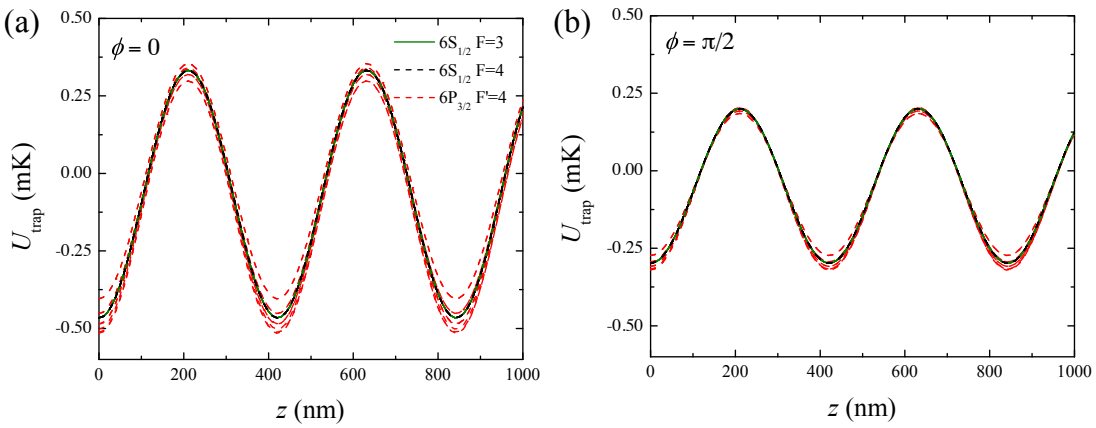

Figure 4.8: **Trap potential along the axial direction.** Axial dependence of the trapping potentials of the ground and excited states for the "magic compensated" trap with the parameters used in Fig. 4.6 for $r - a = 200$ nm. (a) Longitudinal potential along $\phi = 0$. (b) Longitudinal potential along $\phi = \pi/2$ (as corrected in Ref. [65]).

however, as expressed by Eq. (4.8). The remaining splitting of the $F = 4$ ground state is $\delta_\nu \approx 700$ Hz, limiting the coherence time to $\tau \lesssim 1/\delta_\nu = 1.4$ ms. In the case of perfect cancellation of the vector shift with $\delta_{fb} = 0$, a residual non-zero ground state splitting $\delta\nu_\phi$ would still arise from the different scalar dynamic polarizabilities of the $6S_{1/2}$ $F = 3$ and $F = 4$ ground states [157]. For atoms in their azimuthal motional ground state $|n\rangle_\phi = |0\rangle_\phi$, the single-atom distribution half-width is $\sigma_{r_\phi} \simeq 30$ nm (or $\sigma_\phi \simeq 4°$) with azimuthal trap frequency $\nu_{\mathrm{trap}_\phi} \simeq 44$ kHz obtained from a harmonic fit of the potential around $\phi = \pi$. We estimate a spin-wave coherence time $\tau_m = 1/\Delta(\delta\nu_\phi) \leq 30$ ms, coming from the spread $\Delta(\delta\nu_\phi) = \delta\nu_\phi(\phi = \pi) - \delta\nu_\phi(\phi = \pi + \sigma_\phi) \approx 30$ Hz of the atomic ground states for the $F = 3 \rightarrow F = 4$ transition frequency. We note that the longest achievable coherence time in the "magic compensated" adiabatic potential in the absence of ground-state splitting $\delta\nu_\phi$ would be limited by spontaneous Raman scattering driven by the trapping beams [152].

Finally, we also plot the axial potentials in Fig. 4.8, showing the confinement for both the ground and excited states. Due to the magic wavelengths, the excited states are trapped in all directions. This results in greatly suppressed dipole-force fluctuations, allowing for on-resonance driving of the optical transition.

4.4 Conclusion

We have proposed and analyzed in detail a scheme for a state-insensitive optical nanofiber trap which utilizes realistic experimental parameters. The "magic" trapping wavelengths of 935 nm and 685 nm for Cs atoms are readily available using semiconductor laser sources, and require a reasonable power for trapping. Tapered optical fibers can be made with sub-wavelength diameters and high transmission, as has been demonstrated experimentally [174, 175]. In Ref. [64] we describe an experiment for trapping Cs using Fig. 4.4 configuration and explicitly demonstrate features of the "compensated magic" trap for a nanofiber.

Furthermore, extension to other nanoscopic dielectric waveguides [176] would make evanescent optical trapping possible in integrated hybrid quantum devices [177]. It is worthwhile to note that the compensation scheme of the vector shift would work at any wavelength, increasing the ground state coherence time in a straightforward manner.

The proposed "magic compensated" scheme allows for in-trap resonant processes, increasing the trap lifetime under near-resonant driving of the transition, such as optical pumping. The scattering rate in this trap is similar to the one obtained with the parameters of Ref. [61], but the mismatch between the ground and excited states potentials could lead to large heating in Ref. [61]. However, it is not clear that the "magic compensated" trap will be more robust to experimental fluctuations, and experimental studies will be required to investigate the possible limitations of the trap lifetime. An important advantage of the proposed scheme is the large reduction of the splitting of the ground state manifolds compared to the scheme used in Ref. [61], therefore leading to increased ground state coherence time. These properties will make quantum-state engineering more feasible in such a trap, allowing for a wide range of experiments including creating quantum memories, coupling of single atoms and ensembles to optical or mechanical resonators, and studying 1D spin chains.

Chapter 5

Demonstration of a state-insensitive, compensated nanofiber trap

5.1 Introduction

An exciting frontier in quantum information science is the integration of otherwise "simple" quantum elements into complex quantum networks [1]. The laboratory realization of even small quantum networks enables the exploration of physical systems that have not heretofore existed in the natural world. Within this context, there is active research to achieve lithographic quantum optical circuits, for which atoms are trapped near micro- and nano-scopic dielectric structures and "wired" together by photons propagating through the circuit elements. Single atoms and atomic ensembles endow quantum functionality for otherwise linear optical circuits and thereby the capability to build quantum networks component by component.

Creating optical traps compatible with the modal geometries of micro- and nano-scopic optical resonators and waveguides [176, 178] is a long-standing challenge in AMO physics [179–181]. 'Optical tweezers' with tight focussing have succeeded in trapping single atoms within small volumes $\sim \lambda^3$ [182], but the focal geometries of conventional optical elements are not compatible with atomic localization $\simeq 100$ nm near microscopic photonic structures [178, 183]. Moreover, spatially inhomogeneous energy shifts $U(\mathbf{r})$ on a sub-wavelength scale generally depend on the atomic internal state, limiting long-lived trap and coherence times due to single-photon scattering events with energy much larger than the recoil energy and to spatially dependent frequency shifts for the components of atomic superpositions [63, 149, 184]. Nevertheless, important

This chapter is largely based on ref. [64], as corrected in Ref. [65].

advances have been made by loading ultracold atoms into hollow-core optical fibers [52, 131, 132, 185, 186] and by trapping atoms in the evanescent fields of nanoscale waveguides [61, 62, 120, 134, 135, 156, 187–189].

Following the landmark realization of a nanofiber trap [61, 62, 189], in this chapter, we describe the implementation of a state-insensitive, compensated nanofiber trap for atomic Cesium, as illustrated in Fig. 5.1 [63, 65]. For our trap, differential scalar shifts δU_{scalar} between ground and excited states are eliminated by using magic wavelengths for both red- and blue-detuned trapping fields [150]. Inhomogeneous Zeeman broadening due to vector light shifts δU_{vector} is suppressed by way of pairs of counter-propagating red- and blue-detuned fields as described in Chapter 4

The compensation of scalar and vector shifts results in a measured transition linewidth $\Gamma/2\pi = 5.7 \pm 0.1$ MHz for Cs atoms trapped 215 nm from the surface of an SiO_2 fiber of diameter 430 nm, which should be compared to the free-space linewidth $\Gamma_0/2\pi = 5.2$ MHz for the $6S_{1/2}, F = 4 \rightarrow 6P_{3/2}, F' = 5$ Cs transition. Probe light transmitted through the 1D array of trapped atoms exhibits an optical depth $d_N = 66 \pm 17$. From the measurements of optical depth and number N of atoms, we infer a single-atom attenuation $d_1 = d_N/N \simeq 0.08$. The bandwidth Γ_R for reflection from the 1D array is observed to broaden with increasing N, in direct proportion to the entropy for the multiplicity of trapping sites.

5.2 Trap potential with state-insensitive, compensated scheme

Our trapping scheme is based upon the analyses [120, 134, 156, 187] and the demonstrations in Refs. [61, 62, 189]. A dielectric fiber in vacuum with radius a smaller than a wavelength supports the "hybrid" fundamental mode HE_{11}, which carries significant energy in its evanescent field [161]. For linear input polarization at angle ϕ_0, an appropriate combination of attractive and repulsive HE_{11} fields creates a dipole-force trap external to the fiber's surface with trap minima at $\phi - \phi_0 = 0, \pi$.

Following these principles, we have designed a "magic compensation" scheme that traps both ground and excited states and greatly reduces the inhomogeneous broadening for atomic sublevels as described in Chapter 4. By contrast, uncompensated schemes do not provide a stable trapping potential for excited states and suffer large dephasing between ground states over a single vibrational period [61, 62, 189].

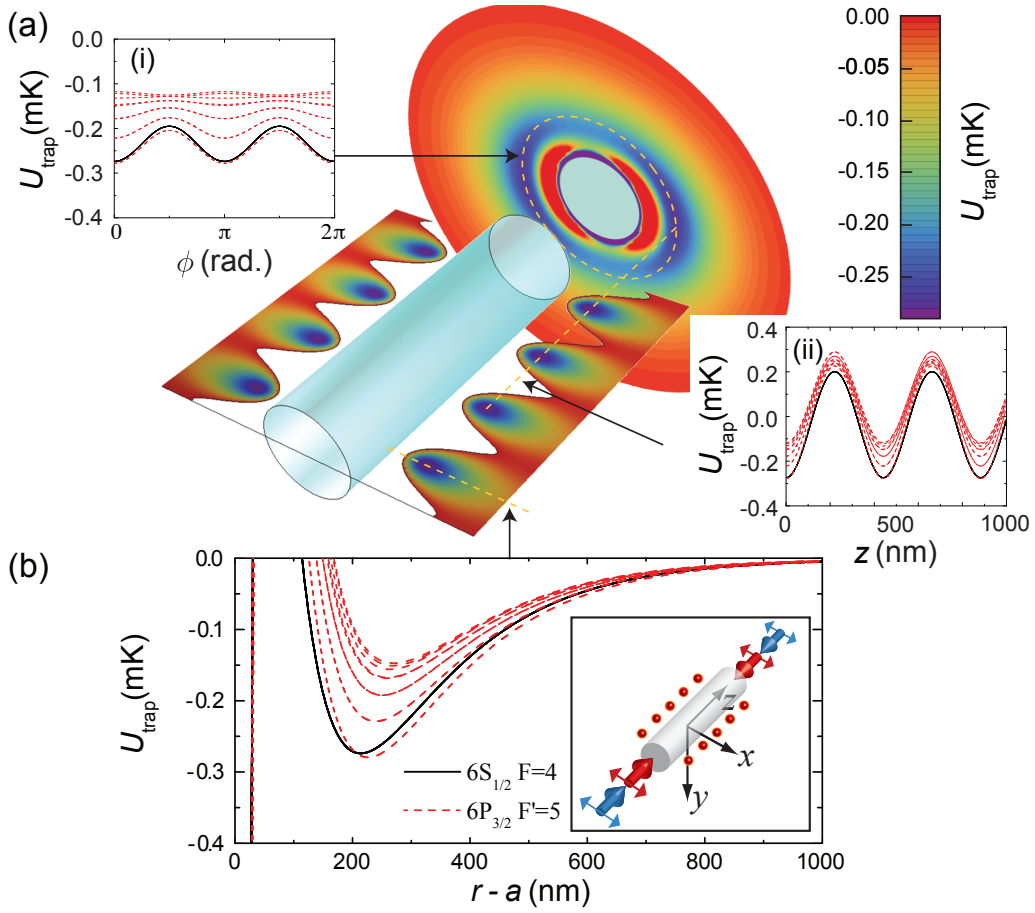

Figure 5.1: **Adiabatic trapping potential U_{trap} for a state-insensitive, compensated nanofiber trap for the $6S_{1/2}, F = 4$ states in atomic Cs outside of a cylindrical waveguide of radius $a = 215$ nm.** U_{trap} for the substates of the ground level $F = 4$ of $6S_{1/2}$ (excited level $F' = 5$ of $6P_{3/2}$) are shown as black (red-dashed) curves. Due to the complex polarizations of the trapping fields, the energy levels are not the eigenstates of the angular momentum operators, but rather superposition states of the Zeeman sublevels). **(a)(i)** azimuthal $U_{\text{trap}}(\phi)$, **(ii)** axial $U_{\text{trap}}(z)$, and **(b)** radial $U_{\text{trap}}(r-a)$ trapping potentials. Input polarizations for the trapping beams are denoted by the red and blue arrows in the inset in (b).

As shown in Fig. 5.1, our trap consists of a pair of counter-propagating x-polarized red-detuned beams at the near magic wavelength [150] $\lambda_{\text{red}} = 937$ nm to form an attractive 1D optical lattice. A second pair of beams at the "magic" wavelength $\lambda_{\text{blue}} = 686$ nm with detuning δ_{blue} provides a repulsive contribution to U_{trap}, thereby protecting the trapped atoms from the short-ranged attractive surface interaction. To avoid a standing wave incommensurate with that at 937 nm, the blue-detuned beams have a relative detuning $\delta_{fb} = 382$ GHz and effectively yield linearly polarized light at all positions, where vector light shifts are suppressed by $\delta_{fb}/\delta_{\text{blue}} \simeq 4 \times 10^{-3}$ [63]. The resulting potential U_{trap} allows for state-insensitive, 3D confinement of Cs atoms along a SiO_2 nanofiber for the $6S_{1/2}$ ground and $6P_{3/2}$ excited states. Note that we didn't use the exact

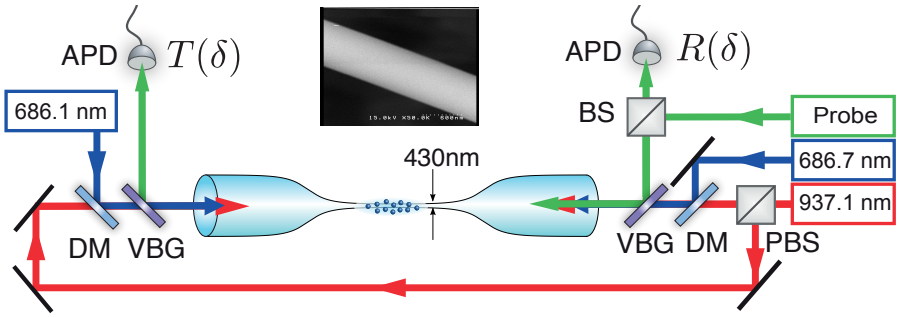

Figure 5.2: **Schematic of the setup for a state-insensitive, compensated nanofiber trap.** VBG: Volume Bragg Grating, DM: Dichroic mirror, PBS: Polarizing beamsplitter, and APD: Avalanche photodetector. The inset shows a SEM image of the nanofiber for atom trapping.

magic wavelength, 685 nm and 936 nm for $6S_{1/2}, F = 4 \rightarrow 6P_{3/2}, F' = 5$ transition in our experiment, since we used the incorrect values of the lifetime and wavelength of the higher excited states, leading to the slightly different evaluation of the magic wavelength by 1nm (as corrected in Ref. [65]).

We calculate the adiabatic potential U_{trap} in Fig. 5.1 from the full light-shift Hamiltonian (i.e., scalar, vector, and tensor shifts), together with the surface potential for Casimir-Polder interactions with the dielectric [63, 65]. The red-detuned beams each have power 0.4 mW, while the blue-detuned beams each have power 5 mW. The trap depth at the minimum is $U_{\text{trap}} = -0.27$ mK located about 215 nm from the fiber surface, with trap frequencies $\{\nu_\rho, \nu_z, \nu_\phi\}/2\pi = \{199, 273, 35\}$ kHz.

5.3 Experimental procedure

An overview of our experiment is given in Fig. 5.2. A cloud of cold Cesium atoms (diameter $\sim$ 1 mm) spatially overlaps the nanofiber. Cold atoms are loaded into U_{trap} during an optical molasses phase ($\sim$ 10 ms) and are then optically pumped to $6S_{1/2}, F = 4$ for 0.5 ms. The red- and blue-detuned trapping fields are constantly 'on' throughout the laser cooling and loading processes with parameters comparable to those in Fig. 5.1.

For the transmission and reflection measurements, the trapped atoms are interrogated by a probe pulse (1 ms) with frequency ω_P, optical power $P_{\text{probe}} \simeq 0.1$ pW, and detuning $\delta = \omega_P - \omega_A$ relative to the $F = 4 \leftrightarrow F' = 5$ transition frequency ω_A. The probe pulse is combined with the forward propagating trapping fields by a pair of Volume Bragg Gratings (VBGs) at the fiber input. The strong trapping beams are

then filtered by a pair of VBGs at the fiber output, with the transmitted probe pulse monitored by a single-photon avalanche photodiode. The polarization of the probe laser is aligned along the trapping beams in order to maximize the overlap with the trapped atoms. We then shelve the atoms to $F = 3$ with a depumping pulse, and probe the fiber transmission with a reference pulse to determine the input power of the probe pulse.

As described in Section 5.7.1, the polarizations of the trapping and probe beams are aligned by observations of Rayleigh scattering [189]. From a simple model described in Section 5.7.1, we infer a transverse polarization vector $\vec{E}_{\text{in}}(z = 0) = (E_x, iE_y)$ with $\beta = \arctan(E_y/E_x) \simeq 12 \pm 3^\circ$ for the probe beam. The principal axes of the polarization ellipse rotate in an approximately linear fashion along z in the trapping region by an angle $\phi(z) \simeq \phi_0 + (d\phi(z)/dz)\delta z$, where $\phi_0 \simeq 16^\circ$ and $d\phi(z)/dz \simeq 12^\circ/\text{mm}$. These results are incorporated into our analysis of the measured transmission and reflection spectra of the trapped atoms (see details in Section 5.7.2).

5.4 Transmission spectroscopy of trapped atoms

The lifetime for atoms in our nanofiber trap is determined from the decay of the resonant optical depth $d_N \simeq N\sigma_0/A_{\text{m}}$ as a function of storage time τ. Here, N is the number of trapped atoms, $\sigma_0 = \lambda^2/(2\pi)$ is the resonant absorption cross-section, and $A_{\text{m}} = P_{\text{probe}}/I_{\text{probe}}(\vec{r}_{\min})$ is the effective optical mode area of the probe's evanescent wave. We observe that d_N decays exponentially with time constant $\tau_0 = 12 \pm 1$ ms. With pulsed polarization-gradient cooling, the lifetime is extended to $\tau_{\text{PG}} = 140 \pm 11$ ms. We are currently characterizing the intensity and polarization noise spectra of the trapping fields to reduce parametric heating [164] with the goal of extending the trap lifetime towards the limit $\tau_r \sim 30$ s set by recoil heating.

Fig. 5.3(a) displays the transmission spectra $T^{(N)}(\delta)$ for the 1D atomic array. The linewidth $\Gamma/2\pi = 5.8 \pm 0.5$ MHz is determined from a model (solid black line) incorporating fiber birefringence and linear atomic susceptibility (see details in Section 5.7.2) in the low density regime ($\tau = 299$ ms). The fitted line profile (solid red line) yields a maximum resonant optical depth $d_N = 66 \pm 17$ at $\tau = 1$ ms. Significantly, our magic, compensated scheme has no discernible shift of the transition frequency $\Delta_A/2\pi \simeq 0 \pm 0.5$ MHz relative to the free-space line center. The measured linewidths from 4 data sets average to $\Gamma/2\pi \simeq 5.7 \pm 0.1$

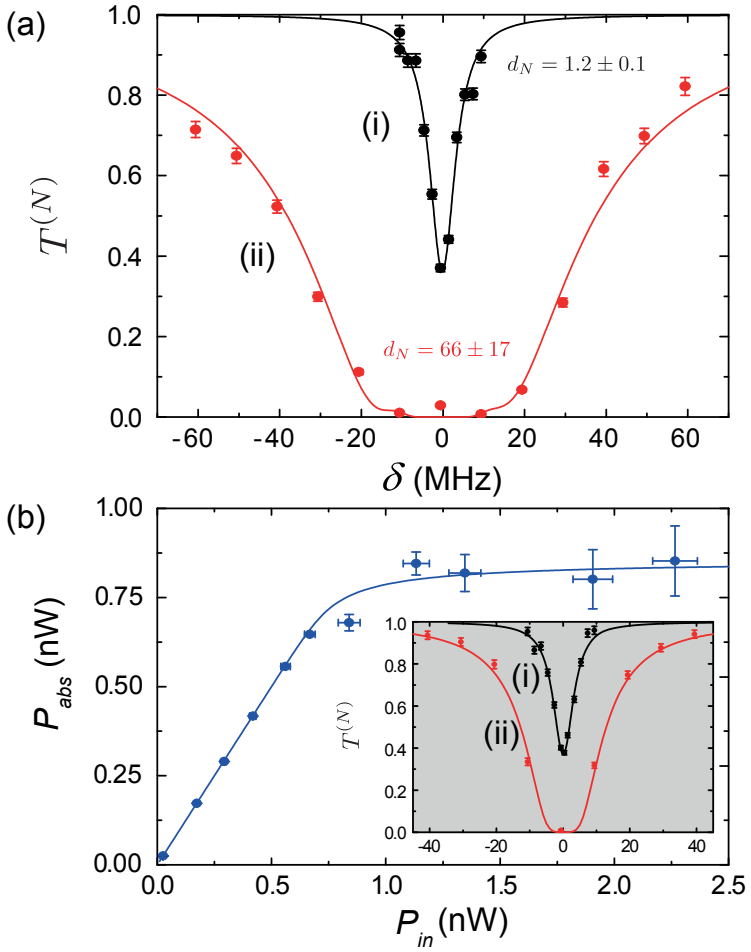

Figure 5.3: **Transmission spectroscopy of trapped atoms. (a)** Probe transmission spectra $T^{(N)}(\delta)$ for N trapped atoms as a function of detuning δ from the $6S_{1/2}, F = 4 \rightarrow 6P_{3/2}, F' = 5$ transition in Cs for x-polarized input. From fits to $T^{(N)}(\delta)$ (full curves), we obtain the optical depths d_N at $\delta = 0$ and linewidths Γ from a model that incorporates the polarization measurements in Fig.5.2 (b),(c). $T^{(N)}(\delta)$ (i) at $\tau = 299$ ms with $d_N = 1.2 \pm 0.1$ and $\Gamma/2\pi = 5.8 \pm 0.5$ MHz and (ii) at $\tau = 1$ ms with $d_N = 66 \pm 17$. **(b)** Measurement of the power P_{abs} absorbed by the trapped atoms as a function of input power P_{in}, together with the associated optical depth $d_N = 18 \pm 2$ from curve (ii) (red line) of the inset, allow an inference of $N = 224 \pm 10$. The linewidth $\Gamma/2\pi = 5.5 \pm 0.4$ MHz and $d_N = 1.1 \pm 0.1$ are determined from curve (i) (black line) of the inset.

MHz, as compared to the free-space radiative linewidth $\Gamma_0/2\pi = 5.2$ MHz for the $6S_{1/2} \leftrightarrow 6P_{3/2}$ transition. By contrast, for a non-compensated scheme without magic wavelengths for Cs [189], the transition frequency is shifted by $\Delta_A/2\pi \simeq 13$ MHz and the linewidth is broadened to $\Gamma/2\pi \simeq 20$ MHz.

The broadening of the absorption linewidth above Γ_0 is predicted for our nanofiber trap because of the enhanced atomic decay into the forward and backward modes of the nanofiber at rate $\Gamma_{1\text{D}}$ [120]. We estimate that an atom at the minimum of U_{trap} decays into the fiber at rate $\Gamma_{1\text{D}}^{(\text{th})}/2\pi \simeq 0.35$ MHz, leading to a predicted linewidth $\Gamma_{\text{tot}}/2\pi \simeq 5.3$ MHz. Additional broadening arises from the tensor shifts of the excited $6P_{3/2}, F' =$

5 manifold ($\simeq 0.7$ MHz) and Casimir-Polder shifts ($\simeq 0.1$ MHz), as well as technical noise of the probe laser ($\simeq 0.3$ MHz). While each of these contributions is being investigated in more detail, the spectra in Fig. 5.3 provide strong support for the effectiveness of our state-insensitive, compensated trapping scheme [63, 65].

To determine the number of trapped atoms, we carry out a saturation measurement at a storage time $\tau = 1$ ms with $\delta = 0$ MHz. As shown in Fig. 5.3(b), we measure the power P_{abs} absorbed by the trapped atomic ensemble in the limit of high saturation $s = P/P_{\text{sat}} \gg 1$ [189]. As described in Section 5.7.3, the fitted curve (blue solid line) yields a number of trapped atoms $N = 224 \pm 10$. Together with the optical depth $d_N = 18$, we find an optical depth per atom $d_1 = (7.8 \pm 1.3) \times 10^{-2}$ for Fig. 5.3(b). A similar measurement in the SM with $d_N = 43 \pm 10$ and $N = 564 \pm 92$ yields $d_1 = (7.7 \pm 2.2) \times 10^{-2}$. These measurements of d_1 and Γ_{tot} were separated by four months and yield consistent results for the nanofiber trap. We thereby estimate $\Gamma_{\text{1D}}/2\pi \simeq 0.2$ MHz [124], similar to $\Gamma_{\text{1D}}^{(\text{th})}$.

5.5 Reflection spectroscopy of trapped atoms

The reflection from the 1D atomic array results from backscattering of the electromagnetic field within the 1D system [124]. The randomness in the distribution of N atoms among n_{site} trapping sites can greatly affect the reflection spectrum $R_N(\delta)$. For each random arrangement Λ of atomic occupation along the nanofiber (e.g., $\Lambda = \{1, 0, 0, \cdots 1, 1, 0\}$), there is a unique narrow reflection spectrum whose resonance frequency δ_Λ is shifted from $\delta = 0$. δ_Λ depends sensitively on the configuration Λ due to the intricate interplay between coherent interference and dispersive phase shifts during the quantum walk of the probe field along the 1D atom array with non-integer $k_{\text{lattice}}/k_{\text{probe}}$, where k_{lattice} (k_{probe}) is the propagation constant for the lattice (probe) field. An ensemble average over Λ thus leads to a reflection spectrum $R_N(\delta)$ that is significantly broadened relative to the transmission spectra in Fig. 5.3.

In Fig. 5.4(a), we observe $R_N(\delta)$ from the 1D atomic array, where the measured Lorentzian linewidth Γ_R is significantly broadened from Γ_0 for large N (with $N \ll n_{\text{site}}$). The solid curves are for $R_N(\delta)$ from Monte-Carlo simulations for the atomic distribution based on the transfer matrix formalism [123]. In order to quantify the microscopic state of disorder for the system, we define an entropy $\mathcal{S}$ for the 1D atomic array

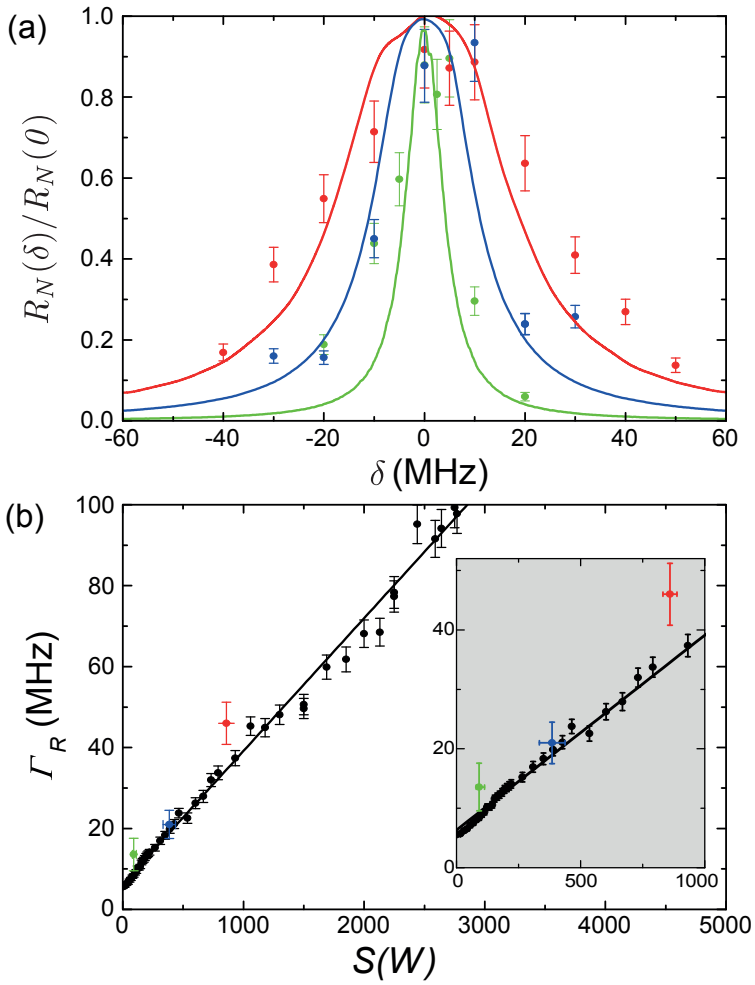

Figure 5.4: **Reflection spectroscopy of trapped atoms.** **(a)** Normalized reflection spectra $R_N(\delta)/R_N(0)$ from the 1D atomic array with $N = 14 \pm 2$ atoms (green points), $N = 79 \pm 13$ atoms (blue points) and $N = 224 \pm 10$ atoms (red points) randomly distributed across $n_{\text{site}} \simeq 4000$ sites. The solid lines are the spectra obtained from Monte Carlo simulations for $N \ll n_{\text{site}}$. **(b)** Simulated linewidth Γ_R of the reflection spectrum as a function of entropy $\mathcal{S}$. The error bars for the red, blue and green data points include both statistical and systematic uncertainties. The black points are the results of a simulation with error bars representing numerical uncertainties. The solid line is a linear fit to the simulation points.

by $\mathcal{S} = \ln W$, where $W = \frac{n_{\text{site}}!}{N!(n_{\text{site}}-N)!}$ is the multiplicity for the atomic distribution in the 1D lattice. In Fig. 5.4(b), we find that the measured reflection linewidth Γ_R (colored points) as well as the linewidth Γ_R^{th} (black points) from the numerical simulation are proportional to the entropy $\mathcal{S}$ of the site-population statistics. These results demonstrate the strong modification of $R_N(\delta)$ due to randomness in the atomic distribution.

5.6 Conclusion and outlook

In conclusion, we have trapped atoms along a nano-fiber by using a state-insensitive, compensated optical trap [63, 65] to achieve an optical depth $d_N \simeq 66$. Compared to previous work with hollow-core and nano-fibers, the atoms are trapped with small perturbations to dipole-allowed transitions. Our scheme is thus well-suited to various applications, including the creation of 1D atomic mirrors for cavity QED and investigations of single-photon nonlinearities and quantum many-body physics in 1D spin chains [124], as well as precision measurements of Casimir-Polder forces near a dielectric waveguide [190].

Currently, the maximum filling factor for sites over the 1 mm loading region is $\sim 19\%$, which can be improved with adiabatic loading and elimination of collisional blockade [191]. The vibrational ground state for axial motion in U_{trap} can be reached by introducing Raman sidebands on the 937 nm trapping fields [192]. The strong axial confinement in our trap implies the presence of a large anharmonicity in the vibrational ladder, which could provide a tool for experiments with single phonons. Furthermore, the design principles of our magic, compensated trap can be extended from simple 'nanowires' to complex photonic crystal structures [176].

5.7 Experimental details

5.7.1 Polarization characterization

The set-up and procedure for measuring and optimizing the polarization state of the nanofiber-guided fields are illustrated in Fig. 5.5 [62, 189]. The angular distribution of the Rayleigh scattered light emitted from the nanofiber is observed by a CCD camera aligned perpendicular to the fiber axis. For the radiation pattern $I(\varphi) \approx \sin^2(\varphi)$ of a dipole induced by linearly polarized light, no light should be detected along the direction that the dipoles oscillate ($\varphi = 0, \pi$). Since the HE_{11} mode has a non-transversal polarization along the fiber axis z, a polarizer (PBS) is placed in front of a CCD camera to block z-polarized light. By rotating the angle θ for the input polarization of the probe field with the half-waveplate ($\lambda/2$) shown in Fig. 5.5(a), a sinusoidal modulation of the scattered intensity $I(z, \theta)$ is observed along the z axis of the fiber. From $I(z, \theta)$, we determine the visibility $V(z) = \frac{I_{\text{max}}(z,\theta) - I_{\text{min}}(z,\theta)}{I_{\text{max}}(z,\theta) + I_{\text{min}}(z,\theta)}$ as a function of z along the nanofiber as shown in Fig.

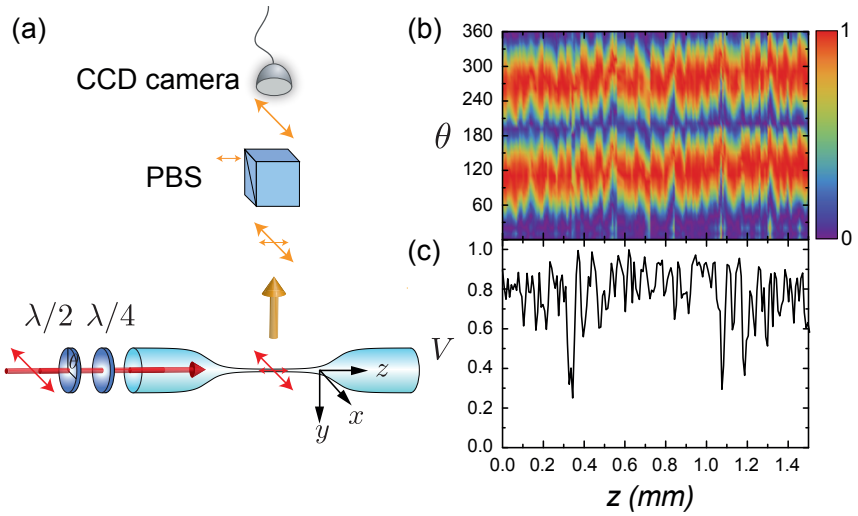

Figure 5.5: **Guided-mode polarization characterization.** **(a)** Setup for polarization characterization of the fields along the nanofiber. **(b)** Intensity $I(z,\theta)$ of scattering from the nanofiber as a function of the angle θ of a half-waveplate for the incident probe field and of distance z along the fiber axis. **(c)** Spatially resolved visibility V as a function of axial position z.

5.5(c).

To describe these measurements, we use a simple model based upon z-dependent birefringence in the fiber that results in elliptical polarization for the transverse fields $E_{x,y}$ along z. From Fig. 5.5(b) in the region of the atom trap, we deduce that the principal axes of the polarization ellipse rotate along z by an angle $\phi(z) \simeq \phi_0 + (d\phi(z)/dz)\delta z$, where ϕ_0 describes a possible offset from the symmetry axes of the trap (i.e., the direction $\phi = 0$ in Fig. 5.1) and $(d\phi(z)/dz) = 12^\circ/\text{mm}$ gives the variation from this offset along z. From fits to transmission spectra described in the next section, we find that $\phi_0 \simeq 16^\circ$.

Fig. 5.5(c) makes clear that there is a wide range of visibility values $V(z)$ for the probe beam along z. For our simple model, we determine the ellipticity of the transverse polarization vector $\vec{E}_{x,y}(z) = (E_x(z), iE_y(z))$, which we describe by the phase $\beta(z) = \arctan(E_y(z)/E_x(z))$. Absent of trapped atoms, the principal axes for the polarization ellipse also rotate by an angle $\phi(z)$ along the nanofiber. From fits to transmission spectra, we find that fixed $\beta(z) = \beta_0$ provides an adequate description of our measurements, with $\beta_0 \simeq 12 \pm 3^\circ$ determined along the high-visibility region in Fig. 5.5(c).

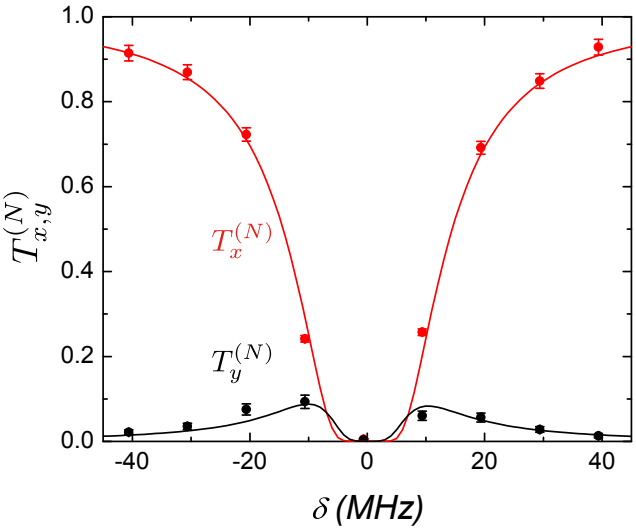

Figure 5.6: **Optical depth estimation with polarization offset.** Measured transmission spectra $T_x^{(N)}$ (red points) and $T_y^{(N)}$(black points) for x, y polarizations of the probe beam as functions of the detuning δ from the $|F = 4\rangle \leftrightarrow |F' = 5\rangle$ transition. From theoretical fits of our model (full curves) that include the interplay of spatially varying birefringence (as in Fig. 5.5) and of atomic absorption and dispersion along the nanofiber, we infer an optical depth $d_N = 18 \pm 2$ with polarization offset $\phi_0 = 16° \pm 3°$ and $\beta_0 = 12°$.

5.7.2 Optical depth estimation

To model the combined effects of the linear atomic susceptibility (i.e., absorption and dispersion) together with the spatially varying birefringence along the nanofiber, we divide the region $0 \leqslant z \leqslant L$ into M 'cells' each of length $\delta z = L/M$. Propagation through a cell at $z_j - \delta z/2 \leqslant z_j \leqslant z_j + \delta z/2$ is generated by the product of two transfer matrices: (1) $\hat{R}(\phi(z))$ produces rotation of the polarization axes from $\phi(z_j)$ to $\phi(z_j) + \delta\phi$, with $\delta\phi = (d\phi(z)/dz)\delta z$, and (2) $T(\delta, d_M)$ specifies the propagation of $E_x(z_j), E_y(z_j)$ through the trapped atoms with detuning δ and optical depth d_M for the x, y polarizations [62]. Here $d_M = d_N/M$ is the optical depth of a single cell, and d_N is the optical depth for the entire sample of N atoms. For each cell, we take the ratio of resonant optical depths to be $d_{0,x}/d_{0,y} = 2.5$ at the trap minimum $r_{\text{min}} = 215$ nm, given by the asymmetry of the evanescent HE_{11} fiber mode [62], where x, y refer to the coordinates for the trap axis as in Fig. 5.1.

In correspondence to the results from Fig. 5.5(b, c), the input polarization to this sequence of cells is set to be elliptically polarized with angle β_0 and offset ϕ_0. After propagation through the fiber in the absence of atoms, our experimental procedure is to compensate the state of the output polarization with the transformation matrix $\hat{R}_{\text{out}}$ to maximize the polarization contrast for the photo-detection after a polarization

beamsplitter aligned along x, y. Hence, in our model, a final rotation $\hat{R}_{\text{out}}$ follows propagation through the M cells before projection of the output fields to obtain intensities $I_x^{\text{out}}, I_y^{\text{out}}$.

Figure 5.6 displays measured transmission spectra $T_{x,y}^{(N)}$ together with fits to the spectra by way of our model. The input parameters for the theoretical spectra are the polarization angle β_0, offset ϕ_0, and optical depth d_N. Typically, we fix $\beta_0 = 12°$ from our measurements of visibility and perform a least-square minimization over ϕ_0 and d_N.

From fits to the data in Fig. 5.6, we find $d_N = 18 \pm 2$ and $\phi_0 = 16° \pm 3°$ for $\beta_0 = 12°$. The quoted uncertainty for d_N includes the contributions from the statistical uncertainty from the photoelectric detection statistics. A second example comparing measured and theoretical transmission spectra is given in Figure 5.7, now for the x polarization at high optical density. From fits to the data in Fig. 5.7, we find $d_N = 43 \pm 10$ and $\phi_0 = 16° \pm 9°$ for $\beta_0 = 12°$.

The theoretical fits to the transmission spectra shown in Fig. 5.3 have been obtained by applying this model. From these and other fits to the measured transmission spectra, we have consistently found that $\overline{\phi_0} \simeq 16° \pm 2°$ with fixed $\beta_0 = 12°$. Numerically, we find that small variations in ϕ_0 can be compensated by corresponding changes in β_0 around the optimal values found from the fits.

5.7.3 Atom number estimation

A generalized Beer's law [61, 189],

$$\frac{dP(z)}{dz} = -n_z \frac{\sigma_0}{A_{\text{m}}} \frac{P(z)}{1 + P(z)/P_{\text{sat}}}, \tag{5.1}$$

describes the saturation behavior of a trapped atom. Here, the saturation power is $P_{\text{sat}} = I_{\text{sat}} A_{\text{m}} = 49.6$ pW, effective optical mode area is $A_{\text{m}} = 1.8\ \mu\text{m}^2$, σ_0 is the resonant absorption cross-section, and $n_z = N/L$ is the atomic line density for a sample length $L = 1$ mm.

For measurements as in Fig. 5.3 (a), the number of trapped atoms $N = 224 \pm 10$ is deduced by fitting the data with the solution of the generalized Beer's law, Eq. 5.1. Together with the optical depth $d_N = 18 \pm 2$ from the curve (ii) of Fig. 5.3 (b), we infer an optical depth $d_1 = (7.8 \pm 1.3) \times 10^{-2}$ for a single atom.

Similar measurements taken in conjunction with the transmission spectrum $T_x^{(N)}$ in Fig. 5.7 lead to an

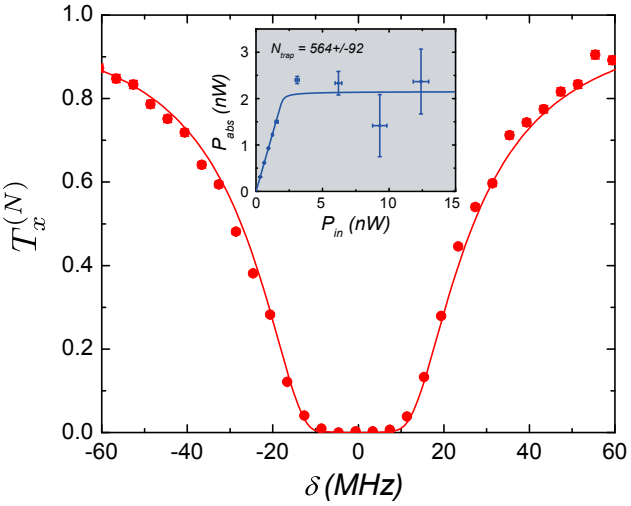

Figure 5.7: **Transmission spectroscopy and saturation measurement.** Measured transmission spectrum $T_x^{(N)}$ (red points) for x polarization of the probe beam as a function of the detuning δ from the $|F = 4\rangle \leftrightarrow |F' = 5\rangle$ transition. From a theoretical fit of our model (full curve) that includes spatially varying birefringence (as in Fig. 5.5) and atomic absorption and dispersion along the nanofiber, we infer an optical depth $d_N = 43 \pm 10$ with polarization offset $\phi_0 = 16° \pm 9°$ and $\beta_0 = 12°$. The inset shows the measurement of the power P_{abs} absorbed by the trapped atoms as a function of input power P_{in}, with the number of trapped atoms, $N = 564 \pm 92$.

estimate $N = 564 \pm 92$ for the number of atoms trapped along the nanofiber. Together with the total optical depth $d_N = 43 \pm 10$ from Fig. 5.7, we infer an optical depth $d_1 = (7.7 \pm 2.2) \times 10^{-2}$ for a single atom.

Chapter 6

Atom-light interactions in photonic crystals

6.1 Introduction

Localizing arrays of atoms in photonic crystal waveguides with strong atom-photon interactions could provide new tools for quantum networks [1, 194, 195] and enable explorations of quantum many-body physics with engineered atom-photon interactions [74, 84–88, 124, 127, 147, 196–202]. Bringing these scientific possibilities to fruition requires creation of an interdisciplinary 'toolkit' from atomic physics, quantum optics, and nanophotonics for the control, manipulation, and interaction of atoms and photons with a complexity and scalability not currently possible. Important initial advances to integrate atomic systems and photonics have been made within the setting of cavity QED with atom-photon interactions enhanced in micro- and nanoscopic optical cavities [34, 38, 40, 178, 203–205] and waveguides [61, 62, 64, 67]. At a minimum, the further migration to photonic crystal structures should allow the relevant parameters associated with these paradigms to be pushed to their limits [40] and greatly facilitate scaling. For example, modern lithographic processing can create nanoscopic dielectric waveguides and resonators with optical quality factors $Q > 10^6$ and with efficient coupling among heterogeneous components [183, 206–210].

A more intriguing possibility that has hardly been explored is the emergence of completely new paradigms beyond the cavity and waveguide models, which exploit the tremendous flexibility for modal and dispersion engineering of photonic crystal waveguides (PCWs). For example, the ability to tune band edges near atomic

This chapter is largely based on Ref. [193].

transition frequencies can give rise to strongly enhanced optical interactions [211–215]. This enables a single atom to exhibit nearly perfect emission into the guided modes ($\Gamma_{1\mathrm{D}} \gg \Gamma'$) and to act as a highly reflective mirror (e.g., reflection $|r_1| \gtrsim 0.95$ and transmission $|t_1| \lesssim 0.05$ for one atom [216]). The entanglement of photon transport with internal states of a single atom can form the basis for optical quantum information processing [1, 194, 195] with on-chip quantum optical circuits. At the many-body level, the strong interplay between the optical response and large optical forces of many atomic "mirrors" can give rise to interesting opto-mechanical behavior, such as self-organization [202].

In this chapter, we describe advances that provide rudimentary capabilities for such a 'toolkit' with atoms coupled to a PCW. As illustrated in Fig. 6.1, we have fabricated an integrated optical circuit with a photonic crystal whose optical bands are aligned with atomic transitions for both trapping and interfacing atoms with guided photons [216, 217]. The quasi-1D PCW incorporates a novel design that has been fabricated in silicon nitride (SiN) [217, 218] (see details in Section 6.5.1) and integrated into an apparatus for delivering cold cesium atoms into the near field of the SiN structure. From a series of measurements of reflection spectra with $\bar{N} = 1.1 \pm 0.4$ atoms coupling to the PCW, we infer that the rate of single-atom radiative decay into the waveguide mode is $\Gamma_{1\mathrm{D}} \simeq (0.32 \pm 0.08)\Gamma'$, where $\Gamma_{1\mathrm{D}}$ is the emission rate without enhancement or inhibition due to an external cavity and Γ' is the radiative decay rate into all other channels. The corresponding single-atom reflectivity is $|r_1| \simeq 0.24$, representing an optical attenuation for one atom greater than 40% [124, 216]. For comparison, atoms trapped near the surface of a fused silica nanofiber exhibit $\Gamma_{1\mathrm{D}} \simeq (0.04 \pm 0.01)\Gamma'$ [61, 62, 64, 67], comparable to observations with atoms and molecules with strongly focused light [219, 220]. By comparing with numerical simulations, our measurements suggest that atoms are guided to unit cells of the PCW by optical dipole forces.

6.2 Design and characterization of 1D photonics crystal waveguide

Turning to our experiment, we begin with an SEM image of a small section of our 1D photonic crystal waveguide shown in Fig. 6.1a. The device consists of two parallel nanobeams with sinusoidal modulation at the outer edges (an 'alligator' PCW or APCW). A challenge in the fabrication of PCWs for atomic physics is

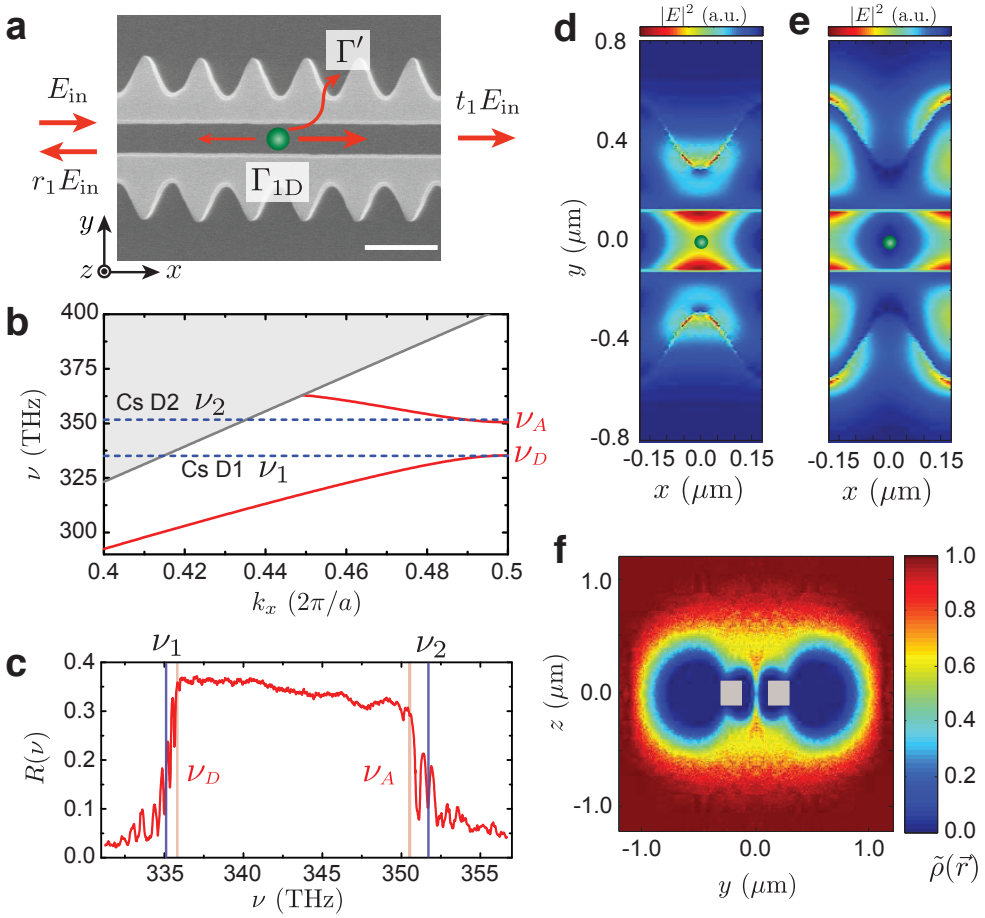

Figure 6.1: **Design and characterization of 1D photonic crystal waveguide.** **a**, SEM image of the 'alligator' photonic crystal waveguide (APCW) made from 200 nm thick (along z-axis) silicon nitride (SiN). Arrows indicate radiative processes of an atom (green circle) coupled to an incident electric field $E_{\rm in}$. Scale bar, 500 nm. **b**, Calculated band structure of fundamental TE-like modes $E_1,\ E_2$ (red solid lines), with dominant electric field polarized in the y-direction. The dashed lines mark the frequencies ν_1 and ν_2 of the cesium $\rm D_1,\ D_2$ lines, respectively. $(\nu_A,\ \nu_D)$ mark near the band edge. The gray solid line marks the light line. **c**, Measured reflection spectrum with fast fringe removed (see Section 6.5.3) around the band gap shown in **b**. **d**, $|E|^2$ cross sections of E_2 mode near ν_2, and **e**, E_1 mode near ν_1 within a unit cell calculated with the MPB software package (see Section 6.5.1). Both modes are polarized with their primary electric field component in the in-plane y direction. **f**, Simulated relative density $\tilde{\rho}(\vec{r})$ of atoms in the $x = 0$ plane of **d**, with the optimal excitation of the blue-detuned E_1 mode at $k_x = \pi/a$ (see text).

placement of the band edges near relevant atomic transition frequencies. Our APCW design facilitates this juxtaposition by fine-tuning the gap between the parallel nanobeams and the amplitude of sinusoidal modulation in the APCW. Figure 6.1b shows the band structure of two fundamental transverse electric (TE-like) modes calculated based on the dimensions measured from SEM images as in Fig. 6.1a [221]. The two blue dashed lines correspond to the transition frequencies of the Cs $(\rm D_1,\ D_2)$ lines at $(\nu_1 = 335, \nu_2 = 351)$ THz $[(895, 852)$ nm] which straddle the band edge frequencies (ν_D, ν_A) at $k_x = \pi/a$ for the lower (dielectric) and

upper (air) TE bands, respectively. To validate these results, we measure the reflection spectrum $R(\nu)$ versus the input frequency ν for the actual device used in the reported experiments; see Fig. 6.1c. The large reflectivity ($R \sim 0.35$) from ν_D to ν_A corresponds to the band gap for the APCW, while the vertical lines mark (ν_1, ν_2) just outside the band gap. Absent propagation loss to and from the APCW, we infer $R_{\mathrm{gap}} \simeq 0.99$ from measurements and numerical simulation.

Beyond band-edge placement, another requirement for realizing strong atom-light interactions in PCWs is to localize atoms in a region of high mode intensity within a unit cell. The use of two bands enables the separate engineering of the modes for trapping (lower band) and control of spontaneous emission (upper band). The blue-detuned E_1 mode excited at ν_1 in Fig. 6.1e can guide atoms into the center of the vacuum space near regions of large $|E_2|^2$, with then a field near ν_2 serving as a probe mode.

The efficacy of this strategy is supported by trajectory calculations of free-space atoms surrounding the APCW (see details in Section 6.5.5). As shown in Fig. 6.1f, atoms are guided from free space into the region of high $|E_2|^2$, resulting in a density approximately 30% of the remote free-space density. For the simulations, the Casimir-Polder potential $U_{CP}(\vec{r})$ for the structure in Fig. 6.1a is computed numerically following Ref. [216]. The optical dipole potential is calculated using a guided mode $E_1(\vec{r})$ at $k_x = \pi/a$ with total power of 1 μW and 10 GHz blue-detuning from the $F = 4 \leftrightarrow F' = 4$ transition frequency of the D_1 line.

An overview of the integrated APCW device is presented in Fig. 6.2, and shows the optical pathways for excitation to and from the APCW, as well as the supporting structures of the SiN device to a silicon substrate. The entire APCW contains 260 unit cells with a lattice constant $a = 371$ nm, and is terminated on each end by a mode matching section of 40 cells with tapered sinusoidal modulation and a transition section from a double- to a single-nanobeam waveguide. Input to and output from the device is achieved through an optical fiber butt-coupled to one of the single-nanobeam waveguides [218] (see details in Section 6.5.1). The one-way efficiency for propagation from the APCW to the fiber mode is $T_{wf} \simeq 0.6$.

To integrate the device into a cold-atom apparatus, the silicon chip in the inset of Fig. 6.2a and its coupling optical fibers are mounted on a vacuum feedthrough with linear translation and rotation stages and inserted into a UHV chamber. Cesium atoms are delivered to the region surrounding the APCW by a three-stage process of transport and cooling (see details in Section 6.5.6). The resulting atomic cloud has a peak number

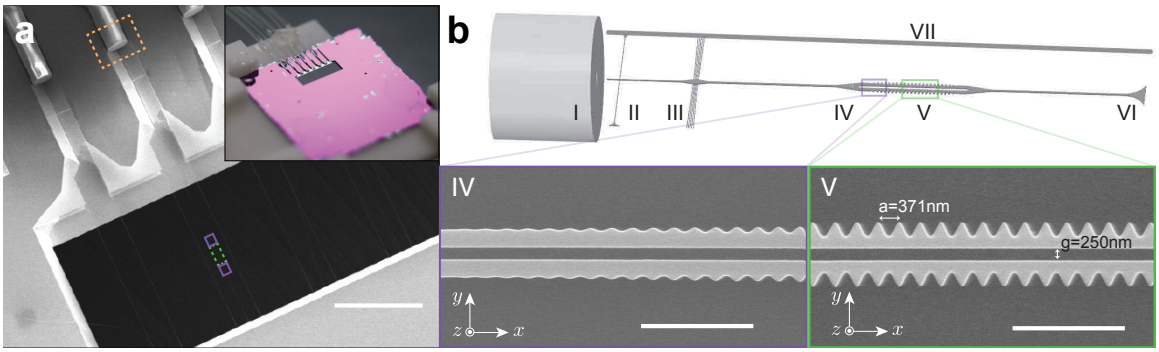

Figure 6.2: **Overview of the integrated APCW device. a** SEM image of the silicon chip showing an integrated optical fiber (orange box) coupled, via a SiN nanobeam waveguide, to the APCW region (purple and green boxes). The APCW is located within a 1×3 mm through window (black region without dielectrics) where free-space atoms and cooling lasers are introduced. Inset shows a picture of the chip and the optical fibers glued to a vacuum-compatible holder. Scale bar, 0.5 mm. **b** Detailed schematic of the suspended SiN waveguide. Light enters the system via the optical fiber (I) butt-coupled to the free end of the waveguide (II) which is supported by a tether array (III). Near the center of the through window, the waveguide transitions into a double-nanobeam, followed by tapering (IV) and APCW (V) sections, and again tapers out to terminate into the substrate (VI). Two parallel rails are added symmetrically to support the structure (one rail is illustrated in VII). The insets, corresponding to the purple and green boxes in **a**, show SEM images of segments of the tapering (IV) and APCW (V) sections, respectively. Scale bars in IV and V, 2 μm.

density of $\rho_0 \simeq 2\times10^{10}$ /cm^3 at temperature $T \simeq 20$ μK measured via time-of-flight absorption imaging.

6.3 Atom-light coupling in the APCW

6.3.1 Reflection measurements at on- and off-resonant cavity

We study atom-light interactions in the APCW by first shutting off the cooling laser, followed by a delay of 0.1 ms, and then interrogating the APCW with atoms by sending a guided probe pulse $E_{\rm probe}$ of frequency ν_p in the E_2 mode, with typical power $\simeq 1$ pW and measuring a reflected pulse of $rE_{\rm probe}$; see Fig. 6.3a and Section 6.5.6. Reflection spectra $R(\Delta_p)$ are recorded for 1 ms with a single-photon avalanche photodiode as a function of detuning $\Delta_p = \nu_p - \nu_{2a}$, where ν_{2a} is the free-space $F = 4 \leftrightarrow F' = 5$ transition frequency of the D_2 line. For 10 ms following termination of the probe pulse, the atom cloud disperses, and then reference spectra $R_0(\Delta_p)$ are recorded for a second probe pulse for 1 ms. For all experiments, the guided mode E_1 is driven continuously with power $\simeq 0.6$ μW at 10 GHz blue-detuning from the $F = 4 \leftrightarrow F' = 4$ transition of the D_1 line.

In the ideal case of a single atom in an infinite PCW, an incident probe beam would be reflected with

amplitude coefficient $|r_1| = \Gamma_{1D}/(\Gamma_{1D} + \Gamma')$ [124], where Γ_{1D} refers to emission into the guided mode of the APCW from the $F = 4 \leftrightarrow F' = 5$ transition of the Cs D_2 line. Strong spontaneous decay into the guided mode (and hence large $|r_1|$) results from the small area over which the guided mode is concentrated together with a reduced group velocity. These two effects are incorporated into an effective mode area for an atom at location $\vec{r}$ within the APCW, namely $A_m(\vec{r}) = n_g\sigma_0\Gamma_0/2\Gamma_{1D}(\vec{r})$, where $n_g \simeq 2$ is the measured group index at ν_2, $\sigma_0 = 1.4 \times 10^{-9}$ cm^2 is the free-space atom-photon cross section for an unpolarized atom, and Γ_0 is the free-space rate of decay. For unpolarized atoms located at the center of a unit cell $\vec{r} = (0, 0, 0)$ in the APCW, we expect $A_m(0) = 0.24\ \mu$m^2, and hence $|r_1| \simeq 0.39$, where $\Gamma' \simeq 0.9\Gamma_0$ from numerical calculations (see details in Section 6.5.2) [216].

In the case of our actual device, the finite lengths of the taper sections lead to imperfect mode matching into the APCW near the band edge. As illustrated in Fig. 6.3a, the matching sections partially reflect an incident probe pulse and form a low-finesse ($\mathcal{F} \simeq 2$) cavity around the APCW. These weak cavity resonances in the reflection spectrum near ν_2 are shown in Fig. 6.1c (without atoms) and complicate the spectra taken with atoms relative to the ideal case, as discussed below.

In Figs.6.3b,c, we measure distinctive reflection spectra with cold atoms under two configurations of the APCW. Figure 6.3b displays $R^{on}(\Delta_p)/R_0^{on}(\Delta_p)$ acquired near a resonance for the matching cavity where the reflectivity with no atoms, R_0^{on}, is very small (see Section 6.5.4). We observe an increased peak reflectivity $R^{on}/R_0^{on} \simeq 1.27 \pm 0.02$. By comparison, with the matching cavity excited midway between two cavity resonances where the reflectivity with no atoms R_0^{off}, we observe decreased reflectivity with a minimum $R^{off}/R_0^{off} \simeq 0.75 \pm 0.01$ in Fig. 6.3b.

These reflection spectra are in accord with those for a low-finesse Fabry-Perot (FP) cavity containing a frequency-dependent intracavity absorber (Fig. 6.3a). In Fig. 6.3b with input frequency resonant with the FP cavity and no atoms, the transmission is high, and there is very small reflection. Atoms inside the PCW reduce light build up by frequency dependent atomic absorption, resulting in an increased reflectivity $R^{on}/R_0^{on} > 1$. By contrast, in Fig. 6.3c without atoms, the device reflectivity is larger $R_0^{off} > R_0^{on}$ due to the off-resonant drive of the FP and is reduced by intracavity atomic absorption, $R^{off}/R_0^{off} < 1$.

The reflection spectra in Figs.6.3b, c represent strong evidence for atomic interactions with the guided

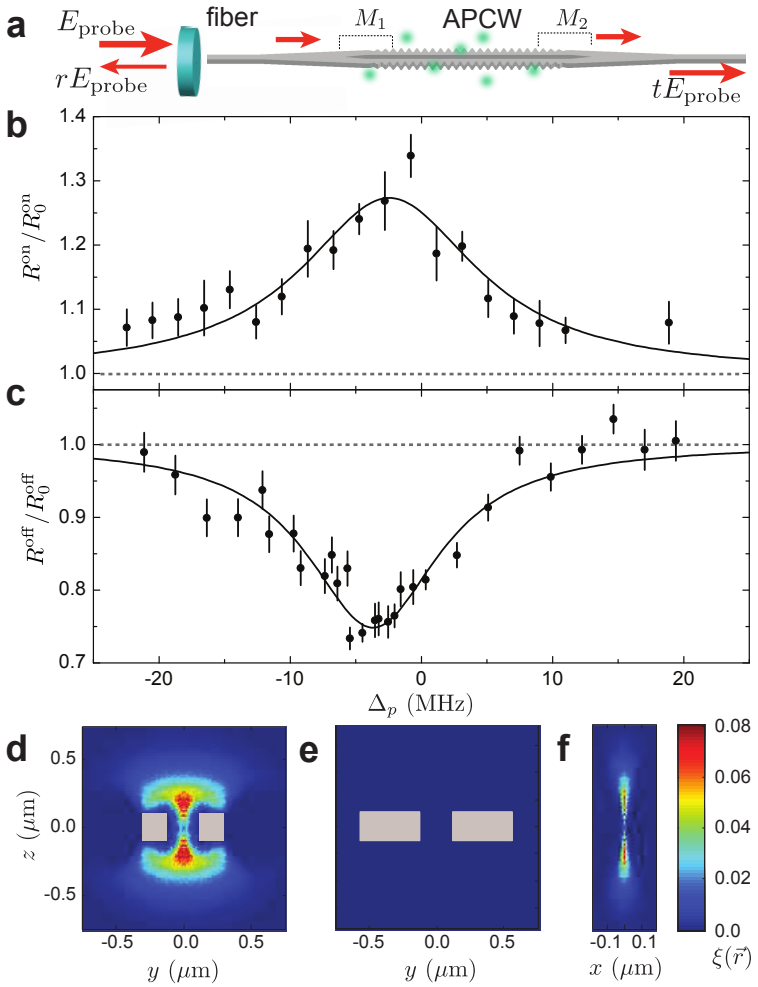

Figure 6.3: **Atom-light coupling in the photonic crystal waveguide section. a**, Simplified schematic of a fiber-coupled photonic crystal waveguide for reflection measurements with atoms (green dots). Dashed lines, marked as M_1 and M_2, illustrate the effective low-finesse $\mathcal{F} \simeq 2$ cavity formed by the tapered matching sections. **b**, **c** Measured reflection spectra (circles) with **b**, an on-resonant cavity and **c**, an off-resonant cavity in the APCW. Solid lines are Lorentzian fits with **b**, linewidth of 15.2±1.8 MHz, peak reflectivity $R^{\rm on}/R_0^{\rm on} = 1.27 \pm 0.02$ where the reflectivity with no atoms $R_0^{\rm on}$ and frequency shift $\Delta_0 = -2.5 \pm 0.6$ MHz, and **c**, linewidth of 11.5±1.1 MHz, $R^{\rm off}/R_0^{\rm off} = 0.75 \pm 0.01$ where the reflectivity with no atoms $R_0^{\rm off}$ and $\Delta_0 = -3.7 \pm 0.3$ MHz. Error bars for the data points reflect 1 s.d. estimated from the statistical uncertainties. **d**, Simulated $\xi(\vec{r}) = \tilde{\rho}(\vec{r}) \times \Gamma_{\rm 1D}(\vec{r})/\Gamma_{\rm 1D}(0)$ in the $x = 0$, **e**, $x = a/2$, and **f**, $y = 0$ planes, with a guided potential of $m_F = 0$ using the experimentally excited blue-detuned E_1 mode at $k_x = 0.99\pi/a$. Due to the deviation from the band edge, a small bump in the optical potential at the center of the unit cells leads to atomic localization near the maxima of $\xi(\vec{r})$ in **d** and **f**; see text for details. Masked areas in gray represent the APCW.

mode E_2 of the APCW. Although the cavity formed by the matching sections has a low finesse, $R(\Delta_p)$ nevertheless depends on the cavity detuning as predicted, i.e., exhibiting approximately Lorentzian profiles for increased (decreased) $R^{\rm on(off)}(\Delta_p)/R_0^{\rm on(off)}(\Delta_p)$ for ν_{2a} coincident with (mid-way between) the weak cavity resonances.

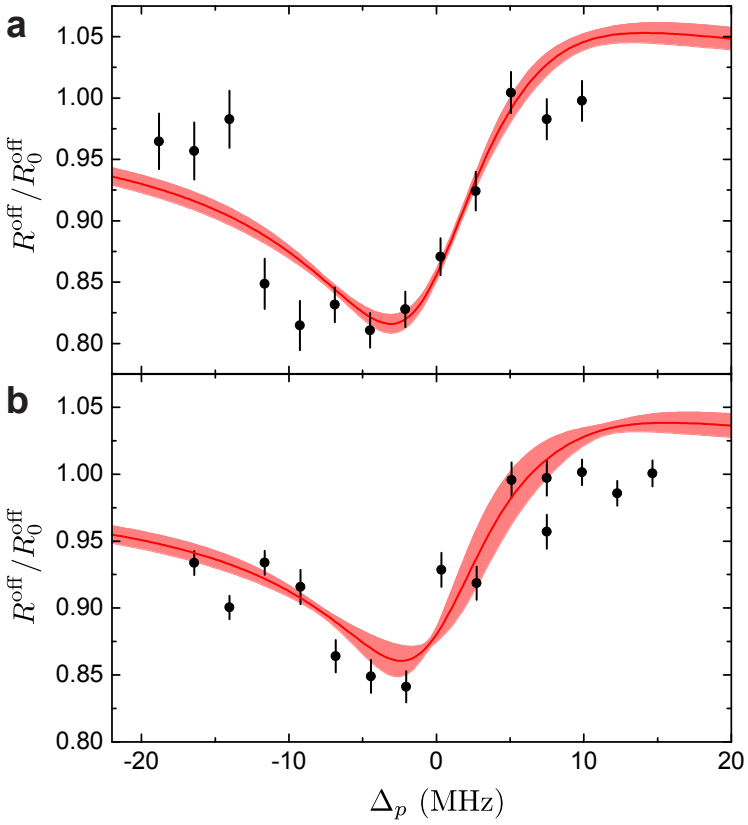

Figure 6.4: **Measured reflection spectra and theoretical fit for the APCW.** Measured reflection spectra (circles) with free-space atomic cloud densities $\rho/\rho_0 = 1$ **(a)**, and 0.75 **(b)** where the reflectivity with no atoms $R_0^{\rm off}$. The full curves are fits with a model derived from transfer matrix calculations. Error bars for the data points reflect 1 s.d. estimated from the statistical uncertainties. We deduce that $(\Gamma_{1D}/\Gamma', \bar{N}, \delta_0/\Gamma_0) \simeq (0.35\pm0.1, 1.0\pm0.1, 0.33\pm0.06)$ **(a)** and $(0.36\pm0.1, 0.76\pm0.13, 0.48\pm0.07)$ **(b)**. Here, $\rho_0 = 2\times10^{10}/\text{cm}^3$; $\Gamma_0/2\pi = 5.2$ MHz (decay rate in free space). The shaded band gives the uncertainty arising from the position of the matching cavity (see details in Section 6.5.7).

Moreover, our numerical simulations as in Fig. 6.3d, 6.3e, and 6.3f suggest that the blue-detuned E_1 mode performs three functions of excluding atoms from the exterior of the APCW, as in Fig. 6.3e, guiding atoms into regions of large E_2 probe intensity near the center of the unit cells, as in Figs.6.3d and 6.3f, and expelling atoms from the vicinity of other parts of the waveguide, e.g., the single-nanobeam regions in Fig. 6.3a, leaving only the APCW region with significant atom-field interactions. Together, these considerations enable us to infer quantitatively the single-atom emission rate absent reflections from the tapered sections, as we now describe.

6.3.2 Reflection measurements and theoretical fit

To obtain quantitative information about atom-light coupling in the APCW region, we compare our measurements with a model based on transfer matrix calculations of the optical pathway to and from the APCW as illustrated in Fig. 6.3a. Details of the optical elements, including the coupling fiber, the supporting structures, and the APCW, are described in Section 6.5.4 and Ref. [217]. Absent atoms, the optical characteristics of these various elements can be deduced from measurements of reflection spectra (c.f., Fig. 6.1c and Fig. 6.9). With atoms, free parameters are the average atom number $\bar{N}$ within the APCW, the ratio $\Gamma_{1\mathrm{D}}(\vec{0})/\Gamma'$ for an atom at the center of the probe mode E_2, and the frequency shift δ_0 of the line center ν_0 relative to free-space, $\delta_0 = \nu_0 - \nu_{2a}$. Here atoms are drawn from a Poisson distribution and placed randomly along the APCW.

Comparisons between measurements and our model for $R^{\mathrm{off}}(\Delta_p)/R_0^{\mathrm{off}}(\Delta_p)$ are given in Fig. 6.4. For these data, the weak cavity formed by the matching sections has a small detuning $\Delta_c \simeq 50$ GHz from the midpoint between two resonances (free spectral range $\sim$600 GHz). With atoms, the cavity detuning results in asymmetric, dispersive-like reflection spectra, which is captured by our model. From fits to the measured reflection spectra in Fig. 6.4, we deduce that $\Gamma_{1\mathrm{D}}/\Gamma' \simeq 0.35 \pm 0.1$ and $\bar{N}_0 \simeq 1 \pm 0.1$ for loading from a free-space cloud of density ρ_0.

The inferred value of $\Gamma_{1\mathrm{D}}$ allows us to determine $A_{\mathrm{m}}(\vec{r}_{\mathrm{eff}})$ for the atom-field interaction in our experiment, namely $A_{\mathrm{m}}(\vec{r}_{\mathrm{eff}}) \simeq 0.44\ \mu\mathrm{m}^2$ for an unpolarized atom. Together with the E_2 mode profile, the value of A_{m} suggests that atoms are distributed in narrow regions around $\vec{r}_{\mathrm{eff}} \simeq (0, 0, \pm 130)$ nm, which is consistent with our numerical simulations (Fig. 6.3d,e,f).

The large ratio $\Gamma_{1\mathrm{D}}/\Gamma' \simeq 0.35$ implies a single-atom reflectivity $|r_1| \simeq 0.26$, which is sufficient to give a nonlinear dependence of $R^{\mathrm{off}}(\Delta_p)/R_0^{\mathrm{off}}(\Delta_p)$ on the atom number N observed in the measured spectra. We are thereby able to disambiguate the product $\bar{N} \times \Gamma_{1\mathrm{D}}$ into separate parameters in fitting our model to measurement.

6.3.3 Saturation measurement

To further investigate the nonlinear dependence of the reflection spectra on atom number, we measure reflection spectra for increasing values of probe power P in the E_2 guided mode for various values of $\bar{N}$. Figure

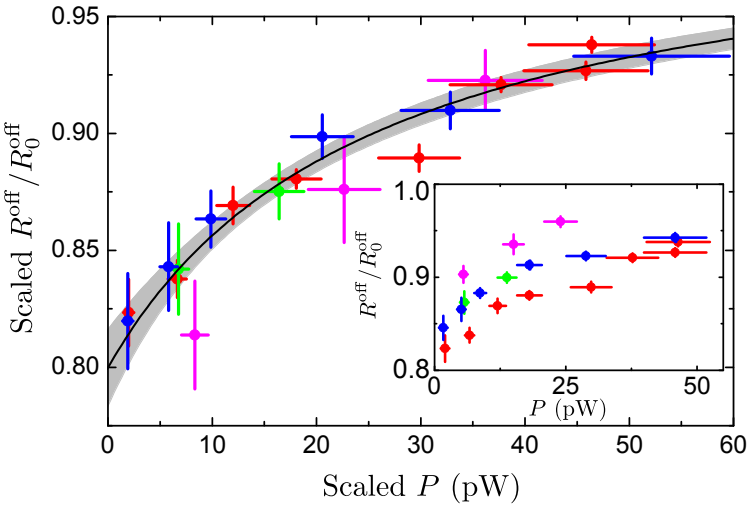

Figure 6.5: **Scaled reflection minimum as a function of averaged probe power inside the APCW.** The saturation spectra (circles) are measured with four free-space densities ρ/ρ_0 = 1 (red), 0.81 (blue), 0.75 (green), 0.44 (magenta), and rescaled to a common free-space density $\rho_0 \simeq 2\times10^{10}/\,\mathrm{cm}^3$; see text. The inset shows the saturation data without scaling. An empirical fit (solid curve) gives a saturation power of 22.7± 2.2 pW. Error bars for the data points are 1 s.d. estimated from the statistical uncertainties and uncertainties of the fit to the model. The gray area shows 95% confidence band.

6.5 presents results for $R^{\rm off}(\Delta_p)/R_0^{\rm off}(\Delta_p)|_{\rm min}$ from a series of measurements as in Fig. 6.4 for increasing P with the plotted points corresponding to the minima of $R^{\rm off}/R_0^{\rm off}$ versus Δ_p for each spectrum. The inset of Fig. 6.5 displays four sets of measurements showing that saturation of the atomic response (i.e., $R^{\rm off}/R_0^{\rm off}\to 1$ with increasing P) requires higher power as the density is increased (i.e., increasing $\bar{N}$).

The observed saturation behavior can be scaled into a common curve using the dependence of cooperative atomic emission on atom number $\bar{N}$. We assume that $R^{\rm off}(P) = R^{\rm off}(P/P_{\rm sat})$ and that the saturation power $P_{\rm sat}$ depends on the average total decay rate as $P_{\rm sat} \propto (\Gamma' + \bar{N}\Gamma_{\rm 1D})^2$ with $\Gamma_{\rm 1D}/\Gamma' = 0.35 \pm 0.1$, as determined from our measurements in Fig. 6.4 with $P \to 0$. We rescale the probe power (horizontal axis) for each density in the inset of Fig. 6.5 to a common density ρ_0. Likewise, $R^{\rm off}(P)/R_0^{\rm off}$ (vertical axis) is rescaled using the density dependence derived from our transfer matrix model (Methods), with $\bar{N}\propto\rho$. The approximate convergence of the data to a common curve in Fig. 6.5 supports our rudimentary understanding of the underlying atom-field interactions in the APCW, including that the observed line shapes for the data in Fig. 6.5 taken at higher power (not shown) are predominately homogeneously broadened.

To estimate the saturation power in the APCW, we adopt an empirical form for the saturation behavior $R^{\rm off}(P,\bar{N})/R_0^{\rm off} = \exp\{-\gamma(\bar{N})/[1+P/P_{\rm sat}(\bar{N})]\}$. From the fit in Fig. 6.5, we determine $P_{\rm sat}(\bar{N}_0) =$

22.7 ± 2.2 pW and $\gamma(\bar{N}_0) = 0.22 \pm 0.01$. Combining with the measured effective mode area, we find the saturation intensity $I_{\rm sat} = P_{\rm sat}/A_{\rm m} \simeq 5.2$ mW/cm^2, close to the expected value $I_{\rm s0} \times (\Gamma' + \bar{N}_0\Gamma_{\rm 1D})^2/\Gamma_0^2 \simeq 4.0$ mW/cm^2, where $I_{\rm s0} = 2.7$ mW/cm^2 is the free-space saturation intensity.

6.4 Conclusion and outlook

We have realized a novel APCW device for interfacing atoms and photons. The measured coupling rate $\Gamma_{\rm 1D}$ (quoted absent Purcell enhancement and inhibition due to an external cavity) is unprecedented in all current atom-photon interfaces, whether for atoms trapped near a nanofiber [61, 62, 64, 67], one atom in free-space [219], or a single molecule on a surface [220]. For example, in Ref. [40] a drop in transmission $\simeq 0.02$ is observed for single atoms trapped outside a photonic crystal cavity. In our work without trapping, we observe a dip in reflection $\simeq 0.25$ for $\bar{N} \simeq 1$ since atoms are channeled to near the peak of the probe mode in the center of unit cells with stronger interactions. Further improvements to the APCW include active tuning of the band edge to near an atomic resonance to achieve an increase $\gtrsim 50$ fold in $\Gamma_{\rm 1D}$ [216, 222], although we are mindful of challenges prevented by disorder-induced localization [223, 224]. Other opportunities could be tuning to place the atomic resonance within the band gap to induce long-range atom-atom interactions [84–87]. By optimizing the power and detuning of the E_1 trap mode, we should be able to achieve stable atomic trapping and ground state cooling [216, 225, 226]. By applying continuous on-site cooling to $N \gg 1$ atoms, we expect to create a 1D atomic lattice with single atoms trapped in unit cells along the APCW, thus opening new opportunities for studying novel quantum transport and many-body phenomena [74, 85–87, 124, 127, 147, 196–202].

6.5 Experimental details

6.5.1 Design principle

An ‘alligator’ photonic crystal waveguide (APCW) is designed on a chip in order to observe strong atom-light interactions, as illustrated in Fig. 6.6. The APCW interacts with a cloud of atoms trapped in a magneto-optical

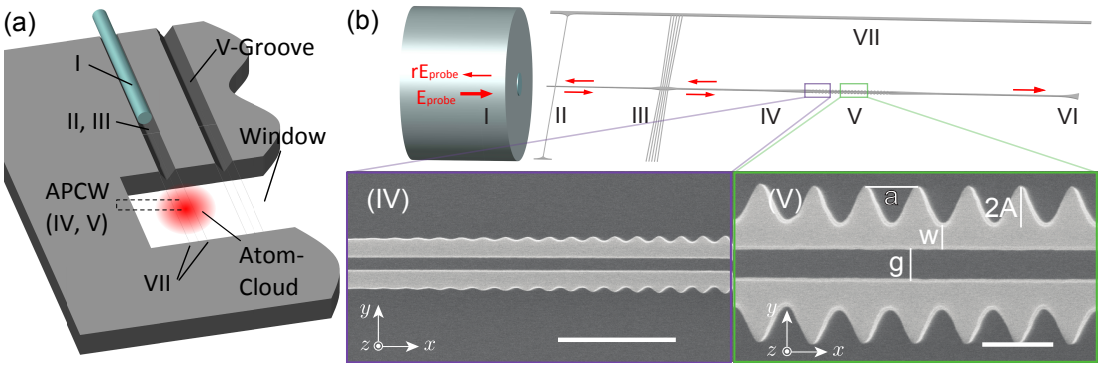

Figure 6.6: **Schematic image of the suspended SiN device.** (a) A schematic of the Si-chip and optical fiber mounted on the V-groove.(b) Probe light enters the system via optical fiber (I) and couples into the free end of a tapered SiN waveguide (II). The guided light transmits through the supporting tether array (III). At the center of the window, the waveguide is tapered into a double-nanobeam, and then tapered (IV) into the nominal APCW section (V) where atom-light interaction occurs. At the end of the window, the waveguide is tapered out and terminated into the substrate (VI). Two support rails are added symmetrically parallel to the APCW for structural integrity (one rail is illustrated in VII). The insets at the bottom are SEM images of (IV) the tapered section, and (V) the 'alligator' photonic crystal. Scale bars in (IV) and (V), 2 μm and 500 nm, respectively.

trap (MOT) which is centered on the photonic crystal. The APCW (see inset V of Fig. 6.6) consists of two parallel nanobeams with sinusoidal corrugations on the outer edges [217]. The atoms are guided into the center of the two nanobeams by a scheme which takes advantages of the TE-like modes (y-polarized) near the band edges [227]. Their highly symmetric mode profiles near the dielectric and air bands at frequencies (ν_D, ν_A) and the proximity to the resonant frequencies (ν_1, ν_2) of the cesium D_1, D_2 lines allow us to create strong dipole potentials with small optical power (< 10 μW) in the E_1 mode, while achieving large atom-photon coupling in the E_2 mode. See Figs. 6.1d, e for calculated mode profiles.

The corrugations in the APCW are used rather than the more traditional holes because the corrugation amplitude can be patterned more accurately than hole radii, resulting in more accurate alignment of the band gaps and better adiabatic tapers. The outside-corrugated double-beam design used in this work allows superior band-edge positioning by placing the modulation of the dielectric away from the strong-field region in the center of the waveguide, thereby reducing the sensitivity of band-edge frequencies to the modulation geometry parameter imprecision. This design also avoids enclosed hole-based geometry, which is difficult to fabricate using available lithography and etching techniques. The design also enables us to build vanishingly small amplitude modulations required for the gradual tapers. The waveguide is made from 200 nm thick stoichiometric silicon nitride (SiN) with index $n = 2.0$ [217]. SiN is a widely used material in standard

silicon-based fabrication processes, which we have chosen for its low absorption for the Cs D-line transition wavelengths where Si itself is opaque. Its high intrinsic stress and Young's modulus makes it mechanically robust, and therefore it was chosen instead of the also low-loss SiO_2. The degrees of freedom for the APCW are the gap g, lattice constant a, width w (inner-edge to center of peaks), and tooth amplitude A. The APCW has 260 cells, a gap 250 nm, a width 173 nm, and tooth amplitude 132 nm. The photonic crystal is tapered on both sides into an unpatterned (translationally invariant) double-nanobeam. The length and profile of the tapering determines the reflections from the edges of the APCW. The taper used here has 40 cells, and is carefully designed such that the band gap symmetrically opens about 873 nm, which is between the D_1 and D_2 lines. The profile and the unpatterned double waveguide width are chosen to minimize reflections from the APCW edge.

In order to provide optical access for the trapping and cooling laser beams, the silicon nitride (SiN) waveguides are suspended across a 1 mm long, 3 mm wide through window on the chip, shown in Fig. 6.2a, and the APCW (the inset (D,E) of Fig. 6.6) is positioned at the center. The suspended waveguide extends beyond the window into a V-groove etched into the Si substrate and then reduces in width for efficient coupling to a conventional optical fiber [218] (sections I-II of Fig. 6.6). The silicon anisotropic etch that forms the window also forms the V-shaped groove, which serves to center the fiber to the waveguide. The far end of the waveguide is extended to a fan shape and terminated into the substrate to minimize reflection (VI).

6.5.2 Atom-photon coupling

To characterize the strength of atom-photon coupling, we calculate the effective mode area for an atom at $\vec{r}_{\mathrm{A}}$:

$$A_{\mathrm{m}}(\vec{r}_{\mathrm{A}}) = \frac{\int \epsilon(\vec{r'})|E_2(\vec{r'})|^2 d^3r'}{a\epsilon(\vec{r}_{\mathrm{A}})|E_2(\vec{r}_{\mathrm{A}})|^2}, \tag{6.1}$$

where a is a lattice constant of 371 nm and the integration runs over the space occupied by a unit cell. Figure 6.7 shows $A_{\mathrm{m}}(\vec{r}_{\mathrm{A}})$ plotted at the central $x = 0$ plane. For single atoms channeled to the center of unit cells, we have $A_{\mathrm{m}}(0) = 0.24\ \mu\mathrm{m}^2$.

To estimate the atomic emission rate into the guided mode, we use $\Gamma_{1\mathrm{D}}(\vec{r}) = \Gamma_0 n_g \sigma_0 / 2A_{\mathrm{m}}(\vec{r}_{\mathrm{A}})$, where

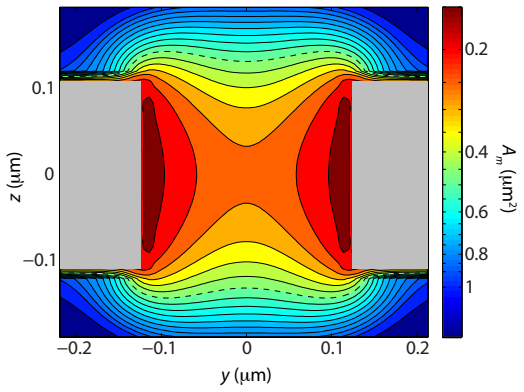

Figure 6.7: **Calculated effective mode area $A_{\rm m}(\vec{r}_{\rm A})$ for an atom at $\vec{r}_{\rm A} = (0, y, z)$ at the central $x = 0$ plane of a unit cell.** Masked areas in gray represent dielectric regions of the APCW. The dashed line represents $A_{\rm m}(\vec{r}_{\rm eff}) \sim 0.44\ \mu{\rm m}^2$, which we extract from measurements shown in Fig.4.

Γ_0 is the atomic decay rate in free space, σ_0 the radiative cross section, and n_g the group index at ν_2. When the band edge frequency ν_A is placed near ν_2, we expect $n_g \gg 1$ due to the slow light effect [216]; $n_g = \frac{c}{2L_{\rm Phc}\Delta\nu} \simeq 2$ for the current device where c the speed of light, $\Delta\nu$ the distance between neighboring resonant dips and $L_{\rm Phc}$ the length of APCW (See Fig. 6.6 (b)). Note that due to our small band gap ($\Delta\omega/\omega_0 \sim 0.04$), we would have to operate much closer to the band gap than in our current experiment in order to observe a significant slow light effect (e.g., $n_g > 10$). For atoms guided to the center of unit cells and driven by the $F = 4, m_F = 0 \leftrightarrow F' = 5, m_{F'} = 0$ transition, $\sigma_0 \simeq 5/9 \times 3\lambda^2/2\pi$, where $\lambda = 852$ nm is the free-space wavelength of the Cs D_2 line, with then $\Gamma_{\rm 1D}/\Gamma_0 \simeq 0.4 n_g$; for unpolarized atoms, we calculate an averaged $\Gamma_{\rm 1D}/\Gamma_0 \simeq 0.29 n_g$.

6.5.3 Device characterization

Figure 6.8 (a) shows a schematic of the setup for device characterization. The reflection spectrum near the band gap is measured by sending a broadband light source into the device via the coupled optical fiber, and then recording the reflection signal with an optical spectrum analyzer. The signal is then normalized by the power spectral density of the light source after considering the loss of each optical element. Finer reflection spectra around the D_1 and D_2 lines are measured by scanning the frequency of narrow bandwidth diode lasers. The polarization in the device is aligned to the TE-like mode by observing the polarization dependent scattering from the first tether in the coupler, or equivalently by maximizing the reflected signal, since the

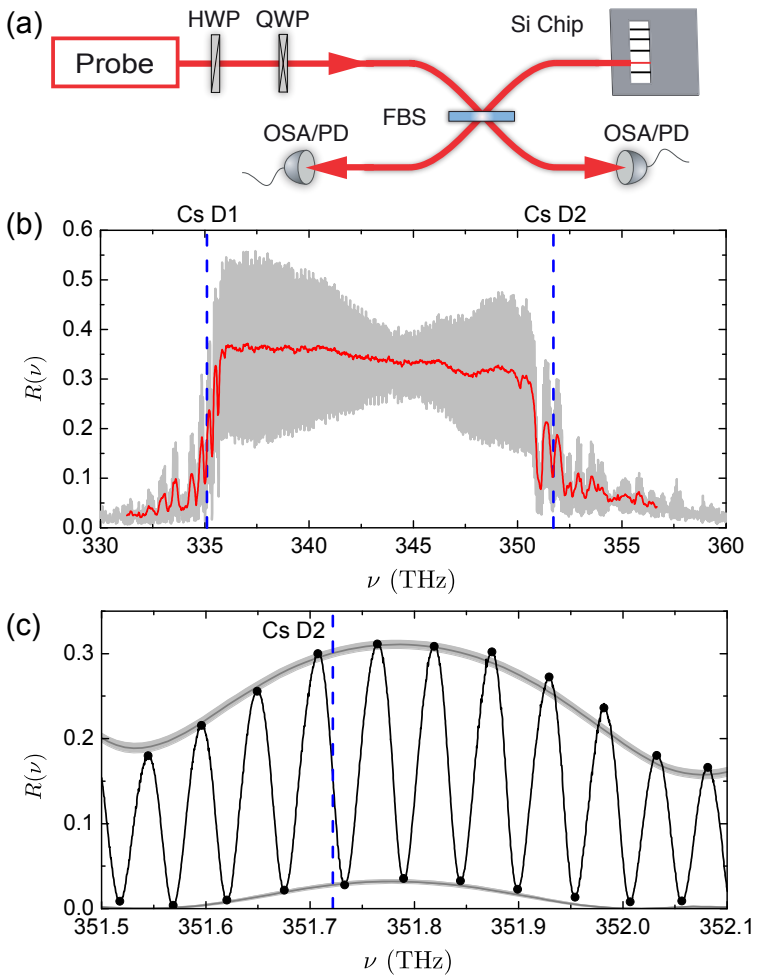

Figure 6.8: **Device characterization.** (a) Schematic of the setup for device characterization. FBS: fiber beam splitter with $T = 50\%$ and $R = 50\%$. HWP: half waveplate. QWP: quarter waveplate. OSA: optical spectrum analyzer. PD: photodetector. (b) Measured reflection spectrum near the band gap. Gray and red curve show the original data and smoothed data, respectively. Blue dashed lines correspond to the Cs D_1 and D_2 resonances. (c) Measured reflection spectrum near the Cs D_2 line (black curve) and envelope fit (gray curve).

transverse magnetic (TM-like) mode band gap is located at a higher frequency.

Figure 6.8 (b) shows the measured reflection spectra around the band gap. The gray curve shows the original data which has a fast fringe (free spectral range $\sim$ 50 GHz) resulting from the (parasitic) etalon formed from the cleaved fiber end-face and the first matching taper. The red curve shows the smoothed reflection spectrum which approximately represents the response of the APCW without the influence of the reflection from the fiber end-face.

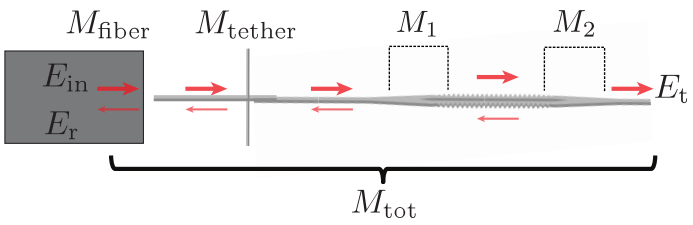

Figure 6.9: **Schematic of a 1D transfer matrix model of the device.** Forward- and backward propagating waves in the structure are coupled to each other through partial reflection from the fiber end-face, tether, and matching mirrors, and also evolve under propagation losses. Their effect on the total reflected and transmitted fields ($E_{\text{r}}, E_{\text{t}}$) can be modeled through a set of four independent transfer matrices M_{fiber}, M_{tether}, M_1, and M_2 (depicted by the dashed lines), which together determine the transfer matrix M_{tot} of the entire system.

6.5.4 Device model

Due to imperfection of the adiabatic tapering, the terminal regions of the APCW form a low finesse cavity. When atoms couple to light in the APCW, the reflected spectrum depends on the position of the frequency ν_2 on the cavity fringe and can take on dispersive line shapes. Further complicating the picture is the presence of a fast ∼50 GHz fringe due to the parasitic etalons formed by the fiber end-face, tethers, and the APCW band edges near ν_D, ν_A. In order to fit the reflected atomic signals, a full model that incorporates all of these elements is developed using the transfer matrix method [227, 228] as show in Figure 6.9. A transfer matrix represents each element, and the reflection, transmission, and loss coefficients are determined by both experiment and FDTD simulations [229].

The light is coupled into the device by matching the modes of a 780HP single mode fiber (mode field diameter 5 μm) to a 130 nm wide rectangular SiN waveguide (I-II in Figs. 6.6 (b)). The fiber end-face reflects 3.8% power due to the index mismatch. A 90 nm wide tether anchors the coupling waveguide 5 μm from the free (input) end of the waveguide, which has a theoretical transmission of 87% and reflection 0.8%. The waveguide width tapers to 200 nm over 300 μm in order to better confine the light to the dielectric, and then the light propagates through the region of the support rails (III in Fig. 6.6 (b)) to the APCW at the center of the window. Our numerical simulations show that the taper, support rails, and guide should have negligible loss and reflection. The loss in these sections is measured to be 22% per mm for a similar device. The details of loss mechanism is currently under investigation. The total loss from the fiber face to the waveguide can be estimated experimentally by measuring the reflected signal for frequencies within the band gap, assuming

that the reflectivity of the APCW from numerical simulations is $\sim 99\%$. By fitting our model to the envelope of the reflection spectrum inside the band gap, we obtain the overall transmission efficiency from the internal face of the fiber to the input of the APCW to be $T_t \simeq 0.60$, including propagation losses in the nanobeam.

The tapers of the APCW (represented by the matching mirrors in Fig. 6.9) also reflect near the band edge. There is also loss inside the APCW due to fabrication disorder and absorption. Near the Cs D_2 line, as shown in the Fig. 6.8 (c), the fitted spectrum (solid gray line) yields the reflection and transmission of the matching sections of the APCW, ($R_{\rm pc} = 0.28, T_{\rm pc} = 0.72$), the slope of the reflection of the APCW $dR_{\rm pc}/d\lambda = 0.082$/nm, and the one-way transmission inside the APCW, $T_{\rm APCW} = 0.40 \pm 0.02$.

At the bottom of the fast fringe, for the experiment presented in Fig. 3b, measured reflection without atoms is $R_0^{\rm on} = |E_{\rm r}|^2/|E_{\rm in}|^2 \simeq 0.3\%$ and reflection in front of M_1 estimated from the device model is $\Re_0^{\rm on} \simeq 9\%$; in Fig. 3c, $R_0^{\rm off} = 3\%$ and estimated reflection in front of M_1, $\Re_0^{\rm off} \simeq 41\%$.

6.5.5 Simulations of relative density

To estimate a relative atomic density near the APCW with a guiding potential, we calculate a relative density $\tilde{\rho}(\vec{r}) = \rho(\vec{r})/\rho_0$, where ρ_0 is a free-space cloud density, with a Monte Carlo simulation of 5×10^6 trajectories of thermal atoms with a temperature of 20 μK [135]. For the simulations, the Casimir-Polder potential $U_{\rm CP}(\vec{r})$ for the APCW is computed numerically following Ref. [216], with an example cut shown in Fig. 6.10 (a). The dipole potential $U_{\rm dipole}(\vec{r})$ of the blue-detuned guided mode $E_1(\vec{r})$ near ν_1 is calculated by using the mode function obtained with MIT Photonic-Band package [221]. Trajectories are obtained by numerically solving the equation of motion with force of $\vec{F} = -\vec{\nabla} U_{\rm tot}(\vec{r}) = -\vec{\nabla}(U_{\rm CP}(\vec{r}) + U_{\rm dipole}(\vec{r}))$. The relative density is inferred from atomic flux crossing each grid. Note that velocity-dependent forces of polarization-gradient cooling (PGC) are not included in the simulations.

In Figs.6.1f and Fig. 6.10 (b), we use a guided mode $E_1(\vec{r})$ at the band edge $k_{A,x} = \pi/a$ at ν_D with total power of 1 μW and 10 GHz blue-detuning from $F = 4 \leftrightarrow F' = 4$ transition frequency of D_1 line, which has zero intensity at the center of unit cells of the APCW. Thus, atoms are channeled into unit cells by the combination of Casimir-Polder and optical dipole force. The relative density at the center of unit cells is $\tilde{\rho}(0) \sim 0.3$.

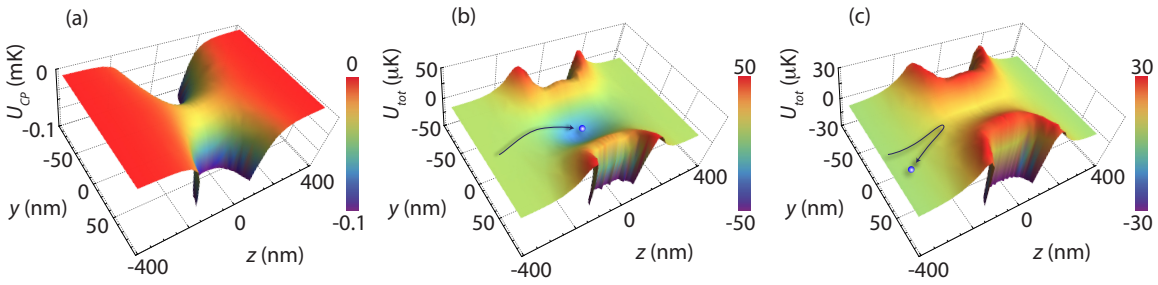

Figure 6.10: **Guiding potential for Cs $F = 4$ hyperfine ground state.** (a) Casimir-Polder potential $U_{\rm CP}(\vec{r})$ and (b, c) total potential $U_{\rm tot}(\vec{r}) = U_{\rm CP}(\vec{r}) + U_{\rm dipole}(\vec{r})$ are plotted at $\vec{r} = (0, y, z)$ at the central $x = 0$ plane of a unit cell. The dipole potential $U_{\rm dipole}(\vec{r})$ is calculated for $m_F = 0$ state, using the E_1 mode at (b) $k_{A,x} = \pi/a$ with total power of 1 μW and (c) $k_{1,x} = 0.99k_{A,x}$ with total power of 0.6 μW, and both with 10 GHz blue-detuning from $F = 4 \leftrightarrow F' = 4$ transition frequency of the D_1 line. The curved arrow in (b)[(c)] illustrates a characteristic trajectory of an atom (solid circle) guided into the trap center [reflected off the bump] in the total potential between the gap.

In Figs.6.3d, 6.3e, 6.3f, and 6.10 (c), we use experimentally excited $E_1(\vec{r})$ with $k_{1,x}$ near ν_1 (Cs D_1 line), which is $\sim 1\%$ below the band edge $k_{A,x}$. Due to the small deviation from the band edge, the intensity of the mode field $E_1(\vec{r})$ near ν_1 has a small bump at the center of unit cells, which for blue detuning, prevents atoms from being channeled to the center. In addition, the intensity of $E_1(\vec{r})$ has a longitudinal component E_x along the propagation direction, which is $\pi/2$ out-of-phase with the transverse components. As a consequence, the polarization of $E_1(\vec{r})$ is elliptical everywhere except for the central $y = 0$ plane of unit cells due to TE symmetry. The resulting guiding potential has vector shifts due to the ellipticity of $E_1(\vec{r})$, which lead to m_F dependent guiding potentials. Since the center of guiding channel for $|m_F| \neq 0$ states moves from $y = 0$ to $|y| > 0$ due to a stronger fictitious magnetic field (along z) closer to the structure, the guiding efficiency from optical dipole forces is reduced as $|m_F|$ increases.

Figure 6.3d, 6.3e, and 6.3f display $\xi(\vec{r}) = \tilde{\rho}(\vec{r}) \times \Gamma_{\rm 1D}(\vec{r})/\Gamma_{\rm 1D}(0)$, where $\tilde{\rho}(\vec{r})$ is simulated relative atomic density with a guided potential for $m_F = 0$, and $\Gamma_{\rm 1D}(0)$ is a decay rate into the APCW at the center of unit cells. Due to the small deviation from the band edge and the resulting potential 'bump', atoms are localized around > 100 nm from the center of unit cells.

We note that, in the case of Fig. 6.10 (c), adding to $U_{\rm dipole}$ the dipole potential from a weak red-detuned $E_2(\vec{r})$ mode can help overcome the potential bump in the gap center and can create a stable trapping condition.

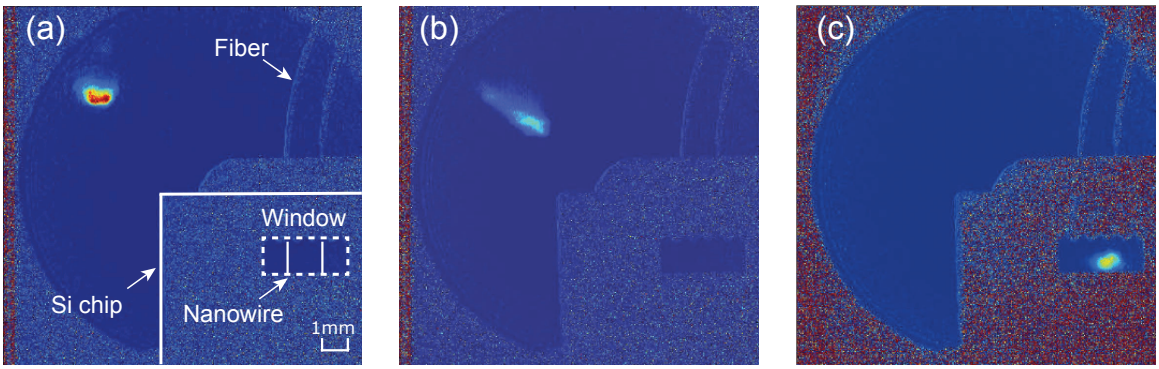

Figure 6.11: **Transporting a cloud of atoms near the APCW, measured by absorption imaging.** (a) First, we prepare a cloud of cold atoms about 1cm away from a silicon chip. (b) After cooling atoms in the moving frame toward the APCW and shutting off the cooling beams, a cloud of atoms freely propagates toward the APCW. (c) By turning on additional MOT beams at the time atoms fly near the APCW, propagating atoms are cooled and recaptured.

6.5.6 Experimental procedure

To prevent cesium contamination of the APCW due to the background vapor pressure, our vacuum system consists of a source chamber and a science chamber, connected via a differential pumping stage. The source chamber runs in a standard MOT loaded from the background Cs vapor. From the source MOT, a pulsed push beam extracts a flux of cold atoms that is slow enough to be recaptured in a science MOT located in the UHV region [230]. We load a science MOT for 1 s and compress it for a duration of 50 ms [231]. We then obtain a cloud of cold atoms with a peak density of $\sim 1 \times 10^{11}$ /cm^3 and a temperature of 40 μK about 1 cm away from the APCW of a silicon chip.

In order to transport cold atoms near the APCW, we cool atoms in the moving frame toward the APCW by abruptly changing the center of magnetic quadrupole field [232], as shown in Fig. 6.11. After shutting off cooling beams, a cloud of atoms freely propagates toward the APCW. By turning on additional MOT beams at the time atoms fly near the APCW, we cool and recapture propagating atoms with an efficiency of $\sim 40\%$. After applying PGC, we obtain a cloud of cold atoms with a peak number density of $\rho_0 \sim 2 \times 10^{10}$ /cm^3, spatially overlapped with the APCW.

An overview of reflection measurements in our experiment with cold atoms near the APCW is given in Fig. 6.12. A blue-detuned guiding beam with power $\sim 0.6\mu$W and detuning of +10 GHz from D_1 ($F = 4 \leftrightarrow F' = 4$) at $k_{1,x} = 0.99k_{A,x}$ is sent into the device, which is kept on throughout the experiment.

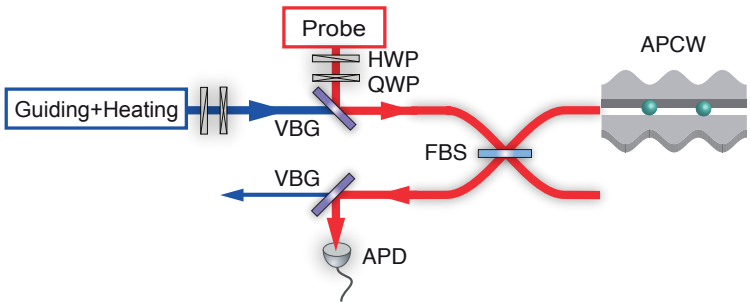

Figure 6.12: **Schematic of the setup for reflection measurements.** VBG: volume Bragg grating. FBS: fiber beam splitter with $T = 99\%$ and $R = 1\%$. HWP: half waveplate. QWP: quarter waveplate. APD: avalanche photodetector.

The probe pulse is combined with the guiding beam by a volume Bragg grating (VBG) and then couples to the APCW via a fiber beam splitter with $T = 99\%$ and $R = 1\%$. The reflected probe signal from the APCW is efficiently picked up by the fiber beam splitter through the transmission path. An additional VBG at the output reflects the return probe beam, which allows us to measure the probe pulses with the guiding beam on. A pair of $\lambda/2$ and $\lambda/4$ waveplates in each path is used for aligning the polarization to only excite the TE-like mode.

To maximize the signal-to-noise ratio, we perform reflection measurements with atoms after aligning the bottom of the fast fringe to the Cs D_2 line, where the probe field is maximized inside the parasitic cavity formed by the fiber end-face and the APCW region; see Fig. 6.13 (a). The alignment of the fast fringe can be tuned by sending an additional few μW of heating beam to heat up the device and adjust the optical path length between the fiber end-face and the APCW region. The heating beam runs at frequency $\nu > \nu_D$ inside the band gap and is $\simeq 5$ nm detuned from the D_1 line, thus does not interfere with atomic-light interaction in the APCW region.

6.5.7 Model of reflection spectrum of atoms

Reflection spectra of guided atoms are obtained by including transfer matrices for atoms [123] in the device model described in Section 6.5.4. Guided atoms inside the APCW are drawn from a Poisson distribution with mean atom number $\bar{N}$ and randomly placed at the center of unit cells along the APCW. Each of the two matching sections that terminate the APCW partially reflects light near the band edge, as depicted in Fig. 6.9. Together the matching sections form a cavity around the APCW (denoted by M_1, M_2 in Fig. 6.9), whose

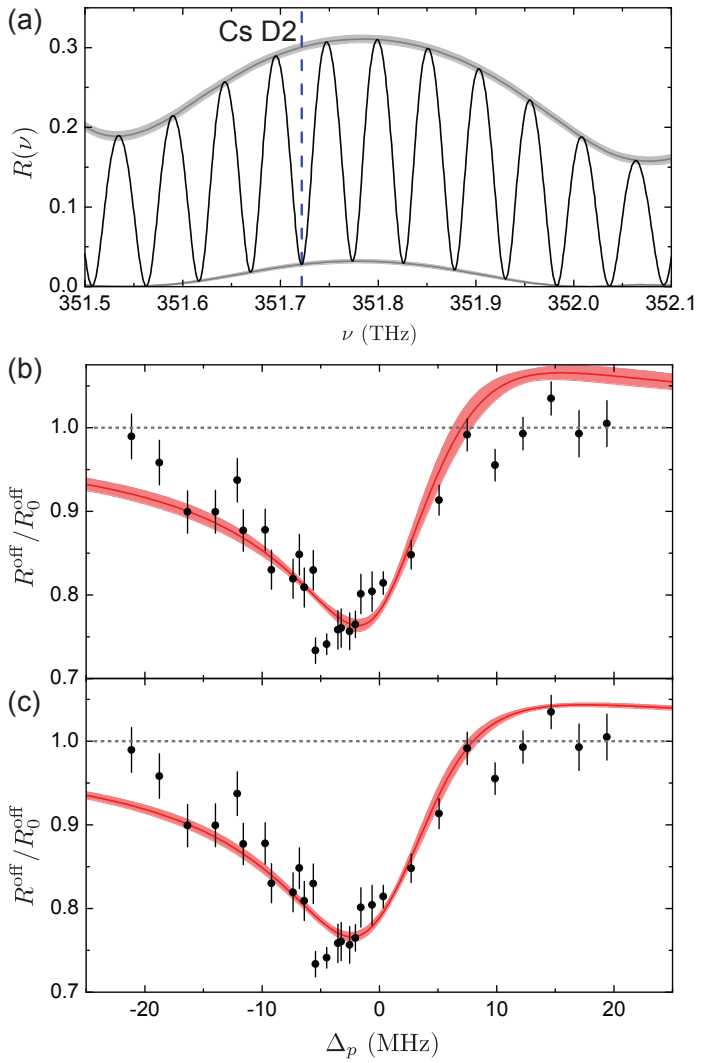

Figure 6.13: **Reflection measurements and theoretical fit.** (a) Simulated reflection spectrum of the optical pathway to and from the APCW derived from the transfer matrix calculation. Blue dashed line shows the Cs D_2 line. (b, c) Measured reflection spectra (circles) with free-space density of $\rho_0 \sim 2\times10^{10}$ /cm^3, where the reflectivity with no atoms $R_0^{\rm off} \simeq 3\%$. These are the data same as Fig.3c. Error bars for the data points reflect 1 s.d. estimated from the statistical uncertainties. The full curves are fits with (b) uniform-absorption model (i) and (c) losses localized to the matching mirrors (ii). From the fits, we deduce (b) $(\Gamma_{1D}/\Gamma', \bar{N}, \delta_0/\Gamma_0) \simeq (0.31\pm0.05, 1.5\pm0.2, 0.56\pm0.06)$ and (c) $(\Gamma_{1D}/\Gamma', \bar{N}, \delta_0/\Gamma_0) \simeq (0.41\pm0.04, 0.9\pm0.1, 0.25\pm0.06)$. The shaded band gives uncertain arising from the position of the matching cavity.

cavity length has a frequency dependence. We incorporate the uncertainty of the location of the matching mirrors and resulting cavity relative to the APCW into our model. This uncertainty gives rise to a variation in the reflection spectra from our model, which is given by the thickness of the lines shown in Fig. 6.13.

The wave vector of probe frequency $k_{{\rm p},x}$ is $\simeq 2\%$ from the band edge at $k_{A,x} = \pi/a$ as shown in Fig. 6.1b. In the case of more than one atom coupled to the APCW, the mismatch between $k_{A,x}$ and $k_{{\rm p},x}$ causes

dephasing since the accumulated phase between atoms is not an integer multiple of π. Due to the moderate one-way transmission of $T_{\rm APCW} \simeq 0.40$ inside the APCW as described in Section III, the cooperative effect of two atoms is sensitive to how loss occurs inside of the APCW. Here, we consider two limiting cases: (i) uniform absorption along the APCW, and (ii) loss at the first matching mirror.

In the case of (i), due to uniform loss along the APCW, only nearby atoms interact equally with the probe field. Thus, cooperative effects survive despite of the mismatch of $k_{{\rm p},x}$ and $k_{A,x}$. On the other hand, in the case of (ii), all atoms contribute equally and cooperative effects are washed out due to the phase mismatch for propagation with $k_{{\rm p},x}$ as compared to $k_{A,x}$ for the unit cell. Given our current limited knowledge of the microscopic details of the loss mechanisms within the APCW, the models (i, ii) provide a means to estimate the uncertainties in our inferences of $\Gamma_{\rm 1D}/\Gamma'$ and average atomic number $\bar{N}$ based upon comparisons of our data with the models.

For the cases shown in Fig. 6.13, the model fits lead to the following: (i) $\Gamma_{\rm 1D}/\Gamma' = 0.31 \pm 0.05$ and average atom number $\bar{N} \simeq 1.5 \pm 0.2$ in (b), and (ii) $\Gamma_{\rm 1D}/\Gamma' = 0.41 \pm 0.04$ and $\bar{N} \simeq 0.9 \pm 0.1$ in (c). From four sets of data as in Fig. 6.13, taken for comparable atomic densities, we make fits based upon the two models (i) and (ii). We average results for parameters determined from the fits to arrive at the values quoted, namely $\Gamma_{\rm 1D}/\Gamma' = 0.32 \pm 0.08$, $\bar{N} = 1.1 \pm 0.4$, and $\delta_0/\Gamma_0 = 0.13 \pm 0.27$.

Chapter 7

Superradiance for atoms trapped along a photonic crystal waveguide

7.1 Introduction

Interfacing light with atoms localized near nanophotonic structures has attracted increasing attention in recent years. Exemplary experimental platforms include nanofibers [61, 64, 67], photonic crystal cavities [40], and waveguides [193, 217]. Owing to their small optical loss and tight field confinement, these nanoscale dielectric devices are capable of mediating long-range atom-atom interactions using photons propagating in their guided modes. This new paradigm for strong interaction of atoms and optical photons offers new tools for scalable quantum networks [1], quantum phases of light and matter [78, 79], and quantum metrology [5].

In particular, powerful capabilities for dispersion and modal engineering in nanoscopic photonic crystal waveguides (PCWs) provide opportunities beyond conventional settings in AMO physics within the new field of *waveguide QED* [60, 61, 64, 74, 193, 234]. For example, the edge of a photonic band gap aligned near an atomic transition strongly enhances single-atom emission into the one-dimensional (1D) PCW due to a van-Hove singularity at the band edge (i.e., a 'slow-light' effect [68, 216, 235]). Because the Bloch function for a guided mode near the band edge approaches a standing-wave, symmetric optical excitations can be induced in an array of trapped atoms, resulting in superradiant emission [18, 129] into the PCW. Superradiance has important applications for realizing quantum memories [4, 236–239], single photon sources [19, 240], laser cooling by way of cooperative emission [241, 242], and narrow linewidth lasers [243]. Related cooperative

This chapter is largely based on Ref. [233].

effects are predicted in nano-photonic waveguides absent an external cavity [126], including atomic Bragg mirrors [124] and self-organizing crystals of atoms and light [123, 202, 244].

Complimentary to superradiant emission is the collective Lamb shift induced by proximal atoms virtually exchanging off-resonant photons [245–248]. With the atomic transition frequency placed in a photonic band gap of a PCW, real photon emission is largely suppressed. Coherent atom-atom interactions then emerge as a dominant effect for QED with atoms in bandgap materials [84, 85, 87, 249–251]. Both the strength and length scale of the interaction can be 'engineered' by suitable band shaping of the PCW, as well as dynamically controlled by external lasers [87, 251]. Exploration of many-body physics with tunable and strong long-range atom-atom interactions are thereby enabled [87, 251].

In this chapter, we present an important advance for the field of waveguide QED. We describe an experiment that cools, stably traps, and interfaces multiple cold atoms along a quasi one-dimensional PCW. Through precise band edge alignment and guided-mode (GM) design, we achieve strong radiative coupling of one trapped atom and a GM of the PCW, such that the inferred single-atom emission rate into the GM is $\Gamma_{1\mathrm{D}}/\Gamma_0 = 1.1 \pm 0.1$, where $\Gamma_{1\mathrm{D}}$ is the peak single-atom radiative decay rate into the PCW guided mode and Γ_0 is the Einstein-A coefficient for free space. With multiple atoms, we observe superradiant emission in both time and frequency domains with measurements of transient decay following pulsed excitation and steady-state transmission spectra, respectively. We infer cooperative, superradiant coupling with rate $\bar{\Gamma}_{\mathrm{SR}}$ that scales with the mean atom number $\bar{N}$ as $\bar{\Gamma}_{\mathrm{SR}} = \eta\bar{N} \cdot \Gamma_{1\mathrm{D}}$ over the range $0.19 \lesssim \bar{N} \lesssim 2.6$ atoms, where $\eta = 0.34 \pm 0.06$.

7.2 Trapping atoms along the APCW

Our experimental platform is based on trapped cesium atoms near a 1D alligator photonic crystal waveguide (APCW) [193, 217]. The APCW is formed by two parallel SiN nanobeams separated by 238 nm with periodic corrugations at the outer edges (Fig. 7.1 (a)). The APCW consists of 150 identical unit cells with lattice constant $a = 371$nm (length $L \simeq 55.7\mu$m) and is terminated at either end by 30 tapered cells for mode matching to parallel nanobeams without corrugation. Photons can be coupled into and out of the APCW

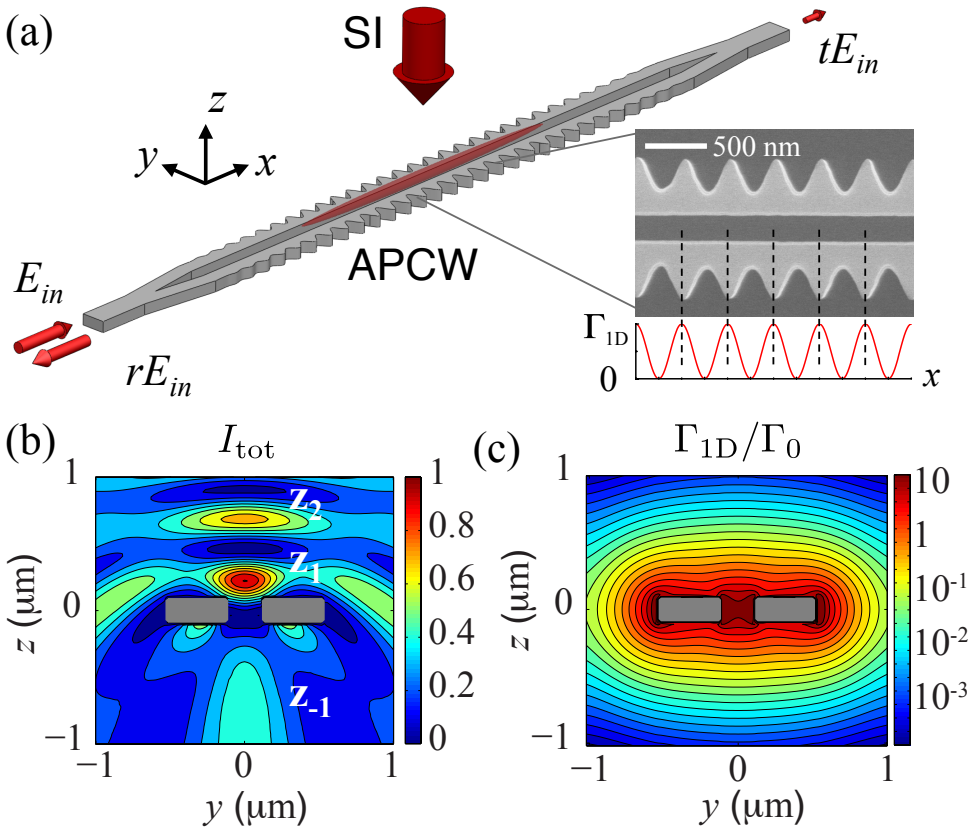

Figure 7.1: **Trapping and interfacing atoms with a 1D photonic crystal waveguide.** (a) A side-illumination (SI) beam is reflected from an 'alligator' photonic crystal waveguide (APCW) to form a dipole trap to localize atoms near the APCW (gray shaded structure). The red shaded region represents trapped atoms along the APCW. An incident field $E_{\rm in}$ excites the TE-like fundamental mode and thereby trapped atoms couple to this guided mode (GM). The transmitted $tE_{\rm in}$ and reflected $rE_{\rm in}$ fields are recorded. The inset shows an SEM image of the APCW and corresponding single-atom coupling rate $\Gamma_{\rm 1D}$ along the x axis at the center of the gap ($y = 0$). (b) Normalized intensity cross section of the total intensity $I_{\rm tot}$ resulting from the SI beam and its reflection, which form an optical dipole trap. Trap locations along the z axis at $y = 0$ are marked by z_i. Masked gray areas represent the APCW. (c) The single-atom coupling rate into the TE guided mode $\Gamma_{\rm 1D}(0, y, z)$ normalized to the free-space decay rate Γ_0 for the cesium D_1 line.

from conventional cleaved-fibers at either end of the structure. Design principles, fabrication methods, and device characterization of the APCW can be found in Section 7.5.1 [193, 217].

For the APCW used here, we align the band edge of the fundamental guided mode (electric field predominantly transverse-electric (TE) polarized in the plane of the waveguide) near the cesium D_1 line at 894.6 nm, with a mode-matched TE input field $E_{\rm in}$ tuned around the $6S_{1/2},\ F = 3 \rightarrow 6P_{1/2},\ F' = 4$ transition. Near the band edge, the atom-photon coupling rate is significantly enhanced by the group index n_g, as well as by reflections from the tapering regions that surround the APCW. From the measured transmission spectrum of the device absent atoms, we estimate a group index $n_g \simeq 11$ and an intensity enhancement $\mathcal{E}_I \sim 4$ from the

taper reflections, including the propagation loss (see details in Section 7.5.1).

To trap atoms along the APCW, we create tight optical potentials using the interference pattern of a side-illumination (SI) beam and its reflection from the surface of the APCW [40]. The polarization of the SI beam is aligned parallel to the x-axis of the 1D waveguide to maximize the reflected field. Figure 7.1(b) shows the calculated near-field intensity distribution in the y-z plane [252]. With a red-detuned SI beam, cold atoms can be localized to intensity maxima (e.g., positions z_{-1}, z_1, z_2 in Fig. 7.1(b)). However, because of the exponential falloff of the GM intensity, only those atoms sufficiently close to the APCW can interact strongly with guided-mode photons of the input field $E_{\rm in}$, Fig. 7.1(c). The trap site with the strongest atom-photon coupling is located at $(y_1, z_1) = (0, 220)$ nm, closest to the center of the unit cell and $\Delta z \sim 120$ nm from the plane of the upper surfaces of the APCW. Other locations are calculated to have coupling to the fundamental TE-like mode less than 1% of that for site z_1 (e.g., the sites at z_{-1}, z_2 have intensity ratios $I(z_{-1})/I(z_1) = 0.01, I(z_2)/I(z_1) = 0.005$).

Along the x axis of the APCW, the dipole trap $U(x, 0, z_1)$ is insensitive to the dielectric corrugation within a unit cell and is nearly uniform to within $< 2\%$ around the central region of the APCW. By contrast, atom emission into the fundamental TE-like mode is strongly modulated with $\Gamma_{\rm 1D}(x, 0, z_1) \simeq \Gamma_{\rm 1D} \cos^2(kx)$ due to the Bloch mode function near the band edge of the APCW ($k \approx \pi/a$), as shown in the inset of Fig. 7.1(a). Thus, even for atoms uniformly distributed along the x axis of the trapping potential, only those close to the center of a unit cell can strongly couple to the guided mode, greatly facilitating phase-matched symmetric excitation of the atoms. In our experiment, we have chosen a 50 μm waist for the SI beam to provide weak confinement along the x axis, with atoms localized near the central region ($\Delta x \simeq \pm 10$ μm) of the APCW for the estimated temperature $\sim 50\mu$K from a time-of-flight measurement in free space. The SI beam for dipole trapping is 220 GHz red-detuned with respect to the D_2 line and has a total power of 50 mW for all measurements reported.

Cold atoms from a MOT that surrounds the APCW [193] are loaded into the dipole trap during an optical molasses phase ($\sim$ 5 ms) and then optically pumped to $6S_{1/2}$, $F = 3$ for $\sim$1 ms. Atoms are held in the dipole trap for time $t_{\rm hold}$ relative to the end of the loading sequence, and then free-space absorption imaging is initiated over the interval ($t_{\rm hold},\ t_{\rm hold} + \Delta t_{\rm m}$) with $\Delta t_{\rm m} = 0.2$ ms. We introduce the measured time

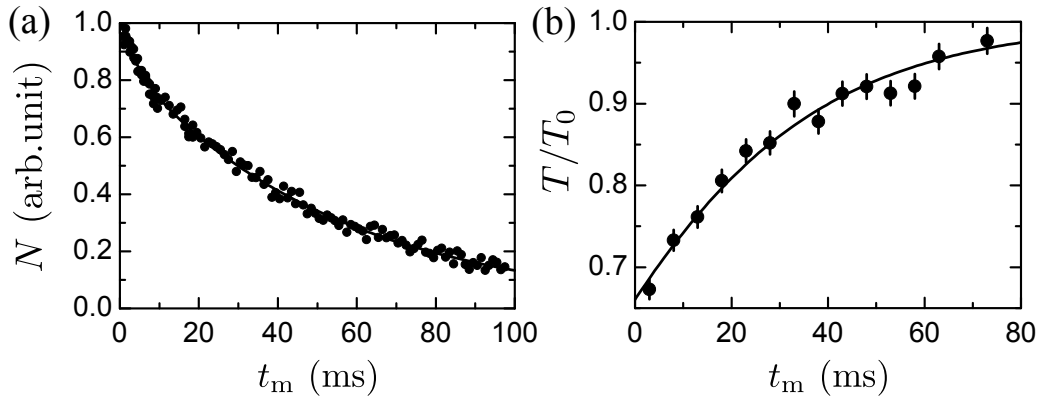

Figure 7.2: **Lifetime of trapped atoms near the APCW.** (a) $1/e$-lifetime of $\tau_{\rm fs} = 54 \pm 5$ ms is determined using free-space absorption imaging of the trapped atom cloud. (b) $1/e$-lifetime of $\tau_{\rm GM} = 28 \pm 2$ ms is observed from the normalized transmission T/T_0 of resonant GM probe pulses.

$t_{\rm m} = t_{\rm hold} + \Delta t_{\rm m}/2$, centered in the measurement window. As shown in Fig. 7.2(a), we measure a trap lifetime $\tau_{\rm fs} = 54 \pm 5$ ms and find a peak density $\rho_0 \approx 2 \times 10^{11}$ cm^{-3} near the APCW. The atom density ρ near the APCW can be adjusted over a wide range $0.06 \lesssim \rho/\rho_0 \leqslant 1$ by varying the duration of the MOT loading cycle while keeping all other procedures identical.

To determine the lifetime for trapped atoms near the APCW, we again hold atoms for $t_{\rm hold}$, and then launch $E_{\rm in}$ as a resonant GM probe in measurement interval $t_{\rm m} \pm \Delta t_{\rm m}/2$ with $\Delta t_{\rm m} = 5$ ms. From the recorded transmitted signals, we compute T/T_0, where T_0 is the transmission without atoms. During the probe period, we also apply free-space repump beams, tuned to the D_2, $6S_{1/2},\ F = 4 \rightarrow 6P_{3/2},\ F' = 4$ resonance, to remove population in the $6S_{1/2}$, $F = 4$, since the probe excites an open transition. Fig. 7.2(b) shows T/T_0 gradually recovering to $T/T_0 = 1$ as $t_{\rm m}$ increases, with a fit to the data giving a $1/e-$time of $\tau_{\rm GM} = 28 \pm 2$ ms (see details in Section 7.5.3). $\tau_{\rm GM}$ is consistently shorter than $\tau_{\rm fs}$ from free-space imaging, which might be attributed to increased heating from the stronger light intensity near the APCW, the effect of surface potentials, or outgassing from the silicon chip and structures that support the APCW. These contributions are being investigated in more detail.

7.3 Observation of superradiance for trapped atoms

Next, we describe our observations of superradiant emission in both time and frequency domains with measurements of transient decay following pulsed excitation and steady-state transmission spectra, respectively.

7.3.1 Superradiant emission in time domain

Our principal investigation of superradiance involves observation of the transient decay of emission from an array of atoms trapped along the APCW. For a collection of $N > 1$ atoms, superradiance is heralded by a total decay rate $\Gamma_{\rm tot} = \Gamma_{\rm SR} + \Gamma^{(1)}_{\rm tot}$ that is enhanced beyond the total rate of decay for one atom $\Gamma^{(1)}_{\rm tot} = \Gamma_{\rm 1D} + \Gamma'$. $\Gamma_{\rm SR}$ is the N-dependent superradiant rate operationally determined from $\Gamma_{\rm tot}$ and $\Gamma^{(1)}_{\rm tot}$. Here, Γ' is the radiative decay rate into all channels other than the TE-like GM of the APCW. We numerically evaluate $\Gamma'/\Gamma_0 \approx 1.1$ for an atom at the trap site z_1 in Fig. 7.1(b) along the APCW, with Γ_0 the free-space decay rate for the D_1 transition [216, 253]. Cooperative level shifts $|H_{\rm dd}| \ll \Gamma_{\rm 1D}$ are neglected for the current configuration of our experiment (see Section 7.5.2).

We record the temporal profiles of atomic emission into the fundamental TE-like GM following short-pulse ($\sim$10 ns FWHM), resonant excitations via $E_{\rm in}$. To ensure small population in the excited state, we choose a pulse intensity well below the saturation intensity ($I/I_{\rm sat} < 0.1$). After a time $t_{\rm hold}$ the excitation cycle is repeated every 500 ns for $\Delta t_{\rm m} = 6$ ms, and detection events are accumulated for the reflected intensity $|rE_{\rm in}|^2$ by an avalanche photodiode (APD). We consider decay curves of GM emission at $15\ {\rm ns} < t_{\rm e} < 70$ ns after the center of the excitation pulse (i.e., after the excitation pulse is sufficiently extinguished, $t_{\rm e} > 15$ ns, and while the background counts are negligible compared to the atomic emission, $t_{\rm e} \lesssim 70$ ns). The total decay rate $\bar{\Gamma}_{\rm tot}$ is extracted by simple exponential fits as shown in the inset of Fig. 7.3(a). The deviation from the exponential fit at $t_{\rm e} \gtrsim 60$ ns is due to the spatially varying coupling rate $\Gamma_{\rm 1D}\cos^2(kx)$, which is captured by a detailed model discussed later (see details in Section 7.5.4).

Enhanced total decay rate with increasing atom number is clearly evidenced in Fig. 7.3(a), where the atom number can be adjusted by varying trap hold time $t_{\rm hold}$ prior to the measurement. At the shortest measurement time $t_{\rm m} = 3$ ms with $t_{\rm hold} = 0$ ms (i.e., the maximum number of trapped atoms), the measured total decay rate is largest at $\bar{\Gamma}_{\rm tot}/\Gamma_0 \approx 2.9$. At $t_{\rm m} = 63$ ms much longer than the trap lifetime $\tau_{\rm GM} = 28 \pm 2$ ms,

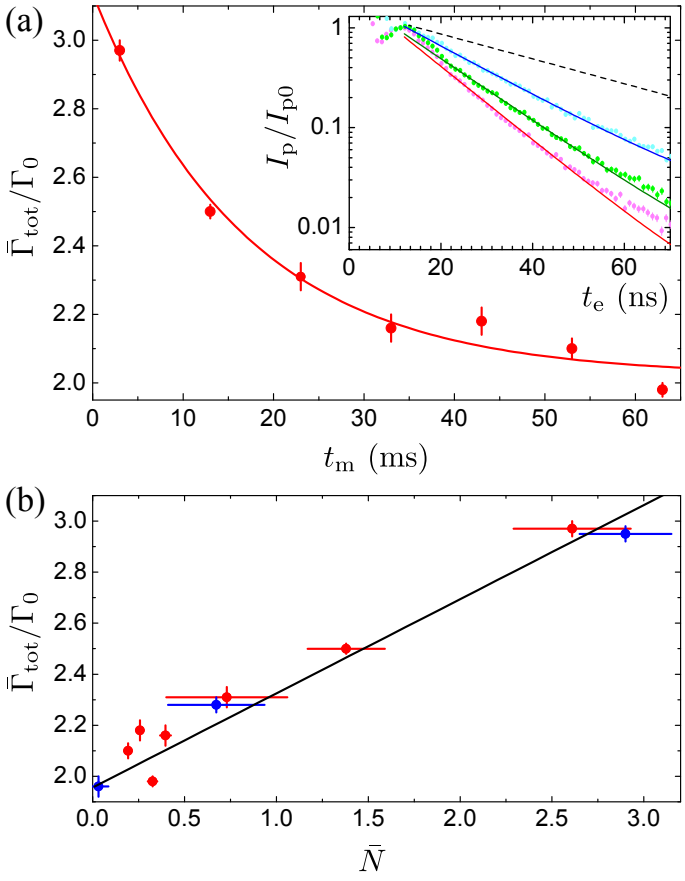

Figure 7.3: **Decay rate and atom number dependence.** (a) Fitted total decay rate $\bar{\Gamma}_{\rm tot}$ normalized with free-space decay rate Γ_0 (circles) as a function of measurement time $t_{\rm m}$. The solid line is a simple exponential fit to determine the superradiant decay rate $\bar{\Gamma}_{\rm SR}/\Gamma_0 = 1.1\pm0.1$ and the single-atom decay rate $\bar{\Gamma}^{(1)}_{\rm tot}/\Gamma_0 = 2.0\pm0.1$ with $\tau_{\rm SR} = 17 \pm 3$ ms. The inset shows the temporal profiles of normalized guided-mode emission $I_{\rm p}/I_{\rm p0}$ (circles) with $I_{\rm p0}$ the peak emission. Exponential fits (solid curves): $t_{\rm m} = 3$ ms (red), 13 ms (green), and 63 ms (blue). The black dashed curve shows a exponential decay with free-space decay rate Γ_0. (b) Fitted total decay rate $\bar{\Gamma}_{\rm tot}$ normalized with Γ_0 as a function of mean number of trapped atoms $\bar{N}$ from a detailed model (see Section 7.5.4). We adjust $\bar{N}$ by changing the trap hold time (red circles) or atom loading time (blue circles). The black line is a linear fit to the combined data sets, giving $\bar{\Gamma}_{\rm SR} = \eta \cdot \bar{N} \cdot \Gamma_{\rm 1D}$ with $\eta = 0.34 \pm 0.06$.

the total decay rate settles to $\bar{\Gamma}_{\rm tot}/\Gamma_0 \approx 2.0$. This asymptotic behavior suggests that $\bar{\Gamma}_{\rm tot}$ at long hold time corresponds to the single-atom decay rate $\bar{\Gamma}^{(1)}_{\rm tot}$.

To determine quantitatively the superradiant and single-atom emission rates from our measurements of decaying GM emission, we present two different analyses that yield consistent results. The first is a simple and intuitive analysis applied to Fig. 3(a) in which we employ an empirical exponential fit, $\bar{\Gamma}_{\rm tot}(t_{\rm m}) = \bar{\Gamma}_{\rm SR} e^{-t_{\rm m}/\tau_{\rm SR}} + \bar{\Gamma}^{(1)}_{\rm tot}$, with the superradiant $\bar{\Gamma}_{\rm SR}$, single-atom $\bar{\Gamma}^{(1)}_{\rm tot}$, and $\tau_{\rm SR}$ characterizing decay of superradiance due to the atom loss. The fit yields the maximum superradiant rate $\bar{\Gamma}_{\rm SR}/\Gamma_0 = 1.1 \pm 0.1$ with

$\tau_{\rm SR} = 17 \pm 3$ ms, and a reasonable correspondence to the measured decay rates $\bar{\Gamma}_{\rm tot}$, as shown by the red curve in Fig. 7.3(a). The asymptote $\bar{\Gamma}^{(1)}_{\rm tot}/\Gamma_0 = 2.0 \pm 0.1$ gives the total single-atom decay rate. With $\Gamma'/\Gamma_0 \approx 1.1$ determined numerically for an atom at trap site z_1 along the APCW (Fig. 7.1(b)), we deduce $\bar{\Gamma}_{\rm 1D}/\Gamma_0 = 0.9 \pm 0.1$ for the single-atom decay rate into the GM of the APCW.

To substantiate this simple empirical model, our second analysis is a detailed numerical treatment based upon transfer matrix calculations (see Section 7.5.4). Decay curves are generated for a fixed number of atoms N distributed randomly along the x-axis of the APCW with uniform probability density but with spatially varying coupling $\Gamma_{\rm 1D}(x) \simeq \Gamma_{\rm 1D}\cos^2(kx)$. These N-dependent, spatially-averaged decay curves are further averaged over a Poisson distribution with mean atom number $\bar{N}$, capturing the variation of atom number N as we repeat experiments for data accumulation. Fitting to this model, we extract $\Gamma_{\rm 1D}/\Gamma_0 = 1.1 \pm 0.1$ for measurements at long hold time (e.g., at $t_{\rm m} = 63$ms in Fig. 7.3(a)). Since the intensity of the fluorescence from a single atom is spatially modulated by $\cos^4(kx)$, only an atom near the center of a unit cell can strongly couple to the GM, resulting in the small difference between averaged $\bar{\Gamma}_{\rm 1D}$ and peak $\Gamma_{\rm 1D}$. Also, the decay curve for GM emission at $t_{\rm m} = 3$ ms can be well fitted with $\bar{N} = 2.6 \pm 0.3$ atoms. The red points in Fig. 7.3 (b) display the total decay rate $\bar{\Gamma}_{\rm tot}$ as a function of $\bar{N}$ extracted from fits of the transfer matrix model to the measured decay curves, which clearly shows that superradiance emission rate is proportional to $\bar{N}$.

The value $\Gamma_{\rm 1D}/\Gamma_0 = 1.1 \pm 0.1$ from our measurements agrees reasonably well with the theoretical value $\Gamma_{\rm 1D}/\Gamma_0 \approx 1.2$ determined by FDTD calculations [254], despite several uncertainties (e.g., locations of trap minima relative to the APCW with uncertainty below 10 nm). The agreement validates the absolute control of our fabrication process (including the negligible effect of loss and disorder along the APCW), as well as the power of the theoretical tools that have been developed [87, 216, 251].

We confirm that the variation of $\bar{\Gamma}_{\rm tot}$ in Fig. 7.3(a) is not due to the heating of atomic motion during the trap hold time. To see this, we adjust $\bar{N}$ via different MOT loading times and measure the decay rate at the shortest hold time ($t_{\rm m} = 3$ ms), as shown by blue points in Fig. 7.3(b) . These observations are consistent with those from varying the trap hold time (red points in Fig. 7.3(b)), and lead to an almost identical single-atom decay rate $\bar{\Gamma}^{(1)}_{\rm tot}/\Gamma_0 = 2.0 \pm 0.1$ at the shortest loading time, corresponding to $\rho/\rho_0 = 0.16$ and $\bar{N} \ll 1$.

The data and our analysis related to Fig. 7.3 strongly support the observation of superradiant decay for

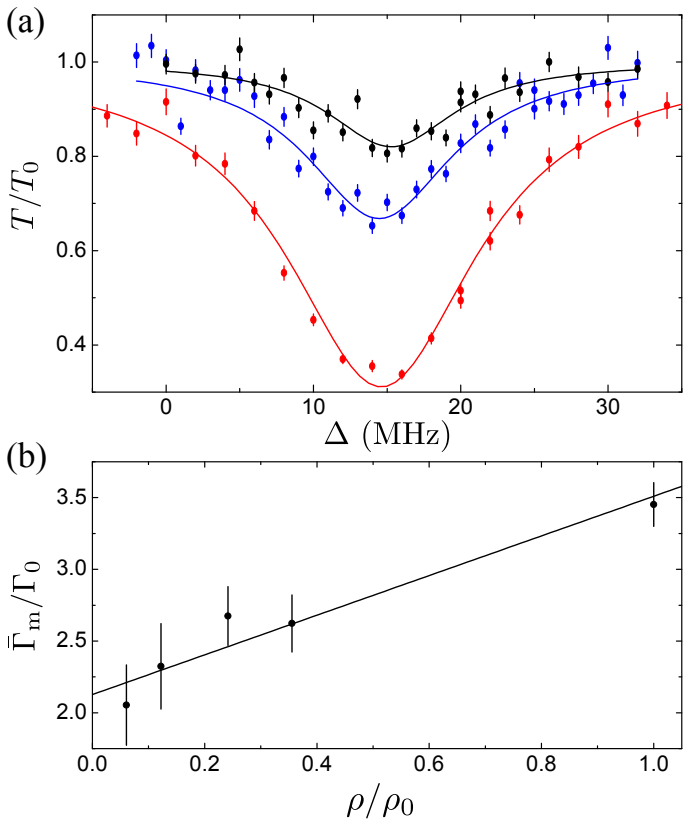

Figure 7.4: **Steady-state transmission spectra $T(\Delta)$ and fitted atomic linewidth $\bar{\Gamma}_{\rm m}$.** (a) $T(\Delta)$ with $\Delta = 0$ corresponding to the free-space line center. The three sets of points are measured at relative densities $\rho/\rho_0 = 0.12$ (black), 0.24 (blue), and 1 (red), where the transmission without atoms is T_0. Solid curves are Lorentzian fits to determine the linewidth $\bar{\Gamma}_{\rm m}$. Each point in the spectra is an average over 10 experiment repetitions. (b) Fitted linewidths (circles) normalized to Γ_0 as a function of ρ/ρ_0. The solid line is a linear fit with intercept of $\bar{\Gamma}_{\rm m}^{(1)}/\Gamma_0 = 2.1 \pm 0.1$.

atoms trapped along the APCW. Assuming $\bar{\Gamma}_{\rm tot} = \bar{\Gamma}_{\rm SR} + \bar{\Gamma}_{\rm tot}^{(1)}$ and fitting $\bar{\Gamma}_{\rm tot}$ linearly with $\bar{N}$, as shown in Fig. 7.3(b), we find that the superradiant rate is given by $\bar{\Gamma}_{\rm SR} = \eta \cdot \bar{N} \cdot \Gamma_{\rm 1D}$ with $\eta = 0.34 \pm 0.06$. The slope η is reduced below unity by the random distribution of atoms along the x-axis.

7.3.2 Superradiant emission in frequency domain

This observation of superradiant decay is complemented by line broadening for steady-state transmission spectra $T(\Delta)$ measured at $t_{\rm m} = 3$ ms with $\Delta t_{\rm m} = 5$ ms, as show in Fig. 7.4. The measured linewidths $\bar{\Gamma}_{\rm m}$ are significantly broader than the free-space width (FWHM) $\Gamma_0/2\pi = 4.56$ MHz [253], predominantly due to cooperative atomic coupling to the GM of the APCW. We also observe a significant drop in T/T_0 at line center due to strong atom-photon coupling. Indeed, in Fig. 7.4 (a), we measure $T/T_0 \simeq 0.30$ (i.e., a

70% attenuation of the GM flux $|E_{\rm in}|^2$) for maximum density ρ_0, and $T/T_0 \simeq 0.95$ at the lowest density investigated, $\rho/\rho_0 \approx 0.06$.

No clear density dependent shift is observed in Fig. 7.4(a), in support of our neglect of cooperative energy shifts $|H_{\rm dd}|$ (see Section 7.5.2). The shift in line center for $T(\Delta)$ from $\Delta = 0$ in free space to $\Delta = 14$ MHz for atoms trapped along the APCW is induced by the dipole trap. Furthermore, trapped atoms should suffer small inhomogeneous broadening in the spectra shown in Fig. 7.4, since the FORT shift is small (< 1 MHz) for the $6P_{1/2}, F = 4'$ excited state, and atoms are well localized around the trap center due to their low temperature $T \sim 50\mu$K, corresponding to a small range of light shifts $\lesssim$ 1MHz for atoms in the ground state.

In Fig. 7.4 (b), we plot the linewidths $\bar{\Gamma}_{\rm m}$ extracted from $T(\Delta)$ as a function of ρ/ρ_0. $\bar{\Gamma}_{\rm m}/\Gamma_0 \approx 3.4$ is largest at $\rho/\rho_0 = 1$, and reduces to $\bar{\Gamma}_{\rm m}/\Gamma_0 \approx 2.1$ at $\rho/\rho_0 = 0.06$. From linear extrapolation, the single-atom linewidth is estimated to be $\bar{\Gamma}^{(1)}_{\rm m}/\Gamma_0 = 2.1 \pm 0.1$. With inhomogeneous broadening absent, we expect that $\bar{\Gamma}^{(1)}_{\rm m} = \bar{\Gamma}_{\rm 1D} + \Gamma'$. With the calculated $\Gamma'/\Gamma_0 \approx 1.1$, the single-atom coupling rate can be simply deduced as $\bar{\Gamma}_{\rm 1D}/\Gamma_0 \approx 1.0 \pm 0.1$. A simple estimate of the maximum mean number of atoms then follows from $\bar{N}_{\rm m} = (\bar{\Gamma}_{\rm m}(\rho_0) - \Gamma')/\bar{\Gamma}_{\rm 1D} \simeq 2.4 \pm 0.4$ atoms. Note that $\bar{N}_{\rm m}$ is defined from $\bar{\Gamma}_{\rm m}(\rho) = \bar{N}_{\rm m}\bar{\Gamma}_{\rm 1D} + \Gamma'$ for an approximate estimate of the number of atoms.

7.4 Conclusion and outlook

In conclusion, we have used an integrated optical circuit with a photonic crystal waveguide to trap and interface atoms with guided photons. Superradiance for atoms trapped along our APCW has been demonstrated and a peak single-atom emission rate into the APCW of $\Gamma_{\rm 1D}/\Gamma_0 = 1.1 \pm 0.1$ inferred. Our current uniform trap along the APCW is a promising platform to study optomechanical behavior induced by the interplay between sizable single-atom reflectivity and large optical forces (e.g., self organization [202, 244]). By optimizing the power and detuning of an auxiliary guided mode field near the air band of the APCW, it should be possible to achieve stable atomic trapping and ground state cooling [225, 226] at trap sites centered within the vacuum gap, thereby increasing $\Gamma_{\rm 1D}$ five-fold [216]. Opportunities for new physics in the APCW arise by fabricating devices with the atomic resonance inside the band gap to induce long-range atom-atom interac-

tions [85, 87, 251], thereby enabling investigations of novel quantum transport and many-body phenomena.

7.5 Experimental details

7.5.1 Device characterization

A schematic of the alligator photonic crystal waveguide (APCW) is illustrated in Fig. 7.5(a). The waveguide is made from 200-nm thick stoichiometric SiN with refractive index $n = 2.0$ [217]. The dimensions of the nominal photonic crystals are the following: lattice constant $a = 371$ nm, gap $g = 238$ nm, width $w = 157$ nm, and tooth amplitude $A = 131$ nm, as shown in Fig. 7.5(b). The nominal photonic crystal section consists of $N_{\mathrm{cell}} = 150$ unit cells, terminated by 30 tapered cells on each side to provide 'mode-matching' to and from double nanobeams sections.

The APCW is characterized by measuring the transmission spectrum $T_0(\nu)$ without atoms. The resonant structure around frequencies ν_i displayed in Fig. 7.6 arises from reflections in the tapered sections at the two ends of the APCW. The free spectral range $\Delta\nu_i = \nu_{i+1} - \nu_i$ between resonances decreases as the band edge frequency ν_{BE} is approached, which is a signature of an increasing group n_g index near ν_{BE}, with $n_g \propto 1/\Delta\nu_i$ for an ideal structure.

Our experiment is operated around the frequency ν_A of the D_1: $6S_{1/2},\ F = 3 \rightarrow 6P_{1/2},\ F' = 4$ transition in atomic Cs, with ν_{BE} aligned near ν_A by absolute control of the fabrication process at a level of 10^{-3}. Fine tuning for $\nu_1 = \nu_A$ is achieved by way of a guided-mode (GM) heating beam with a wavelength

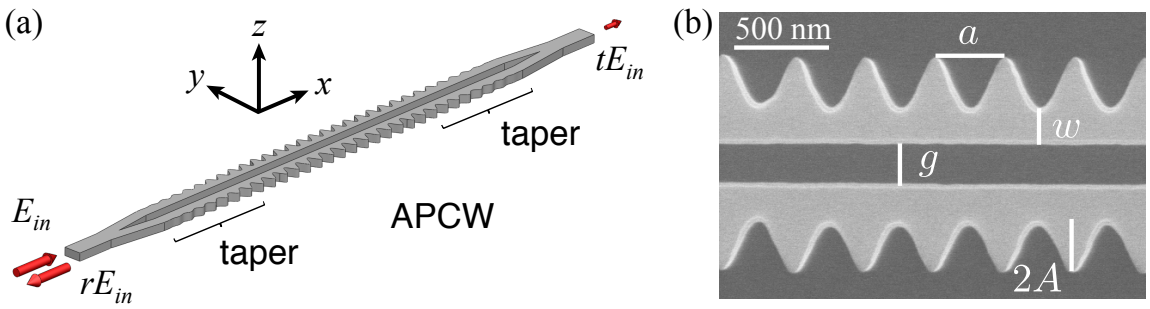

Figure 7.5: **Schematic of the APCW and an SEM image.** (a) An incident field E_{in} excites the TE-like fundamental mode, and the intensities fro the transmitted tE_{in} and reflected field rE_{in} are recorded for device characterization. (b) SEM image of APCW with lattice constant a, gap g, width w, and tooth amplitude A.

of 850 nm and optimum power, typically $P \geq 100\mu$W. In addition, we turn on a strong GM heating beam $\sim 700\mu$W input power and $\sim$ 2nm blue-detuned from D_2 transition for 100 ms at the end of each experimental cycle in order to keep the device clean by desorbing Cs from the APCW.

In order to estimate the group index n_g, single-taper reflectivity R_t, and intensity loss $e^{-2\zeta}$, we use a model based on the transfer matrix formalism for a periodic system to fit the transmission spectrum [122], which we now briefly describe. The dispersion relation for the wavevector $k(\nu)$ near the band edge is approximated by the fitting function [122],

$$k(\nu) = k_0 \left(1 - \sqrt{\frac{(\nu_0 - \nu(1+i\kappa))^2 - \Delta_g^2}{\nu_{\mathrm{F}}^2 - \Delta_g^2}} \right), \tag{7.1}$$

where the wavevector at the band edge is $k_0 = \pi/a$. Here, fitting parameters are the frequency at the center of the band gap ν_0, the size of the band gap $2\Delta_g$, the asymptotic group velocity far from the band edge $2\pi\nu_{\mathrm{F}}/k_0$, and the loss parameter κ. The loss parameter κ comes from using perturbation theory to add a small imaginary component to the dielectric constant of the material, resulting in an imaginary propagation constant that is approximately given by

$$\mathrm{Im}[k(\nu)] \approx \frac{2\pi\nu}{v_{\mathrm{g}}}\kappa. \tag{7.2}$$

It provides a convenient way to model losses that scale with inverse group velocity.

Next we consider the weak cavity formed by the taper reflections R_t. The single-pass phase accumulation ϕ and single-pass power transmission $e^{-2\zeta}$ through the cavity are written by

$$\phi = N_{\mathrm{cell}} a\, \mathrm{Re}[k] \quad \text{and} \quad \zeta = N_{\mathrm{cell}} a\, \mathrm{Im}[k], \tag{7.3}$$

where N_{cell} is the number of unit cells of the APCW and a is the lattice constant. Then, the transmission through a symmetric cavity with mirrors R_t is given by

$$T_{\text{cavity}} = \frac{1}{1 + \mathcal{L} + F\sin^2[\phi]}, \tag{7.4}$$

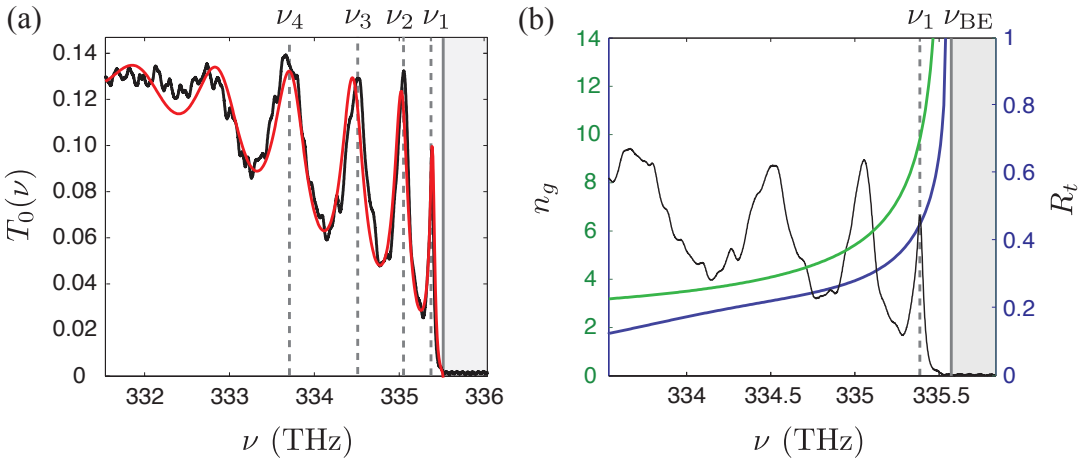

Figure 7.6: **Transmission spectra of the APCW and fitted group index n_g.** (a) Measured transmission spectrum $T_0(\nu)$ for the APCW (black) around the edge of the dielectric band and the model fit (red). The dashed lines mark the resonant frequencies ν_i from reflections in the taper sections and the solid line marks the band edge frequency ν_{BE}. (b) Estimated group index n_g (green) and taper reflection R_t (blue) from the fitted model. For the reference, the transmission spectrum $T_0(\nu)$ is overlaid. At the first resonance ν_1 marked by the dashed line, the group index is $n_g \approx 11$, and the taper reflection is $R_t \approx 0.48$.

where the coefficient F and loss coefficient $\mathcal{L}$ are given by

$$\mathcal{L} = \frac{\left(1 - R_t\, e^{-2\zeta}\right)^2}{e^{-2\zeta}\,(1 - R_t)^2} - 1 \quad \text{and} \quad F = \frac{4R_t}{(1 - R_t)^2}. \tag{7.5}$$

In order to fit this model to the measured transmission spectrum, first we use the dispersion model (Eq. (7.1) with $\kappa = 0$) to fit the positions of the cavity resonances. Second, we fit Eq. (7.4) with no loss ($\mathcal{L} = 0$) to the transmitted spectrum by using the fitted dispersion model to find ϕ and by using a fitting function for F [122], namely

$$(F)^{-1/2} = A_1(\mathrm{d}\nu/\Delta_g) + A_2(\mathrm{d}\nu/\Delta_g)^2 + A_3(\mathrm{d}\nu/\Delta_g)^3, \tag{7.6}$$

where $d\nu$ is the distance in frequency from the band edge. Finally, we find the loss parameter ζ that makes the on-resonant peak heights of the model best match our measurement.

Figure 7.6 (a) shows the measured transmission spectrum (black curve), overlaid with the model fit (red curve). The fitted parameters for the dispersion model are $2\Delta_g$ = 14.44 THz, ν_{F}/ν_0 = 0.60, and ν_0 = 342.8 THz. The fitted parameters for F are A_1 = 9, A_2 =-48, and A_3 = 128. The fitted loss parameter is $\kappa = 1.5 \times 10^{-5}$. At the first resonance ν_1, the model linewidth is 55 GHz, in reasonable agreement with the

measured linewidth of 66 GHz. The fitted dispersion relation is used to estimate the group index, and the fitted cavity model is used to estimate R_t and the single pass transmission $e^{-2\zeta}$, as shown in Fig. 7.6 (b). At the first resonance, the group index is $n_g \approx 11$, and the single-pass transmission is $e^{-2\zeta} \approx 0.89$, the taper reflection is $R_t \approx 0.48$, resulting in a peak intensity enhancement $\mathcal{E}_I \approx 4$ including the propagation loss [122]. Since the propagation loss in the APCW is reasonably small, we ignore the loss in our analysis in the following sections.

7.5.2 Finite different time domain calculations for collective coupling rates

Due to strong coupling to the TE-like GM in the APCW, trapped atoms experience both enhanced atomic decay rates as well as collective Lamb shifts. To estimate the size of these effects, we perform FDTD calculations and Fourier analysis as described in Ref. [216] to obtain the two-point Green's tensor $\mathbf{G}(\mathbf{r}_1, \mathbf{r}_2, \omega)$ for the APCW shown in Fig. 7.5. We then evaluate dissipative and coherent coupling rates, respectively, as [255–257]

$$\Gamma(\mathbf{r}_1, \mathbf{r}_2) = \frac{2\mu_0\omega_a^2}{\hbar}\mathbf{d}\cdot\mathrm{Im}[\mathbf{G}(\mathbf{r}_1, \mathbf{r}_2, \omega_a)]\cdot\mathbf{d} \tag{7.7}$$

$$J(\mathbf{r}_1, \mathbf{r}_2) = -\frac{\mu_0\omega_a^2}{\hbar}\mathbf{d}\cdot\mathrm{Re}[\mathbf{G}_{sc}(\mathbf{r}_1, \mathbf{r}_2, \omega_a)]\cdot\mathbf{d}, \tag{7.8}$$

where $\mathbf{d}$ is the transition dipole moment, ω_a the transition frequency, μ_0 the vacuum permeability, and $\hbar$ Planck's constant divided by 2π. Here, $\mathbf{G}_{sc} = \mathbf{G} - \mathbf{G}_0$ is the scattering Green's tensor, in which the vacuum contribution $\mathbf{G}_0$ is subtracted from the total Green's tensor $\mathbf{G}$; $\mathrm{Im}[.]$ and $\mathrm{Re}[.]$ represent imaginary and real parts, respectively. The coupling rate $\tilde{\Gamma} = \Gamma/2 + iJ$ controls collective excitation dynamics of trapped atoms along the APCW.

We obtain single-atom rates by setting $\mathbf{r}_1 = \mathbf{r}_2 = \mathbf{r}_a$ at the location of a trapped atom, and evaluate the single-atom total decay rate $\Gamma^{(1)}_{\mathrm{tot}}(\nu_a) = \Gamma(\mathbf{r}_a, \mathbf{r}_a, \nu_a)$ and excited state level shift $J^{(1)}(\nu_a) = J(\mathbf{r}_a, \mathbf{r}_a, \nu_a)$. Figure 7.7(a) shows the calculation for $\mathbf{r}_a = (0, 0, z_1)$ nm at the center of the trap shown in Fig. 7.1(b). Here the total decay rate $\Gamma^{(1)}_{\mathrm{tot}} = \Gamma_{1\mathrm{D}} + \Gamma'$ (black curve) includes the contribution from the GM of interest ($\Gamma_{1\mathrm{D}}$), which strongly depends on the atomic resonant frequency $\nu_a = \omega_a/2\pi$ and position r_a, as well as the coupling

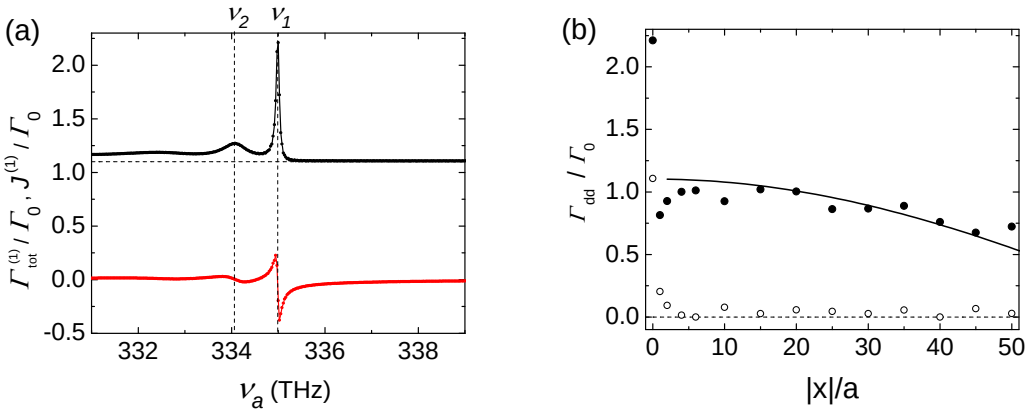

Figure 7.7: **Calculated total decay rate of a single atom and cooperative decay rate of two atoms.** (a) Single-atom decay rate $\Gamma^{(1)}_{\rm tot}$ (black circles) and excited state level shift $J^{(1)}$ (red circles) at $\mathbf{r}_a = (0, 0, z_1)$ nm. Vertical dashed lines mark the frequencies of the first two guided mode resonances, ν_1 and ν_2, near the band gap (frequency range $\nu_a \gtrsim \nu_{\rm BE} = 335.5$ THz where $\Gamma_{\rm tot}$ appears constant) that are supported by the finite length of the APCW. Horizontal dashed line indicates $\Gamma'/\Gamma_0 = 1.1$, estimated from the constant $\Gamma^{(1)}_{\rm tot}$ in the band gap region. (b) Dissipative coupling rate $\Gamma_{\rm dd}(x) \equiv |\Gamma(\mathbf{r}_a, \mathbf{r}_a + x\hat{\mathbf{x}})|$ between two trapped atoms separated by x, with their resonant frequencies at either $\nu_a = \nu_1$ (solid circles) or $\nu_a = 336$ THz $> \nu_{\rm BE}$ inside the band gap (open circles), respectively. Solid line is an analytical calculation considering actual finite size of the APCW (Fig. 7.5).

rate to all other modes (Γ'). Γ' can be estimated from $\Gamma^{(1)}_{\rm tot}(\nu_a)$ inside the band gap ($\nu_a \gtrsim \nu_{\rm BE}$); $\Gamma'/\Gamma_0 \approx 1.1$ remains constant over a broad frequency range. Coupling rate to the TE-like GM, $\Gamma_{\rm 1D} = \Gamma^{(1)}_{\rm tot} - \Gamma'$, can be obtained from this analysis with $\Gamma_{\rm 1D}/\Gamma_0 = 1.2$.

In Fig. 7.7 (a), we calculate a small excited state level shift $|J^{(1)}|/\Gamma_0 < 0.4$ over a frequency range around $\nu_1 = 335$ THz. For our experimental configuration, with $\nu_a \approx \nu_1$, we find $|J^{(1)}(\nu_a)|/\Gamma_0 \sim 0$. This also suggests that the collective level shift for two trapped atoms, $|H_{\rm dd}(x)| \equiv |J(\mathbf{r}_a, \mathbf{r}_a + x\hat{\mathbf{x}})| \ll (\Gamma_0, \Gamma_{\rm 1D})$, is negligible, where x is the atomic separation. Indeed, we do not see clear evidence of N-dependent level shifts in the steady-state transmission spectra shown in Fig. 7.4 (a).

Figure 7.7 (b) shows $\Gamma_{\rm dd}(x) \equiv |\Gamma(\mathbf{r}_a, \mathbf{r}_a + x\hat{\mathbf{x}})|$ for two trapped atoms located at the center of unit cells ($x/a \in \mathbb{Z}$) and with resonant frequencies at $\nu_a = \nu_1$ or $\nu_a > \nu_{\rm BE}$ inside the band gap, where $\Gamma^{(1)}_{\rm tot} - \Gamma' \sim 0$. For $|x| > a$, $\Gamma_{\rm dd}(x)$ can be used to estimate the dissipative coupling rate between two atoms. When $\nu_a = \nu_1$ and $|x|/a > 2$, $\Gamma_{\rm dd}(x)$ slowly drops from $\Gamma_{\rm dd}(0) - \Gamma' = 1.2\ \Gamma_0$ to smaller values as $|x|$ becomes comparable to the size of the APCW (black circles). This is caused by interference with reflections from the tapering regions surrounding the APCW. Solid line in Fig. 7.7(b) shows an analytical

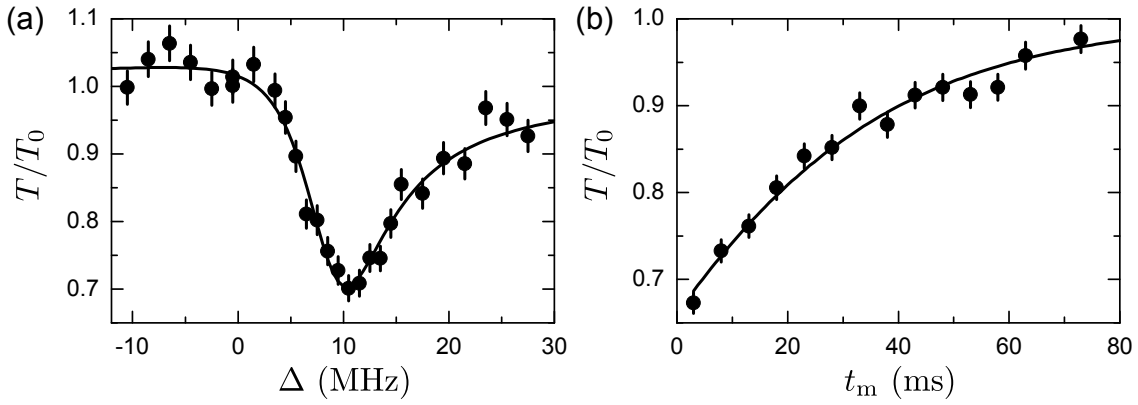

Figure 7.8: **Lifetime measurements of trapped atoms along the APCW.** (a) Normlaized transmission spectrum. Black curve shows the fit to Eq. (7.9) at $t_{\rm m} = 2.5$ ms with $\theta = -0.6 \pm 0.1$, $C_0 = 0.24 \pm 0.1$, $\Gamma = 8.2 \pm 0.6$ MHz and $\Delta_0 = 9.3 \pm 0.3$ MHz. (b) Normalized transmission T/T_0 as a function of the holding time, measured by the on resonant guided-mode probe with $\Delta = 10.5$ MHz. By fitting the measured data to Eq. (7.9) with fitted parameters extracted in Fig. 7.8 (a), we obtain the lifetime of $\tau_{\rm GM} = 28 \pm 2$ ms (black curve).

calculation $\Gamma_{\rm dd}(x) = (\Gamma_{\rm dd}(0) - \Gamma')\cos(\pi|x|/N_{\rm eff}a)$ that compares to the numerical result, where the fitted effective number of cells $N_{\rm eff} = 162 \pm 9$ is larger than $N_{\rm cell}$ due to the leakage of the fields into the taper regions. Small variations between the analytical and numerical calculations are due to residual coupling via other channels. On the other hand, when $\nu_a > \nu_{\rm BE}$ inside the band gap, $\Gamma_{\rm dd}(x)$ quickly drops below $0.1\Gamma_0$ at $|x|/a > 2$. This is expected because, inside the band gap, atoms can only cooperatively decay via photonic channels that contribute to Γ', which are either weakly-coupled or are lost quickly into freepace within distances $|x| < 2a$.

7.5.3 Lifetime of trapped atoms along the APCW

To characterize the lifetime of trapped atoms near the APCW, we measure the normalized transmission T/T_0 as a function of the measurement time $t_{\rm m}$, as shown in Fig. 7.2 and replotted in Fig. 7.8. During the lifetime measurement, the frequency ν_a of the D_1 transition for the probe field $E_{\rm in}$ is located between the first and second taper resonances, which leads to the dispersive spectrum shown in Fig 7.8 (a). In order to estimate the lifetime of the trap with off resonant cavity, we employ the steady-state equation [258],

$$T/T_0 = (1+\theta^2)/\left[\left(1+\frac{2C(t_{\rm m})}{1+\delta_{\rm m}^2}\right)^2 + \left(\theta - \frac{2C(t_{\rm m})\delta_{\rm m}}{1+\delta_{\rm m}^2}\right)^2\right], \tag{7.9}$$

where the normalized detuning from the light shifted resonance Δ_0 is $\delta_{\rm m} = \frac{\Delta-\Delta_0}{\Gamma}$, the cooperativity parameter is $C(t_{\rm m}) = C_0 \exp(-t_{\rm m}/\tau_{\rm GM})$ with peak cooperatively C_0, lifetime $\tau_{\rm GM}$, and normalized detuning from taper resonance θ. First, we fit the measured spectrum at $t_{\rm m} = 2.5$ ms to Eq. (7.9) and obtain the fitted parameters, $\theta = -0.6 \pm 0.1$, $C_0 = 0.24 \pm 0.1$, $\Gamma = 8.2 \pm 0.6$ MHz and $\Delta_0 = 9.3 \pm 0.3$ MHz as shown in black curve in Fig. 7.8 (a). Then, to estimate the lifetime $\tau_{\rm GM}$, the measured data for $\Delta = 10.5$ MHz in Fig. 7.8 (b) are fitted to Eq. (7.9) with fitted parameters from Fig. 7.8 (a). We obtain the lifetime of $\tau_{\rm GM} = 28 \pm 2$ ms shown in black curve in Fig. 7.8 (b).

7.5.4 Model for superradiance of trapped atoms

Our model of superradiance of trapped atoms is obtained by including transfer matrices for atoms in the device model described in Section 7.5.1 [74, 122–124]. Since the first resonance of the taper reflections is aligned to the D_1 transition for the probe $E_{\rm in}$, the wavevector of the probe mode is $k = \left(1 - \frac{1}{N_{\rm eff}}\right)\frac{\pi}{a}$ with number of cells $N_{\rm eff}$, and the probe field inside the unit cell forms a nearly perfect standing wave due to the Bloch-periodic function. In addition, atoms are trapped near the central region of the APCW along the x axis ($\Delta x = \pm 10$ μm). Thus, we ignore the dephasing between atoms and envelope from the taper reflections due to the small mismatch of the wavevector $\Delta k = \frac{1}{N_{\rm eff}}\frac{\pi}{a}$ relative to $k_0 = \frac{\pi}{a}$ at the band edge. In the following, we set the wavevector $k = k_0 = \frac{\pi}{a}$ and will discuss effects due to the Δk mismatch later.

The reflection of N atoms randomly distributed at the location x_i with the coupling rate $\Gamma_{\rm 1D}\cos^2(kx_i)$ is given by,

$$r_N(\delta) = \frac{i\xi_N}{1 - i\xi_N} \qquad \text{where} \qquad \xi_N = -\frac{\xi_0}{i+\delta}\sum_i \cos^2(kx_i)\,, \tag{7.10}$$

where the single-atom fractional coupling rate is $\xi_0 = \Gamma_{\rm 1D}/\Gamma'$ and normalized detuning is $\delta = 2\Delta/\Gamma'$ with $\Gamma'/\Gamma_0 \approx 1.1$ from the numerical simulation in Section 7.5.2 [216]. The temporal profile of superradiance from N atoms is obtained by Fourier transforming $r_N(\delta)$ to yield $r_N(t)$, and taking the convolution of $r_N(t)$ with a Gaussian pulse of the half width $\sigma \sim 5$ ns for the excitation pulse $E_{\rm in}(t)$. Furthermore, the temporal

profile at $t > 2\sigma$ can be approximated by

$$I_{r_N^{\rm conv}}(t) = |r_N^{\rm conv}(t)|^2 \propto \left(\Gamma_{\rm 1D}\sum_i \cos^2(kx_i)\right)^2 \cdot \exp\left[-\left(\sum_i \Gamma_{\rm 1D}\cos^2(kx_i) + \Gamma'\right)t\right]. \quad (7.11)$$

Considering the assumed random locations of atoms with uniform probability density in the unit cells along x, the spatially averaged temporal profile is obtained by integrating Eq. (7.11) along x, yielding

$$\begin{aligned}\mathcal{I}_N(t) &= \gamma^2 e^{-(N\gamma+\Gamma')t}\cdot I_0(\gamma t)^{N-2}\cdot \\ &\left[\frac{N(N+1)}{4}I_0(\gamma t)^2 - \left(\frac{N}{4\gamma t}+\frac{N^2}{2}\right)I_0(\gamma t)\,I_1(\gamma t) + \frac{N(N-1)}{4}I_1(\gamma t)^2\right], \quad (7.12)\end{aligned}$$

where $I_k(z)$ is a modified Bessel function of the first kind and $\gamma = \Gamma_{\rm 1D}/2$. In addition, the number of trapped atoms along the APCW is drawn from a Poisson distribution $p(\bar{N}, N)$ with mean number of atoms $\bar{N}$. The total decay curve then becomes

$$\mathcal{I}_{\rm tot}(t) = c_0 \sum_N p(\bar{N}, N)\cdot \mathcal{I}_N(t) + \mathcal{I}_{\rm BG}, \quad (7.13)$$

where c_0 is a constant. Here, the background intensity $\mathcal{I}_{\rm BG}$ is measured separately without atoms and is given by the black circles in Fig. 7.9. As shown in Fig. 7.3, the total decay rate asymptotes to $\bar{\Gamma}_{\rm tot}^{(1)}/\Gamma_0 = 2.0 \pm 0.1$ at the longer hold times, which suggests that atomic decay at $t_{\rm m} = 63$ ms mostly originates from a single atom for mean atom number $\bar{N} \ll 1$. Thus, we fit the decay curve at $t_{\rm m} = 63$ ms to Eq. (7.12) with $N = 1$, and obtain $\xi_0 = \Gamma_{\rm 1D}/\Gamma' = 1.0 \pm 0.1$ shown in Fig. 7.9 (a). Then, by using the fitted ξ_0, the shortest hold time data ($t_{\rm m} = 3$ ms) is reasonably well fitted to Eq. (7.13) with $\bar{N} = 2.6 \pm 0.3$, as shown in Fig. 7.9 (b).

We also numerically estimate the contribution of the envelope from the taper reflections and dephasing between atoms along the APCW. We employ the transfer matrix model with $k = k_0 - \Delta k$, which includes the coupling rate $\Gamma_{\rm 1D}(x) \simeq \Gamma_{\rm 1D}^{(0)}\cos^2(k_0 x)\cos^2(\Delta k x)$ along the x-axis of the APCW and propagation phase $\Delta k \cdot \delta x$ between atoms separated by δx. Here, $\Gamma_{\rm 1D}^{(0)}$ denotes the peak coupling rate of both the unit cell and the envelope from taper reflections. The position of the atoms is generated from a normal distribution with $\sigma_x = 10$ μm at the temperature of 50μK. Then we numerically generate the decay curve and extract the total

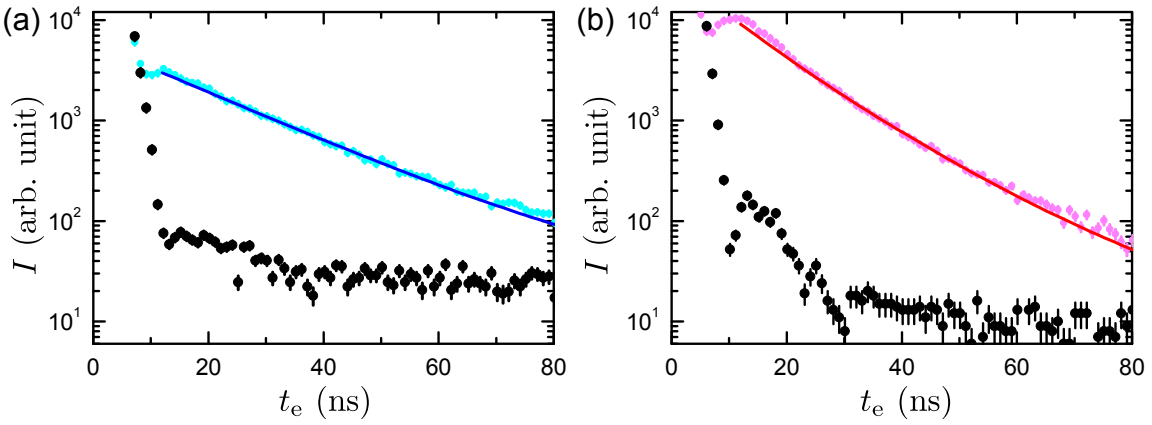

Figure 7.9: **Atomic emission into the GM and the model fit.** (a) Temporal profiles of atomic emission into the GM at $t_m = 63$ ms with and without atoms, shown in cyan and black circles, respectively. The blue curve shows Eq. (7.12) fitted for a single atom with $\Gamma_{1D}/\Gamma' = 1.0 \pm 0.1$. (b) Temporal profiles of atomic emission into the GM at $t_m = 3$ ms with and without atoms, shown in pink and black circles, respectively. The red curve shows Eq. (7.13) fitted to yield with $\bar{N} = 2.6 \pm 0.3$. The background level of (a) is higher than (b) due to the drift of the intensity modulator during the 5 times longer data accumulation time.

decay rate, suggesting that Γ_{1D} extracted from Eq. (7.12) with $N = 1$ is underestimated by $\sim 10\%$ and $\bar{N}$ from the fits to Eq. (7.13) by $\sim 15\%$. Note that we do not incorporate these corrections in our estimation of Γ_{1D} and $\bar{N}$, since the temperature of the atoms trapped along the APCW could be different from the measured temperature in free space. Indeed, the calculated trap potential combined with Casimir-Polder potential suggests that atoms trapped along the APCW could be much colder ($\lesssim 20$ μK) than the measured temperature for the free-space FORT (~ 50 μK) due to the smaller trap depth near the APCW, leading to a smaller correction of Γ_{1D} and $\bar{N}$ due to tighter localization of the atoms around the center of the APCW. The distribution of atoms along the APCW is being investigated in more detail.

To support our assumption of $\bar{N}$-dependent superradiance, $\bar{\Gamma}_{tot} = \bar{\Gamma}_{SR} + \bar{\Gamma}_{1D}$ with $\bar{\Gamma}_{SR} = \eta \cdot \bar{N} \cdot \Gamma_{1D}$, we generate the decay curve from Eq. (7.13) with $\Gamma_{1D}/\Gamma_0 = 1.0$ and various $\bar{N}$, and extract $\bar{\Gamma}_{tot}$ by fitting to an exponential. The dashed curve in Fig. 7.10 shows the calculated $\bar{\Gamma}_{tot}$, overlaid with measured hold time (red circles) and loading time (blue circles) dependence and the linear fit (solid black line). Although the dashed curve generated from the model deviates from the linear dependence at $\bar{N} < 1$, the linear fit captures the $\bar{N}$ dependence reasonably well. As clearly seen in the inset of Fig. 7.10, the nonlinear dependence on $\bar{N}$ at $\bar{N} \ll 1$ is due to the "conditional" character of decay rate measurements, meaning that the decay curve consists mostly of fluorescence from a single atom, despite $\bar{N} \ll 1$. Due to the negligible background counts

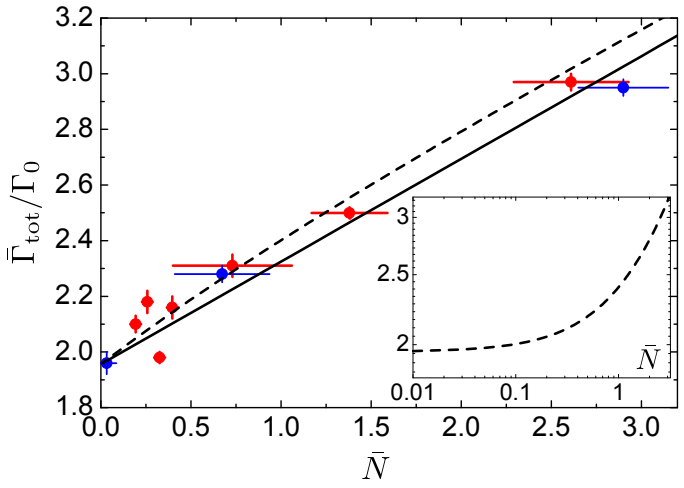

Figure 7.10: **Fitted total decay rate $\bar{\Gamma}_{\rm tot}$ normalized by Γ_0 as a function of the mean number of trapped atoms $\bar{N}$.** The dashed curve shows the calculated $\bar{\Gamma}_{\rm tot}$ from the model, overlaid with results measured for various hold times (red circles) and for loading times (blue circles). A linear fit to the combined data (solid black line) gives $\bar{\Gamma}_{\rm SR} = \eta \cdot \bar{N} \cdot \Gamma_{\rm 1D}$ with $\eta = 0.34 \pm 0.06$. The inset shows a log-log plot of the curve generated from the model.

in our measurements, single detection events at $\bar{N} \ll 1$ herald the presence of single atoms.

The linear fit to the combined data sets gives $\bar{\Gamma}_{\rm SR} = \eta \cdot \bar{N} \cdot \Gamma_{\rm 1D}$ with $\eta = 0.34 \pm 0.06$, consistent with the model for $\bar{N} \gtrsim 0.7$. A qualitative understanding of this value of η is the following. Due to the random distribution of atoms along the APCW, the intensity of atomic emission into the GM is spatially modulated by $\cos^4(kx)$ as shown in Eq. (7.11), meaning that both GM excitation of atoms and emission into the GM are proportional to $\cos^2(kx)$, resulting in $\cos^4(kx)$ dependence. With the spatial averaging along the x-axis of the APCW, the superradiant decay rate is then reduced by a factor of roughly $\eta \sim 3/8$ (i.e., the average of $\cos^4(kx)$ over a unit cell).

Chapter 8

Outlook

After exploring several systems, we believe that photonic crystal devices have a great potential endowed by the capabilities for dispersion and modal engineering. Most recently, we have achieved a rudimentary but crucial first step of observing a dissipative cooperative effect, superradiance, mediated by guided photons near the band edge of the PCW. The next important step is to demonstrate a dispersive cooperative effect, dipole-dipole interaction, mediated by exchange of virtual photons inside the band gap. These cooperative effects provide two major directions this project could take.

The first promising direction is to study many-body physics with strongly correlated photons, inspired by recent progress in quantum simulation realized with ultracold atoms [259] and ions [260]. Recently, there have been many efforts to introduce strong long-range dipole-dipole interactions by using ultracold polar molecules [261], dipolar atoms [262, 263], and Rydberg atoms [264]. While the interaction strengths in those systems are determined by atomic properties, the capabilities for dispersion engineering in PCWs enable the creation of dipole-dipole interactions whose range and strength are tunable [87, 251].

Another direction is the application to quantum information processing. Instead of minimizing the coupling to the environment, engineering the interaction with the reservoir can induce quantum correlations between atoms with dissipation. In contrast to DLCZ protocol, this dissipation-based approach is deterministic and unconditional, and has been experimentally proven to be advantageous to generate entanglement between atomic ensembles [265]. Recent proposals are predicted to yield steady-state entanglement under continuous pumping due to the dissipative collective coupling mediated by guided photons [266–268].

Appendix A

Atom-light interaction along a 1D waveguide

A.1 Hesienberg-Langevin equations and input-output relation

Here, we briefly describe the basic formalism for the atoms coupled to the waveguide as discussed in Ref [74, 124, 125, 202, 269–273]. Specifically, to calculate the mean values of atomic operators using the Heisenberg-Langevin equations, the strategy is to write down the equations of motion for both atomic and photonic operators, and then to integrate out the photonic degree of freedom, yielding a set of first-order differential equations for only atomic operators. Then, one can solve the coupled equations and obtain the steady-state values of the atomic response. Substituting these values back into the formal solution of the field gives the photonic response. We briefly describe the derivation in the following. The evolution of N atoms is described by a master equation for the density operator ρ,

$$\dot{\rho} = \frac{1}{i\hbar}\left[H, \rho\right] + L[\rho], \tag{A.1}$$

where the Hamiltonian is composed of a term denoting the energy levels of the atoms $H_{\rm atom}$, freely propagating photons in a waveguide $H_{\rm ph}$, and the interaction between guided-mode photons and atoms $H_{\rm int}$,

$$\begin{aligned} H &= H_{\rm atom} + H_{\rm ph} + H_{\rm int} \\ &= \sum_j \hbar\omega_0 \sigma_{ee}^j + \int dk \hbar\omega_k a_k^\dagger a_k + \sum_j \int dk \hbar g_k \left(\sigma_{eg} a_k e^{ikx_j} + \text{h.c.}\right), \end{aligned} \tag{A.2}$$

with the dipole-coupling amplitude $g_k = d\sqrt{\frac{\omega_k}{4\pi\varepsilon_0\hbar A_{\rm m}}}$ assumed to be identical for all atoms, while phases depend on the position of atoms. The Lindblad term is given by,

$$L[\rho] = -\frac{\Gamma'}{2}\sum_j \left(\sigma_{eg}^j\sigma_{ge}^j\rho + \rho\sigma_{eg}^j\sigma_{ge}^j - 2\sigma_{ge}^j\rho\sigma_{eg}^j\right), \tag{A.3}$$

where Γ' is the decay rate into all the channels other than the related guided mode.

First, we linearize the dispersion relation of the photon in the waveguide around the atomic frequency ω_0 with the corresponding wave vector $\pm k_0$. One approximates ω_k around $\pm k_0$ as $\omega_k \approx v_g|k_{R/L}|$, where R and L denote a right-going and left-going mode. Since we are only interested in a narrow bandwidth in the vicinity of the atomic transition ω_0, we can extend the range of $k_{R/L}$ to $(-\infty, +\infty)$ and replace g_k by a constant g. For later convenience, we introduce the field operators in real space by Fourier transformation,

$$a_{k_{R(L)}} = \frac{1}{\sqrt{2\pi}}\int dx e^{-ikx} a_{R(L)}(x), \tag{A.4}$$

where $a_{R(L)}^\dagger(x)$ creates a right (left) going photon at x. After linearizing the dispersion, we rewrite the Hamiltonian in real space as

$$\begin{aligned} H/\hbar &= \sum_j \omega_0\sigma_{ee}^j + \int dx\left\{-iv_g a_R^\dagger(x)\frac{\partial}{\partial x}a_R(x) + iv_g a_L^\dagger(x)\frac{\partial}{\partial x}a_L(x)\right\} \\ &+ \sqrt{2\pi}g\int dx\sum_j \delta(x-x_j)\left(a_R^\dagger(x)\sigma_{ge}^j + \sigma_{eg}^j a_R(x) + a_L^\dagger(x)\sigma_{ge}^j + \sigma_{eg}^j a_L(x)\right). \end{aligned} \tag{A.5}$$

The Heisenberg equations of motion for the fields can be formally integrated to yield the solutions of photonic operators,

$$\begin{aligned} a_R(x,t) &= a_{R,\rm in}(x-v_g t) - i\frac{\sqrt{2\pi}g}{v_g}\sum_j \sigma_{ge}^j\left(t - \frac{x-x_j}{v_g}\right)\theta(x-x_j), \\ a_L(x,t) &= a_{L,\rm in}(x+v_g t) - i\frac{\sqrt{2\pi}g}{v_g}\sum_j \sigma_{ge}^j\left(t + \frac{x-x_j}{v_g}\right)\theta(x_j-x). \end{aligned} \tag{A.6a}$$

Next, one substitutes these formal solutions into the equations of motion for the atomic operators σ_{ge}^{j},

$$\dot{\sigma}_{ge}^{j} = -\left(i\omega_0 + \frac{\Gamma'}{2}\right)\sigma_{ge}^{j} + i\sqrt{2\pi}g\left(\sigma_{ee}^{j} - \sigma_{gg}^{j}\right)\left[a_{\rm tot}(x_j,t) - i\frac{\sqrt{2\pi}g}{v_g}\sum_{j'}\sigma_{ge}^{j'}\left(t - \frac{|x_j - x_{j'}|}{v_g}\right)\right] + F_{ge}^{j}, \quad \text{(A.7)}$$

where a total input field $a_{\rm tot}(x,t) = a_{R,\rm in}(x - v_g t) + a_{L,\rm in}(x + v_g t)$ and an associated noise operator F_{ge}^{j} which arises from the system-reservoir interaction [274]. For simplicity, we define the slowly varying variables in the rotating frame as $\tilde{\sigma}_{ge}^{j} = \sigma_{ge}^{j} e^{i\omega_{\rm L} t}$ and $\tilde{F}_{ge}^{j} = F_{ge}^{j} e^{i\omega_{\rm L} t}$. Furthermore, we assume that $\tilde{\sigma}_{ge}$ is slowly varying, $\tilde{\sigma}_{ge}^{j}(t-\epsilon) = \tilde{\sigma}_{ge}^{j}(t)e^{i\omega_0\epsilon}$, with Markov approximation, meaning that we neglect the retardation of atomic response. Then, we can rewrite Eq. (A.7) in the rotating frame,

$$\begin{aligned}\dot{\tilde{\sigma}}_{ge}^{j} &= \left(i\Delta - \frac{\Gamma'}{2} - \frac{2\pi g^2}{v_g}\right)\tilde{\sigma}_{ge}^{j} + i\sqrt{2\pi}g\left(\tilde{\sigma}_{ee}^{j} - \tilde{\sigma}_{gg}^{j}\right)a_{\rm tot}(x_j) \\ &\quad + \frac{\Gamma_{\rm 1D}}{2}\sum_{j'\neq j}\left(\tilde{\sigma}_{ee}^{j} - \tilde{\sigma}_{gg}^{j}\right)\tilde{\sigma}_{ge}^{j'}e^{ik|x_j - x_{j'}|} + \tilde{F}_{ge}^{j}, \end{aligned} \quad \text{(A.8)}$$

where a detuning $\Delta = \omega_{\rm L} - \omega_0$. Here, we have identified $\Gamma_{\rm 1D} = \frac{4\pi g^2}{v_g} = \frac{1}{2}\frac{c}{v_g}\frac{\sigma_0}{A_{\rm m}}\Gamma_0$ as the single-atom decay rate into the guided mode. Similarly, we obtain the equation of motion for $\tilde{\sigma}_z^j = \frac{\tilde{\sigma}_{ee}^{j} - \tilde{\sigma}_{gg}^{j}}{2}$ as

$$\begin{aligned}\dot{\tilde{\sigma}}_{z}^{j} &= -\Gamma_{\rm tot}\left(\tilde{\sigma}_{z}^{j} + \frac{1}{2}\right) - i\sqrt{2\pi}g\left(\tilde{\sigma}_{eg}^{j}a_{\rm tot}(x_j) - a_{\rm tot,in}^{\dagger}(x_j)\tilde{\sigma}_{ge}^{j}\right) \\ &\quad - \frac{\Gamma_{\rm 1D}}{2}\sum_{j'\neq j}\left(\tilde{\sigma}_{eg}^{j}\tilde{\sigma}_{ge}^{j'}e^{ik|x_j - x_{j'}|} + \tilde{\sigma}_{eg}^{j'}\tilde{\sigma}_{ge}^{j}e^{-ik|x_j - x_{j'}|}\right) + \tilde{F}_{z}^{j}, \end{aligned} \quad \text{(A.9)}$$

where an associated noise operator $\tilde{F}_z$ with $\langle\tilde{F}_z\rangle = 0$ [274] and total decay rate $\Gamma_{\rm tot} = \Gamma_{\rm 1D} + \Gamma'$. By using the solution of Eq. (A.8) and (A.9), one can find an input-output relation,

$$a_{R,\rm out}(x) = a_{R,\rm in}(x) - i\sqrt{\frac{\Gamma_{\rm 1D}}{2v_g}}\sum_{j}\tilde{\sigma}_{ge}^{j}(t)e^{ik(x - x_j)}, \quad \text{(A.10a)}$$

$$a_{L,\rm out}(x) = a_{L,\rm in}(x) - i\sqrt{\frac{\Gamma_{\rm 1D}}{2v_g}}\sum_{j}\tilde{\sigma}_{ge}^{j}(t)e^{-ik(x - x_j)}, \quad \text{(A.10b)}$$

where the output field is defined outside of the distribution of atoms (for the right (left)-going field, $x > x_N (x < x_1)$). Considering the interaction with a right-going coherent field with the field amplitude $\mathcal{E}_0$, the input field operator $a_{\rm tot}$ is mapped to $a_{\rm tot} + \mathcal{E}_0$ via a displacement operator [74, 269]. The transformation

maps the initial coherent state to a classical Rabi frequency, while mapping the initial photonic state to vacuum. Then, the equation of motion for the operator mean values $s_i^j = \langle \tilde{\sigma}_i^j \rangle$ with a right-going coherent input $\mathcal{E}_0$ are given by

$$\dot{s}_{ge}^j = \left(i\Delta - \frac{\Gamma_{\rm tot}}{2}\right) s_{ge}^j + i2\Omega_c e^{ikx_j} s_z^j + \Gamma_{\rm 1D} \sum_{j' \neq j} s_{z,ge}^{j,j'} e^{ik|x_j - x_{j'}|}, \tag{A.11a}$$

$$\dot{s}_z^j = -\Gamma_{\rm tot}\left(s_z^j + \frac{1}{2}\right) - i\Omega_c\left(s_{eg}^j e^{ikx_j} - s_{ge}^j e^{-ikx_j}\right) - \frac{\Gamma_{\rm 1D}}{2} \sum_{j' \neq j} \left(s_{eg,ge}^{j,j'} e^{ik|x_j - x_{j'}|} + s_{eg,ge}^{j',j} e^{-ik|x_j - x_{j'}|}\right), \tag{A.11b}$$

where a Rabi frequency $\Omega_c = \sqrt{2\pi} g \mathcal{E}_0$, expectation values of higher-order correlators $s_{z,ge}^{j,j'} = \langle \tilde{\sigma}_z^j \tilde{\sigma}_{ge}^{j'} \rangle$ and $s_{eg,ge}^{j',j} = \langle \tilde{\sigma}_{eg}^{j'} \tilde{\sigma}_{ge}^{j} \rangle$. Here, we explicitly write down the differential equation only for s_{ge}^j and s_z^j, although the total number of differential equations is $4^N - 1$. In the weak excitation limit, one can simplify Eq. (A.11) by using $\langle \tilde{\sigma}_m^j \tilde{\sigma}_n^{j'} \rangle = \langle \tilde{\sigma}_m^j \rangle \langle \tilde{\sigma}_n^{j'} \rangle$, allowing to evaluate steady state solutions easily.

A.2 Effective spin Hamiltonian: waveguide

One can reconstruct an open, interacting spin model that only involves the internal degree of freedom of the atoms [124]. The atomic dynamics is equivalently described by a master equation for an atomic operator ρ,

$$\dot{\rho} = \frac{1}{i\hbar}[H_{\rm tot}, \rho] + \mathcal{L}_{\rm dd}[\rho] + \mathcal{L}_{\rm ind}[\rho], \tag{A.12}$$

where the interacting spin Hamiltonian is

$$H_{\rm tot}/\hbar = \sum_j \left[-\Delta \tilde{\sigma}_{ee}^j - \Omega_c\left(\tilde{\sigma}_{eg}^j e^{ikx_j} + \text{h.c.}\right)\right] + \frac{\Gamma_{\rm 1D}}{2} \sum_{j' \neq j} \sin(k|x_j - x_{j'}|) \tilde{\sigma}_{eg}^j \tilde{\sigma}_{ge}^{j'}, \tag{A.13}$$

and Limblad term for collective emission and independent emission are,

$$\mathcal{L}_{\rm dd}[\rho] = -\frac{\Gamma_{\rm 1D}}{2} \sum_{j,j'} \cos(k|x_j - x_{j'}|) \cdot \left(\tilde{\sigma}_{eg}^j \tilde{\sigma}_{ge}^{j'} \rho + \rho \tilde{\sigma}_{eg}^j \tilde{\sigma}_{ge}^{j'} - 2\tilde{\sigma}_{ge}^{j'} \rho \tilde{\sigma}_{eg}^j\right),$$

$$\mathcal{L}_{\rm ind}[\rho] = -\frac{\Gamma'}{2} \sum_j \left(\tilde{\sigma}_{eg}^j \tilde{\sigma}_{ge}^j \rho + \rho \tilde{\sigma}_{eg}^j \tilde{\sigma}_{ge}^j - 2\tilde{\sigma}_{ge}^j \rho \tilde{\sigma}_{eg}^j\right). \tag{A.14}$$

The infinite-range interaction between a pair of atoms j, j' in the last term of Eq. (A.13) is due to the propagation of a mediated photon between a pair of atoms with a propagation phase. We also see that we can derive Eq. (A.8) and (A.9) from a non Hermitian effective Hamiltonian,

$$H_{\rm eff}/\hbar = \sum_j \left[-\Delta\tilde{\sigma}^j_{ee} - \Omega_c\left(\tilde{\sigma}^j_{eg}e^{ikx_j} + \text{h.c.}\right)\right] - i\frac{\Gamma_{\rm 1D}}{2}\sum_{j,j'}\tilde{\sigma}^j_{eg}\tilde{\sigma}^{j'}_{ge}e^{ik|x_j - x_{j'}|} - i\frac{\Gamma'}{2}\sum_j\tilde{\sigma}^j_{ee}, \quad \text{(A.15)}$$

which can be used for a quantum jump description of the atomic dynamics in an open system. The effective Hamiltonian accurately describes the dynamics provided that the thermal energy $k_BT \ll \hbar\omega_0$ where k_B is the Boltzmann constant.

A.3 Effective spin Hamiltonian: photonic crystal waveguide

Near the band edge $\omega_{\rm atom} \lesssim \omega_{\rm BE}$, the Bloch function for a guided mode approaches a standing-wave, resulting in the effective spin Hamiltonian given by

$$H_{\rm eff}/\hbar = -\sum_j\left(\Delta + i\frac{\Gamma_{\rm 1D}+\Gamma'}{2}\right)\tilde{\sigma}^j_{ee} - i\frac{\Gamma_{\rm 1D}}{2}\sum_{j\neq j'}\cos(kx_j)\cos(kx_{j'})\tilde{\sigma}^j_{eg}\tilde{\sigma}^{j'}_{ge}, \quad \text{(A.16)}$$

where the position of the atom x_j and the wavevector near the band edge $k = \pi/a$ with a lattice constant a. The last term of Eq. (A.16) shows the correlated decay of N atoms with position-dependent coupling rate.

On the other hand, inside the band gap $\omega_{\rm atom} \gtrsim \omega_{\rm BE}$, the effective spin Hamiltonian is written by

$$H_{\rm eff}/\hbar = -\sum_j\left(\Delta - \frac{\Gamma_{\rm 1D}}{2} + i\frac{\Gamma'}{2}\right)\tilde{\sigma}^j_{ee} + \frac{\Gamma_{\rm 1D}}{2}\sum_{j\neq j'}\cos(kx_j)\cos(kx_{j'})\tilde{\sigma}^j_{eg}\tilde{\sigma}^{j'}_{ge}e^{-\kappa|x_j - x_{j'}|}, \quad \text{(A.17)}$$

where the single-atom coupling rate turns into the frequency shift $\frac{\Gamma_{\rm 1D}}{2}$ and the last term of Eq. (A.16) shows the collective frequency shift of N atoms with position-dependent coupling rate.

Appendix B

Atomic polarizability

B.1 Formalism of the light shift Hamiltonian

Here, we briefly summarize atomic polarizability for ac stark shift based on the derivation of Refs. [65, 157, 158] and express explicitly the polarizability tensor. At the end of this appendix, we attach the correction of our calculation [65]. When the light field is far off resonant from the atomic transition, the second-order ac Stark shift of an atomic state $|i\rangle$ is given by

$$\delta U_i^{(2)} = -\frac{|E|^2}{\hbar}\sum_{i\neq j}\left(\frac{\langle i|\varepsilon^*\cdot\mathbf{d}|j\rangle\langle j|\varepsilon\cdot\mathbf{d}|i\rangle}{\omega_{ji}-\omega}+\frac{\langle i|\varepsilon\cdot\mathbf{d}|j\rangle\langle j|\varepsilon^*\cdot\mathbf{d}|i\rangle}{\omega_{ji}+\omega}\right),$$

where ε and $\mathbf{d}$ are the polarization vector and the electric dipole operator, respectively, and $\omega_{ji}=\omega_j-\omega_i$ is the transition frequency between atomic states $|i\rangle$ and $|j\rangle$. In turn, we can consider that the light shift comes from the expectation values $\delta U_i^{(2)}=\langle i|H_{ls}|i\rangle$, where the light shift Hamiltonian is written by

$$H_{ls}=|E|^2\left\{(\varepsilon^*\cdot\mathbf{d})R_i^{(+)}(\varepsilon\cdot\mathbf{d})+(\varepsilon\cdot\mathbf{d})R_i^{(-)}(\varepsilon^*\cdot\mathbf{d})\right\}, \tag{B.1}$$

with a resolvent operator $R_i^{(\pm)}=-\frac{1}{\hbar}\sum_{j\neq i}\frac{|j\rangle\langle j|}{\omega_{ji}\mp\omega}$. After decoupling polarization vectors dipole operators, and transforming from the spherical coordinates to Cartesian coordinates, the light shift Hamiltonian for an

atom in the hyperfine state $|n, J, F\rangle$, parameterized by the dynamic polarizability $\alpha^{(K)}$, is then rewritten by

$$H_{\rm ls} = -\alpha^{(0)}\mathbf{E}^{(-)}\cdot\mathbf{E}^{(+)} - i\alpha^{(1)}\frac{\left(\mathbf{E}^{(-)}\times\mathbf{E}^{(+)}\right)\cdot\mathbf{F}}{2F} - \sum_{\mu,\nu}\alpha^{(2)}E_\mu^{(-)}E_\nu^{(+)}\frac{3}{F(2F-1)}\left[\frac{1}{2}(F_\mu F_\nu + F_\nu F_\mu) - \frac{1}{3}F^2\delta_{\mu\nu}\right]. \tag{B.2}$$

The dynamic polarizabilities are given explicitly by

$$\begin{aligned}
\alpha^{(0)}(n,J,F) &= \sum_{n'J'F'}\frac{d^2_{nJn'J'}}{3}(2F'+1)\left\{\begin{array}{ccc} J & J' & 1 \\ F' & F & I\end{array}\right\}^2 G^{(0)}_{FF'} \\
\alpha^{(1)}(n,J,F) &= 2\sum_{n'J'F'}(-1)^{F+F'}d^2_{nJn'J'}\sqrt{\frac{3F(2F+1)}{2(F+1)}}\left\{\begin{array}{ccc} 1 & 1 & 1 \\ F & F & F'\end{array}\right\} \\
&\quad\times(2F'+1)\left\{\begin{array}{ccc} J & J' & 1 \\ F' & F & I\end{array}\right\}^2 G^{(1)}_{FF'} \qquad \text{(B.3)} \\
\alpha^{(2)}(n,J,F) &= \sum_{n'J'F'}(-1)^{F+F'}d^2_{nJn'J'}\sqrt{\frac{10F(2F+1)(2F-1)}{3(F+1)(2F+3)}}\left\{\begin{array}{ccc} 1 & 1 & 2 \\ F & F & F'\end{array}\right\} \qquad \text{(B.4)} \\
&\quad\times(2F'+1)\left\{\begin{array}{ccc} J & J' & 1 \\ F' & F & I\end{array}\right\}^2 G^{(2)}_{FF'}. \qquad \text{(B.5)}
\end{aligned}$$

where the dipole matrix element $d_{nJn'J'}$ and the rank-dependent propagator $G^{(K)}_{ij}$ are given by

$$\begin{aligned}
d^2_{nJn'J'} &= |\langle n,J||\mathbf{d}||n',J'\rangle|^2 = \frac{3\pi\epsilon_0\hbar c^3}{\omega^3_{nJn'J'}}\frac{2J'+1}{\tau_{nJn'J'}} \qquad \text{(B.6)} \\
G^{(K)}_{ij} &= \frac{1}{\hbar}\left\{\frac{1}{\omega_{ji}-\omega} + \frac{(-1)^K}{\omega_{ji}+\omega}\right\}. \qquad \text{(B.7)}
\end{aligned}$$

Note that we neglect the mixing of energy levels between different hyperfine states since typically, the hyperfine splitting is much larger than the ac Stark shift. In general, H_{ls} is not diagonal in $|nJ, F, m_F\rangle$ basis, suggesting that m_F is not a good quantum number. Therefore, we need to diagonalize the light shift Hamiltonian to obtain the eigenvalues and eigenbasis.

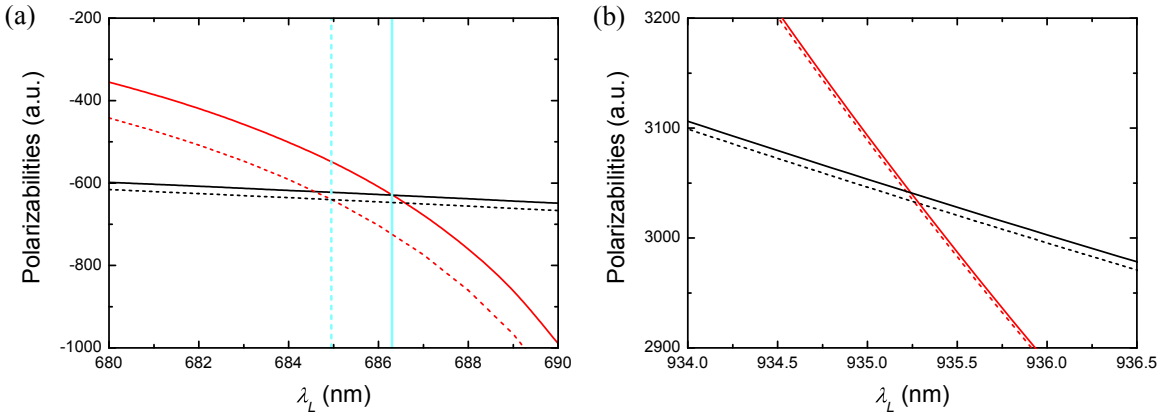

Figure B.1: **Scalar polarizabilities around the magic wavelengths.** We display the scalar polarizabilities (a) near the blue-detuned magic wavelength and (b) the red-detuned magic wavelength with the parameters described in the Appendix B.2 (the ground state $6S_{1/2}$: solid black, the excited state $6P_{3/2}$: solid red). and with the parameters used in Fig. 4.5 ($6S_{1/2}$: dashed black, $6P_{3/2}$: dashed red). The polarizabilities are given in the atomic unit.

B.2 Contribution of higher excited states

Next, we consider the contribution of higher excited states to the polarizability around the magic wavelengths. The calculations for the polarizability $\alpha_{g,\mathrm{full}}$ of the ground state $6S_{1/2}$ and $\alpha_{e,\mathrm{full}}$ of the excited state $6P_{3/2}$ incorporate the couplings $6S_{1/2} \leftrightarrow (6-42)P_{3/2}$, and $6P_{3/2} \leftrightarrow (7-40)S_{1/2}$ and $6P_{3/2} \leftrightarrow (5-42)D_{1/2,3/2}$, respectively. The energy levels and the reduced matrix elements are taken from the Appendix. D in Ref. [158]. The contribution of the core polarizability, 15.8 a.u., is added to the results for the scalar polarizabilities [166], where the core polarizability is given in the atomic unit.

Figure B.1(a) shows the scalar polarizabilities, $\alpha^{(0)}_{g,\mathrm{full}}$ (solid black) and $\alpha^{(0)}_{e,\mathrm{full}}$ (solid red), around the blue-detuned magic wavelength, overlaid with the scalar polarizabilities with the parameters used in Fig. 4.5 (the ground state: dashed black, the excited state: dashed red). Clearly, the higher excited states contribute to both the ground and excited state polarizabilties around the blue-detuned magic wavelength, which suggests that the blue-detuned magic wavelength $\alpha_{g,\mathrm{full}}(\lambda_{\mathrm{blue}}) = \alpha_{e,\mathrm{full}}(\lambda_{\mathrm{blue}})$ is $\lambda_{\mathrm{blue}} \sim 686.3$ nm, marked by the solid cyan line in Fig. B.1. We also find that the higher excited states' contribution to the red-detuned magic wavelength (~ 935 nm) is negligible due to the larger detuning as shown in Fig. B.1 (b).

Corrections to our results for optical nanofiber traps in Cesium

D. Ding,[1] A. Goban,[1] K. S. Choi,[1,2] and H. J. Kimble[1]

[1] *Norman Bridge Laboratory of Physics, California Institute of Technology*
[2] *Spin Convergence Research Center, Korea Institute of Science and Technology*

(Dated: April 28, 2015)

Several errors in Refs. [1, 2] are corrected related to the optical trapping potentials for a state-insensitive, compensated nanofiber trap for the D_2 transition of atomic Cesium. Section I corrects our basic formalism in Ref. [1] for calculating dipole-force potentials. Section II corrects erroneous values for a partial lifetime and a transition wavelength in Ref. [1]. Sections III and IV present corrected figures for various trapping configurations considered in Refs. [1] and [2], respectively.

I. FORMALISM

The light shifts calculated in Ref. [1] are based upon Eq. (2) in Ref. [1]. The text states that the basis for Eq. (2) is 'spherical' (i.e., irreducible spherical tensors). In fact, the basis for Eq. (2) is actually a Cartesian basis (i.e., x, y, z), which we used to perform all calculations in Ref. [1].

In Eq. (2) of Ref. [1], $\alpha^{(0)}$,$\alpha^{(1)}$ and $\alpha^{(2)}$ are the scalar, vector and tensor atomic dynamic polarizabilities defined in Ref. [3]. The dipole matrix element in Ref. [1] is $d_{JJ'}^2 = |\langle J||\mathbf{d}||J'\rangle|^2 = \frac{3\pi\epsilon_0\hbar c^3}{\omega_{J'J}^3}\frac{2J'+1}{2J+1}\frac{1}{\tau_{J'J}}$, as defined in Ref. [4]. However, as Ref. [3] only considered light shifts of the ground states, the definition for $d_{JJ'}$ in Ref. [4] becomes problematic when defining $d_{JJ'}$ for the excited states. J and J' are defined with respect to states of lower to higher energy, respectively, rather than with respect to initial and final states. This notation is therefore ambiguous if the initial state is an excited state. Also, the counter-rotating term was not taken into account in Ref. [3]. Therefore, we follow the formalism in Refs. [5–7], in which case Eq. (2) of Ref. [1] should be rewritten as follows:

$$\hat{H}_{\rm ls} = -\alpha^{(0)}\hat{\mathbf{E}}^{(-)}\cdot\hat{\mathbf{E}}^{(+)} - i\alpha^{(1)}\frac{(\hat{\mathbf{E}}^{(-)}\times\hat{\mathbf{E}}^{(+)})\cdot\hat{\mathbf{F}}}{2F} - \sum_{\mu,\nu}\alpha^{(2)}\hat{E}_\mu^{(-)}\hat{E}_\nu^{(+)}\frac{3}{F(2F-1)}\left[\tfrac{1}{2}(\hat{F}_\mu\hat{F}_\nu+\hat{F}_\nu\hat{F}_\mu)-\tfrac{1}{3}\hat{F}^2\delta_{\mu\nu}\right], \quad (1)$$

where the dipole matrix element in Refs. [5–7] is $d_{JJ'}^2 = |\langle J||\mathbf{d}||J'\rangle|^2 = \frac{3\pi\epsilon_0\hbar c^3}{\omega_{J'J}^3}(2J'+1)\frac{1}{\tau_{J'J}}$, where (J, J') are for (lower, upper) levels, respectively. $\alpha^{(0)}$, $\alpha^{(1)}$, and $\alpha^{(2)}$ of Eq. (1) include counter-rotating terms. However, in Ref. [1], we made an error in the definition of the vector polarizability, $\alpha^{(1)}$, by neglecting the rank dependence of the counter-rotating terms. In this errata, we correct the definition of $\alpha^{(1)}$ to incorporate the rank dependence of the counter-rotating terms in our calculations of light shifts [5–7].

The dynamic polarizabilities are then given by

$$\alpha^{(0)}(J,F) = \sum_{nJ'F'}\frac{d_{JJ'}^2}{3}(2F'+1)\begin{Bmatrix} J & J' & 1\\ F' & F & I\end{Bmatrix}^2 G_{FF'}^{(0)} \quad (2)$$

$$\alpha^{(1)}(J,F) = 2\sum_{nJ'F'}(-1)^{F+F'}d_{JJ'}^2\sqrt{\frac{3F(2F+1)}{2(F+1)}}\begin{Bmatrix} 1 & 1 & 1\\ F & F & F'\end{Bmatrix} \times(2F'+1)\begin{Bmatrix} J & J' & 1\\ F' & F & I\end{Bmatrix}^2 G_{FF'}^{(1)} \quad (3)$$

$$\alpha^{(2)}(J,F) = \sum_{nJ'F'}(-1)^{F+F'}d_{JJ'}^2\sqrt{\frac{10F(2F+1)(2F-1)}{3(F+1)(2F+3)}}\begin{Bmatrix} 1 & 1 & 2\\ F & F & F'\end{Bmatrix} \times(2F'+1)\begin{Bmatrix} J & J' & 1\\ F' & F & I\end{Bmatrix}^2 G_{FF'}^{(2)}, \quad (4)$$

where $G_{ij}^{(K)}$ is the rank-K propagator defined as

$$G_{ij}^{(K)} = \frac{1}{\hbar}\left\{\frac{1}{\omega_{ji}-\omega} + \frac{(-1)^K}{\omega_{ji}+\omega}\right\}. \quad (5)$$

We note that the counter-rotating term gains an overall minus sign for $K = 1$ in the expression for the vector propagator $G_{FF'}^{(1)}$. We have confirmed that our corrected formula for the dynamic polarizabilities (i.e., Eqs. (1-5)) is now consistent with the expressions in Ref. [5].

II. PARTIAL LIFETIMES AND TRANSITION WAVELENGTHS

In addition to corrections to our formalism discussed above, we correct two numerical errors for the atomic data used to calculate the light shifts in Refs. [1, 2]. These errors stem from a mistake for a partial lifetime τ and from an error for a transition wavelength λ. All values for τ and λ of Ref. [1] were taken from Tables 7.1–7.3 of J. McKeever's Ph.D Thesis [8]. The specific errors are as follows:

1. The wavelength for the transition $7S_{1/2} \leftrightarrow 6P_{3/2}$ in Table 7.2 of Ref. [8] is listed as 469.5 nm, whereas the correct value is 1469.5 nm.

2. The partial lifetime for the transition $7D_{3/2} \leftrightarrow 6P_{3/2}$ in Table 7.3 of Ref. [8] is listed as 709.7 μs, but instead should be 0.7097 μs.

The corrected values for Tables 7.1–7.3 of Ref. [8] are highlighted with green color in Tables I and II of this errata.

The partial lifetimes and wavelengths from Table 7.1–7.3 of Ref. [8] were obtained from Refs. [9, 10] with the exception of the values for $6P \rightarrow 6S$ from Ref. [11] and $6D \rightarrow 6P$ from Ref. [12].

To further confirm the accuracy of the corrected values from Ref. [8], we refer to Tables V and VI of Arora *et al.* [13] (heretofore, labelled as 'Clark'). Tables I and II in this errata compare the corrected tables from Ref. [8] to Tables V–VI of Ref. [13]. Our values agree well with those from Ref. [13].

We note that all previous publications prior to Ref. [1] from our group, including Ref. [14], have used the correct values in Tables I–II and not those from McKeever's thesis [8]. Furthermore, these earlier results are for linearly polarized trapping fields for which the contribution of the vector term $\alpha^{(1)}$ vanishes. Therefore, these earlier results from our group stand without revision.

Using the revised formalism from Section I and based on the corrected numerical values in Tables I–II from Section II, we present corrected figures to replace those in Refs. [1, 2] as described in the following sections.

III. CORRECTED FIGURES FOR REF. [1]

The figure numbering in this errata mirrors that of Ref.[1] with corrected figures given here in Roman numerals. Fig. VI[1] relates to magic wavelengths for the Cs D_2 line and replaces Fig. 6 in Ref. [1]. The magic wavelength in this note is defined by the weighted average of the Zeeman sublevels m_F (i.e., not by $\alpha^{(0)}$ alone).

As in Ref. [1], we include a surface interaction potential of an atom with the dielectric nanofiber in our calculation of the total atomic trap potential. The surface potential of the ground state Cs atom near a planar dielectric surface can be approximated by the van der Waals potential $-\frac{C_3}{d^3}$, where $d = r - a$ and $C_3/\hbar = 1.16$ kHz μm^3 [1, 15].

In Figs. VII[1], VIII[1], and IX[1], the two-color evanescent trap from Ref. [16] is constructed from a pair of counter-propagating x-polarized ($\varphi_0 = 0$) red-detuned beams ($P_{\rm red} = 2 \times 2.2$ mW) at $\lambda_{\rm red} = 1064$ nm, forming an optical lattice, and a single repulsive y-polarized ($\varphi_0 = \pi/2$) blue-detuned beam ($P_{\rm blue} = 25$ mW) at $\lambda_{\rm blue} = 780$ nm. The SiO_2 tapered optical fiber has radius $a = 250$ nm in the trapping region. Figs. VII[1],VIII[1], IX[1] replace figures of Fig. 7, 8, 9 of Ref. [1].

For the magic, compensated trap in Figs. X[1], XI[1], XII[1], we use a pair of counter-propagating x-polarized ($\varphi_0 = 0$) red-detuned beams ($P_{\rm red} = 2 \times 0.95$ mW) at the magic wavelength $\lambda_{\rm red} = 935.3$ nm. Counter-propagating, x-polarized blue-detuned beams at a second magic wavelength $\lambda_{\rm blue} = 684.9$ nm are used with a power $P_{\rm blue} = 2 \times 16$ mW. The resulting interference is averaged out by detuning the beams to $\delta_{fb} = 30$ GHz. Figs. X[1], XI[1], XII[1] replace Figs. 10, 11, 12 of Ref. [1].

IV. CORRECTED FIGURES FOR REF. [2]

Because of the errors described in Sections I and II, our experiment in Ref. [2] used red- and blue-detuned beams at wavelengths $\lambda_{\rm red} = 937.1$ nm and $\lambda_{\rm blue} = 686.1$ nm instead of the correct values of $\lambda_{\rm red} \simeq 935.7$ nm and $\lambda_{\rm blue} \simeq 684.8$ nm calculated in the same fashion as Fig. VI[1] but now for $F = 4$ of $6S_{1/2}$ to $F' = 5$ of $6P_{3/2}$. Fig. A[2] shows the trapping potentials for the ground and excited states for the correct magic wavelengths of $\lambda_{\rm red} \simeq 935.7$ nm and $\lambda_{\rm blue} \simeq 684.8$ nm for this transition.

For the actual wavelengths $\lambda_{\rm red} = 937.1$ nm and $\lambda_{\rm blue} = 686.1$ nm used in our experiment [2], Fig.1 and Fig. SM5 of Ref. [2] are here replaced by Figs. B[2] and C[2], respectively, which incorporate the revisions described in Sections I and II.

V. CONCLUSION

Our emphasis has been to correct the formalism (Section I) and atomic data (Section II and Tables I, II) that are the basis for our calculations in Refs. [1, 2]. Recently a more extensive set of atomic data than in Tables I and

II has become available [7]. We have confirmed that these data with our formalism in Eqs. (1-5) reproduce Figs. (4, 5) from Ref. [7].

However, the expanded set of atomic levels and lifetimes in Ref. [7] lead to small differences between Figs. (4, 5) [7] and corresponding figures computed from our Tables I, II. These differences are most pronounced around 685nm (e.g., our Fig. VI(a)) principally due to excited-state contributions up to $n \sim 25$, which are not included in Tables I, II. We therefore recommend that the data set from Ref. [7] be employed for the calculation of ac Stark shifts for the D_2 line in atomic Cesium rather than the less extensive data in our Tables I, II.

Acknowledgments

We thank Dr. F. Le Kien and Prof. A. Rauschenbeutel for contacting us directly to alert us to the errors in Ref. [1] and for subsequent critical correspondence.

[1] C. Lacroute *et al. New J. Phys.*, **14**, 023056 (2012).
[2] A. Goban *et al. Phys. Rev. Lett.*, **109**, 033603 (2012).
[3] I. H. Deutsch and P. S. Jessen *Opt. Comm.*, **283**, 681 (2010).
[4] D. A. Steck *Quantum and Atom Optics textbook.* http://atomoptics.uoregon.edu/ dsteck/teaching/quantum-optics/, 2011.
[5] P. Rosenbusch *et al. Phys. Rev. A*, **79**, 013404 (2009).
[6] K. Beloy, *PhD Thesis*, Theory of the ac Stark Effect on the Atomic Hyper Fine Structure and Applications to Microwave Atomic Clocks, (2009). http://wolfweb.unr.edu/homepage/andrei/WWW-tap/Student_ work/Beloy_ Dissertation_ 2009.pdf
[7] Fam Le Kien, P. Schneeweiss, and A. Rauschenbeutel arXiv:1211.2673v1 (2012)
[8] J. McKeever *PhD Thesis* (2004) http://thesis.library.caltech.edu/2421, 2004. In Tables I and II of this errata, two errors from McKeever's thesis have been corrected and are highlighted in green, as described in Section II.
[9] G. Laplanche *et al. Phys. Rev. A*, **30**, 2881 (1984).
[10] M. Fabry and J. R. Cussenot *Can. J. Phys.*, **54**, 836 (1976).
[11] D. A. Steck *Cesium D Line Data* http://steck.us/alkalidata/, 2003.
[12] C. J. Hood *PhD Thesis* (2000). http://thesis.library.caltech.edu/3688.
[13] B. Arora, M. S. Safronova, C. W. Clark *Phys. Rev. A*, **76**, 052509 (2007).
[14] J. McKeever *et al. Phys. Rev. Lett.*, **90**, 133602 (2003).
[15] N. P. Stern *et al. New J. Phys.*, **13**, 085004(2011).
[16] E. Vetsch *et al. Phys. Rev. Lett.*, **104**, 203603 (2010).

Level nS	$\lambda_{\text{McKeever}}$ (nm)	λ_{Clark} (nm)	τ_{McKeever} (μs)	τ_{Clark} (μs)
6	852.4	852.35	0.03051	0.0306
7	1469.5	1469.89	0.07529	0.0749
8	794.4	794.61	0.2599	0.2319
9	658.8	658.83	0.5533	0.4759
10	603.4	603.58	0.9924	0.8374
11	574.6		1.607	
12	557.3		2.428	
13	546.3		3.49	
14	538.5		4.809	
15	532.9		6.431	

TABLE I: Comparison between corrected partial lifetimes in Ref. [8] with Ref. [13] for $6P_{3/2} \rightarrow 6S_{1/2}$ [11] and $nS_{1/2} \rightarrow 6P_{3/2}$ for $n = 7 - 15$ [9]. Partial lifetime (τ_{McKeever}) and wavelength ($\lambda_{\text{McKeever}}$) are from Ref. [8] with the corrected value highlighted in green. τ_{Clark} and λ_{Clark} are from Ref. [13]. The conversion from d to τ from Ref. [13] is done using Eq. (7.8) in Ref. [8].

Level nD	$\lambda_{3/2\ \text{McKeever}}$ (nm)	$\lambda_{3/2\ \text{Clark}}$ (nm)	$\tau_{3/2\ \text{McKeever}}$ (μs)	$\tau_{3/2\ \text{Clark}}$ (μs)	$\lambda_{5/2\ \text{McKeever}}$ (nm)	$\lambda_{5/2\ \text{Clark}}$ (nm)	$\tau_{5/2\ \text{McKeever}}$ (μs)	$\tau_{5/2\ \text{Clark}}$ (μs)
5	3612.7	3614.09	10.09	9.2931	3489.2	3490.97	1.433	1.3692
6	921.1	921.11	0.3466	0.3497	917.2	917.48	0.0587	0.0604
7	698.3	698.54	0.7097	0.7061	697.3	697.52	0.1198	0.1203
8	621.7	621.93	1.284	1.2884	621.3	621.48	0.217	0.1566
9	584.7		2.131		584.5		0.3587	
10	563.7		3.29		563.5		0.5527	
11	550.4		4.807		550.3		0.8063	

TABLE II: Comparison between corrected partial lifetimes in Ref. [8] with Ref. [13] for $nD_{(3/2,5/2)} \rightarrow 6P_{3/2}$. Partial lifetime ($\tau_{(3/2,5/2)\ \text{McKeever}}$) and wavelength ($\lambda_{(3/2,5/2)\ \text{McKeever}}$) are from Ref. [8] with the corrected value highlighted in green. $\tau_{(3/2,5/2)\ \text{Clark}}$ and $\lambda_{(3/2,5/2)\ \text{Clark}}$ are from Ref. [13]. The conversion from d to $\tau_{(3/2,5/2)}$ from Ref. [13] is done using Eq. (7.8) in Ref. [8].

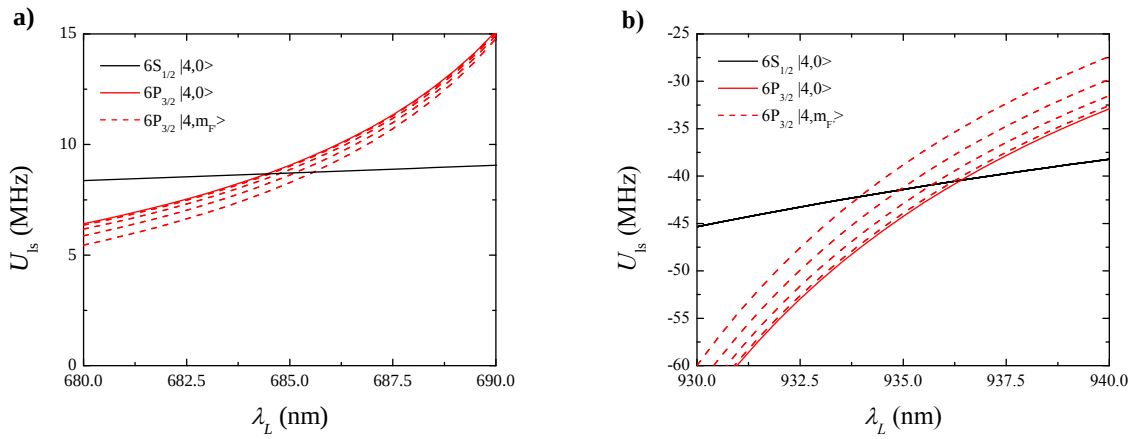

FIG. VI[1]: Replacement for Fig. 6 in Ref. [1] for determination of the magic wavelengths for the $6S_{1/2}, F = 4 \rightarrow 6P_{3/2}, F' = 4$ transition of the Cs D_2 line. The light shifts U_{ls} are for a linearly polarized beam with constant intensity 2.9×10^9 W m^{-2} around (a) the blue-detuned magic wavelength at $\lambda_{\text{blue}} \simeq 684.9$ nm and (b) red-detuned magic wavelength at $\lambda_{\text{red}} \simeq 935.3$ nm.

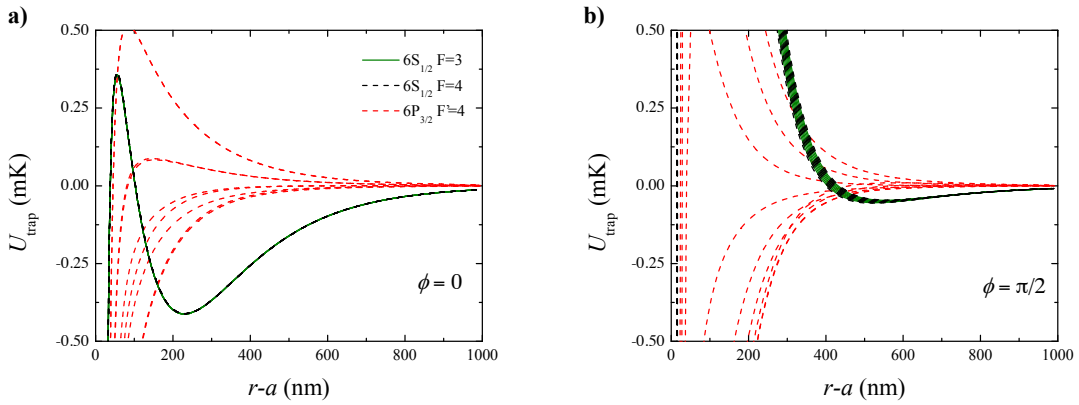

FIG. VII[1]: Replacement for Fig. 7 in Ref. [1]. Radial dependence of the trapping potential of the ground and excited states for the parameters used in Ref. [16] at $z = 0$. The polarization configuration is the same as Fig. 1(b) of Ref. [1]. The energy sublevels of the ground states $F = 3$ and $F = 4$ of $6S_{1/2}$ are shown as solid green and dashed black curves, and the $F' = 4$ sublevels of the electronically excited state ($6P_{3/2}$) are shown as red dashed curves. (a) Radial potential along $\phi = 0$. The trap minimum is located at about 230 nm from the fiber surface. (b) Radial potential along $\phi = \pi/2$.

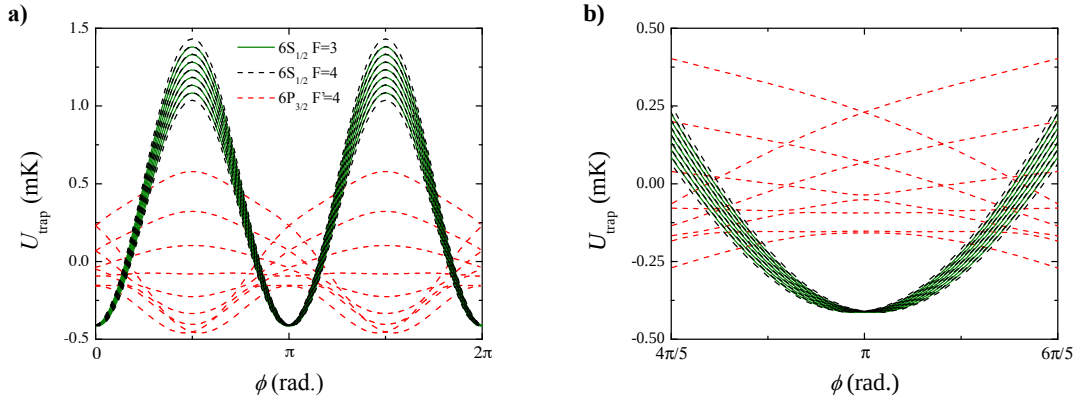

FIG. VIII[1]: Replacement for Fig. 8 in Ref. [1] for the configuration of Ref. [16]. Azimuthal dependence of the trapping potential of the ground and excited states for the parameters used in Fig. VII[1]. $r - a = 230$ nm and $z = 0$. (a) The ground-state splitting is minimum for $\phi = 0$ and $\phi = \pi$. (b) Expanded view of (a) near a trap minimum at $\phi \simeq \pi$.

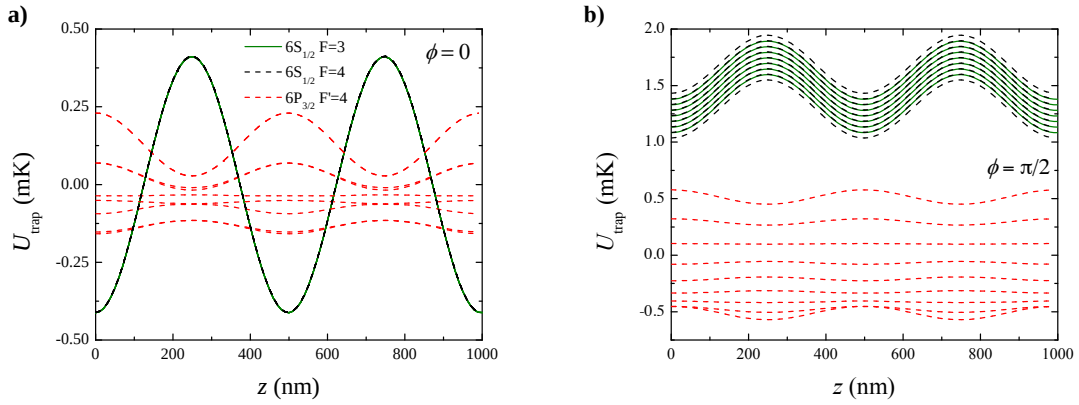

FIG. IX[1]: Replacement for Fig. 9 in Ref. [1] for the configuration of Ref. [16]. Axial dependence of the trapping potential for the ground and excited states for the parameters used in Fig. VII[1]. (a) Longitudinal potential along $\phi = 0$. The distance from the fiber surface is set to $r - a = 230$ nm at the trap minimum. (b) Longitudinal potential along $\phi = \pi/2$. The distance from the fiber surface is again set to 230 nm.

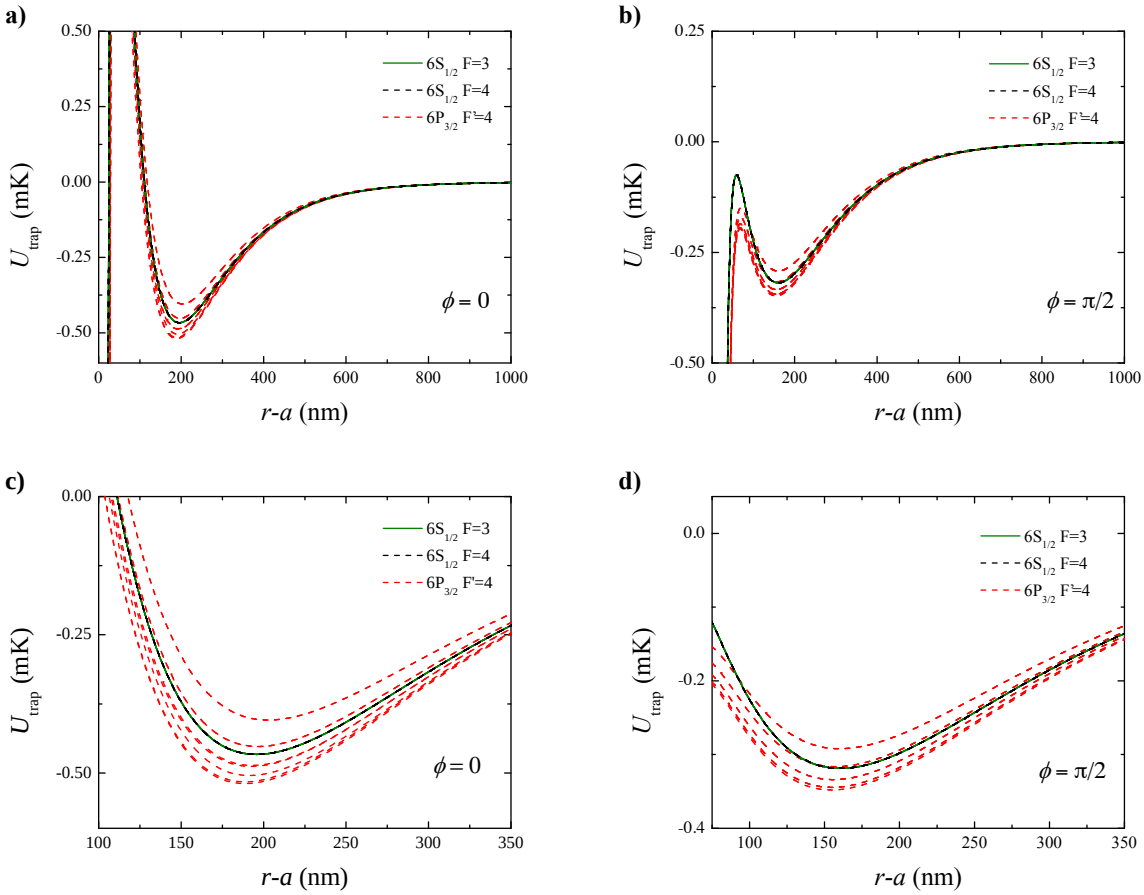

FIG. X[1]: Replacement for Fig. 10 in Ref. [1]. Radial dependence of the trapping potentials of the ground and excited states using the magic wavelengths and the compensated configuration shown in Fig. 1(d) of Ref. [1]. All beams are polarized along $\phi = 0$ (i.e., $\varphi_0 = 0$). The 935.3 nm beams each have a power of 0.95 mW. The 684.9 nm beams each have a power of 16 mW. (a) Radial potentials along $\phi = 0$ (i.e., $\varphi_0 = 0$). The trap minimum for $6S_{1/2}$ is located at about 200 nm from the fiber surface. (b) Radial potential along $\phi = \pi/2$. (c), (d) Expanded views of (a) and (b) around the trap mininum.

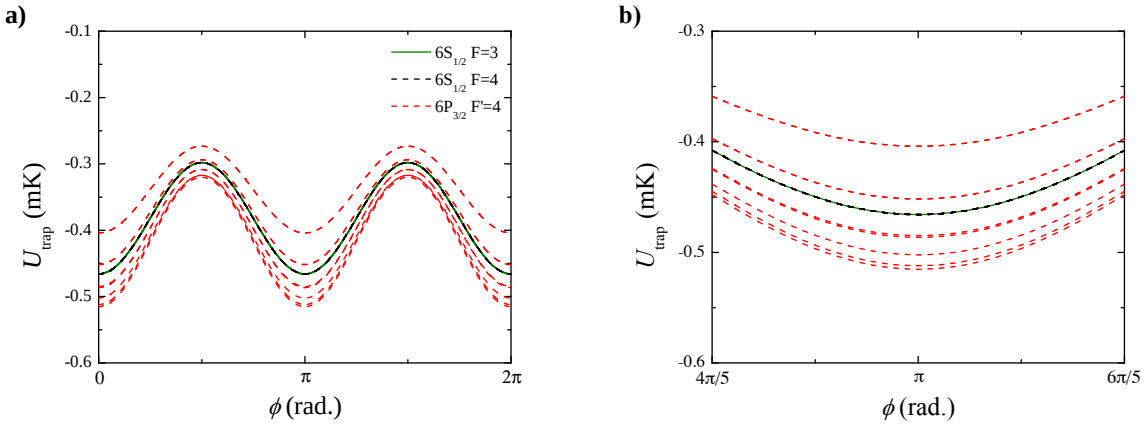

FIG. XI[1]: Replacement for Fig. 11 in Ref. [1] for the magic, compensated scheme with $\lambda_{\rm red} = 935.3$ nm and $\lambda_{\rm blue} = 684.9$ nm. Azimuthal dependence of the trapping potential of the ground and excited states for the parameters used in Fig. X[1]. $r - a = 200$ nm and $z = 0$. (b) Expanded view of (a) near a trap minimum at $\phi = \pi$.

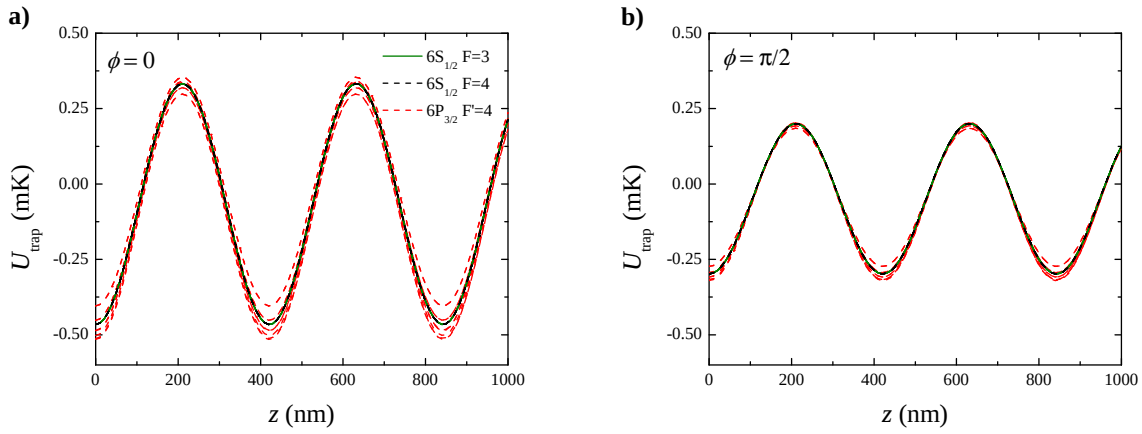

FIG. XII[1]: Replacement for Fig. 12 in Ref. [1] for the magic, compensated scheme with $\lambda_{\rm red} = 935.3$ nm and $\lambda_{\rm blue} = 684.9$ nm. Axial dependence of the trapping potential for the ground and excited states for the parameters used in Fig. X[1]. (a) Longitudinal potential along $\phi = 0$. The distance from the fiber surface is set to $r - a = 200$ nm at the trap minimum. (b) Longitudinal potential along $\phi = \pi/2$. The distance from the fiber surface is again set to 200 nm.

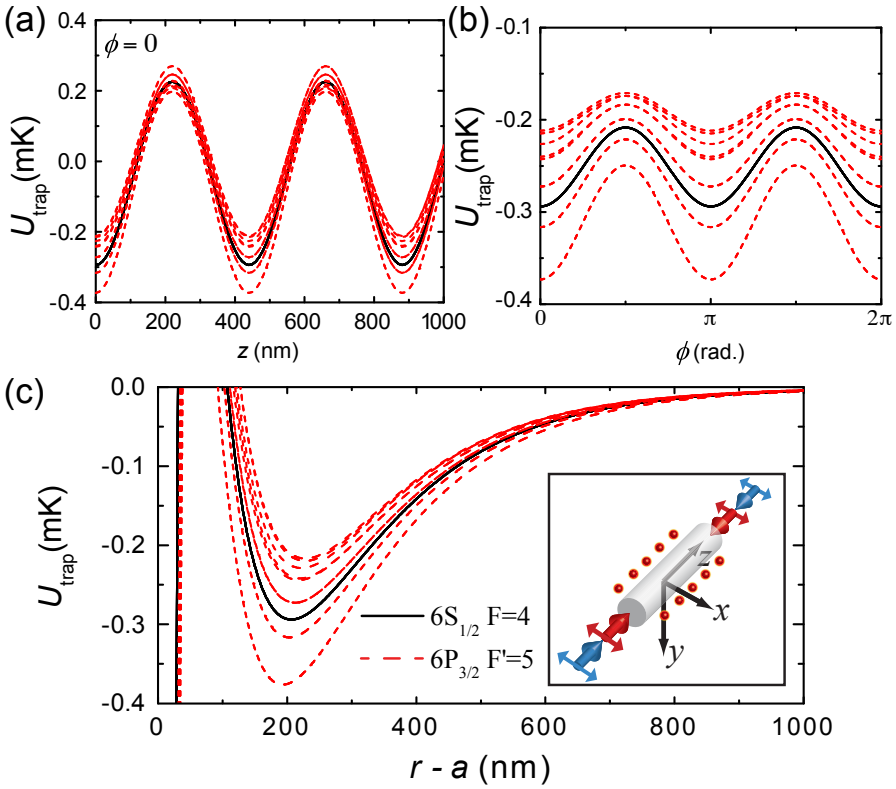

FIG. A[2]: The magic, compensated scheme with a pair of counter-propagating x-polarized ($\varphi_0 = 0$) red-detuned beams ($P_{\rm red} = 2 \times 0.4$ mW) at $\lambda_{\rm red} = 935.7$ nm and counter-propagating, x-polarized blue-detuned beams ($P_{\rm blue} = 2 \times 5$ mW) at $\lambda_{\rm blue} = 684.8$ nm. The distance from the fiber surface is set to 207 nm. (a) Azimuthal $U_{\rm trap}(\phi)$, (b) axial $U_{\rm trap}(z)$, (c) radial $U_{\rm trap}(r - a)$. Each black and red line corresponds to different energy eigenstates of the ground state ($6S_{1/2}, F = 4$) and excited state ($6P_{3/2}, F' = 5$), respectively.

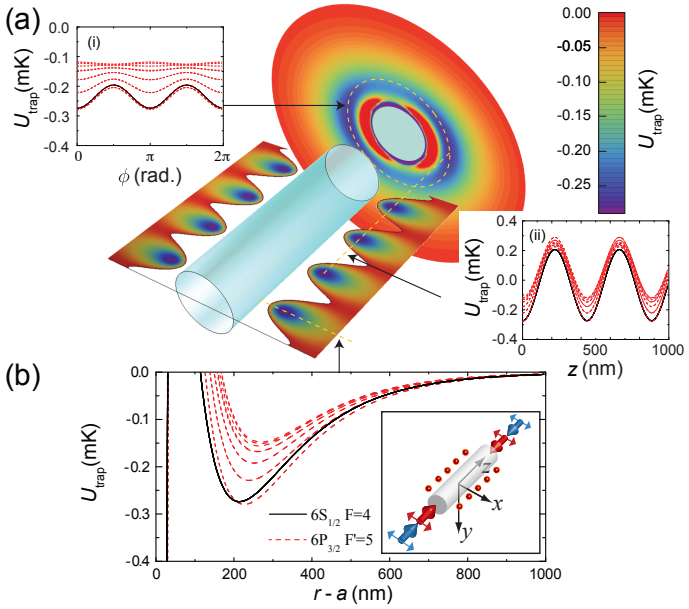

FIG. B[2]: Replacement for Fig. 1 in Ref. [2] for the actual wavelengths used in our experiment [2]. We used a pair of counter-propagating x-polarized ($\varphi_0 = 0$) red-detuned beams ($P_{\rm red} = 2 \times 0.4$ mW) at $\lambda_{\rm red} = 937.1$ nm, and counter-propagating, x-polarized blue-detuned beams ($P_{\rm blue} = 2 \times 5$ mW) at $\lambda_{\rm blue} = 686.1$ nm in our experiment [2]. The resulting interference is averaged out by detuning the beams to $\delta_{fb} = 382$ GHz. Adiabatic trapping potential $U_{\rm trap}$ for a state-insensitive, compensated nanofiber trap for the $6S_{1/2}, F = 4$ states in atomic Cs outside of a cylindrical waveguide of radius $a = 215$ nm. $U_{\rm trap}$ for the substates of the ground level $F = 4$ of $6S_{1/2}$ (excited level $F' = 5$ of $6P_{3/2}$) are shown as black (red-dashed) curves. **(a)(i)** azimuthal $U_{\rm trap}(\phi)$, **(ii)** axial $U_{\rm trap}(z)$ and **(b)** radial $U_{\rm trap}(r - a)$ trapping potentials. The trap minimum for $6S_{1/2}$ is located at about 215 nm from the fiber surface. Input polarizations for the trapping beams are denoted by the red and blue arrows in the inset in (b).

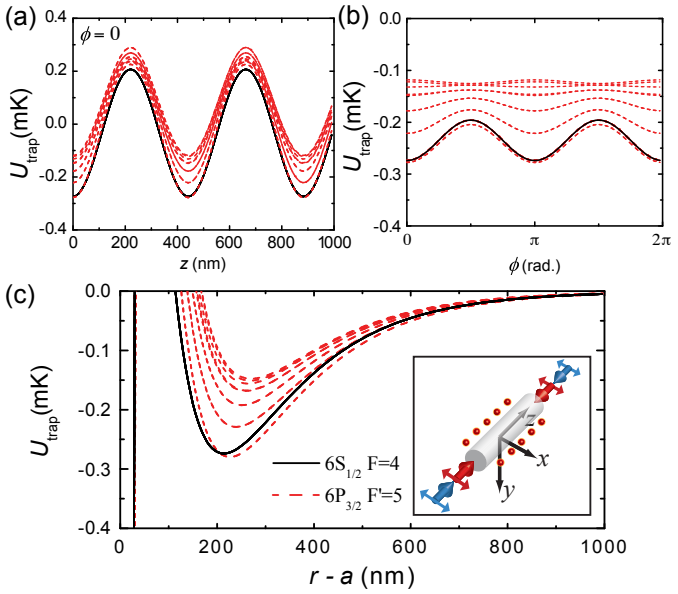

FIG. C[2]: Replacement for Fig. SM5 in the supplemental material of Ref. [2] for actual wavelengths used in our experiment [2]. We used a pair of counter-propagating x-polarized ($\varphi_0 = 0$) red-detuned beams ($P_{\rm red} = 2 \times 0.4$ mW) at $\lambda_{\rm red} = 937.1$ nm, and counter-propagating, x-polarized blue-detuned beams ($P_{\rm blue} = 2 \times 5$ mW) at $\lambda_{\rm blue} = 686.1$ nm in our experiment [2]. Expanded view of the insets in Fig. B[2]. The distance from the fiber surface is set to 215 nm. (a) Azimuthal $U_{\rm trap}(\phi)$, (b) axial $U_{\rm trap}(z)$, (c) radial $U_{\rm trap}(r - a)$. Each black and red line corresponds to different energy eigenstates of the ground state ($6S_{1/2}, F = 4$) and excited state ($6P_{3/2}, F' = 5$), respectively.

Bibliography

[1] H. J. Kimble, "The quantum internet," *Nature*, vol. 453, no. 7198, p. 1023, 2008.

[2] M. A. Nielsen and I. L. Chuang, *Quantum Computation and Quantum Information*. 10th Anniversary Edition, Cambridge University Press, 2010.

[3] J. Preskill, *Lecture notes for physics 229: Quantum information and computation*. California Institute of Technology, 1998.

[4] L. M. Duan, M. D. Lukin, J. I. Cirac, and P. Zoller, "Long-distance quantum communication with atomic ensembles and linear optics," *Nature*, vol. 414, p. 413, 2001.

[5] P. Kómár, E. M. Kessler, M. Bishof, L. Jiang, A. S. Sørensen, J. Ye, and M. D. Lukin, "A quantum network of clocks," *Nature Physics*, vol. 10, p. 582, 2014.

[6] S. Lloyd, "Universal Quantum Simulators," *Science*, vol. 273, p. 1073, 1996.

[7] A. Acin, J. I. Cirac, and M. Lewenstein, "Entanglement percolation in quantum networks," *Nature Physics*, vol. 3, p. 256, 2007.

[8] D. E. Chang, V. Vuletić, and M. D. Lukin, "Quantum nonlinear optics — photon by photon," *Nature Photonics*, vol. 8, p. 685, 2014.

[9] K. M. Birnbaum, A. Boca, R. Miller, A. D. Boozer, T. E. Northup, and H. J. Kimble, "Photon blockade in an optical cavity with one trapped atom," *Nature*, vol. 436, p. 87, 2005.

[10] I. Schuster, A. Kubanek, A. Fuhrmanek, T. Puppe, P. W. H. Pinkse, K. Murr, and G. Rempe, "Nonlinear spectroscopy of photons bound to one atom," *Nature Physics*, vol. 4, p. 382, 2008.

[11] A. Stute, B. Casabone, P. Schindler, T. Monz, P. O. Schmidt, B. Brandstaetter, T. E. Northup, and R. Blatt, "Tunable ion-photon entanglement in an optical cavity," *Nature*, vol. 485, p. 482, 2012.

[12] Q. A. Turchette, C. J. Hood, W. Lange, H. Mabuchi, and H. J. Kimble, "Measurement of conditional phase shifts for quantum logic," *Physical Review Letters*, vol. 75, p. 4710, 1995.

[13] A. Reiserer, N. Kalb, G. Rempe, and S. Ritter, "A quantum gate between a flying optical photon and a single trapped atom," *Nature*, vol. 508, p. 237, 2014.

[14] J. McKeever, A. Boca, A. D. Boozer, R. Miller, J. R. Buck, A. Kuzmich, and H. J. Kimble, "Deterministic Generation of Single Photons from One Atom Trapped in a Cavity," *Science*, vol. 303, p. 1992, 2004.

[15] S. Ritter, C. Noelleke, C. Hahn, A. Reiserer, A. Neuzner, M. Uphoff, M. Muecke, E. Figueroa, J. Bochmann, and G. Rempe, "An elementary quantum network of single atoms in optical cavities," *Nature*, vol. 484, p. 195, 2012.

[16] S. Haroche and J. M. Raimond, *Exploring the Quantum: Atoms, Cavities, and Photons*. Oxford Univ. Press, 2006.

[17] M. H. Devoret and R. J. Schoelkopf, "Superconducting Circuits for Quantum Information: An Outlook," *Science*, vol. 339, p. 1169, 2013.

[18] R. H. Dicke, "Coherence in Spontaneous Radiation Processes," *Physical Review*, vol. 93, p. 99, 1954.

[19] C. Chou, S. Polyakov, A. Kuzmich, and H. Kimble, "Single-Photon Generation from Stored Excitation in an Atomic Ensemble," *Physical Review Letters*, vol. 92, p. 213601, 2004.

[20] M. Eisaman, L. Childress, A. André, F. Massou, A. Zibrov, and M. Lukin, "Shaping Quantum Pulses of Light Via Coherent Atomic Memory," *Physical Review Letters*, vol. 93, p. 233602, 2004.

[21] M. D. Eisaman, A. André, F. Massou, M. Fleischhauer, A. S. Zibrov, and M. D. Lukin, "Electromagnetically induced transparency with tunable single-photon pulses," *Nature*, vol. 438, p. 837, 2005.

[22] T. Chaneliere, D. N. Matsukevich, S. D. Jenkins, S. Y. Lan, T. A. B. Kennedy, and A. Kuzmich, "Storage and retrieval of single photons transmitted between remote quantum memories," *Nature*, vol. 438, p. 833, 2005.

[23] J. K. Thompson, J. Simon, H. Loh, and V. Vuletić, "A High-Brightness Source of Narrowband, Identical-Photon Pairs," *Science*, vol. 313, p. 74, 2006.

[24] C. W. Chou, H. De Riedmatten, D. Felinto, S. V. Polyakov, S. J. van Enk, and H. J. Kimble, "Measurement-induced entanglement for excitation stored in remote atomic ensembles," *Nature*, vol. 438, p. 828, 2005.

[25] J. Simon, H. Tanji, S. Ghosh, and V. Vuletić, "Single-photon bus connecting spin-wave quantum memories," *Nature Physics*, vol. 3, p. 765, 2007.

[26] K. S. Choi, H. Deng, J. Laurat, and H. J. Kimble, "Mapping photonic entanglement into and out of a quantum memory," *Nature*, vol. 452, p. 67, 2008.

[27] R. Zhao, Y. O. Dudin, S. D. Jenkins, C. J. Campbell, D. N. Matsukevich, T. A. B. Kennedy, and A. Kuzmich, "Long-lived quantum memory," *Nature Physics*, vol. 5, p. 100, 2008.

[28] B. Zhao, Y.-A. Chen, X.-H. Bao, T. Strassel, C.-S. Chuu, X.-M. Jin, J. Schmiedmayer, Z.-S. Yuan, S. Chen, and J.-W. Pan, "A millisecond quantum memory for scalable quantum networks," *Nature Physics*, vol. 5, p. 95, 2008.

[29] U. Schnorrberger, J. D. Thompson, S. Trotzky, R. Pugatch, N. Davidson, S. Kuhr, and I. Bloch, "Electromagnetically Induced Transparency and Light Storage in an Atomic Mott Insulator," *Physical Review Letters*, vol. 103, p. 033003, 2009.

[30] R. Zhang, S. R. Garner, and L. V. Hau, "Creation of Long-Term Coherent Optical Memory via Controlled Nonlinear Interactions in Bose-Einstein Condensates," *Physical Review Letters*, vol. 103, p. 233602, 2009.

[31] P. Lougovski, S. J. van Enk, K. S. Choi, S. B. Papp, H. Deng, and H. J. Kimble, "Verifying multipartite mode entanglement of W states," *New Journal of Physics*, vol. 11, p. 063029, 2009.

[32] S. B. Papp, K. S. Choi, H. Deng, P. Lougovski, S. J. van Enk, and H. J. Kimble, "Characterization of multipartite entanglement for one photon shared among four optical modes," *Science*, vol. 324, p. 764, 2009.

[33] K. S. Choi, A. Goban, S. B. Papp, S. J. van Enk, and H. J. Kimble, "Entanglement of spin waves among four quantum memories," *Nature*, vol. 468, p. 412, 2010.

[34] T. Aoki, B. Dayan, E. Wilcut, W. P. Bowen, A. S. Parkins, T. J. Kippenberg, K. J. Vahala, and H. J. Kimble, "Observation of strong coupling between one atom and a monolithic microresonator," *Nature*, vol. 443, p. 671, 2006.

[35] B. Dayan, A. S. Parkins, T. Aoki, E. P. Ostby, K. J. Vahala, and H. J. Kimble, "A Photon Turnstile Dynamically Regulated by One Atom," *Science*, vol. 319, p. 1062, 2008.

[36] I. Shomroni, S. Rosenblum, Y. Lovsky, O. Bechler, G. Guendelman, and B. Dayan, "All-optical routing of single photons by a one-atom switch controlled by a single photon," *Science*, vol. 345, p. 903, 2014.

[37] C. Junge, D. O'Shea, J. Volz, and A. Rauschenbeutel, "Strong Coupling between Single Atoms and Nontransversal Photons," *Physical Review Letters*, vol. 110, p. 213604, 2013.

[38] J. Volz, R. Gehr, G. Dubois, J. Estève, and J. Reichel, "Measurement of the internal state of a single atom without energy exchange," *Nature*, vol. 475, p. 210, 2011.

[39] M. Steiner, H. M. Meyer, C. Deutsch, J. Reichel, and M. Köhl, "Single Ion Coupled to an Optical Fiber Cavity," *Physical Review Letters*, vol. 110, p. 043003, 2013.

[40] J. D. Thompson, T. G. Tiecke, N. P. de Leon, J. Feist, A. V. Akimov, M. Gullans, A. S. Zibrov, V. Vuletić, and M. D. Lukin, "Coupling a Single Trapped Atom to a Nanoscale Optical Cavity," *Science*, vol. 340, p. 1202, 2013.

[41] L. M. Duan and H. J. Kimble, "Scalable photonic quantum computation through cavity-assisted interactions," *Physical Review Letters*, vol. 92, p. 127902, 2004.

[42] T. G. Tiecke, J. D. Thompson, N. P. de Leon, L. R. Liu, V. Vuletić, and M. D. Lukin, "Nanophotonic quantum phase switch with a single atom," *Nature*, vol. 508, p. 241, 2014.

[43] P. Michler, A. Kiraz, C. Becher, W. V. Schoenfeld, P. M. Petroff, L. Zhang, E. Hu, and A. Imamoglu, "A Quantum Dot Single-Photon Turnstile Device," *Science*, vol. 290, p. 2282, 2000.

[44] Z. Yuan, B. E. Kardynal, R. M. Stevenson, A. J. Shields, C. J. Lobo, K. Cooper, N. S. Beattie, D. A. Ritchie, and M. Pepper, "Electrically Driven Single-Photon Source," *Science*, vol. 295, p. 102, 2002.

[45] I. Fushman, D. Englund, A. Faraon, N. Stoltz, P. Petroff, and J. Vuckovic, "Controlled phase shifts with a single quantum dot," *Science*, vol. 320, p. 769, 2008.

[46] D. Englund, B. Shields, K. Rivoire, F. Hatami, J. Vuckovic, H. Park, and M. D. Lukin, "Deterministic Coupling of a Single Nitrogen Vacancy Center to a Photonic Crystal Cavity," *Nano Letters*, vol. 10, p. 3922, 2010.

[47] A. Faraon, P. E. Barclay, C. Santori, K.-M. C. Fu, and R. G. Beausoleil, "Resonant enhancement of the zero-phonon emission from a colour centre in a diamond cavity," *Nature Photonics*, vol. 5, p. 301, 2011.

[48] B. J. M. Hausmann, B. Shields, Q. Quan, P. Maletinsky, M. McCutcheon, J. T. Choy, T. M. Babinec, A. Kubanek, A. Yacoby, M. D. Lukin, and M. Loncar, "Integrated Diamond Networks for Quantum Nanophotonics," *Nano Letters*, vol. 12, p. 1578, 2012.

[49] T. Volz, A. Reinhard, M. Winger, A. Badolato, K. J. Hennessy, E. L. Hu, and A. Imamoglu, "Ultrafast all-optical switching by single photons," *Nature Photonics*, vol. 6, p. 605, 2012.

[50] A. Reinhard, T. Volz, M. Winger, A. Badolato, K. J. Hennessy, E. L. Hu, and A. Imamoglu, "Strongly correlated photons on a chip," *Nature Photonics*, vol. 6, p. 93, 2012.

[51] A. V. Akimov, A. Mukherjee, C. L. Yu, D. E. Chang, and A. S. Zibrov, "Generation of single optical plasmons in metallic nanowires coupled to quantum dots," *Nature*, vol. 450, p. 402, 2007.

[52] M. Bajcsy, S. Hofferberth, V. Balic, T. Peyronel, M. Hafezi, A. Zibrov, V. Vuletić, and M. Lukin, "Efficient All-Optical Switching Using Slow Light within a Hollow Fiber," *Physical Review Letters*, vol. 102, p. 203902, 2009.

[53] S. Okaba, T. Takano, F. Benabid, T. Bradley, L. Vincetti, Z. Maizelis, V. Yampol'skii, F. Nori, and H. Katori, "Lamb-Dicke spectroscopy of atoms in a hollow-core photonic crystal fibre," *Nature Communications*, vol. 5, p. 4096, 2014.

[54] R. Yalla, F. Le Kien, M. Morinaga, and K. Hakuta, "Efficient Channeling of Fluorescence Photons from Single Quantum Dots into Guided Modes of Optical Nanofiber," *Physical Review Letters*, vol. 109, p. 063602, 2012.

[55] J. Claudon, J. Bleuse, N. S. Malik, M. Bazin, P. Jaffrennou, N. Gregersen, C. Sauvan, P. Lalanne, and J.-M. Gerard, "A highly efficient single-photon source based on a quantum dot in a photonic nanowire," *Nature Photonics*, vol. 4, p. 174, 2010.

[56] T. M. Babinec, B. J. M. Hausmann, M. Khan, Y. Zhang, J. R. Maze, P. R. Hemmer, and M. Loncar, "A diamond nanowire single-photon source," *Nature Nanotechnology*, vol. 5, p. 195, 2010.

[57] J. Bleuse, J. Claudon, M. Creasey, N. S. Malik, J.-M. Gerard, I. Maksymov, J.-P. Hugonin, and P. Lalanne, "Inhibition, Enhancement, and Control of Spontaneous Emission in Photonic Nanowires," *Physical Review Letters*, vol. 106, p. 103601, 2011.

[58] O. Astafiev, A. M. Zagoskin, A. A. J. Abdumalikov, Y. A. Pashkin, T. Yamamoto, K. Inomata, Y. Nakamura, and J. S. Tsai, "Resonance Fluorescence of a Single Artificial Atom," *Science*, vol. 327, p. 840, 2010.

[59] I.-C. Hoi, T. Palomaki, J. Lindkvist, G. Johansson, P. Delsing, and C. M. Wilson, "Generation of Nonclassical Microwave States Using an Artificial Atom in 1D Open Space," *Physical Review Letters*, vol. 108, p. 263601, 2012.

[60] A. F. van Loo, A. Fedorov, K. Lalumière, B. C. Sanders, A. Blais, and A. Wallraff, "Photon-Mediated Interactions Between Distant Artificial Atoms," *Science*, vol. 342, p. 1494, 2013.

[61] E. Vetsch, D. Reitz, G. Sagué, R. Schmidt, S. T. Dawkins, and A. Rauschenbeutel, "Optical Interface Created by Laser-Cooled Atoms Trapped in the Evanescent Field Surrounding an Optical Nanofiber," *Physical Review Letters*, vol. 104, p. 203603, 2010.

[62] S. T. Dawkins, R. Mitsch, D. Reitz, E. Vetsch, and A. Rauschenbeutel, "Dispersive Optical Interface Based on Nanofiber-Trapped Atoms," *Physical Review Letters*, vol. 107, p. 243601, 2011.

[63] C. Lacroûte, K. S. Choi, A. Goban, D. J. Alton, D. Ding, N. P. Stern, and H. J. Kimble, "A state-insensitive, compensated nanofiber trap," *New Journal of Physics*, vol. 14, p. 023056, 2012.

[64] A. Goban, K. S. Choi, D. J. Alton, D. Ding, C. Lacroûte, M. Pototschnig, T. Thiele, N. P. Stern, and H. J. Kimble, "Demonstration of a State-Insensitive, Compensated Nanofiber Trap," *Physical Review Letters*, vol. 109, p. 033603, 2012.

[65] D. Ding, A. Goban, K. S. Choi, and H. J. Kimble, "Corrections to our results for optical nanofiber traps in cesium," *arXiv:1212.4941*, 2012.

[66] R. Mitsch, C. Sayrin, B. Albrecht, P. Schneeweiss, and A. Rauschenbeutel, "Quantum state-controlled directional spontaneous emission of photons into a nanophotonic waveguide," *Nature Communications*, vol. 5, p. 5713, 2014.

[67] J. B. Beguin, E. M. Bookjans, S. L. Christensen, H. L. Sørensen, J. H. Mueller, E. S. Polzik, and J. Appel, "Generation and Detection of a Sub-Poissonian Atom Number Distribution in a One-Dimensional Optical Lattice," *Physical Review Letters*, vol. 113, p. 263603, 2014.

[68] T. Baba, "Slow light in photonic crystals," *Nature Photonics*, vol. 2, p. 465, 2008.

[69] A. Laucht, S. Putz, T. Günthner, N. Hauke, R. Saive, S. Frédérick, M. Bichler, M. C. Amann, A. W. Holleitner, M. Kaniber, and J. J. Finley, "A Waveguide-Coupled On-Chip Single-Photon Source," *Physical Review X*, vol. 2, p. 011014, 2012.

[70] M. Arcari, I. Söllner, A. Javadi, S. Lindskov Hansen, S. Mahmoodian, J. Liu, H. Thyrrestrup, E. H. Lee, J. D. Song, S. Stobbe, and P. Lodahl, "Near-Unity Coupling Efficiency of a Quantum Emitter to a Photonic Crystal Waveguide," *Physical Review Letters*, vol. 113, p. 093603, 2014.

[71] J.-T. Shen and S. Fan, "Coherent Single Photon Transport in a One-Dimensional Waveguide Coupled with Superconducting Quantum Bits," *Physical Review Letters*, vol. 95, p. 213001, 2005.

[72] J.-T. Shen and S. Fan, "Strongly Correlated Two-Photon Transport in a One-Dimensional Waveguide Coupled to a Two-Level System," *Physical Review Letters*, vol. 98, p. 153003, 2007.

[73] H. Zheng, D. J. Gauthier, and H. U. Baranger, "Cavity-Free Photon Blockade Induced by Many-Body Bound States," *Physical Review Letters*, vol. 107, p. 223601, 2011.

[74] D. E. Chang, A. S. S. Sørensen, E. A. Demler, and M. D. Lukin, "A single-photon transistor using nanoscale surface plasmons," *Nature Physics*, vol. 3, p. 807, 2007.

[75] P. Longo, P. Schmitteckert, and K. Busch, "Few-Photon Transport in Low-Dimensional Systems: Interaction-Induced Radiation Trapping," *Physical Review Letters*, vol. 104, p. 023602, 2010.

[76] P. Kolchin, R. F. Oulton, and X. Zhang, "Nonlinear Quantum Optics in a Waveguide: Distinct Single Photons Strongly Interacting at the Single Atom Level," *Physical Review Letters*, vol. 106, p. 113601, 2011.

[77] H. Zheng and H. U. Baranger, "Persistent Quantum Beats and Long-Distance Entanglement from Waveguide-Mediated Interactions," *Physical Review Letters*, vol. 110, p. 113601, 2013.

[78] M. J. Hartmann, F. G. S. L. Brandão, and M. B. Plenio, "Strongly interacting polaritons in coupled arrays of cavities," *Nature Physics*, vol. 2, p. 849, 2006.

[79] A. D. Greentree, C. Tahan, J. H. Cole, and L. C. L. Hollenberg, "Quantum phase transitions of light," *Nature Physics*, vol. 2, p. 856, 2006.

[80] M. J. Hartmann and F. Brandao, "Quantum many-body phenomena in coupled cavity arrays," *Laser & Photonics Reviews*, vol. 2, p. 527, 2008.

[81] D. E. Chang, V. Gritsev, G. Morigi, V. Vuletić, M. D. Lukin, and E. A. Demler, "Crystallization of strongly interacting photons in a nonlinear optical fibre," *Nature Physics*, vol. 4, p. 884, 2008.

[82] A. V. Gorshkov, J. Otterbach, M. Fleischhauer, T. Pohl, and M. D. Lukin, "Photon-Photon Interactions via Rydberg Blockade," *Physical Review Letters*, vol. 107, p. 133602, 2011.

[83] J. Otterbach, M. Moos, D. Muth, and M. Fleischhauer, "Wigner Crystallization of Single Photons in Cold Rydberg Ensembles," *Physical Review Letters*, vol. 111, p. 113001, 2013.

[84] S. John and J. Wang, "Quantum electrodynamics near a photonic band gap: Photon bound states and dressed atoms," *Physical Review Letters*, vol. 64, p. 2418, 1990.

[85] E. Shahmoon and G. Kurizki, "Nonradiative interaction and entanglement between distant atoms," *Physical Review A*, vol. 87, p. 033831, 2013.

[86] E. Shahmoon and G. Kurizki, "Nonlinear theory of laser-induced dipolar interactions in arbitrary geometry," *Physical Review A*, vol. 89, p. 043419, 2014.

[87] J. S. Douglas, H. Habibian, C. L. Hung, A. V. Gorshkov, H. J. Kimble, and D. E. Chang, "Quantum many-body models with cold atoms coupled to photonic crystals," *Nature Photonics*, vol. 9, p. 326, 2015.

[88] D. E. Chang, K. Sinha, J. M. Taylor, and H. J. Kimble, "Trapping atoms using nanoscale quantum vacuum forces," *Nature Communications*, vol. 5, p. 4343, 2014.

[89] B. Weber, H. P. Specht, T. Mueller, J. Bochmann, M. Muecke, D. L. Moehring, and G. Rempe, "Photon-Photon Entanglement with a Single Trapped Atom," *Physical Review Letters*, vol. 102, p. 030501, 2009.

[90] M. Steffen, M. Ansmann, R. C. Bialczak, N. Katz, E. Lucero, R. McDermott, M. Neeley, E. M. Weig, A. N. Cleland, and J. M. Martinis, "Measurement of the entanglement of two superconducting qubits via state tomography," *Science*, vol. 313, p. 1423, 2006.

[91] D. L. Moehring, P. Maunz, S. Olmschenk, K. C. Younge, D. N. Matsukevich, L. M. Duan, and C. Monroe, "Entanglement of single-atom quantum bits at a distance," *Nature*, vol. 449, p. 68, 2007.

[92] L. DiCarlo, J. M. Chow, J. M. Gambetta, L. S. Bishop, B. R. Johnson, D. I. Schuster, J. Majer, A. Blais, L. Frunzio, S. M. Girvin, and R. J. Schoelkopf, "Demonstration of two-qubit algorithms with a superconducting quantum processor," *Nature*, vol. 460, p. 240, 2009.

[93] J. D. Jost, J. P. Home, J. M. Amini, D. Hanneke, R. Ozeri, C. Langer, J. J. Bollinger, D. Leibfried, and D. J. Wineland, "Entangled mechanical oscillators," *Nature*, vol. 459, p. 683, 2009.

[94] L. Amico, A. Osterloh, and V. Vedral, "Entanglement in many-body systems," *Reviews of Modern Physics*, vol. 80, p. 517, 2008.

[95] O. Gühne and G. Tóth, "Entanglement detection," *Physics Reports*, vol. 474, p. 1, 2009.

[96] R. Horodecki, M. Horodecki, and K. Horodecki, "Quantum entanglement," *Reviews of Modern Physics*, vol. 81, p. 865, 2009.

[97] S. J. van Enk, N. Lutkenhaus, and H. J. Kimble, "Experimental procedures for entanglement verification," *Physical Review A*, vol. 75, p. 052318, 2007.

[98] D. Leibfried, E. Knill, S. Seidelin, J. Britton, R. B. Blakestad, J. Chiaverini, D. B. Hume, W. M. Itano, J. D. Jost, C. Langer, R. Ozeri, R. Reichle, and D. J. Wineland, "Creation of a six-atom 'Schrodinger cat' state," *Nature*, vol. 438, p. 639, 2005.

[99] H. Haffner, W. Hansel, C. F. Roos, J. Benhelm, D. Chek-al kar, M. Chwalla, T. Korber, U. D. Rapol, M. Riebe, P. O. Schmidt, C. Becher, O. Gühne, W. Dür, and R. Blatt, "Scalable multiparticle entanglement of trapped ions," *Nature*, vol. 438, p. 643, 2005.

[100] T. Aoki, N. Takei, H. Yonezawa, K. Wakui, T. Hiraoka, A. Furusawa, and P. van Loock, "Experimental creation of a fully inseparable tripartite continuous-variable state," *Physical Review Letters*, vol. 91, p. 080404, 2003.

[101] X. Su, A. Tan, X. Jia, J. Zhang, C. Xie, and K. Peng, "Experimental preparation of quadripartite cluster and Greenberger-Horne-Zeilinger entangled states for continuous variables," *Physical Review Letters*, vol. 98, p. 070502, 2007.

[102] W.-B. Gao, C.-Y. Lu, X.-C. Yao, P. Xu, O. Guehne, A. Goebel, Y.-A. Chen, C.-Z. Peng, Z.-B. Chen, and J.-W. Pan, "Experimental demonstration of a hyper-entangled ten-qubit Schrodinger cat state," *Nature Physics*, vol. 6, p. 331, 2010.

[103] A. I. Lvovsky, B. C. Sanders, and W. Tittel, "Optical quantum memory," *Nature Photonics*, vol. 3, p. 706, 2009.

[104] P. Lougovski, S. J. van Enk, K. S. Choi, S. B. Papp, H. Deng, and H. J. Kimble, "Verifying multipartite mode entanglement of W states," *New Journal of Physics*, vol. 11, p. 063029, 2009.

[105] J. Simon, H. Tanji, J. K. Thompson, and V. Vuletić, "Interfacing Collective Atomic Excitations and Single Photons," *Physical Review Letters*, vol. 98, p. 183601, 2007.

[106] H. F. Hofmann and S. Takeuchi, "Violation of local uncertainty relations as a signature of entanglement," *Physical Review A*, vol. 68, p. 032103, 2003.

[107] L. Heaney, A. Cabello, M. F. Santos, and V. Vedral, "Extreme nonlocality with one photon," *New Journal of Physics*, vol. 13, p. 053054, 2011.

[108] V. Balic, D. A. Braje, P. Kolchin, G. Y. Yin, and S. E. Harris, "Generation of paired photons with controllable waveforms," *Physical Review Letters*, vol. 94, p. 183601, 2005.

[109] J. Eisert, C. Simon, and M. B. Plenio, "On the quantification of entanglement in infinite-dimensional quantum systems," *Journal of Physics a-Mathematical and General*, vol. 35, p. 3911, 2002.

[110] C.-W. Chou, J. Laurat, H. Deng, K. S. Choi, H. de Riedmatten, D. Felinto, and H. J. Kimble, "Functional quantum nodes for entanglement distribution over scalable quantum networks," *Science*, vol. 316, p. 1316, 2007.

[111] J. Laurat, C. Chou, H. Deng, K. S. Choi, D. Felinto, H. d. Riedmatten, and H. J. Kimble, "Towards experimental entanglement connection with atomic ensembles in the single excitation regime," *New Journal of Physics*, vol. 9, p. 207, 2007.

[112] K. Hammerer, A. S. Sørensen, and E. S. Polzik, "Quantum interface between light and atomic ensembles," *Reviews of Modern Physics*, vol. 82, p. 1041, 2010.

[113] Y. Colombe, T. Steinmetz, G. Dubois, F. Linke, D. Hunger, and J. Reichel, "Strong atom-field coupling for Bose-Einstein condensates in an optical cavity on a chip," *Nature*, vol. 450, p. 272, 2007.

[114] C. Deutsch, F. Ramirez-Martinez, C. Lacroûte, F. Reinhard, T. Schneider, J. N. Fuchs, F. Piechon, F. Laloe, J. Reichel, and P. Rosenbusch, "Spin Self-Rephasing and Very Long Coherence Times in a Trapped Atomic Ensemble," *Physical Review Letters*, vol. 105, p. 020401, 2010.

[115] N. Sangouard, C. Simon, H. de Riedmatten, and N. Gisin, "Quantum repeaters based on atomic ensembles and linear optics," *Reviews of Modern Physics*, vol. 83, p. 33, 2011.

[116] I. D. Ivanovic, "How to differentiate between non-orthogonal states," *Physics Letters A*, vol. 123, p. 257, 1987.

[117] D. Dieks, "Overlap and Distinguishability of Quantum States," *Physics Letters A*, vol. 126, p. 303, 1988.

[118] A. Peres, "How to Differentiate Between Non-Orthogonal States," *Physics Letters A*, vol. 128, p. 19, 1988.

[119] A. Chefles, "Unambiguous discrimination between linearly independent quantum states," *Physics Letters A*, vol. 239, p. 339, 1998.

[120] F. Le Kien, S. Dutta Gupta, V. I. Balykin, and K. Hakuta, "Spontaneous emission of a cesium atom near a nanofiber: Efficient coupling of light to guided modes," *Physical Review A*, vol. 72, p. 032509, 2005.

[121] H. Zheng, D. J. Gauthier, and H. U. Baranger, "Waveguide QED: Many-body bound-state effects in coherent and Fock-state scattering from a two-level system," *Physical Review A*, vol. 82, p. 063816, 2010.

[122] J. D. Hood *in preparation*, 2015.

[123] I. Deutsch, R. Spreeuw, S. Rolston, and W. Phillips, "Photonic band gaps in optical lattices," *Physical Review A*, vol. 52, p. 1394, 1995.

[124] D. E. Chang, L. Jiang, A. V. Gorshkov, and H. J. Kimble, "Cavity QED with atomic mirrors," *New Journal of Physics*, vol. 14, p. 063003, 2012.

[125] T. Caneva, M. T. Manzoni, T. Shi, J. S. Douglas, J. I. Cirac, and D. E. Chang, "Quantum dynamics of propagating photons with strong interactions: a generalized input-output formalism," *arXiv:1501.04427*, 2015.

[126] F. Le Kien, S. Gupta, K. Nayak, and K. Hakuta, "Nanofiber-mediated radiative transfer between two distant atoms," *Physical Review A*, vol. 72, p. 063815, 2005.

[127] F. Le Kien and K. Hakuta, "Cooperative enhancement of channeling of emission from atoms into a nanofiber," *Physical Review A*, vol. 77, p. 013801, 2008.

[128] K. Lalumière, B. C. Sanders, A. F. van Loo, A. Fedorov, A. Wallraff, and A. Blais, "Input-output theory for waveguide QED with an ensemble of inhomogeneous atoms," *Physical Review A*, vol. 88, p. 043806, 2013.

[129] M. Gross and S. Haroche, "Superradiance: an essay on the theory of collective spontaneous emission," *Physics Reports*, vol. 93, p. 301, 1982.

[130] M. J. Renn, D. Montgomery, O. Vdovin, D. Z. Anderson, C. E. Wieman, and E. A. Cornell, "Laser-Guided Atoms in Hollow-Core Optical Fibers," *Physical Review Letters*, vol. 75, p. 3253, 1995.

[131] H. Ito, T. Nakata, K. Sakaki, M. Ohtsu, K. Lee, and W. Jhe, "Laser Spectroscopy of Atoms Guided by Evanescent Waves in Micron-Sized Hollow Optical Fibers," *Physical Review Letters*, vol. 76, p. 4500, 1996.

[132] C. Christensen, S. Will, M. Saba, G.-B. Jo, Y.-I. Shin, W. Ketterle, and D. Pritchard, "Trapping of ultracold atoms in a hollow-core photonic crystal fiber," *Physical Review A*, vol. 78, p. 033429, 2008.

[133] F. L. Kien, J. Q. Liang, K. Hakuta, and V. I. Balykin, "Field intensity distributions and polarization orientations in a vacuum-clad subwavelength-diameter optical fiber," *Optics Communications*, vol. 242, p. 445, 2004.

[134] K. P. Nayak, P. N. Melentiev, M. Morinaga, F. Le Kien, V. I. Balykin, and K. Hakuta, "Optical nanofiber as an efficient tool for manipulating and probing atomic fluorescence," *Optics Express*, vol. 15, p. 5431, 2007.

[135] G. Sagué, E. Vetsch, W. Alt, D. Meschede, and A. Rauschenbeutel, "Cold-Atom Physics Using Ultrathin Optical Fibers: Light-Induced Dipole Forces and Surface Interactions," *Physical Review Letters*, vol. 99, p. 163602, 2007.

[136] V. I. Balykin, V. S. Letokhov, Y. B. Ovchinnikov, and A. I. SIDOROV, "Quantum-State Selective Mirror Reflection of Atoms by Laser-Light," *Physical Review Letters*, vol. 60, p. 2137, 1988.

[137] A. D. Cronin, J. Schmiedmayer, and D. E. Pritchard, "Optics and interferometry with atoms and molecules," *Reviews of Modern Physics*, vol. 81, p. 1051, 2009.

[138] Y. B. Ovchinnikov, I. Manek, and R. Grimm, "Surface trap for Cs atoms based on evanescent-wave cooling," *Physical Review Letters*, vol. 79, p. 2225, 1997.

[139] D. Rychtarik, B. Engeser, H. C. Nagerl, and R. Grimm, "Two-dimensional Bose-Einstein condensate in an optical surface trap," *Physical Review Letters*, vol. 92, p. 173003, 2004.

[140] W. S. Bakr, A. Peng, M. E. Tai, R. Ma, J. Simon, J. I. Gillen, S. Fölling, L. Pollet, and M. Greiner, "Probing the Superfluid–to–Mott Insulator Transition at the Single-Atom Level," *Science*, vol. 329, p. 547, 2010.

[141] A. Boozer, A. Boca, R. Miller, T. Northup, and H. Kimble, "Reversible State Transfer between Light and a Single Trapped Atom," *Physical Review Letters*, vol. 98, p. 193601, 2007.

[142] P. E. Barclay, K. Srinivasan, O. Painter, B. Lev, and H. Mabuchi, "Integration of fiber-coupled high-Q SiN_x microdisks with atom chips," *Applied Physics Letters*, vol. 89, p. 131108, 2006.

[143] M. Trupke, J. Goldwin, B. Darquie, G. Dutier, S. Eriksson, J. Ashmore, and E. A. Hinds, "Atom detection and photon production in a scalable, open, optical microcavity," *Physical Review Letters*, vol. 99, p. 063601, 2007.

[144] D. J. Alton, N. P. Stern, T. Aoki, H. Lee, E. Ostby, and K. J. Vahala, "Strong interactions of single atoms and photons near a dielectric boundary," *Nature Physics*, vol. 7, p. 159, 2011.

[145] N. P. Stern, D. J. Alton, and H. J. Kimble, "Simulations of atomic trajectories near a dielectric surface," *New Journal of Physics*, vol. 13, p. 085004, 2011.

[146] J. T. Shen and S. H. Fan, "Coherent photon transport from spontaneous emission in one-dimensional waveguides," *Optics letters*, vol. 30, p. 2001, 2005.

[147] H. Zoubi and H. Ritsch, "Hybrid quantum system of a nanofiber mode coupled to two chains of optically trapped atoms," *New Journal of Physics*, vol. 12, p. 103014, 2010.

[148] T. Kitagawa, M. A. Broome, A. Fedrizzi, M. S. Rudner, E. Berg, I. Kassal, A. Aspuru-Guzik, E. Demler, and A. G. White, "Observation of topologically protected bound states in photonic quantum walks," *Nature Communications*, vol. 3, p. 882, 2012.

[149] K. Corwin, S. Kuppens, D. Cho, and C. Wieman, "Spin-Polarized Atoms in a Circularly Polarized Optical Dipole Trap," *Physical Review Letters*, vol. 83, p. 1311, 1999.

[150] J. Ye, H. J. Kimble, and H. Katori, "Quantum State Engineering and Precision Metrology Using State-Insensitive Light Traps," *Science*, vol. 320, p. 1734, 2008.

[151] T. Ido, Y. Isoya, and H. Katori, "Optical-dipole trapping of Sr atoms at a high phase-space density," *Physical Review A*, vol. 61, p. 061403(R), 2000.

[152] J. McKeever, J. R. Buck, A. D. Boozer, A. Kuzmich, H. C. Nagerl, D. M. Stamper-Kurn, and H. J. Kimble, "State-insensitive cooling and trapping of single atoms in an optical cavity," *Physical Review Letters*, vol. 90, p. 133602, 2003.

[153] F. Le Kien, V. I. Balykin, and K. Hakuta, "State-insensitive trapping and guiding of cesium atoms using a two-color evanescent field around a subwavelength-diameter fiber," *Journal of the Physical Society of Japan*, vol. 74, p. 910, 2005.

[154] D. J, N. Polonsky, C. C, and A. Kastler, "Lifting of a Zeeman Degeneracy by Interaction with a Light Beam," *Physics Letters A*, vol. 25, p. 87, 1967.

[155] D. Felinto, C. W. Chou, H. De Riedmatten, S. V. Polyakov, and H. J. Kimble, "Control of decoherence in the generation of photon pairs from atomic ensembles," *Physical Review A*, vol. 72, p. 053809, 2005.

[156] V. I. Balykin, K. Hakuta, F. Le Kien, J. Q. Liang, and M. Morinaga, "Atom trapping and guiding with a subwavelength-diameter optical fiber," *Physical Review A*, vol. 70, p. 011401, 2004.

[157] P. Rosenbusch, S. Ghezali, V. Dzuba, V. Flambaum, K. Beloy, and A. Derevianko, "ac Stark shift of the Cs microwave atomic clock transitions," *Physical Review A*, vol. 79, p. 013404, 2009.

[158] F. Le Kien, P. Schneeweiss, and A. Rauschenbeutel, "Dynamical polarizability of atoms in arbitrary light fields: general theory and application to cesium," *The European Physical Journal D*, vol. 67, p. 1, 2013.

[159] J. M. Geremia, J. K. Stockton, and H. Mabuchi, "Tensor polarizability and dispersive quantum measurement of multilevel atoms," *Physical Review A*, vol. 73, p. 042112, 2006.

[160] R. Chicireanu, K. D. Nelson, S. Olmschenk, N. Lundblad, A. Derevianko, and J. V. Porto, "Differential Light-Shift Cancellation in a Magnetic-Field-Insensitive Transition of Rb_{87}," *Physical Review Letters*, vol. 106, p. 063002, 2011.

[161] L. Tong, J. Lou, and E. Mazur, "Single-mode guiding properties of subwavelength-diameter silica and silicon wire waveguides," *Optics Express*, vol. 12, p. 1025, 2004.

[162] G. Sagué, A. Baade, and A. Rauschenbeutel, "Blue-detuned evanescent field surface traps for neutral atoms based on mode interference in ultrathin optical fibres," *New Journal of Physics*, vol. 10, p. 113008, 2008.

[163] M. M. Ashraf, "The effects of phase and Stark shift on two-photon process," *Journal of Optics B: Quantum and Semiclassical Optics*, vol. 3, p. 39, 2001.

[164] T. Savard, K. O'Hara, and J. Thomas, "Laser-noise-induced heating in far-off resonance optical traps," *Physical Review A*, vol. 56, p. 1095(R), 1997.

[165] H. Katori, M. Takamoto, V. Pal'chikov, and V. Ovsiannikov, "Ultrastable Optical Clock with Neutral Atoms in an Engineered Light Shift Trap," *Physical Review Letters*, vol. 91, p. 173005, 2003.

[166] B. Arora, M. Safronova, and C. Clark, "Magic wavelengths for the $np - ns$ transitions in alkali-metal atoms," *Physical Review A*, vol. 76, p. 052509, 2007.

[167] D. DiBerardino, C. E. Tanner, and A. Sieradzan, "Lifetime measurements of cesium $5d^2D_{5/2,3/2}$ and $11s^2S_{1/2}$ states using pulsed-laser excitation," *Physical Review A*, vol. 57, p. 4204, 1998.

[168] V. Sandoghdar, C. Sukenik, E. Hinds, and S. Haroche, "Direct measurement of the van der Waals interaction between an atom and its images in a micron-sized cavity," *Physical Review Letters*, vol. 68, p. 3432, 1992.

[169] C. Sukenik, M. Boshier, D. Cho, V. Sandoghdar, and E. Hinds, "Measurement of the Casimir-Polder force," *Physical Review Letters*, vol. 70, p. 560, 1993.

[170] E. A. Hinds, K. S. Lai, and M. Schnell, "Atoms in micron-sized metallic and dielectric waveguides," *Philosophical Transactions of the Royal Society a-Mathematical Physical and Engineering Sciences*, vol. 355, p. 2353, 1997.

[171] M. Bordag, U. Mohideen, and V. M. Mostepanenko, "New developments in the Casimir effect," *Physics Reports*, vol. 353, p. 1, 2001.

[172] T. Emig, R. L. Jaffe, M. Kardar, and A. Scardicchio, "Casimir Interaction between a Plate and a Cylinder," *Physical Review Letters*, vol. 96, p. 080403, 2006.

[173] A. Laliotis, I. Maurin, and P. Todorov, "Testing the distance-dependence of the van der Waals interaction between an atom and a surface through spectroscopy in a vapor nanocell," *Proc. SPIE 6604,14th International School on Quantum Electronics: Laser Physics and Applications*, p. 660406, 2007.

[174] A. Stiebeiner, R. Garcia-Fernandez, and A. Rauschenbeutel, "Design and optimization of broadband tapered optical fibers with a nanofiber waist," *Optics Express*, vol. 18, p. 22677, 2010.

[175] T. Aoki, "Fabrication of Ultralow-Loss Tapered Optical Fibers and Microtoroidal Resonators," *Japanese Journal of Applied Physics*, vol. 49, p. 118001, 2010.

[176] M. Eichenfield, J. Chan, R. M. Camacho, and K. J. Vahala, "Optomechanical crystals," *Nature*, vol. 462, p. 78, 2009.

[177] M. Wallquist, K. Hammerer, P. Rabl, M. Lukin, and P. Zoller, "Hybrid quantum devices and quantum engineering," *Physica Scripta*, vol. T137, p. 014001, 2009.

[178] K. J. Vahala, "Optical microcavities," *Nature*, vol. 424, p. 839, 2003.

[179] Y. B. Ovchinnikov, S. V. Shul'ga, and V. I. Balykin, "An atomic trap based on evanescent light waves," *Journal of Physics B: Atomic, Molecular and Optical Physics*, vol. 24, p. 3173, 1991.

[180] D. W. Vernooy and H. J. Kimble, "Quantum structure and dynamics for atom galleries," *Physical Review A*, vol. 55, p. 1239, 1997.

[181] J. Burke, S.-T. Chu, G. Bryant, C. Williams, and P. Julienne, "Designing neutral-atom nanotraps with integrated optical waveguides," *Physical Review A*, vol. 65, p. 043411, 2002.

[182] N. Schlosser, G. Reymond, I. Protsenko, and P. Grangier, "Sub-poissonian loading of single atoms in a microscopic dipole trap," *Nature*, vol. 411, p. 1024, 2001.

[183] M. Eichenfield, R. Camacho, J. Chan, K. J. Vahala, and O. Painter, "A picogram- and nanometre-scale photonic-crystal optomechanical cavity," *Nature*, vol. 459, p. 550, 2009.

[184] I. H. Deutsch, "Quantum-state control in optical lattices," *Physical Review A*, vol. 57, p. 1972, 1998.

[185] M. J. Renn, D. Montgomery, O. Vdovin, D. Z. Anderson, C. E. Wieman, and others, "Laser-Guided Atoms in Hollow-Core Optical Fibers," *Physical Review Letters*, vol. 75, p. 3253, 1995.

[186] P. Londero, V. Venkataraman, A. Bhagwat, A. Slepkov, and A. Gaeta, "Ultralow-Power Four-Wave Mixing with Rb in a Hollow-Core Photonic Band-Gap Fiber," *Physical Review Letters*, vol. 103, p. 043602, 2009.

[187] F. Le Kien, V. I. Balykin, and K. Hakuta, "Atom trap and waveguide using a two-color evanescent light field around a subwavelength-diameter optical fiber," *Physical Review A*, vol. 70, p. 063403, 2004.

[188] D. Chang, J. Thompson, H. Park, V. Vuletić, A. Zibrov, P. Zoller, and M. Lukin, "Trapping and Manipulation of Isolated Atoms Using Nanoscale Plasmonic Structures," *Physical Review Letters*, vol. 103, p. 123004, 2009.

[189] E. Vetsch, *Optical interface based on a nanofiber atom-trap*. PhD thesis, Johannes Gutenberg-Universitat, 2010.

[190] J. Obrecht, R. Wild, M. Antezza, L. Pitaevskii, S. Stringari, and E. Cornell, "Measurement of the Temperature Dependence of the Casimir-Polder Force," *Physical Review Letters*, vol. 98, p. 063201, 2007.

[191] T. Grünzweig, A. Hilliard, M. McGovern, and M. F. Andersen, "Near-deterministic preparation of a single atom in an optical microtrap," *Nature Physics*, vol. 6, p. 951, 2010.

[192] A. Boozer, A. Boca, R. Miller, T. Northup, and H. Kimble, "Cooling to the Ground State of Axial Motion for One Atom Strongly Coupled to an Optical Cavity," *Physical Review Letters*, vol. 97, p. 083602, 2006.

[193] A. Goban, C. L. Hung, S. P. Yu, J. D. Hood, J. A. Muniz, J. H. Lee, M. J. Martin, A. C. McClung, K. S. Choi, D. E. Chang, O. Painter, and H. J. Kimble, "Atom–light interactions in photonic crystals," *Nature communications*, vol. 5, p. 3808, 2014.

[194] J. I. Cirac, P. Zoller, H. J. Kimble, and H. Mabuchi, "Quantum state transfer and entanglement distribution among distant nodes in a quantum network," *Physical Review Letters*, vol. 78, p. 3221, 1997.

[195] L. M. Duan and H. J. Kimble, "Scalable photonic quantum computation through cavity-assisted interactions," *Physical Review Letters*, vol. 92, p. 127902, 2004.

[196] J. T. Shen and S. Fan, "Coherent photon transport from spontaneous emission in one-dimensional waveguides," *Optics letters*, vol. 30, p. 2001, 2005.

[197] F. Le Kien, S. D. Gupta, K. P. Nayak, and K. Hakuta, "Nanofiber-mediated radiative transfer between two distant atoms," *Physical Review A*, vol. 72, p. 063815, 2005.

[198] N. Bhat and J. Sipe, "Hamiltonian treatment of the electromagnetic field in dispersive and absorptive structured media," *Physical Review A*, vol. 73, p. 063808, 2006.

[199] J. K. Asbóth, H. Ritsch, and P. Domokos, "Optomechanical coupling in a one-dimensional optical lattice," *Physical Review A*, vol. 77, p. 063424, 2008.

[200] D. Dzsotjan, A. S. Sørensen, and M. Fleischhauer, "Quantum emitters coupled to surface plasmons of a nanowire: a Green's function approach," *Physical Review B*, vol. 82, p. 075427, 2010.

[201] M. Gullans, T. G. Tiecke, D. E. Chang, and J. Feist, "Nanoplasmonic lattices for ultracold atoms," *Physics Review Letters*, vol. 109, p. 235309, 2012.

[202] D. Chang, J. Cirac, and H. Kimble, "Self-Organization of Atoms along a Nanophotonic Waveguide," *Physical Review Letters*, vol. 110, p. 113606, 2013.

[203] D. W. Vernooy, A. Furusawa, and N. P. Georgiades, "Cavity QED with high-Q whispering gallery modes," *Physical Review A*, p. R2293(R), 1998.

[204] B. Lev, K. Srinivasan, P. Barclay, O. Painter, and H. Mabuchi, "Feasibility of detecting single atoms using photonic bandgap cavities," *Nanotechnology*, vol. 15, p. S556, 2004.

[205] G. Lepert, M. Trupke, M. J. Hartmann, M. B. Plenio, and E. A. Hinds, "Arrays of waveguide-coupled optical cavities that interact strongly with atoms," *New Journal of Physics*, vol. 13, p. 113002, 2011.

[206] P. E. Barclay, *Fiber-coupled nanophotonic devices for nonlinear optics and cavity QED*. PhD thesis, California Institute of Technology, 2007.

[207] G. D. Marshall, A. Politi, J. C. F. Matthews, P. Dekker, M. Ams, M. J. Withford, and J. L. O'Brien, "Laser written waveguide photonic quantum circuits," *Optics Express*, vol. 17, p. 12546, 2009.

[208] Y. Taguchi, Y. Takahashi, Y. Sato, T. Asano, and S. Noda, "Statistical studies of photonic heterostructure nanocavities with an average Q factor of three million," *Optics Express*, vol. 19, p. 11916, 2011.

[209] M. C. Tien, J. F. Bauters, M. Heck, and D. T. Spencer, "Ultra-high quality factor planar Si 3 N 4 ring resonators on Si substrates," *Optics Express*, vol. 19, p. 13551, 2011.

[210] K. Luke, A. Dutt, C. B. Poitras, and M. Lipson, "Overcoming Si_3N_4 film stress limitations for high quality factor ring resonators," *Optics Express*, vol. 21, p. 22829, 2013.

[211] M. Soljacic, S. G. Johnson, S. H. Fan, M. Ibanescu, E. Ippen, and J. D. Joannopoulos, "Photonic-crystal slow-light enhancement of nonlinear phase sensitivity," *Journal of the Optical Society of America B-Optical Physics*, vol. 19, p. 2052, 2002.

[212] A. F. Koenderink, M. Kafesaki, C. M. Soukoulis, and V. Sandoghdar, "Spontaneous emission rates of dipoles in photonic crystal membranes," *Journal of the Optical Society of America B-Optical Physics*, vol. 23, p. 1196, 2006.

[213] T. Lund-Hansen, S. Stobbe, B. Julsgaard, H. Thyrrestrup, T. Sünner, M. Kamp, A. Forchel, and P. Lodahl, "Experimental Realization of Highly Efficient Broadband Coupling of Single Quantum Dots to a Photonic Crystal Waveguide," *Physical Review Letters*, vol. 101, p. 113903, 2008.

[214] P. Yao, V. S. C. M. Rao, and S. Hughes, "On-chip single photon sources using planar photonic crystals and single quantum dots," *Laser & Photonics Reviews*, vol. 4, p. 499, 2010.

[215] T. Ba Hoang, J. Beetz, L. Midolo, M. Skacel, M. Lermer, M. Kamp, S. Höfling, L. Balet, N. Chauvin, and A. Fiore, "Enhanced spontaneous emission from quantum dots in short photonic crystal waveguides," *Applied Physics Letters*, vol. 100, p. 061122, 2012.

[216] C. L. Hung, S. M. Meenehan, D. E. Chang, O. Painter, and H. J. Kimble, "Trapped atoms in one-dimensional photonic crystals," *New Journal of Physics*, vol. 15, p. 083026, 2013.

[217] S. P. Yu, J. D. Hood, J. A. Muniz, M. J. Martin, R. Norte, C. L. Hung, S. M. Meenehan, J. D. Cohen, O. Painter, and H. J. Kimble, "Nanowire photonic crystal waveguides for single-atom trapping and strong light-matter interactions," *Applied Physics Letters*, vol. 104, p. 111103, 2014.

[218] J. D. Cohen, S. M. Meenehan, and O. Painter, "Optical coupling to nanoscale optomechanical cavities for near quantum-limited motion transduction," *Optics Express*, vol. 21, p. 11227, 2013.

[219] M. K. Tey, Z. Chen, S. A. Aljunid, B. Chng, F. Huber, G. Maslennikov, and C. Kurtsiefer, "Strong interaction between light and a single trapped atom without the need for a cavity," *Nature Physics*, vol. 4, p. 924, 2008.

[220] G. Wrigge, I. Gerhardt, J. Hwang, G. Zumofen, and V. Sandoghdar, "Efficient coupling of photons to a single molecule and the observation of its resonance fluorescence," *Nature Physics*, vol. 4, p. 60, 2008.

[221] S. J. J. Joannopoulos, "Block-iterative frequency-domain methods for Maxwell's equations in a planewave basis," *Optics Express*, vol. 8, p. 173, 2001.

[222] A. Gomez-Iglesias, D. O'Brien, L. O'Faolain, A. Miller, and T. F. Krauss, "Direct measurement of the group index of photonic crystal waveguides via Fourier transform spectral interferometry," *Applied Physics Letters*, vol. 90, p. 261107, 2007.

[223] J. Topolancik, B. Ilic, and F. Vollmer, "Experimental Observation of Strong Photon Localization in Disordered Photonic Crystal Waveguides," *Physical Review Letters*, vol. 99, p. 253901, 2007.

[224] P. D. García, S. Smolka, S. Stobbe, and P. Lodahl, "Density of states controls Anderson localization in disordered photonic crystal waveguides," *Physical Review B*, vol. 82, p. 165103, 2010.

[225] A. M. Kaufman, B. J. Lester, and C. A. Regal, "Cooling a Single Atom in an Optical Tweezer to Its Quantum Ground State," *Physical Review X*, vol. 2, p. 041014, 2012.

[226] J. Thompson, T. Tiecke, A. Zibrov, V. Vuletić, and M. Lukin, "Coherence and Raman Sideband Cooling of a Single Atom in an Optical Tweezer," *Physical Review Letters*, vol. 110, p. 133001, 2013.

[227] P. Markos and C. M. Soukoulis, *Wave Propagation*. From Electrons to Photonic Crystals and Left-Handed Materials, Princeton University Press, 2008.

[228] S. H. Fan, "Sharp asymmetric line shapes in side-coupled waveguide-cavity systems," *Applied Physics Letters*, vol. 80, p. 908, 2002.

[229] Lumerical Solution Inc., *http://www.lumerical.com/tcad-products/fdtd/*.

[230] W. Wohlleben, F. Chevy, K. Madison, and J. Dalibard, "An atom faucet," *European Physical Journal D*, vol. 15, p. 237, 2001.

[231] M. T. DePue, S. L. Winoto, D. J. Han, and D. S. Weiss, "Transient compression of a MOT and high intensity fluorescent imaging of optically thick clouds of atoms," *Optics Communications*, vol. 180, p. 73, 2000.

[232] S. Q. Shang, B. Sheehy, H. Metcalf, P. Vanderstraten, and G. Nienhuis, "Velocity-Selective Resonances and Sub-Doppler Laser Cooling," *Physical Review Letters*, vol. 67, p. 1094, 1991.

[233] A. Goban, C. L. Hung, J. D. Hood, S. P. Yu, J. A. Muniz, O. Painter, and H. J. Kimble, "Superradiance for atoms trapped along a photonic crystal waveguide," *arXiv:150.04503*, 2015.

[234] J. A. Mlynek, A. A. Abdumalikov, C. Eichler, and A. Wallraff, "Observation of Dicke superradiance for two artificial atoms in a cavity with high decay rate," *Nature Communications*, vol. 5, p. 5186, 2014.

[235] P. Lodahl, S. Mahmoodian, and S. Stobbe, "Interfacing single photons and single quantum dots with photonic nanostructures," *arXiv:1312.1079*, 2013.

[236] A. Kuzmich, W. P. Bowen, A. D. Boozer, A. Boca, and C. W. Chou, "Generation of nonclassical photon pairs for scalable quantum communication with atomic ensembles," *Nature*, vol. 423, p. 731, 2003.

[237] C. H. van der Wal, M. D. Eisaman, A. André, R. L. Walsworth, D. F. Phillips, A. S. Zibrov, and M. D. Lukin, "Atomic Memory for Correlated Photon States," *Science*, vol. 301, p. 196, 2003.

[238] B. Casabone, K. Friebe, B. Brandstaetter, K. Schueppert, R. Blatt, and T. E. Northup, "Enhanced Quantum Interface with Collective Ion-Cavity Coupling," *Physical Review Letters*, vol. 114, p. 023602, 2015.

[239] R. Reimann, W. Alt, T. Kampschulte, T. Macha, L. Ratschbacher, N. Thau, S. Yoon, and D. Meschede, "Cavity-Modified Collective Rayleigh Scattering of Two Atoms," *Physical Review Letters*, vol. 114, p. 023601, 2015.

[240] A. T. Black, J. K. Thompson, and V. Vuletić, "On-demand superradiant conversion of atomic spin gratings into single photons with high efficiency," *Physical Review Letters*, vol. 95, p. 133601, 2005.

[241] H. W. Chan, A. T. Black, and V. Vuletić, "Observation of collective-emission-induced cooling of atoms in an optical cavity," *Physical Review Letters*, vol. 90, p. 063003, 2003.

[242] M. Wolke, J. Klinner, H. Kessler, and A. Hemmerich, "Cavity Cooling Below the Recoil Limit," *Science*, vol. 337, p. 75, 2012.

[243] J. G. Bohnet, Z. Chen, J. M. Weiner, D. Meiser, M. J. Holland, and J. K. Thompson, "A steady-state superradiant laser with less than one intracavity photon," *Nature*, vol. 484, p. 78, 2012.

[244] T. Grießer and H. Ritsch, "Light-Induced Crystallization of Cold Atoms in a 1D Optical Trap," *Physical Review Letters*, vol. 111, p. 055702, 2013.

[245] A. Svidzinsky and J.-T. Chang, "Cooperative spontaneous emission as a many-body eigenvalue problem," *Physical Review A*, vol. 77, p. 043833, 2008.

[246] M. O. Scully, "Collective Lamb Shift in Single Photon Dicke Superradiance," *Physical Review Letters*, vol. 102, no. 14, p. 143601, 2009.

[247] R. Roehlsberger, K. Schlage, B. Sahoo, S. Couet, and R. Rueffer, "Collective Lamb Shift in Single-Photon Superradiance," *Science*, vol. 328, p. 1248, 2010.

[248] J. Keaveney, A. Sargsyan, U. Krohn, I. G. Hughes, D. Sarkisyan, and C. S. Adams, "Cooperative Lamb Shift in an Atomic Vapor Layer of Nanometer Thickness," *Physical Review Letters*, vol. 108, p. 173601, 2012.

[249] G. Kurizki, "Two-atom resonant radiative coupling in photonic band structures," *Physical Review A*, vol. 42, p. 2915, 1990.

[250] P. Lambropoulos, G. M. Nikolopoulos, T. R. Nielsen, and S. Bay, "Fundamental quantum optics in structured reservoirs," *Reports on Progress in Physics*, vol. 63, p. 455, 2000.

[251] A. Gonzalez-Tudela, C. L. Hung, D. E. Chang, J. I. Cirac, and H. J. Kimble, "Subwavelength vacuum lattices and atom-atom interactions in photonic crystals," *Nature photonics*, vol. 9, p. 320, 2015.

[252] COMSOL, "http://www.comsol.com ."

[253] R. J. Rafac, C. E. Tanner, A. E. Livingston, and H. G. Berry, "Fast-beam laser lifetime measurements of the cesium $6p^2P_{1/2,3/2}$ states," *Physical Review A*, vol. 60, p. 3648, 1999.

[254] A. F. Oskooi, D. Roundy, M. Ibanescu, P. Bermel, J. D. Joannopoulos, and S. G. Johnson, "MEEP: A flexible free-software package for electromagnetic simulations by the FDTD method," *Computer Physics Communications*, vol. 181, p. 687, 2010.

[255] G. Agarwal, "Quantum electrodynamics in the presence of dielectrics and conductors. I. Electromagnetic-field response functions and black-body fluctuations in finite geometries," *Physical Review A*, vol. 11, p. 230, 1975.

[256] S. Y. Buhmann, L. Knoll, D. G. Welsch, and H. T. Dung, "Casimir-Polder forces: A nonperturbative approach," *Physical Review A*, vol. 70, p. 052117, 2004.

[257] S. Y. Buhmann and D.-G. Welsch, "Casimir-Polder forces on excited atoms in the strong atom-field coupling regime," *Physical Review A*, vol. 77, p. 012110, 2008.

[258] R. J. Thompson, Q. A. Turchette, O. Carnal, and H. J. Kimble, "Nonlinear spectroscopy in the strong-coupling regime of cavity QED," *Physical Review A*, vol. 57, p. 3084, 1998.

[259] I. Bloch and W. Zwerger, "Many-body physics with ultracold gases," *Reviews of Modern Physics*, vol. 80, p. 885, 2008.

[260] R. Blatt and C. F. Roos, "Quantum simulations with trapped ions," *Nature Physics*, vol. 8, p. 277, 2012.

[261] B. Yan, S. A. Moses, B. Gadway, J. P. Covey, and K. Hazzard, "Observation of dipolar spin-exchange interactions with lattice-confined polar molecules," *Nature*, vol. 501, p. 521, 2013.

[262] M. Lu, N. Q. Burdick, S. H. Youn, and B. L. Lev, "Strongly dipolar Bose-Einstein condensate of dysprosium," *Physical Review Letters*, vol. 107, p. 190401, 2011.

[263] K. Aikawa, A. Frisch, M. Mark, S. Baier, A. Rietzler, R. Grimm, and F. Ferlaino, "Bose-Einstein Condensation of Erbium," *Physical Review Letters*, vol. 108, p. 210401, 2012.

[264] M. Saffman, T. G. Walker, and K. Mølmer, "Quantum information with Rydberg atoms," *Reviews of Modern Physics*, vol. 82, p. 2313, 2010.

[265] H. Krauter, C. A. Muschik, K. Jensen, W. Wasilewski, J. M. Petersen, J. I. Cirac, and E. S. Polzik, "Entanglement Generated by Dissipation and Steady State Entanglement of Two Macroscopic Objects," *Physical Review Letters*, vol. 107, p. 080503, 2011.

[266] A. Gonzalez-Tudela, D. Martin-Cano, E. Moreno, L. Martin-Moreno, C. Tejedor, and F. J. Garcia-Vidal, "Entanglement of Two Qubits Mediated by One-Dimensional Plasmonic Waveguides," *Physical Review Letters*, vol. 106, no. 2, p. 020501, 2011.

[267] A. Gonzalez-Tudela and D. Porras, "Mesoscopic Entanglement Induced by Spontaneous Emission in Solid-State Quantum Optics," *Physical Review Letters*, vol. 110, p. 080502, 2013.

[268] A. Gonzalez-Tudela, V. Paulisch, D. E. Chang, H. J. Kimble, and J. I. Cirac, "Deterministic generation of arbitrary photonic states assisted by dissipation," *arXiv:1504.07600*, 2015.

[269] P. Domokos, P. Horak, and H. Ritsch, "Quantum description of light-pulse scattering on a single atom in waveguides," *Physical Review A*, vol. 65, p. 033832, 2002.

[270] J.-T. Shen and S. Fan, "Theory of single-photon transport in a single-mode waveguide. II. Coupling to a whispering-gallery resonator containing a two-level atom," *Physical Review A*, vol. 79, p. 023838, 2009.

[271] J.-T. Shen and S. Fan, "Theory of single-photon transport in a single-mode waveguide. I. Coupling to a cavity containing a two-level atom," *Physical Review A*, vol. 79, p. 023837, 2009.

[272] Ş. E. Kocabaş, E. Rephaeli, and S. Fan, "Resonance fluorescence in a waveguide geometry," *Physical Review A*, vol. 85, p. 023817, 2012.

[273] Y.-L. L. Fang and H. U. Baranger, "Waveguide QED: Two Photons, Many Qubits, and a Mirror," *arXiv:1502.03803*, 2015.

[274] C. Cohen-Tannoudji, J. Dupont-Roc, and G. Grynberg, *Atom-Photon Interactions*. Wiley-VCH, 1998.